



PhD Thesis

UNIVERSITAT POLITÈNICA DE CATALUNYA (UPC)
ESCOLA T.S. D'ENGINEYERS DE CAMINS, CANALS I PORTS
(Technical University of Catalonia)
(School of Civil Engineering)

Department of Geotechnical Engineering and Geosciences

**Numerical modelling of delayed and
progressive failure in stiff clays with two-
stage softening behaviour**

by

Zhifeng Zhan

Advisor

Antonio Gens Solé

Barcelona, May, 2012

Abstract

The stress-strain behaviour of stiff overconsolidated clays is now well known to be highly inelastic and nonlinear. Before peak strength mobilises, strain-hardening processes. Just after peak strength, strain softening happens, and this is different from behaviour of soft clays and loose sands. The post-failure behaviour of stiff overconsolidated clays has been delineated by laboratory tests, microstructure examination and constitutive models.

Peak strength and residual strength characteristics of stiff clays have been studied through laboratory tests. Especially, optical and scanning electron microscope methods have been used successfully to examine the structure change of failure zone in stiff clays until the arrival of residual strength. The results of these tests elucidate a point dividing the post-failure softening feature of stiff clays into two stages. This point is defined firstly by Burland (1990) as post-rupture strength. The two stages include a relatively rapid reduction from peak to post-rupture strength, followed by a gradual reduction to residual strength. In this paper, data from tests and numerical analyses related with post-rupture strength is collected and analysed. Laboratory, field and numerical results verify the existence and robustness of post-rupture strength for stiff overconsolidated clays. In addition, analysis of the collected data demonstrates that the post-peak strain-softening characteristics of stiff clays can be divided into two stages. The microstructure studies indicate that the first softening stage is induced by the loss of interbonding between particles, i.e. the cohesive component of strength at relatively small displacement and hence termed as cementation loss; while the second is due to the gradual realignment, i.e. reorientation of clay particles at large displacements and can be called as gradual frictional resistance loss.

So far, only experimental studies have been conducted to investigate the post-rupture strength property of stiff clays. Existing constitutive soil models do not consider this observed two-stage post-peak softening behaviour. Models such as the non-linear strain-softening and strain-hardening model based on improved Mohr-Coulomb model can describe the mobilised soil strength between peak and residual states via assuming linear or exponential softening rules for strength parameters c' and ϕ' . However, this model is unable to distinguish the two-stage softening feature of stiff clays. In view of this point, this thesis aims to establish a generalised constitutive model to simulate the two-stage softening characteristics of stiff overconsolidated clays by modifying the existing models mentioned above. The formulation of this model is illustrated at length and then implemented into an explicit finite difference program *FLAC* (ITASCA) based on an embedded strain-hardening/softening model.

Afterwards the new model is applied to simulate laboratory tests such as triaxial compression tests and direct shear box test to depict the new model. All the numerical results demonstrate the capability and efficiency of the modified softening model via *FLAC* to model the two-stage strain-softening behaviour of stiff clays. The mesh influence can be eliminated efficiently with a special scheme, which relates the slope of softening to a characteristic dimension of the mesh elements in such a way that their ratio is kept constant.

Furthermore, this model can be used to simulate realistic engineering problems in which progressive failure is a quite traditional and common one. A series of analyses of delayed progressive failure of cut slopes in stiff clays with *FLAC* similar to those conducted by Potts et al. (1997) have been performed using two-stage softening model incorporating post-rupture strength. The numerical results reproduce well the progressive failure process, position of failure surface and failure time, which proves further the validity of the new model. Meanwhile, parametric analyses such as K_0 effect, surface suction effect, slope geometry effect, influence of post-rupture strength parameters and critical stable cutting height are also carried out to demonstrate the general influence of post-rupture strength. All the results demonstrate that the slope stability with the adoption of two-stage softening model is reduced compared with that using one-stage softening model due to the quicker cohesion reduction with deviatoric plastic strain in the first softening stage of two-stage softening model. Post-rupture strength is of significance to account for the quicker cohesion degradation at the first stage in two-stage softening model.

Especially, both post-rupture strength concept and two-stage softening model are applied to the modelling of a famous case—Aznalcóllar dam failure (Alonso & Gens, 2006a; Gens & Alonso, 2006) under both inhomogeneous and homogeneous hypotheses. This modelling is the complement of numerical simulation performed by Gens & Alonso (2006) and makes up the deficiency of numerical modelling by Olalla & Cuéllar (2001) and Gens & Alonso (2006) with the use of realistic and reasonable modelling procedure of softening. The simulations reproduced well the failure of Aznalcóllar dam including the location and shape of the slip surface, the progressive failure course and the development of pore water pressure in terms of the developments of shear strain rate, shear strain increment, displacement, velocity and strength parameter softening. The mechanism of Aznalcóllar dam failure is deemed to be progressive failure mainly due to the softening of Guadalquivir blue clay. Moreover, the developments of average stress ratio, average residual factor, average brittleness, average stress path, the distribution of shear stress and mobilised strength parameters along the slip surface confirm further the mechanism of progressive failure of Aznalcóllar dam with these values to be intermediate between relevant peak and residual values during the failure course. The post-rupture state could be thought as the average one at initial failure. At final failure, most part of the slip surface is at residual state, especially along the horizontal part. In addition, the Aznalcóllar dam failure is sensitive to the softening rate denoted by γ_{pr} and γ_r . Larger rates will induce earlier failure and no failure will occur with slow softening rate. Only an appropriate setting of softening rate can cause failure at final phase under both inhomogeneous and homogeneous hypotheses.

Finally, the post-rupture strength for stiff overconsolidated clays is introduced to analytical solutions to cylindrical cavity expansion in stiff overconsolidated clay. The analytical solutions to limit pressure, the stress, strain, and displacement fields for the expansion of cylindrical cavity have been derived in a simple way. This method can cope especially with stiff overconsolidated clays and overcome the defects in the classical theory about the expansion of elastoplastic cylindrical cavity. The computational examples indicate that the quadrilinear softening model can degenerate to the original trilinear model and gives the same results as those published. The similarity between numerical solution and analytical one verifies the reasonableness of the analytical solution to cavity expansion in stiff clays with two-stage softening



characteristics. This analysis illuminates the possibility of generalisation of post-rupture strength concept and the relevant two-stage softening model in geotechnical engineering problems.



Résumé

Il est bien connu que le comportement contrainte-déformation de l'argile est très inélastique, sur-consolidé, rigide et non-linéaire. Préalablement à la mobilisation de la résistance maximale du sol, d'un processus de l'écroutissage, tandis que, après avoir atteint le pic de force, le sol subit un processus de ramollissement souche. Ce comportement est différent de celui présenté en argile et sable. Le comportement post-rupture, rigide et sur-consolidé est caractéristique des expériences de laboratoire, de l'examen de la microstructure et constituant les modèles.

Les caractéristiques de résistance et de teneur résiduelle maximale en argile dure ont été étudiées à travers des expériences de laboratoire. En particulier, les méthodes de microscopie électronique et optique de scanner ont été utilisées avec succès pour envisager de modifier la structure de la zone de rupture de l'argile dure pour atteindre la résistance résiduelle. Les résultats de ces tests révèlent l'existence d'un point qui divise le ramollissement post-courbe de rupture de l'argile dure en deux étapes. Ce point a été initialement défini par Burland (1990) comme la résistance post-rupture. Les deux mesures comprennent une réduction rapide de la résistance de la force de pointe après la pause, suivie d'une réduction progressive jusqu'à ce que la résistance résiduelle. Dans cette vue, les résultats des tests de laboratoire et de l'analyse numérique liées à la résistance post-rupture ont été recueillies et analysées. Les résultats des tests de laboratoire, sur le terrain et l'analyse numérique de vérifier l'existence et la force de la résistance après la rupture de l'argile rigide sur-consolidé. L'analyse statistique a pour sa part, montré que la réaction de la souche de ramollissement post-pic des argiles rigides peut être divisé en deux étapes. Les études indiquent que la microstructure de la première phase de l'amortissement est induite par la perte d'interconnexion entre les particules, ou de la cohésion du mouvement de résistance relativement faible, connue comme la perte de ciment, tandis que la deuxième phase est, en raison de la réorganisation ou la réorientation progressive des particules d'argile, pour les grands déplacements et peut être appelé comme une perte graduelle de la résistance de frottement.

Jusqu'à présent, seuls des études expérimentales ont été réalisées pour étudier les caractéristiques de la résistance après la rupture des argiles rigide constituant les modèles existants ne considèrent pas le sol pour effectuer le ramollissement post-pic en deux étapes. Les modèles non linéaires tels que la souche de ramollissement et de l'écroutissage sur la base du modèle amélioré de Mohr-Coulomb mobilisés pour décrire la résistance du sol entre le sommet et les résidus en supposant que les États des règles de ramollissement exponentielle ou linéaire pour les paramètres de résistance c' et ϕ' . Toutefois, ce modèle ne permet pas de distinguer la fonction d'amortir en deux étapes de l'argile dure. En raison de cette limitation, l'objectif de cette thèse est d'établir un modèle pour simuler les caractéristiques de ramollissement en deux étapes de l'argile dure sur-consolidé modifiant les modèles existants mentionnés ci-dessus. La formulation de ce modèle est illustrée dans le détail et mis en œuvre explicite des différences finies *FLAC* (Itasca) basé sur un modèle de mise en œuvre de durcissement/adoucissement de la souche.

Après cela, le nouveau modèle est validé par la simulation des tests de laboratoire tels que les tests de compression triaxial et la coupe directe. Numerical résultats démontrent la capacité et l'efficacité du modèle modifié par le ramollissement *FLAC* pour reproduire le comportement de la souche de ramollissement en deux étapes de l'argile dure. L'influence de la maille peut être éliminée de manière efficace avec un régime spécial qui provoque à un ramollissement de la caractéristique de l'échelle, de sorte que leur rapport reste constant.

En outre, ce modèle peut être utilisé pour simuler de réels problèmes d'ingénierie, y compris le phénomène de rupture qui en est un très commun et traditionnelle. *FLAC* a été réalisée avec une série d'analyses progressive de retard de la rupture de digues sur l'argile à la rigidité similaire mené par Potts et al. (1997), en utilisant le nouveau modèle de ramollissement en deux étapes avec l'ajout de la résistance post-rupture. Les résultats numériques reproduisent assez bien le processus de la rupture, la position de la surface de rupture et temps de pause; ce qui fournit d'autres à la validité du nouveau modèle. De plus, il a effectué une analyse paramétrique de l'effet K_0 , de l'effet d'aspiration de la surface, l'effet de la géométrie de la pente, l'influence des paramètres de la résistance post-rupture et la hauteur minimale de la pente à démontrer l'influence de la résistance post-rupture. Tous les résultats démontrent que la stabilité des pentes avec l'adoption du modèle de ramollissement en deux étapes est réduit par rapport à ce modèle de ramollissement en une étape, en raison de la réduction plus rapide de cohésion avec la déformation plastique déviatorique dans la première phase de ramollissement du modèle de ramollissement en deux étapes. Et la résistance post-rupture est important d'expliquer la dégradation plus rapide de la cohésion dans la première phase de ramollissement dans le modèle en deux étapes.

En particulier, le concept de la résistance à la post-rupture et le mode de ramollissement en deux étapes sont appliquées dans la simulation numérique du célèbre cas de rupture du barrage d'Aznalcóllar (Alonso et Gens, 2006a; Gens & Alonso, 2006) sous les deux scénarios homogènes et hétérogènes. La simulation est un complément à la simulation numérique par Gens et Alonso (2006) et compense la carence de la simulation numérique par Olalla et Cuellar (2001) et Gens et Alonso (2006), en utilisant une modélisation de processus de ramollissement plus réaliste et raisonnable. La simulation reproduit bien brisé la barrière de Aznalcóllar y compris le processus de rupture de la forme de la surface et le développement de la pression de l'eau dans les pores de la peau, en fonction de l'état de la plasticité, réduction du taux de déformation, l'augmentation de la coupe de déformation, de déplacement, la vitesse et des paramètres de résistance au ramollissement.

Le mécanisme de rupture du barrage est considéré Aznalcóllar rupture due principalement à l'adoucissement progressif de la masse d'argile bleue du Guadalquivir. En outre, le développement de la moyenne des tensions, le facteur résiduel, fragile milieu tensions moitié et la distribution de crack et de paramètres de coupe mobilisé mobilisés résistance le long de la surface de glissement, confirmant le mécanisme de la rupture du barrage d'Aznalcóllar progressive de ces valeurs dans l'intervalle entre la crête et la valeur résiduelle au cours du processus de rupture. L'état post-rupture pourrait être considéré comme un moyen à la première fracture. À la fin de la pause de plus la surface est à l'état résiduel, en particulier le long de la partie horizontale. En outre, la rupture du barrage Aznalcóllar est sensible à la vitesse de ramollissement de la déformation plastique de la coupe (γ_p , γ_{pr} et γ_r). Une vitesse

plus élevée provoquera la rupture plus tôt et pas de rupture se produit avec la lenteur de ramollissement. Seule une valeur appropriée de la vitesse de ramollissement de la déformation plastique de la coupe peut causer une défaillance dans l'étape finale dans les scénarios à la fois homogènes et inhomogènes.

Enfin, la résistance post-rupture de l'argile rigide sur-consolidé est une des solutions analytiques dans l'expansion de la cavité cylindrique en argile dure sur-consolidé. L'analyse des solutions pour limiter la pression, le stress, la déformation et le déplacement des champs d'expansion de la cavité cylindrique ont été dérivé d'une façon simple. Cette méthode peut être utilisée avec de l'argile sur-consolidé et peut aussi corriger les lacunes de la théorie classique de l'expansion d'une cavité cylindrique elastoplastique. Les exemples numériques montrent que le modèle peut conduire à un ramollissement quadrilinéaire trilineaire modèle original et donne les mêmes résultats que ceux publiés. La similitude entre la solution analytique et numérique de vérifier le caractère raisonnable de la solution analytique de l'élargissement de la cavité dans l'argile dure avec des caractéristiques de ramollissement en deux étapes. Cette analyse permet la généralisation de la notion de la résistance post-rupture et l'importance de l'adoucissement de modèle en deux étapes pour résoudre certains problèmes géotechniques.



Resumen

Es bien conocido que el comportamiento tensión-deformación de las arcillas rígidas sobreconsolidadas es altamente inelástico y no-lineal. Antes de la movilización de resistencia pico el suelo experimenta un proceso de endurecimiento por deformación, mientras que luego de alcanzar la resistencia pico, el suelo experimenta un proceso de ablandamiento por deformación. Este comportamiento es diferente al que se presenta en arcillas blandas y arenas sueltas. El comportamiento post-ruptura de las arcillas rígidas sobreconsolidadas ha sido caracterizado mediante experimentos de laboratorio, el examen de la microestructura y los modelos constitutivos.

Las características de resistencia máxima y residual de las arcillas rígidas se han estudiado a través de experimentos de laboratorio. En particular, los métodos de microscopio electrónico de escáner y óptico, se han utilizado exitosamente para examinar el cambio de la estructura de la zona de rotura en las arcillas rígidas hasta alcanzar la resistencia residual. Los resultados de estas pruebas dejan ver la existencia de un punto que divide la curva de ablandamiento post-ruptura de las arcillas rígidas en dos etapas. Este punto fue definido inicialmente por Burland (1990) como la resistencia post-ruptura. Las dos etapas incluyen una reducción relativamente rápida de la resistencia desde el pico a la resistencia post-ruptura, seguida por una reducción gradual hasta la resistencia residual. En esta tesis, los resultados existentes de pruebas de laboratorio y de análisis numéricos relacionados con la resistencia post-ruptura se han recopilado y analizado. Los resultados de las pruebas de laboratorio, de campo y los análisis numéricos verifican la existencia y la robustez de la resistencia post-ruptura de las arcillas rígidas sobreconsolidadas. El análisis estadístico por su parte, demuestra que la respuesta de ablandamiento por deformación post-pico de las arcillas rígidas se puede dividir en dos etapas. Los estudios de la microestructura indican que la primera etapa del ablandamiento está inducida por la pérdida de interconexión entre las partículas, o de la componente cohesiva de la resistencia a desplazamientos relativamente pequeños, conocida como pérdida de cementación; mientras que la segunda etapa es debida al realineamiento gradual o reorientación de las partículas de arcilla a grandes desplazamientos y se puede llamar como pérdida gradual de la resistencia friccional.

Hasta el momento solo se han conducido estudios experimentales para investigar las características de la resistencia post-ruptura de las arcillas rígidas, los modelos constitutivos existentes del suelo no consideran el comportamiento observado de ablandamiento post-pico en dos etapas. Modelos como el no lineal de ablandamiento por deformación y endurecimiento por deformación basado en el modelo mejorado de Mohr-Coulomb permiten describir la resistencia movilizada del suelo entre los estados pico y residual suponiendo reglas de ablandamiento lineales o exponenciales para los parámetros de resistencia c' y ϕ' . Sin embargo, este modelo no puede distinguir el rasgo característico de ablandamiento en dos etapas de las arcillas rígidas. Debido a esta limitación, el objetivo de esta tesis es establecer un modelo constitutivo generalizado para simular las características de ablandamiento en dos etapas de las arcillas rígidas sobreconsolidadas, modificando los modelos existentes mencionados

anteriormente. La formulación de este modelo es ilustrada detalladamente y luego implementada en un programa explícito de diferencia finitas *FLAC* (ITASCA) basado en un modelo implementado de endurecimiento/ablandamiento por deformación.

Después de esto, el nuevo modelo es validado mediante la simulación de ensayos de laboratorio como ensayos de compresión triaxial y ensayos de corte directo. Los resultados numéricos demuestran la capacidad y eficiencia del modelo modificado de ablandamiento a través de *FLAC* para reproducir el comportamiento de ablandamiento por deformación en dos etapas de las arcillas rígidas. La influencia de la malla se puede eliminar eficientemente con un esquema especial que relaciona la pendiente del ablandamiento con una dimensión característica de los elementos de tal manera que su cociente se mantiene constante.

Adicionalmente, este modelo puede utilizarse para simular problemas realistas de ingeniería entre los cuales el fenómeno de la rotura progresiva es uno muy común y tradicional. Se han realizado con *FLAC* una serie de análisis de la rotura progresiva diferida de taludes en arcillas rígidas similar a los conducidos por Potts et al., (1997), utilizando el nuevo modelo de ablandamiento en dos etapas con incorporación de la resistencia de post-ruptura. Los resultados numéricos reproducen bastante bien el proceso progresivo de la rotura, la posición de la superficie de rotura y el tiempo de rotura, lo cual brinda validez adicional al nuevo modelo. Adicionalmente, se ha llevado a cabo un análisis paramétrico del efecto de K_0 , el efecto de la succión superficial, el efecto de geometría del talud, la influencia de los parámetros de la resistencia de post-ruptura y la altura mínima de seguridad del talud, para demostrar la influencia general de la resistencia de post-ruptura. Todos los resultados demuestran que se reduce la estabilidad de los taludes con la adopción del modelo de ablandamiento de dos etapas en comparación con lo de solo una etapa, debido a la reducción más rápida de la cohesión con la deformación plástica en primera fase de ablandamiento del modelo de ablandamiento de dos etapas. Y la resistencia post-ruptura es importante de explicar la degradación de la cohesión más rápida en la primera etapa en el modelo de ablandamiento de dos etapas.

En particular, el concepto de la resistencia post-ruptura y el modelo de ablandamiento en dos etapas son aplicados en la simulación numérica del famoso caso de la rotura de la presa de Aznalcóllar (Alonso & Gens, 2006a; Gens & Alonso, 2006) bajo las dos hipótesis no homogéneas y homogénea. La simulación es un complemento de la simulación numérica presentada por Gens & Alonso (2006) y compensa la deficiencia de las simulaciones numéricas presentadas por Olalla & Cuéllar (2001) y Gens & Alonso (2006), al utilizar un procedimiento de modelización del ablandamiento más realista y razonable. Las simulaciones reproduce bien la rotura de la presa de Aznalcóllar incluyendo el proceso progresivo de la rotura, la ubicación y la forma de la superficie de deslizamiento y el desarrollo de la presión del agua en los poros, según el desarrollo del estado de la plasticidad, la velocidad de la deformación de corte, el incremento de la deformación de corte, el desplazamiento, la velocidad y parámetros de resistencia del ablandamiento.

El mecanismo de rotura de la presa de Aznalcóllar es considerado como de rotura progresiva debida principalmente al ablandamiento de la masa de arcilla azul del Guadalquivir. Por otra parte, el desarrollo de la relación media de las tensiones, el factor residual, la fragilidad media, la trayectoria de tensiones media y la distribución de las tensiones de corte movilizadas y los parámetros de resistencia movilizadas a lo

largo de la superficie de deslizamiento, confirman adicionalmente el mecanismo de rotura progresiva de la presa de Aznalcóllar, con estos valores en el intermedio entre los valores pico y residual durante el proceso de la rotura. El estado post-ruptura podría ser considerado como uno medio en la rotura inicial. Al final de la rotura la mayor parte de la superficie de deslizamiento se encuentra en el estado residual, especialmente a lo largo de la parte horizontal. Además, la rotura de la presa de Aznalcóllar es sensible a la velocidad de ablandamiento de la deformación de corte plástica (γ_p , γ_{pr} y γ_r). Mayor velocidad inducirá la rotura más temprano y ningún fallo se producirá con la velocidad de ablandamiento lenta. Sólo un valor adecuado de la velocidad de ablandamiento de la deformación de corte plástica puede causar una falla en la fase final en ambas hipótesis no homogénea y homogénea.

Finalmente, la resistencia post-ruptura de las arcillas rígidas sobreconsolidadas es introducida en las soluciones analíticas de la expansión de cavidades cilíndricas en arcillas rígidas sobreconsolidadas. Las soluciones analíticas para la presión límite, las tensiones, las deformaciones y campos de desplazamientos para la expansión de la cavidad cilíndrica se han derivado de una manera simple. Este método puede utilizarse especialmente con las arcillas rígidas sobreconsolidadas y corrige las deficiencias de la teoría clásica sobre la expansión de una cavidad cilíndrica elastoplástica. Los ejemplos numéricos indican que el modelo de ablandamiento quadralineal puede degenerar al modelo trilineal original y da los mismos resultados que los publicados. La similitud entre la solución numérica y la analítica verifica el carácter razonable de la solución analítica para la expansión de la cavidad en arcillas rígidas con características de ablandamiento en dos etapas. Este análisis abre la posibilidad de la generalización del concepto de la resistencia de post-ruptura y de la importancia del modelo de ablandamiento en dos etapas para resolver ciertos problemas de ingeniería geotécnica.



Resum

És ben conegut que el comportament tensió-deformació de les argiles rígides sobreconsolidades és altament inelàstic i no-lineal. Abans de la mobilització de resistència pico el sòl experimenta un procés d'enduriment per deformació, mentre que després d'arribar a la resistència bec, el sòl experimenta un procés d'estovament per deformació. Aquest comportament és diferent al que es presenta en argiles toves i sorres soltes. El comportament post-trencament de les argiles rígides sobreconsolidades ha estat caracteritzat mitjançant experiments de laboratori, l'examen de la microestructura i els models constitutius.

Les característiques de resistència màxima i residual de les argiles rígides s'han estudiat a través d'experiments de laboratori. En particular, els mètodes de microscopi electrònic d'escàner i òptic, s'han utilitzat a bastament per a examinar el canvi de l'estructura de la zona de trencament en les argiles rígides fins a arribar a la resistència residual. Els resultats d'aquestes proves deixen veure l'existència d'un punt que divideix la corba d'estovament post-trencament de les argiles rígides en dues etapes. Aquest punt va ser definit inicialment per Burland (1990) com la resistència post-trencament. Les dues etapes inclouen una reducció relativament ràpida de la resistència des del bec a la resistència post-trencament, seguida per una reducció gradual fins a la resistència residual. En aquesta tesi, els resultats existents de proves de laboratori i d'anàlisis numèriques relacionats amb la resistència post-trencament s'han recopilat i analitzat. Els resultats de les proves de laboratori, de camp i les anàlisis numèriques verifiquen l'existència i la robustesa de la resistència post-trencament de les argiles rígides sobreconsolidades. L'anàlisi estadística per la seva banda, demostra que la resposta d'estovament per deformació post-bec de les argiles rígides es pot dividir en dues etapes. Els estudis de la microestructura indiquen que la primera etapa de l'estovament està induïda per la pèrdua de inter-connexió entre les partícules, o de la component cohesiva de la resistència a desplaçaments relativament petits, coneguda com pèrdua de cimentació; mentre que la segona etapa és deguda al realineament gradual o reorientació de les partícules d'argila a grans desplaçaments i es pot anomenar com pèrdua gradual de la resistència friccional.

Fins ara solsament s'han conduït estudis experimentals per a investigar les característiques de la resistència post-trencament de les argiles rígides, els models constitutius existents del sòl no consideren el comportament observat d'estovament post-bec en dues etapes. Models com el no lineal d'estovament per deformació i enduriment per deformació basat en el model millorat de Mohr-Coulomb permeten descriure la resistència mobilitzada del sòl entre els estats bec i residual suposant regles d'estovament lineals o exponencials per als paràmetres de resistència c' i ϕ' . No obstant això, aquest model no pot distingir el tret característic d'estovament en dues etapes de les argiles rígides. A causa d'aquesta limitació, l'objectiu d'aquesta tesi és establir un model constitutiu generalitzat per a simular les característiques d'estovament en dues etapes de les argiles rígides sobreconsolidades, modificant els models existents esmentats anteriorment. La formulació d'aquest model és il·lustrada detalladament i després implementada en un programa explícit de diferència finites

FLAC (ITASCA) basat en un model implementat d'enduriment/estovament per deformació.

Després d'això, el nou model és validat mitjançant la simulació d'assajos de laboratori com assajos de compressió triaxial i assajos de tall directe. Els resultats numèrics demostren la capacitat i eficiència del model modificat d'estovament a través de *FLAC* per a reproduir el comportament d'estovament per deformació en dues etapes de les argiles rígides. La influència de la malla es pot eliminar eficientment amb un esquema especial que relaciona el pendent de l'estovament amb una dimensió característica dels elements de tal manera que el seu quocient es manté constant.

Adicionalment, aquest model pot utilitzar-se per a simular problemes realistes d'enginyeria entre els quals el fenomen del trencament progressiu és un molt comú i tradicional. S'han realitzat amb *FLAC* una sèrie d'anàlisi del trencament progressiu diferida de talussos en argiles rígides similar als conduïts per Potts et al., (1997), utilitzant el nou model d'estovament en dues etapes amb incorporació de la resistència de post-trencament. Els resultats numèrics reproduïen bastant bé el procés progressiu del trencament, la posició de la superfície de trencament i el temps de trencament, la qual cosa brinda validesa addicional al nou model. Adicionalment, s'ha portat a terme una anàlisi paramètrica de l'efecte de K_0 , l'efecte de la succió superficial, l'efecte de geometria del talús, la influència dels paràmetres de la resistència de post-trencament i l'altura mínima de seguretat del talús, per a demostrar la influència general de la resistència de post-trencament. Tots els resultats demostren que es redueix l'estabilitat dels talussos amb l'adopció del model de ablaniment de dues etapes en comparació amb el de només una etapa, a causa de la reducció més ràpida de la cohesió amb la deformació plàstica en primera fase d'estovament del model de ablaniment de dues etapes. I la resistència de post-trencament és important d'explicar la degradació de la cohesió més ràpida en la primera etapa en el model de ablaniment de dues etapes.

En particular, el concepte de la resistència post-trencament i el model d'estovament en dues etapes són aplicats en la simulació numèrica del famós cas del trencament de la presa de Aznalcóllar (Alonso & Gens, 2006a; Gens & Alonso, 2006) sota les dues hipòtesis no homogènies i homogènia. La simulació és un complement de la simulació numèrica presentada per Gens & Alonso (2006) i compensa la deficiència de les simulacions numèriques presentades per Olalla & Cuéllar (2001) i Gens & Alonso (2006), a l'utilitzar un procediment de modelització de l'estovament més realista i raonable. Les simulacions reproduïen bé el trencament de la presa de Aznalcóllar incloent el procés progressiu del trencament, la ubicació i la forma de la superfície de lliscament i el desenvolupament de la pressió de l'aigua en els porus, segons el desenvolupament de l'estat de la plasticitat, la velocitat de la deformació de tall, l'increment de la deformació de tall, el desplaçament, la velocitat i paràmetres de resistència de l'estovament.

El mecanisme de trencament de la presa de Aznalcóllar és considerat com de trencament progressiu deguda principalment a l'estovament de la massa d'argila blava del Guadalquivir. Per altra banda, el desenvolupament de la relació mitja de les tensions, el factor residual, la fragilitat mitja, la trajectòria de tensions mitja i la distribució de les tensions de tall mobilitzades i els paràmetres de resistència mobilitzats al llarg de la superfície de lliscament, confirmen addicionalment el mecanisme de trencament progressiu de la presa de Aznalcóllar, amb aquests valors

situats al mig entre els valors bec i residual durant el procés del trencament. L'estat post-trencament podria ser considerat com un mitjà en el trencament inicial. Al final del trencament la major part de la superfície de lliscament es troba en l'estat residual, especialment al llarg de la part horitzontal. A més, el trencament de la presa d'Aznalcóllar és sensible a la velocitat de estovament de la deformació de tall plàstica (γ_p , γ_{pr} i γ_r). Major velocitat induirà el trencament més d'hora i cap trencament es produirà amb la velocitat de estovament lenta. Només un valor adequat de la velocitat de estovament de la deformació de tall plàstica pot causar una falla en la fase final en ambdues hipòtesis no homogenis i homogènia.

Finalment, la resistència post-trencament de les argiles rígides sobreconsolidades és introduïda en les solucions analítiques de l'expansió de cavitats cilíndriques en argiles rígides sobreconsolidades. Les solucions analítiques per a la pressió límit, les tensions, les deformacions i camps de desplaçaments per a l'expansió de la cavitat cilíndrica s'han derivat d'una manera simple. Aquest mètode pot fer-se servir especialment amb les argiles rígides sobreconsolidadas i corregeix les deficiències de la teoria clàssica sobre l'expansió d'una cavitat cilíndrica elastoplàstica. Els exemples numèrics indiquen que el model d'estovament quadrilineal pot degenerar al model trilineal original i dona els mateixos resultats que els publicats. La similitud entre la solució numèrica i l'analítica verifica el caràcter raonable de la solució analítica per a l'expansió de la cavitat en argiles rígides amb característiques d'estovament en dues etapes. Aquesta anàlisi obre la possibilitat de la generalització del concepte de la resistència de post-trencament i de la importància del model d'estovament en dues etapes per resoldre alguns problemes d'enginyeria geotècnica.



摘要

超固结硬质粘土的应力应变特性主要表现为高度地非弹性和非线性。在达到峰值强度之前会发生应变硬化。而在峰值强度之后则发生应变软化，这明显不同于软粘土和松砂土。室内试验、微观观察和本构模型已经被用于研究超固结硬质粘土的破坏后力学特性。

到目前为止已有一些室内试验被用于研究硬粘土的峰值强度和残余强度。特别是光学和电镜方法已成功地应用于观察硬粘土从峰值到残余过程破坏区的结构变化。这些试验结果表明超固结硬质粘土具有明显的双阶段软化的破坏后特征。本文通过分析已有现场试验、室内试验和数值分析结果证实了超固结硬粘土破坏后强度的存在性和稳健性。同时本文收集了超固结硬质粘土的峰值强度、破坏后强度和残余强度的试验和数值分析数据，并进行了数据分析，进而得到其峰值后双阶段软化的机制：

(1) 第一阶段：从峰值强度到破坏后强度的变化主要是因为相对较小变形条件下土体颗粒间的联结受到很大程度的破坏，也就是土粒间粘聚力的大量丧失，而土粒间的摩擦力则减小较少；

(2) 第二阶段：第一阶段之后，经过较大变形后，土体颗粒主要是粘土颗粒沿着剪切方向重新定向排列，从而导致土粒间摩擦力的减小直至达到残余强度值。

至今，硬粘土的破坏后强度主要集中在试验研究方面。通过假定力学强度参数线性或指数软化法则，一些基于摩尔库仑准则的非线性应变软化和硬化模型可以用来描述硬粘土在峰值和残余状态之间的强度变化。然而，这些模型并不能用来模拟其双阶段破坏后强度特征。基于此背景，本文通过对已有模型的修改建立了双阶段软化模型，编制了相应的模型代码，并将其植入有限差分软件 *FLAC* (ITASCA) 之中。

之后，此模型被应用于典型的室内试验（三轴压缩试验、固结试验及抗剪试验）模拟，进行因子分析（如网格对软化模拟结果的影响等），并和已有试验或数值结果进行对比，结果证明了此模型的正确性和有效性。

同时，此模型也被应用于边坡滞后渐近破坏，并与已有数值模拟结果进行对比，进而分析破坏后强度参数对边坡稳定的影响。模拟结果表明此模型很好地模拟了渐近破坏过程、破坏面的位置以及破坏时间。因子分析（如 K_0 、边界基质吸力、几何参数、破坏后强度参数变化影响和安全开挖高度等）也进一步说明了破坏后强度对边坡稳定性的影响。

特别地，本文基于均质与非均质两种假定将双阶段软化模型应用于 Aznalcóllar 大坝破坏的全过程系统化数值模拟。两种假定下的模拟结果很好地模拟了大坝破坏过程、破坏面的形成和贯通以及孔隙水压力的发展变化。数值分析表明 Aznalcóllar 大

坝因 Guadalquivir 粘土体的软化而发生渐近破坏。沿破坏面的平均应力比、残余因子、平均脆性、强度参数的变化进一步证实了 Aznalcóllar 大坝渐进破坏机制。平均应力路径和实际剪切应力分布说明了破坏后强度可被作为大坝初始破坏时的平均强度。大坝在破坏初期破坏面上的强度处于峰值强度和残余强度之间，而在最后破坏阶段破坏面强度除了后部分外大部分处于残余状态。累积塑性软化剪切应变 γ_p , γ_{pr} 和 γ_r 对 Aznalcóllar 大坝渐进破坏具有控制作用。在两种假定下，只有设定合适的累积塑性软化剪切应变值，大坝才会在最后建筑阶段发生破坏。

最后，本文将破坏后强度的概念扩展到其他如圆柱形孔扩张等岩土工程问题中，并提供双阶段软化流动法则，在此基础上推算出相应的解析解。与此同时，进行圆柱形孔扩张的数值模拟，并和解析解进行比较，结果进一步证实了破坏后强度的工程意义和实用性。

Acknowledgement

Firstly, I would like to thank my supervisor Professor Antonio Gens for giving me the chance to take part in the doctoral program and pursue scientific research, guiding me and assisting me throughout the whole doctoral period and affording me the encouraging financial support in the final stage of my doctoral study. His attitude to science has inspired me greatly and will keep inspiring me along all my life.

The general financial support from the International Graduate School of Catalonia (IGSOC) and L'Agència de Gestió d'Ajuts Universitaris i de Recerca (AGAUR), is gratefully acknowledged.

I appreciate so much the help of Professor Carlos Agelet de Saracibar Bosch. Thanks for the continuous care of all aspects of my doctoral study.

I would express my thanks to Dr. Jean Vaunat for always kindly affording me useful literature and to PhD students Nubia Aurora González Molano and Sergio Samat Aon for the interesting discussions and information exchanges about geotechnical issues with me.

Thanks are also due to Dr. Carlos Carranza-Torres for his special help information and suggestion about the use of *FLAC* and Dr. Ming Yang for sending me beneficial documents of *FLAC* from faraway United States.

I would also like to thank all my friends, especially my UPC colleagues and friends—Dr. Giuseppe Vigliano, Dr. Jordi Poblet Puig, Dr. Vanessa Zavala and many PhD students including Paolo Trincherio, Georgina Rendon Poujol, Gonzalo Valdés V., Jorge Luis Acevedo Cabello, Oscar Iván Montenegro, Isabel Tubau Fernández, Leonardo Donado Garzón, Juan José Cruz Solis, Eduardo Castro and etc. for their encouragement, care and enriching my life at Barcelona.

I am very grateful to my two big Spanish brothers Jaume Baratech and German Rodriguez Herrera for their homy hospitality at Barcelona far away from China.

I would like to express my cordial thanks to my former tutor in China Professor Qiang Xie and my former colleagues Dr. Yongchun Guo and Dr. Wen Zhao and etc. of the School of Civil Engineering of Southwest Jiaotong University (Chengdu, China) for their enduring care and support of my PhD study since I arrived at Barcelona.

Special thanks are due to Dr. Guangjing Chen and his wife Li Yu, for not only being friends from the very beginning but also for helping me in both my PhD study and my life at Barcelona in numerous ways.

Finally, my thanks go to my family—my dear grandma, my adorable mother, my great father, my clever younger brother and particularly my beloved wife Xia He, for loving me, supporting me and encouraging me all the time. I hope I make you proud.



Acknowledgement



to my whole family, my beloved wife Xia and my lovely baby Cathaysa

for their consistent care, continual support and endless love

Contents

| | |
|---|-----------|
| CHAPTER 1. INTRODUCTION..... | 1 |
| 1.1 GENERAL..... | 1 |
| 1.1.1 <i>Post-peak softening behaviour of stiff clays.....</i> | <i>1</i> |
| 1.1.2 <i>Progressive failure in stiff clays.....</i> | <i>4</i> |
| 1.1.3 <i>Solution schemes of softening.....</i> | <i>6</i> |
| 1.1.4 <i>Setting up of modified constitutive model incorporating post-rupture strength for stiff clays.....</i> | <i>7</i> |
| 1.1.5 <i>Verification and application of new modified constitutive model for stiff clays.....</i> | <i>7</i> |
| 1.2 OBJECTIVES OF RESEARCH..... | 8 |
| 1.3 THESIS LAYOUT..... | 9 |
| CHAPTER 2. THEORETICAL BACKGROUND OF SOFTENING BEHAVIOUR OF STIFF CLAYS..... | 11 |
| 2.1 PEAK STRENGTH..... | 11 |
| 2.2 RESIDUAL STRENGTH..... | 12 |
| 2.2.1 <i>Definition of residual strength.....</i> | <i>12</i> |
| 2.2.2 <i>Characteristics of residual strength of clays.....</i> | <i>12</i> |
| 2.2.3 <i>Summary from examination of residual strength.....</i> | <i>15</i> |
| 2.3 FULLY SOFTENED STRENGTH (CRITICAL-STATE STRENGTH)..... | 15 |
| 2.4 POST-RUPTURE STRENGTH OF STIFF OVERCONSOLIDATED CLAYS..... | 18 |
| 2.4.1 <i>Introduction and definition of post-rupture strength.....</i> | <i>18</i> |
| 2.4.2 <i>Laboratory test observations of post-rupture strength.....</i> | <i>19</i> |
| 2.4.2.1 Results from Burland (1990)..... | 19 |
| 2.4.2.2 Results from Burland et al. (1996)..... | 22 |
| 2.4.2.3 Results from Georgiannou & Burland (2001)..... | 24 |
| 2.4.2.4 Results from Georgiannou & Burland (2006)..... | 26 |
| 2.4.3 <i>Data collection of post-peak strength parameters of stiff clays.....</i> | <i>28</i> |
| 2.4.4 <i>Summary of post-peak shear strength of stiff clays.....</i> | <i>39</i> |
| 2.4.4.1 General feature of post-peak softening behaviour of stiff clays..... | 39 |
| 2.4.4.2 General phenomena and observation of post-rupture strength..... | 40 |
| 2.4.4.3 Relationship between post-rupture and critical-state strengths..... | 41 |
| 2.4.4.4 Relationship between operational and post-rupture strengths..... | 42 |
| 2.4.4.5 Application of post-rupture strength in geotechnical engineering..... | 43 |
| 2.4.4.6 Generalised descriptive indices based on post-rupture strength..... | 45 |
| 2.4.4.7 Representative descriptive curves for post-rupture behaviour..... | 47 |
| CHAPTER 3. FORMULATION AND IMPLEMENTATION OF TWO-STAGE SOFTENING CONSTITUTIVE MODEL FOR STIFF CLAYS..... | 49 |



| | | |
|---|--|-----------|
| 3.1 | INTRODUCTION | 49 |
| 3.2 | CLASSICAL THEORY OF ELASTOPLASTICITY | 49 |
| 3.2.1 | <i>Basic concepts</i> | 49 |
| 3.2.1.1 | Yield surface | 49 |
| 3.2.1.2 | Flow rule..... | 50 |
| 3.2.1.3 | Hardening/softening rule | 50 |
| 3.2.1.4 | Elastic response..... | 50 |
| 3.2.1.5 | Determination of the scalar multiplier, Λ | 50 |
| 3.2.2 | <i>Formulation of the elastoplastic constitutive matrix</i> | 51 |
| 3.3 | BASIC MOHR-COULOMB MODEL..... | 52 |
| 3.4 | ONE-STAGE SOFTENING MODEL | 56 |
| 3.4.1 | <i>General concept of softening of strength parameters</i> | 56 |
| 3.4.2 | <i>Other basic model parameters</i> | 59 |
| 3.5 | TWO-STAGE SOFTENING MODEL | 60 |
| 3.5.1 | <i>General concept of two-stage strength parameter softening</i> | 60 |
| 3.5.2 | <i>Detailed two-stage softening of frictional angle and cohesion</i> | 62 |
| 3.5.3 | <i>Formulation of the new model</i> | 63 |
| 3.5.3.1 | General description of two-stage softening of strength parameters | 63 |
| 3.5.3.2 | Elastoplastic description of modified two-stage softening model..... | 65 |
| 3.5.4 | <i>Determination and calibration of model parameters</i> | 66 |
| 3.5.4.1 | Comprehensive methods..... | 66 |
| 3.5.4.2 | Determination of elastic parameters..... | 67 |
| 3.5.4.3 | Determination of shear strength parameters of stiff clays | 67 |
| 3.5.4.4 | Determination of deviatoric plastic strains— ε_{DPR}^P , ε_{DP}^P and ε_{DR}^P | 68 |
| 3.6 | IMPLEMENTATION OF TWO-STAGE SOFTENING MODEL..... | 69 |
| 3.6.1 | <i>Introduction</i> | 69 |
| 3.6.2 | <i>Built-in strain hardening/softening model in FLAC</i> | 69 |
| 3.6.2.1 | Introduction..... | 69 |
| 3.6.2.2 | Hardening/Softening Parameters | 70 |
| 3.6.2.3 | User-defined functions for strength parameters | 71 |
| 3.6.3 | <i>Implementation of two-stage softening model into FLAC</i> | 73 |
| 3.6.3.1 | Implementation procedure of hardening/softening model..... | 73 |
| 3.6.3.2 | Combination of <i>FISH</i> and built-in model | 73 |
| 3.6.3.3 | Two-stage softening model written with <i>FISH</i> | 74 |
| 3.6.3.4 | Two-stage softening model written with C++..... | 75 |
| 3.6.3.5 | Summary..... | 76 |
| CHAPTER 4. LABORATORY TEST SIMULATION VIA TWO-STAGE SOFTENING MODEL..... | | 77 |
| 4.1 | ACCURACY OF PLASTIC DEFORMATION CALCULATION IN FLAC | 77 |
| 4.2 | SIMULATION OF TRIAXIAL TESTS | 81 |

| | | |
|---|--|------------|
| 4.2.1 | <i>Basic model configuration and simulation schemes</i> | 81 |
| 4.2.2 | <i>Theoretical solution with 1×1 grid</i> | 85 |
| 4.2.3 | <i>Simulation with different grids</i> | 87 |
| 4.2.4 | <i>Verification of undrained triaxial test simulation</i> | 97 |
| 4.3 | SIMULATION OF DIRECT SHEAR BOX TESTS | 99 |
| 4.3.1 | <i>Theoretical solution with 1×1 grid</i> | 99 |
| 4.3.2 | <i>Simulation of direct shear box test with finer grid</i> | 103 |
| 4.3.2.1 | Scheme I without interfaces | 104 |
| 4.3.2.2 | Scheme II with interfaces..... | 107 |
| 4.4 | SUMMARY | 108 |
| CHAPTER 5. NUMERICAL MODELLING OF DELAYED PROGRESSIVE SLOPE FAILURE IN STIFF CLAYS USING STRAIN-SOFTENING MODELS | | 109 |
| 5.1 | DEVELOPMENT OF PROGRESSIVE SLOPE FAILURE IN STIFF CLAYS | 109 |
| 5.1.1 | <i>Developing history of slope movements</i> | 109 |
| 5.1.2 | <i>Transition from local soil failure to general slope failure</i> | 110 |
| 5.2 | REPRESENTATIVE CASE HISTORIES OF PROGRESSIVE FAILURE | 112 |
| 5.2.1 | <i>Progressive failure of Carsington dam</i> | 112 |
| 5.2.2 | <i>Field evidence of progressive failure—Selborne cut failure</i> | 114 |
| 5.3 | ANALYSIS OF DELAYED PROGRESSIVE SLOPE FAILURE IN STIFF CLAYS | 116 |
| 5.3.1 | <i>Original FEM results from Potts et al. (1997)</i> | 117 |
| 5.3.2 | <i>General description of numerical model for delayed failures of cut slopes</i> | 120 |
| 5.3.3 | <i>Non-softening analyses</i> | 123 |
| 5.3.3.1 | <i>LEM results</i> | 125 |
| 5.3.3.2 | <i>Results of FOS analysis via FLAC</i> | 126 |
| 5.3.3.3 | <i>Summary</i> | 127 |
| 5.3.4 | <i>One-stage softening analyses</i> | 128 |
| 5.3.4.1 | <i>Results of representative analysis (S3)</i> | 129 |
| 5.3.4.2 | <i>K₀ effect</i> | 134 |
| 5.3.4.3 | <i>Effect of surface suction</i> | 138 |
| 5.3.4.4 | <i>Effect of slope geometry</i> | 139 |
| 5.3.4.5 | <i>Summary for non-softening and one-stage softening analyses</i> | 141 |
| 5.3.5 | <i>Two-stage softening analyses with bulk peak strength</i> | 142 |
| 5.3.5.1 | <i>Results of analysis TS3</i> | 143 |
| 5.3.5.2 | <i>Effect of K₀</i> | 153 |
| 5.3.5.3 | <i>Effect of slope geometry</i> | 156 |
| 5.3.5.4 | <i>Summary for two-stage softening with bulk peak strength</i> | 158 |
| 5.3.6 | <i>Sensitivity analysis of softening strength parameters</i> | 159 |
| 5.3.6.1 | <i>Comparison of analyses TS1-TS11 with analyses TS1N-TS11N</i> | 160 |
| 5.3.6.2 | <i>Comparisons among results of analyses TS3A-TS3F</i> | 162 |

| | | |
|--|---|------------|
| 5.3.7 | <i>Softening analyses with intact peak strength</i> | 163 |
| 5.3.7.1 | Results of analysis TS12H14 | 166 |
| 5.3.7.2 | Results of analysis S12H14..... | 171 |
| 5.3.7.3 | Results of analysis TS12H14N3 | 174 |
| 5.3.8 | <i>Determination of critical stable cutting height</i> | 177 |
| 5.3.8.1 | Results of softening analyses with bulk peak strength | 177 |
| 5.3.8.2 | Results of softening analyses with intact peak strength | 180 |
| 5.4 | SUMMARY | 181 |
| CHAPTER 6. ANALYSIS OF AZNALCÓLLAR DAM FAILURE MECHANISM WITH POST-RUPTURE STRENGTH CONCEPT AND PROGRESSIVE FAILURE | | 183 |
| 6.1 | INTRODUCTION TO DAM GEOMETRY AND CONSTRUCTION PROCESS..... | 183 |
| 6.2 | DESCRIPTION OF THE FAILURE | 185 |
| 6.3 | GEOTECHNICAL PROPERTIES OF FOUNDATION MATERIALS | 187 |
| 6.3.1 | <i>Basic identification</i> | 187 |
| 6.3.2 | <i>Mineralogy</i> | 187 |
| 6.3.3 | <i>Results from direct shear tests</i> | 187 |
| 6.3.4 | <i>Structure of Guadalquivir blue clay</i> | 192 |
| 6.4 | REPORTED NUMERICAL ANALYSES OF AZNALCÓLLAR DAM FAILURE | 193 |
| 6.4.1 | <i>Numerical results from Olalla and Cuéllar (2001)</i> | 193 |
| 6.4.2 | <i>Numerical results from Gens & Alonso (2006)</i> | 194 |
| 6.4.3 | <i>Numerical results from Zabala & Alonso (2011)</i> | 197 |
| 6.5 | SIMULATION OF AZNALCÓLLAR DAM FAILURE WITH THE TWO-STAGE CONSTITUTIVE MODEL | 197 |
| 6.5.1 | <i>General description of numerical simulation</i> | 197 |
| 6.5.2 | <i>Two hypotheses of numerical simulation</i> | 202 |
| 6.5.2.1 | Inhomogeneous hypothesis | 202 |
| 6.5.2.2 | Homogeneous hypothesis | 202 |
| 6.5.3 | <i>Analysis with inhomogeneous hypothesis</i> | 202 |
| 6.5.3.1 | Description of pre-failure, initial failure and post-failure phases | 205 |
| 6.5.3.2 | Development of shear strain rate and shear strain increment | 206 |
| 6.5.3.3 | Development of velocity and total displacement | 208 |
| 6.5.3.4 | Development of maximum unbalanced force | 211 |
| 6.5.3.5 | Development of pore water pressure..... | 211 |
| 6.5.3.6 | Development of strength parameters in softening clays..... | 213 |
| 6.5.3.7 | Geometry of slip surface..... | 218 |
| 6.5.3.8 | Post-failure evolution of representative horizontal displacements | 219 |
| 6.5.3.9 | Representative model results along profile A-E..... | 220 |
| 6.5.3.10 | Representative model results along slip surface..... | 221 |
| 6.5.3.11 | Verification of position of failure surface | 250 |
| 6.5.4 | <i>Analysis with homogeneous hypothesis</i> | 256 |
| 6.5.4.1 | Development of shear strain rate and shear strain increment | 258 |

| | | |
|--|---|------------|
| 6.5.4.2 | Development of velocity and total displacement | 260 |
| 6.5.4.3 | Development of pore water pressure..... | 262 |
| 6.5.4.4 | Development of strength parameters in softening clays..... | 265 |
| 6.5.4.5 | Geometry of slip surface | 270 |
| 6.5.4.6 | Development of representative horizontal displacements | 271 |
| 6.5.4.7 | Representative results along profile A-E | 272 |
| 6.5.4.8 | Representative results along slip surface | 273 |
| 6.5.5 | <i>Supplementary analyses</i> | 284 |
| 6.5.5.1 | Supplementary analysis with homogeneous assumption..... | 284 |
| 6.5.5.2 | Supplementary analysis with inhomogeneous assumption | 285 |
| 6.6 | SUMMARY | 286 |
| CHAPTER 7. ANALYTICAL SOLUTION TO CYLINDRICAL CAVITY EXPANSION IN STIFF CLAYS WITH THE TWO-STAGE SOFTENING MODEL..... | | 289 |
| 7.1 | INTRODUCTION | 289 |
| 7.2 | GOVERNING EQUATIONS AND SIMPLIFIED QUADRILINEAR MODEL..... | 290 |
| 7.3 | ANALYTICAL SOLUTIONS..... | 294 |
| 7.3.1 | <i>Stress, strain and displacement fields in elastic zone ($r \geq R_1$)</i> | <i>294</i> |
| 7.3.2 | <i>Stress, strain and displacement fields in softening I zone ($R_2 \leq r \leq R_1$)</i> | <i>294</i> |
| 7.3.3 | <i>Stress, strain and displacement fields in softening II zone ($R_3 \leq r \leq R_2$).....</i> | <i>296</i> |
| 7.3.4 | <i>Stress, strain and displacement fields in residual flow zone ($R_u \leq r \leq R_3$).....</i> | <i>298</i> |
| 7.3.5 | <i>Calculation of radii for different zones and the ultimate internal pressure.....</i> | <i>299</i> |
| 7.3.6 | <i>Remarks</i> | <i>301</i> |
| 7.4 | COMPUTATIONAL EXAMPLES..... | 301 |
| 7.4.1 | <i>Verification of maple program with trilinear model.....</i> | <i>301</i> |
| 7.4.2 | <i>Examples with quadrilinear model and parametric study</i> | <i>302</i> |
| 7.4.2.1 | Effect of shear dilation h , f and g | 302 |
| 7.4.2.2 | Effect of β | 305 |
| 7.4.2.3 | Effect of ω | 306 |
| 7.4.2.4 | Effect of initial stress p_0 | 307 |
| 7.4.2.5 | Effect of E and ν | 309 |
| 7.4.2.6 | Effect of post-rupture strength parameters c_{pr} and ϕ_{pr} | 310 |
| 7.4.3 | <i>Numerical simulation of cavity expansion.....</i> | <i>311</i> |
| 7.5 | SUMMARY | 315 |
| CHAPTER 8. CONCLUSIONS | | 317 |
| REFERENCES | | 321 |
| APPENDIX I. DEFINITIONS OF STRESS AND STRAIN VARIABLES..... | | 341 |
| APPENDIX II. DERIVATIVES OF STRESS INVARIANTS | | 347 |



| | |
|---|------------|
| APPENDIX III. SPECIFICATION OF STRENGTH PARAMETERS AND SOFTENING RATE | 349 |
| APPENDIX IV. PROCEDURE TO OBTAIN THEORETICAL SHEAR STRESS VS. SHEAR STRAIN CURVE FOR THE TWO-STAGE SOFTENING MODEL | 351 |

List of figures

| | |
|---|----|
| FIG. 1.1 SCHEMATIC REPRESENTATION OF $\tau - \delta$ AND RELEVANT $\tau - \sigma$ RELATIONSHIP FOR DIRECT SHEAR TESTS ON STIFF CLAYS (AFTER CIVIDINI & GIODA, 1992) | 2 |
| FIG. 2.1 RING SHEAR TESTS ON SAND-BENTONITE MIXTURES (AFTER LUPINI ET AL., 1981, AND SKEMPTON, 1985) | 13 |
| FIG. 2.2 SUMMARY OF POST-FAILURE STRUCTURE OF HAPPISBURG-LONDON CLAY MIXTURES IN RING SHEAR TEST (AFTER LUPINI ET AL., 1981) | 14 |
| FIG. 2.3 RELATIONSHIP BETWEEN DRAINED FULLY SOFTENED FRICTION ANGLES AND LIQUID LIMIT FOR TRIAXIAL COMPRESSION MODE OF SHEAR (STARK & EID, 1997) | 16 |
| FIG. 2.4 STRESS RATIO-DISPLACEMENT CURVE AT CONSTANT σ'_n (STARK & EID, 1997)..... | 17 |
| FIG. 2.5 MOBILISED, FULLY SOFTENED, AND RESIDUAL STRESS RATIOS FOR FIELD CASE HISTORIES (STARK & EID, 1997). ALSO PLOTTED ARE CALCULATED VALUES FOR AZNALCÓLLAR DAM FAILURE (GENS & ALONSO, 2006) | 17 |
| FIG. 2.6 TODI CLAY: UNCONSOLIDATED UNDRAINED TRIAXIAL TEST WITH PORE PRESSURE MEASUREMENT SHOWING POST-RUPTURE BEHAVIOUR (BURLAND, 1990) | 20 |
| FIG. 2.7 TODI CLAY: POST-RUPTURE ENVELOPE FOR (A) HIGH PRESSURES (B) LOW TO MEDIUM PRESSURES COMPARED WITH INTACT, INTRINSIC AND RESIDUAL FAILURE LINES (BURLAND,1990)..... | 21 |
| FIG. 2.8 LONDON CLAY AT ASHFORD COMMON: POST-RUPTURE ENVELOPE FOR (A) HIGH PRESSURES (B) LOW TO MEDIUM PRESSURES COMPARED WITH INTRINSIC FAILURE LINES (BURLAND,1990) | 22 |
| FIG. 2.9 PIETRAFITTA CLAY: POST-RUPTURE COULOMB STRENGTH ENVELOPE COMPARED WITH PEAK INTACT AND INTRINSIC FAILURE LINES (BURLAND ET AL., 1996) | 23 |
| FIG. 2.10 TODI CLAY: POST-RUPTURE STRENGTHS COMPARED WITH PEAK INTACT AND INTRINSIC FAILURE LINES (BURLAND ET AL., 1996) | 23 |
| FIG. 2.11 VALLERICCA CLAY: POST-RUPTURE STRENGTH ENVELOPE COMPARED WITH PEAK INTACT AND INTRINSIC FAILURE LINES (BURLAND ET AL., 1996) | 24 |
| FIG. 2.12 MOHR-COULOMB STRENGTH ENVELOPES FOR COMPRESSION TESTS ON VALLERICCA CLAY (GEORGIANNOU & BURLAND, 2001)..... | 25 |
| FIG. 2.13 MOHR-COULOMB STRENGTH ENVELOPES FOR EXTENSION AND COMPRESSION TESTS ON VALLERICCA CLAY (GEORGIANNOU AND BURLAND, 2001)..... | 26 |
| FIG. 2.14 RELATIONSHIPS BETWEEN τ / σ'_n AND DISPLACEMENT ACROSS SLIP SURFACE FOR INITIALLY INTACT CORINTH MARL SPECIMENS (GEORGIANNOU & BURLAND, 2006) | 26 |
| FIG. 2.15 PEAK STRENGTHS AND POST-RUPTURE STRENGTHS FOR CONSTANT- p' TESTS ON CORINTH MARL (GEORGIANNOU & BURLAND, 2006) | 27 |
| FIG. 2.16 VARIATION OF COHESION WITH CLAY FRACTION | 28 |
| FIG. 2.17 VARIATION OF COHESION WITH ACTIVITY | 29 |
| FIG. 2.18 VARIATION OF FRICTIONAL ANGLE WITH CLAY FRACTION | 29 |
| FIG. 2.19 VARIATION OF FRICTIONAL ANGLE WITH ACTIVITY..... | 30 |
| FIG. 2.20 SCHEMATIC $\tau - \delta$ CURVE (BASED ON ALONSO & GENS, 2006A)..... | 31 |
| FIG. 2.21 SCHEMATIC STRESS-STRAIN CURVE FOR STIFF CLAYS | 39 |
| FIG. 2.22 INTACT AND POST-RUPTURE STRENGTH ENVELOPES FOR DIRECT-DRAINED SHEAR TESTS ON STIFF CLAY (GEORGIANNOU, 2003)..... | 44 |

| | |
|---|----|
| FIG. 2.23 SKETCH DIAGRAM OF SHEAR STRENGTH ENVELOPES OF STIFF CLAY | 48 |
| FIG. 3.1 MOHR-COULOMB FAILURE CRITERION IN $J - p'$ PLANE..... | 53 |
| FIG. 3.2 MOHR-COULOMB FAILURE CRITERION IN DEVIATORIC PLANE..... | 53 |
| FIG. 3.3 VARIATION OF THE ANGLE OF SHEARING RESISTANCE ϕ' , AND THE COHESION INTERCEPT c' , WITH THE DEVIATORIC PLASTIC STRAIN INVARIANT ε_D^P (POTTS ET AL., 1990) | 56 |
| FIG. 3.4 VARIATION OF THE ANGLE OF SHEARING RESISTANCE WITH PLASTIC DEVIATORIC STRAIN ε_D^P (DOUNIAS ET AL., 1988 & 1996) | 56 |
| FIG. 3.5 VARIATIONS OF STATE PARAMETERS WITH PLASTIC STRAINS..... | 57 |
| FIG. 3.6 MOHR-COULOMB YIELD SURFACE ON THE $p' - J$ PLANE, DEFINITION OF STRESS LEVEL S (POTTS ET AL., 1990 AND DOUNIAS ET AL., 1988 & 1996) | 59 |
| FIG. 3.7 CONCEPTUAL TWO-STAGE POST-PEAK SOFTENING MODEL FOR STIFF CLAYS..... | 61 |
| FIG. 3.8 DISTINCT TWO-STAGE MODELS FOR FRICTIONAL ANGLE AND COHESION..... | 62 |
| FIG. 3.9 VARIATIONS OF STATE PARAMETERS WITH PLASTIC STRAINS..... | 63 |
| FIG. 3.10 SCHEMATIC $\tau - \delta$ CURVE AND VARIATIONS OF STATE PARAMETERS IN $\tau - \sigma'$ PLANE..... | 64 |
| FIG. 3.11 SIMPLIFIED ONE-DIMENSIONAL STRESS-STRAIN CURVE..... | 71 |
| FIG. 3.12 VARIATION OF (A) COHESION AND (B) FRICTION ANGLE WITH PLASTIC STRAIN | 71 |
| FIG. 3.13 PIECE-WISE LINEAR APPROXIMATION OF VARIATION OF (A) COHESION AND (B) FRICTION ANGLE WITH PLASTIC STRAIN..... | 72 |
| FIG. 3.14 (A) FRICTION (B) COHESION (C) DILATION (D) TENSILE STRENGTH DEFINED BY TWO LINEAR SEGMENTS | 73 |
| FIG. 4.1 TEST MODEL WITH TWO ELEMENTS (AFTER CIVIDINI AND GIODA, 1992)..... | 77 |
| FIG. 4.2 VERTICAL STRAINS OF BOTH ELEMENTS WITH $c1 = c2 = 2e4$ Pa | 78 |
| FIG. 4.3 VERTICAL STRAINS OF BOTH ELEMENTS WITH $c2 = 2.1e4$ Pa | 79 |
| FIG. 4.4 VERTICAL STRAINS OF BOTH ELEMENTS WITH $c2 = 2.5e4$ Pa | 79 |
| FIG. 4.5 VERTICAL STRAINS OF BOTH ELEMENTS WITH $c2 = 3.0e4$ Pa | 80 |
| FIG. 4.6 VERTICAL STRAINS OF BOTH ELEMENTS WITH $c2 = 4.0e4$ Pa | 80 |
| FIG. 4.7 VERTICAL STRAINS OF BOTH ELEMENTS WITH $c2 = 6.0e4$ Pa | 81 |
| FIG. 4.8 GEOMETRY AND BOUNDARY CONDITIONS | 81 |
| FIG. 4.9 (A) PEAK AND RESIDUAL YIELD CONDITIONS (B) ADOPTED VARIATION OF THE SHEAR STRENGTH PARAMETERS AFTER THE ONSET OF LOCALIZATION (AFTER STERPI AND CIVIDINI, 2004)..... | 83 |
| FIG. 4.10 VERTICAL STRESS VS. VERTICAL STRAIN FOR 1×1 GRID | 86 |
| FIG. 4.11 VOLUMETRIC STRAIN VS. SHEAR STRAIN ($(\varepsilon_1 - \varepsilon_3) / 2$) FOR 1×1 GRID..... | 86 |
| FIG. 4.12 STRESS RATIO VS. VERTICAL STRAIN FOR 1×1 GRID | 87 |
| FIG. 4.13 VERTICAL STRESS VS. VERTICAL STRAIN WITH DIFFERENT DILATION ANGLES FOR 5×10 GRID | 88 |
| FIG. 4.14 VERTICAL PRESSURE RATIO VS. VERTICAL STRAIN WITH DIFFERENT p_0 FOR 5×10 GRID | 88 |
| FIG. 4.15 VERTICAL STRESS VS. VERTICAL STRAIN WITH DIFFERENT DILATION ANGLES FOR 10×20 GRID | 89 |

FIG. 4.16 VERTICAL PRESSURE RATIO VS. VERTICAL STRAIN WITH DIFFERENT p_0 FOR 10×20 GRID... 89

FIG. 4.17 VERTICAL STRESS VS. VERTICAL STRAIN WITH DIFFERENT DILATION ANGLES FOR 16×32 GRID 90

FIG. 4.18 VERTICAL PRESSURE RATIO VS. VERTICAL STRAIN WITH DIFFERENT p_0 FOR 16×32 GRID ... 90

FIG. 4.19 VERTICAL STRESS VS. VERTICAL STRAIN WITH DIFFERENT DILATION ANGLES FOR 25×50 GRID 91

FIG. 4.20 VERTICAL PRESSURE RATIO VS. VERTICAL STRAIN WITH DIFFERENT p_0 FOR 25×50 GRID .. 91

FIG. 4.21 VERTICAL STRESS VS. VERTICAL STRAIN WITH DIFFERENT DILATION ANGLES FOR 50×100 GRID 92

FIG. 4.22 VERTICAL PRESSURE RATIO VS. VERTICAL STRAIN WITH DIFFERENT p_0 50×100 GRID..... 92

FIG. 4.23 VERTICAL STRESS VS. VERTICAL STRAIN FOR DIFFERENT GRIDS WITH DILATION SCHEME A 93

FIG. 4.24 VERTICAL STRESS VS. VERTICAL STRAIN FOR DIFFERENT GRIDS WITH DILATION SCHEME B..... 93

FIG. 4.25 VERTICAL STRESS VS. VERTICAL STRAIN FOR DIFFERENT GRIDS WITH DILATION SCHEME C..... 94

FIG. 4.26 VERTICAL STRESS VS. VERTICAL STRAIN FOR DIFFERENT GRIDS WITH DILATION SCHEME D 94

FIG. 4.27 VERTICAL STRESS VS. VERTICAL STRAIN FOR DIFFERENT GRIDS WITH ADJUSTED STRENGTH PARAMETERS ACCORDING TO MESH SIZE (SCHEME I AND A) 95

FIG. 4.28 VERTICAL STRESS VS. VERTICAL STRAIN FOR DIFFERENT GRIDS WITH ADJUSTED STRENGTH PARAMETERS ACCORDING TO MESH SIZE (SCHEME II AND A)..... 95

FIG. 4.29 VERTICAL STRESS VS. VERTICAL STRAIN FOR DIFFERENT GRIDS WITH ADJUSTED STRENGTH PARAMETERS ACCORDING TO MESH SIZE (SCHEME II AND B)..... 96

FIG. 4.30 VERTICAL STRESS VS. VERTICAL STRAIN FOR DIFFERENT GRIDS WITH ADJUSTED STRENGTH PARAMETERS ACCORDING TO MESH SIZE (SCHEME II AND C)..... 96

FIG. 4.31 VERTICAL STRESS VS. VERTICAL STRAIN FOR DIFFERENT GRIDS WITH ADJUSTED STRENGTH PARAMETERS ACCORDING TO MESH SIZE (SCHEME II AND D)..... 97

FIG. 4.32 MEASURED AND PREDICTED SHEAR STRESS VS. AXIAL STRAIN CURVE IN UNDRAINED TRIAXIAL TESTS ON BROWN LONDON CLAY 98

FIG. 4.33 MEASURED AND PREDICTED PORE PRESSURE VS. AXIAL STRAIN CURVE IN UNDRAINED TRIAXIAL TESTS ON BROWN LONDON CLAY 98

FIG. 4.34 GEOMETRY AND BOUNDARY CONDITIONS 100

FIG. 4.35 SHEAR STRESS VS. HORIZONTAL DISPLACEMENT RATIO WITH DIFFERENT DILATION SCHEMES ($K_0=2$ AND $\sigma_n=100$ kPA)..... 100

FIG. 4.36 VERTICAL DISPLACEMENT RATIO VS. HORIZONTAL DISPLACEMENT RATIO WITH DIFFERENT DILATION SCHEMES ($K_0=2$ AND $\sigma_n=100$ kPA) 101

FIG. 4.37 STRESS RATIO VS. HORIZONTAL DISPLACEMENT RATIO UNDER DIFFERENT NORMAL STRESSES ($K_0=3$ AND $\psi=0$) 101

FIG. 4.38 VERTICAL DISPLACEMENT RATIO VS. HORIZONTAL DISPLACEMENT RATIO UNDER DIFFERENT NORMAL STRESSES ($K_0=3$ AND $\psi=0$)..... 102

FIG. 4.39 SHEAR STRESS VS. HORIZONTAL DISPLACEMENT RATIO UNDER DIFFERENT NORMAL STRESSES ($\psi=0$) 103

FIG. 4.40 VERTICAL DISPLACEMENT RATIO VS. HORIZONTAL DISPLACEMENT RATIO UNDER DIFFERENT NORMAL STRESSES ($\psi=0$)..... 103

FIG. 4.41 MATERIAL MODELS 104

FIG. 4.42 GEOMETRY AND GRID 105

FIG. 4.43 APPLIED FORCE AND BOUNDARY CONDITIONS 105

FIG. 4.44 SHEAR STRESS VS. SHEAR STRAIN FOR BOTH SCHEMES..... 106

FIG. 4.45 VOLUMETRIC STRAIN VS. SHEAR STRAIN FOR BOTH SCHEMES 106

FIG. 4.46 DEFORMED GRID WITHOUT INTERFACES..... 107

FIG. 4.47 SHEAR STRAIN CONTOUR WITHOUT INTERFACES 107

FIG. 4.48 DEFORMED GRID WITH INTERFACES 107

FIG. 4.49 SHEAR STRAIN CONTOUR WITH INTERFACES 108

FIG. 5.1 SHEAR-INDUCED FABRIC DURING A DIRECT SHEAR TESTS (PICARELLI ET AL., 2000, ADJUSTED AFTER SKEMPTON, 1967) 111

FIG. 5.2 WEAKENED ZONE, SHEAR ZONE AND SLIP SURFACE IN A SLOPE (LEROUEIL, 2001) 111

FIG. 5.3 A HYPOTHETICAL PROCESS OF SLOPE FAILURE INDUCED BY CUTTING (URCIUOLI ET AL., (2007) 112

FIG. 5.4 CROSS SECTION OF CARSINGTON EMBANKMENT (POTTS ET AL., 1990)..... 113

FIG. 5.5 ASSUMED SOFTENING OF FRICTIONAL ANGLE WITH PLASTIC STRAIN FOR YELLOW CLAY (POTTS ET AL., 1990)..... 113

FIG. 5.6 (A)-(C) DEVELOPMENT OF STRAINS AS COLLAPSE IS APPROACHED; (D) STRENGTH MOBILISED JUST BEFORE FAILURE IN STRAIN-SOFTENING ZONE (POTTS ET AL., 1990)..... 113

FIG. 5.7 GEOLOGICAL SECTION AND SLOPE PROFILE..... 114

FIG. 5.8 DEVELOPMENT OF THE SLIP SURFACE AT SELBORNE (AFTER BROMHEAD ET AL., 1998) 115

FIG. 5.9 CRITICAL INCLINOMETER ELEMENT DISPLACEMENTS WITH TIME (COOPER ET AL., 1998)..... 116

FIG. 5.10 RUPTURE SURFACES PREDICTED BY THE ANALYSES ON 3:1 SLOPES, 10 M HIGH, WITH SURFACE SUCTION 10 kPA AND VARYING K_0 (POTTS ET AL., 1997)..... 118

FIG. 5.11 CONTOURS OF ACCUMULATED DEVIATORIC PLASTIC STRAIN (3:1 SLOPE, 10 M HIGH, $K_0=1.5$ AND SURFACE SUCTION 10 kPA) (POTTS ET AL., 1997)..... 119

FIG. 5.12 VECTORS OF CURRENT DISPLACEMENT (14.5 YEARS AFTER EXCAVATION, 3:1 SLOPE, 10 M HIGH, $K_0=1.5$ AND SURFACE SUCTION 10 kPA) (POTTS ET AL., 1997)..... 119

FIG. 5.13 (A) DEVELOPMENT OF AVERAGE PORE PRESSURE RATIO ON THE RUPTURE SURFACE, AND (B) MID-SLOPE HORIZONTAL DISPLACEMENT WITH TIME (14.5 YEARS AFTER EXCAVATION, 3:1 SLOPE, 10 M HIGH, $K_0=1.5$ AND SURFACE SUCTION 10 kPA) (POTTS ET AL., 1997) 120

FIG. 5.14 MODEL GEOMETRY OF SLOPE IN STIFF CLAY 121

FIG. 5.15 SHEAR STRAIN RATE JUST AFTER COLLAPSE (NS1) 123

FIG. 5.16 SHEAR STRAIN RATE JUST AFTER COLLAPSE (NS2) 123

FIG. 5.17 SHEAR STRAIN RATE JUST AFTER COLLAPSE (NS3) 123

FIG. 5.18 MID-SLOPE HORIZONTAL DISPLACEMENT WITH TIME FOR NS1-NS3 124

FIG. 5.19 FOS AND PREDICTED SLIP SURFACE WITH PEAK STRENGTH PARAMETERS 125

FIG. 5.20 FOS AND PREDICTED SLIP SURFACE WITH POST-STRENGTH PARAMETERS 126

FIG. 5.21 FOS AND PREDICTED SLIP SURFACE WITH RESIDUAL STRENGTH PARAMETERS 126

FIG. 5.22 SHEAR STRAIN RATE USING PEAK STRENGTH WITH $\psi = 0$ (FOS=1.25)..... 126

FIG. 5.23 SHEAR STRAIN RATE USING PEAK STRENGTH WITH $\psi = \phi'$ (FOS=1.29) 126

| | |
|--|-----|
| FIG. 5.24 SHEAR STRAIN RATE USING POST-RUPTURE STRENGTH WITH $\psi = 0$ (FOS=0.92)..... | 127 |
| FIG. 5.25 SHEAR STRAIN RATE USING POST-RUPTURE STRENGTH WITH $\psi = \phi'$ (FOS=0.96) | 127 |
| FIG. 5.26 SHEAR STRAIN RATE USING RESIDUAL STRENGTH WITH $\psi = 0$ (FOS=0.64)..... | 127 |
| FIG. 5.27 SHEAR STRAIN RATE USING RESIDUAL STRENGTH WITH $\psi = \phi'$ (FOS=0.67)..... | 127 |
| FIG. 5.28 COMPARISON OF PREDICTED RUPTURE SURFACES FROM NON-SOFTENING ANALYSES | 128 |
| FIG. 5.29 GEOMETRY OF SLOPE IN STIFF CLAY IN TYPICAL ANALYSIS (S3) | 129 |
| FIG. 5.30 VECTORS OF DISPLACEMENT FOR TYPICAL ANALYSIS (S3)..... | 129 |
| FIG. 5.31 ACCUMULATED PLASTIC SHEAR STRAIN FOR TYPICAL ANALYSIS (S3) | 130 |
| FIG. 5.32 CONTOURS OF VOLUMETRIC STRAIN FOR TYPICAL ANALYSIS (S3) | 130 |
| FIG. 5.33 CONTOURS OF PORE PRESSURE FOR TYPICAL ANALYSIS (S3) (JUST AFTER EXCAVATION) | 131 |
| FIG. 5.34 PORE PRESSURE CHANGE IN MIDDLE PROFILE..... | 131 |
| FIG. 5.35 PORE PRESSURE CHANGE IN BOTTOM PROFILE..... | 132 |
| FIG. 5.36 DEVELOPMENT OF AVERAGE PORE PRESSURE RATIO ON THE RUPTURE SURFACE | 132 |
| FIG. 5.37 COMPREHENSIVE SHEAR STRENGTH ENVELOPES | 133 |
| FIG. 5.38 COMPARISON OF FINAL SLIP SURFACE WITH ORIGINAL RESULT (POTTS ET AL., 1997)..... | 134 |
| FIG. 5.39 MID-SLOPE HORIZONTAL DISPLACEMENT WITH TIME FOR S1-S6..... | 135 |
| FIG. 5.40 VARIATION OF COLLAPSE TIME WITH K_0 | 135 |
| FIG. 5.41 VECTORS OF DISPLACEMENT FOR S1-S6 | 136 |
| FIG. 5.42 ACCUMULATED PLASTIC SHEAR STRAIN FOR S1-S6 | 137 |
| FIG. 5.43 MID-SLOPE HORIZONTAL DISPLACEMENT WITH TIME FOR S5 AND S7 | 138 |
| FIG. 5.44 VECTORS OF DISPLACEMENT FOR S5 AND S7 | 138 |
| FIG. 5.45 ACCUMULATED PLASTIC SHEAR STRAIN FOR S5 AND S7 | 139 |
| FIG. 5.46 MID-SLOPE HORIZONTAL DISPLACEMENT WITH TIME FOR S9-S11..... | 139 |
| FIG. 5.47 DISPLACEMENT VECTORS FOR S8-S11 | 140 |
| FIG. 5.48 ACCUMULATED PLASTIC SHEAR STRAIN FOR S8-S11 | 141 |
| FIG. 5.49 FRICTION ANGLE AND COHESION VARIATIONS WITH PLASTIC SHEAR STRAIN | 142 |
| FIG. 5.50 VECTORS OF DISPLACEMENT FOR TS3..... | 143 |
| FIG. 5.51 ACCUMULATED PLASTIC SHEAR STRAIN FOR TS3 | 144 |
| FIG. 5.52 CONTOURS OF VOLUMETRIC STRAIN FOR TS3 | 145 |
| FIG. 5.53 REPRESENTATIVE ELEMENTS..... | 145 |
| FIG. 5.54 DEVELOPMENT OF SHEAR STRAIN INCREMENT WITH TIME | 146 |
| FIG. 5.55 DEVELOPMENT OF PRINCIPAL STRESS DIFFERENCE WITH TIME (TS3)..... | 147 |
| FIG. 5.56 SHEAR STRESS DISTRIBUTION ALONG FAILURE SURFACE JUST AFTER EXCAVATION | 148 |
| FIG. 5.57 SHEAR STRESS DISTRIBUTION ALONG FAILURE SURFACE 9 YEARS AFTER EXCAVATION | 148 |
| FIG. 5.58 SHEAR STRESS DISTRIBUTION ALONG FAILURE SURFACE 15.2 YEARS AT COLLAPSE..... | 149 |
| FIG. 5.59 DEVELOPMENT OF COHESION ALONG FAILURE SURFACE..... | 149 |
| FIG. 5.60 DEVELOPMENT OF FRICTION ALONG FAILURE SURFACE | 150 |
| FIG. 5.61 DEVELOPMENT OF PORE PRESSURE ALONG FAILURE SURFACE | 151 |

| | |
|---|-----|
| FIG. 5.62 DEVELOPMENT OF LOCAL PORE PRESSURE RATIO ALONG FAILURE SURFACE | 151 |
| FIG. 5.63 DEVELOPMENT OF LOCAL FACTOR OF STABILITY ALONG FAILURE SURFACE..... | 152 |
| FIG. 5.64 MID-SLOPE HORIZONTAL DISPLACEMENT WITH TIME FOR TS1-TS6..... | 153 |
| FIG. 5.65 DISPLACEMENT VECTORS FOR TS1-TS6 | 154 |
| FIG. 5.66 ACCUMULATED PLASTIC SHEAR STRAIN FOR TS1-TS6 | 155 |
| FIG. 5.67 MID-SLOPE HORIZONTAL DISPLACEMENT WITH TIME FOR TS9-TS11..... | 156 |
| FIG. 5.68 DISPLACEMENT VECTORS FOR TS8-TS11 | 157 |
| FIG. 5.69 ACCUMULATED PLASTIC SHEAR STRAIN FOR TS8-TS11 | 158 |
| FIG. 5.70 COHESION VARIATION WITH PLASTIC SHEAR STRAIN FOR DIFFERENT ANALYSES | 160 |
| FIG. 5.71 FRICTION ANGLE VARIATION WITH PLASTIC SHEAR STRAIN FOR DIFFERENT ANALYSES | 160 |
| FIG. 5.72 VARIATION OF COLLAPSE TIME WITH K_0 | 161 |
| FIG. 5.73 COHESION VARIATION WITH PLASTIC SHEAR STRAIN FOR DIFFERENT ANALYSES | 162 |
| FIG. 5.74 FRICTION ANGLE VARIATION WITH PLASTIC SHEAR STRAIN FOR DIFFERENT ANALYSES | 162 |
| FIG. 5.75 COHESION VARIATION WITH PLASTIC SHEAR STRAIN FOR DIFFERENT ANALYSES | 164 |
| FIG. 5.76 FRICTION ANGLE VARIATION WITH PLASTIC SHEAR STRAIN FOR DIFFERENT ANALYSES | 165 |
| FIG. 5.77 GEOMETRY OF SLOPE IN STIFF CLAY IN ANALYSES S12H14, TS12H14 AND TS12H14N3 | 166 |
| FIG. 5.78 VECTORS OF DISPLACEMENT FOR TS12H14..... | 167 |
| FIG. 5.79 ACCUMULATED PLASTIC SHEAR STRAIN FOR TS12H14..... | 167 |
| FIG. 5.80 COHESION SOFTENING FOR TS12H14 (UNIT: PA) | 168 |
| FIG. 5.81 FRICTION ANGLE SOFTENING FOR TS12H14 (UNIT: °) | 168 |
| FIG. 5.82 CONTOURS OF PORE PRESSURE FOR TS12H14..... | 169 |
| FIG. 5.83 POSITION OF ELEMENT (15,9) FOR S12H14, TS12H14 AND TS12H14N3 | 169 |
| FIG. 5.84 DEVELOPMENT OF PORE PRESSURE OF ELEMENT (15,9) WITH TIME FOR S12H14, TS12H14 AND TS12H14N3..... | 170 |
| FIG. 5.85 MID-SLOPE HORIZONTAL DISPLACEMENT WITH TIME FOR S12H14, TS12H14 AND TS12H14N3 | 170 |
| FIG. 5.86 VECTORS OF DISPLACEMENT FOR S12H14 | 171 |
| FIG. 5.87 ACCUMULATED PLASTIC SHEAR STRAIN FOR S12H14..... | 172 |
| FIG. 5.88 COHESION SOFTENING FOR S12H14 (UNIT: PA)..... | 172 |
| FIG. 5.89 FRICTION ANGLE SOFTENING FOR S12H14 (UNIT: °) | 173 |
| FIG. 5.90 CONTOURS OF PORE PRESSURE FOR S12H14 | 173 |
| FIG. 5.91 VECTORS OF DISPLACEMENT FOR TS12H14N3 | 174 |
| FIG. 5.92 ACCUMULATED PLASTIC SHEAR STRAIN FOR TS12H14N3..... | 175 |
| FIG. 5.93 COHESION SOFTENING FOR TS12H14N3 (UNIT: PA) | 175 |
| FIG. 5.94 FRICTION ANGLE SOFTENING FOR TS12H14N3 (UNIT: °) | 176 |
| FIG. 5.95 CONTOURS OF PORE PRESSURE FOR TS12H14N3..... | 176 |
| FIG. 5.96 DEVELOPMENT OF MID-SLOPE DISPLACEMENT WITH TIME FOR S3H8-S3H10 | 178 |
| FIG. 5.97 DEVELOPMENT OF MID-SLOPE DISPLACEMENT WITH TIME FOR TS3H7.5-TS3H10 | 178 |
| FIG. 5.98 DEVELOPMENT OF MID-SLOPE DISPLACEMENT WITH TIME FOR TS3H7.5N-TS3H10N..... | 179 |

| | |
|---|-----|
| FIG. 6.1 LOCATION OF AZNALCÓLLAR TAILINGS DEPOSIT (ALONSO & GENS, 2006A)..... | 183 |
| FIG. 6.2 PLAN VIEW OF THE AZNALCÓLLAR TAILINGS DEPOSIT AND REPRESENTATIVE CROSS SECTION OF THE FAILED DAM (ALONSO & GENS, 2006A)..... | 184 |
| FIG. 6.3 ORIGINAL DAM DESIGN (ALONSO & GENS, 2006A)..... | 184 |
| FIG. 6.4 EVOLUTION OF REPRESENTATIVE CROSS-SECTION OF THE DAM ACTUALLY BUILT (EAST SIDE) (GENS & ALONSO, 2006)..... | 185 |
| FIG. 6.5 TWO VIEWS OF THE BREACHED DAM A FEW HOURS AFTER THE FAILURE (ALONSO & GENS, 2006A)..... | 186 |
| FIG. 6.6 CROSS-SECTION OF THE SLIDE AT THE POSITION OF PROFILE 4. (A) GEOMETRY AFTER THE SLIDE AS INTERPRETED FROM BOREHOLE RESULTS AND SURFACE TOPOGRAPHY (B) RECONSTRUCTION OF THE POSITION OF THE SLIDING SURFACES BEFORE THE FAILURE (ALONSO & GENS, 2006A) | 186 |
| FIG. 6.7 DIRECT SHEAR TEST ON SPECIMEN OF GUADALQUIVIR BLUE CLAY FROM BOREHOLE SAMPLE AT AZNALCÓLLAR DAM (NORMAL EFFECTIVE STRESS: 400 kPa) (ALONSO & GENS, 2006A) | 188 |
| FIG. 6.8 DATA FROM DIRECT SHEAR TEST WITH SHEAR DIRECTION REVERSALS ON GUADALQUIVIR BLUE CLAY (OLALLA & CUÉLLAR, 2001)..... | 188 |
| FIG. 6.9 NORMALISED LOSS OF STRENGTH OF GUADALQUIVIR BLUE CLAY, IMMEDIATELY POST-PEAK, AS A FUNCTION OF VERTICAL STRESS (ALONSO & GENS, 2006A)..... | 189 |
| FIG. 6.10 VARIATION OF BRITTLINESS INDICES I_f AND I_B OF GUADALQUIVIR BLUE CLAY WITH EFFECTIVE VERTICAL STRESS (ALONSO & GENS, 2006A) | 190 |
| FIG. 6.11 COMPARISON OF BRITTLINESS INDEX I_B WITH OTHER VALUES REPORTED BY BISHOP ET AL. (1971) (ALONSO & GENS, 2006A)..... | 190 |
| FIG. 6.12 DIRECT SHEAR STRENGTH ENVELOPES FOR GUADALQUIVIR BLUE CLAY (ALONSO & GENS, 2006A) | 191 |
| FIG. 6.13 SLICKENSIDES EXPOSED ON A SEDIMENTATION PLANE. RIVER BANK OF AGRIO RIVER (ALONSO & GENS, 2006A)..... | 192 |
| FIG. 6.14 SLICKENSIDES OBSERVED IN A CORE RECOVERED IN BOREHOLE S1-3 AT 13.5 M DEPTH (ALONSO & GENS, 2006A)..... | 193 |
| FIG. 6.15 SLIP BAND OBTAINED USING THE FINITE ELEMENT TECHNIQUE (OLALLA & CUÉLLAR, 2001) | 193 |
| FIG. 6.16 MOST UNFAVOURABLE SLIP PLANE OBTAINED FROM LIMIT EQUILIBRIUM ANALYSIS (OLALLA & CUÉLLAR, 2001)..... | 194 |
| FIG. 6.17 COMPARISON OF SLIDE SURFACES OBTAINED FROM DIFFERENT METHODS (OLALLA & CUÉLLAR, 2001)..... | 194 |
| FIG. 6.18 CONTOURS OF EQUAL SHEAR STRAIN CALCULATED AT FAILURE IN A 2-D ELASTOPLASTIC FINITE ELEMENT ANALYSIS: HOMOGENEOUS CLAY (GENS & ALONSO, 2006)..... | 196 |
| FIG. 6.19 (A) CONTOURS OF ACCUMULATED SHEAR DEFORMATIONS FROM ORIGIN OF CALCULATIONS (MAXIMUM DEFORMATION 22.35%) (B) MESH DEFORMATION DURING FAILURE PROCESS (GENS & ALONSO, 2006) | 197 |
| FIG. 6.20 INITIAL GRID | 200 |
| FIG. 6.21 WHOLE GRID | 200 |
| FIG. 6.22 MATERIAL AND CONSTRUCTION GROUPS | 201 |
| FIG. 6.23 SOFTENING OF COHESION WITH PLASTIC SHEAR STRAIN FOR BLUE CLAY MASS..... | 203 |
| FIG. 6.24 SOFTENING OF FRICTION ANGLE WITH PLASTIC SHEAR STRAIN FOR BLUE CLAY MASS..... | 203 |
| FIG. 6.25 SOFTENING OF COHESION WITH PLASTIC SHEAR STRAIN FOR WEAK LAYER | 204 |
| FIG. 6.26 SOFTENING OF FRICTION ANGLE WITH PLASTIC SHEAR STRAIN FOR WEAK LAYER | 204 |

FIG. 6.27 POSITION OF WEAK CLAY LAYER IN THE NUMERICAL MODEL 204

FIG. 6.28 STRESS DISPLACEMENT RELATIONSHIP ADOPTED FOR INTACT CLAY MASS AND WEAK LAYER 205

FIG. 6.29 SHEAR STRAIN RATE DEVELOPMENT OF AZNALCÓLLAR DAM FAILURE 207

FIG. 6.30 SHEAR STRAIN INCREMENT DEVELOPMENT OF AZNALCÓLLAR DAM FAILURE 208

FIG. 6.31 VELOCITY DEVELOPMENT OF AZNALCÓLLAR DAM FAILURE 209

FIG. 6.32 TOTAL DISPLACEMENT DEVELOPMENT OF AZNALCÓLLAR DAM FAILURE..... 210

FIG. 6.33 HORIZONTAL DISPLACEMENT AT PHASE 35P11 210

FIG. 6.34 DEFORMED GRID WITH MAGNIFICATION=5 211

FIG. 6.35 MAXIMUM UNBALANCED FORCE VS. STEP TILL PHASE 35P11 211

FIG. 6.36 PORE WATER PRESSURE DEVELOPMENT OF AZNALCÓLLAR DAM FAILURE 213

FIG. 6.37 DEVELOPMENT OF ACCUMULATED PLASTIC SHEAR STRAIN OF AZNALCÓLLAR DAM FAILURE 214

FIG. 6.38 EVOLUTION OF COHESION IN AZNALCÓLLAR DAM FAILURE (CONTOUR INTERVAL=1.5 kPa) 216

FIG. 6.39 EVOLUTION OF FRICTION ANGLE IN AZNALCÓLLAR DAM FAILURE (CONTOUR INTERVAL=1.5°)
..... 217

FIG. 6.40 FINAL SLIP SURFACE PREDICTED ACCORDING TO PLASTICITY POINTS..... 218

FIG. 6.41 SLIP SURFACE OBTAINED DIRECTLY FROM PLASTICITY POINTS..... 218

FIG. 6.42 SLIP SURFACE: COMPARISON OF *FLAC*, *FEM*, *LEM* AND FIELD BORINGS..... 218

FIG. 6.43 LOCATION OF SLIP SURFACE AND REPRESENTATIVE POINTS 219

FIG. 6.44 HORIZONTAL DISPLACEMENT DEVELOPMENT ALONG DOWNSTREAM DAM EMBANKMENT 219

FIG. 6.45 DEVELOPMENT OF PORE PRESSURE AT POINTS (A-E) ALONG PROFILE ABCDE..... 220

FIG. 6.46 DISTRIBUTION OF PORE PRESSURE JUST AT FAILURE ALONG PROFILE A-E AT ELEVATION=30.5:
COMPARISON OF THE PRESENT MODEL, *FEM* AND SIMPLIFIED ELASTIC-CONSOLIDATION
ANALYSES 221

FIG. 6.47 POST-FAILURE EVOLUTION OF PORE PRESSURE DISTRIBUTION ALONG PROFILE A-E 221

FIG. 6.48 REPRESENTATIVE POINTS I-P ALONG SLIP SURFACE 222

FIG. 6.49 DEVELOPMENT OF HORIZONTAL DISPLACEMENTS OF POINTS I-P..... 222

FIG. 6.50 DEVELOPMENT OF PORE WATER PRESSURE OF POINTS I-P 223

FIG. 6.51 DEVELOPMENT OF HORIZONTAL VELOCITY OF POINTS I-P TILL FAILURE (STEP=939103)..... 224

FIG. 6.52 DEVELOPMENT OF SHEAR STRAIN RATE OF POINTS I-P TILL FAILURE (STEP=939103)..... 224

FIG. 6.53 DEVELOPMENT OF SHEAR STRAIN INCREMENT OF POINTS I-P TILL FINAL FAILURE..... 225

FIG. 6.54 STRESS PATH OF POINT I..... 225

FIG. 6.55 STRESS PATH OF POINT J..... 226

FIG. 6.56 STRESS PATH OF POINT K 226

FIG. 6.57 STRESS PATH OF POINT L..... 226

FIG. 6.58 STRESS PATH OF POINT M..... 227

FIG. 6.59 STRESS PATH OF POINT N 227

FIG. 6.60 STRESS PATH OF POINT O 227

FIG. 6.61 STRESS PATH OF POINT P 228

FIG. 6.62 COHESION VARIATION WITH $e_{plastic}$ OF POINT I..... 228

FIG. 6.63 COHESION VARIATION WITH $e_{plastic}$ OF POINT J..... 229

FIG. 6.64 COHESION VARIATION WITH $E_{PLASTIC}$ OF POINT K 229

FIG. 6.65 COHESION VARIATION WITH $E_{PLASTIC}$ OF POINT L 229

FIG. 6.66 COHESION VARIATION WITH $E_{PLASTIC}$ OF POINT M 230

FIG. 6.67 COHESION VARIATION WITH $E_{PLASTIC}$ OF POINT N 230

FIG. 6.68 COHESION VARIATION WITH $E_{PLASTIC}$ OF POINT O 230

FIG. 6.69 COHESION VARIATION WITH $E_{PLASTIC}$ OF POINT P 231

FIG. 6.70 VARIATION OF FRICTION ANGLE WITH $E_{PLASTIC}$ OF POINT I 231

FIG. 6.71 VARIATION OF FRICTION ANGLE WITH $E_{PLASTIC}$ OF POINT J 231

FIG. 6.72 VARIATION OF FRICTION ANGLE WITH $E_{PLASTIC}$ OF POINT K 232

FIG. 6.73 VARIATION OF FRICTION ANGLE WITH $E_{PLASTIC}$ OF POINT L 232

FIG. 6.74 VARIATION OF FRICTION ANGLE WITH $E_{PLASTIC}$ OF POINT M 233

FIG. 6.75 VARIATION OF FRICTION ANGLE WITH $E_{PLASTIC}$ OF POINT N 233

FIG. 6.76 VARIATION OF FRICTION ANGLE WITH $E_{PLASTIC}$ OF POINT O 233

FIG. 6.77 VARIATION OF FRICTION ANGLE WITH $E_{PLASTIC}$ OF POINT P 234

FIG. 6.78 SHEAR STRESS VS. SHEAR STRAIN AT POINT J 234

FIG. 6.79 SHEAR STRESS VS. SHEAR STRAIN AT POINT L 234

FIG. 6.80 SHEAR STRESS VS. SHEAR STRAIN AT POINT N 235

FIG. 6.81 SHEAR STRESS VS. SHEAR STRAIN AT POINT P 235

FIG. 6.82 HORIZONTAL DISPLACEMENT VS. SHEAR STRAIN AT POINT J 235

FIG. 6.83 HORIZONTAL DISPLACEMENT VS. SHEAR STRAIN AT POINT L 236

FIG. 6.84 HORIZONTAL DISPLACEMENT VS. SHEAR STRAIN AT POINT N 236

FIG. 6.85 HORIZONTAL DISPLACEMENT VS. SHEAR STRAIN AT POINT P 236

FIG. 6.86 RESIDUAL FACTOR VS. SHEAR STRAIN AT POINT J 237

FIG. 6.87 RESIDUAL FACTOR VS. SHEAR STRAIN AT POINT L 237

FIG. 6.88 RESIDUAL FACTOR VS. SHEAR STRAIN AT POINT N 238

FIG. 6.89 RESIDUAL FACTOR VS. SHEAR STRAIN AT POINT P 238

FIG. 6.90 BRITTLENESS INDEX VS. SHEAR STRAIN AT POINT J 238

FIG. 6.91 BRITTLENESS INDEX VS. SHEAR STRAIN AT POINT L 239

FIG. 6.92 BRITTLENESS INDEX VS. SHEAR STRAIN AT POINT N 239

FIG. 6.93 BRITTLENESS INDEX VS. SHEAR STRAIN AT POINT P 239

FIG. 6.94 PRE-FAILURE DEVELOPMENT OF AVERAGE STRESS RATIO ALONG SLIP SURFACE 240

FIG. 6.95 PRE-FAILURE DEVELOPMENT OF EQUIVALENT MOBILISED FRICTION ANGLE 240

FIG. 6.96 POST-FAILURE DEVELOPMENT OF AVERAGE STRESS RATIO ALONG SLIP SURFACE 241

FIG. 6.97 POST-FAILURE DEVELOPMENT OF EQUIVALENT MOBILISED FRICTION ANGLE 242

FIG. 6.98 PRE-FAILURE DEVELOPMENT OF AVERAGE RESIDUAL FACTOR 242

FIG. 6.99 POST-FAILURE DEVELOPMENT OF AVERAGE RESIDUAL FACTOR 243

FIG. 6.100 PRE-FAILURE DEVELOPMENT OF AVERAGE BRITTLENESS ALONG SLIP SURFACE 243

FIG. 6.101 POST-FAILURE DEVELOPMENT OF AVERAGE BRITTLENESS ALONG SLIP SURFACE 244

FIG. 6.102 PRE-FAILURE DEVELOPMENT OF AVERAGE PORE PRESSURE RATIO ALONG SLIP SURFACE 244

| | |
|--|-----|
| FIG. 6.103 DEVELOPMENT OF AVERAGE STRESS CONDITION ALONG SLIP SURFACE | 245 |
| FIG. 6.104 DISTRIBUTION OF SHEAR STRESS ALONG FAILURE SURFACE AT PHASE 23 (STEP=587500)... | 245 |
| FIG. 6.105 DISTRIBUTION OF SHEAR STRESS ALONG FAILURE SURFACE AT PHASE 26 (STEP=649650)... | 246 |
| FIG. 6.106 DISTRIBUTION OF SHEAR STRESS ALONG FAILURE SURFACE AT INITIAL FAILURE PHASE (STEP=939103)..... | 246 |
| FIG. 6.107 DISTRIBUTION OF SHEAR STRESS ALONG FAILURE SURFACE AT FINAL FAILURE PHASE (STEP=1018000)..... | 247 |
| FIG. 6.108 COHESION DISTRIBUTION ALONG SLIP SURFACE AT PHASE 23 (STEP=587500) | 247 |
| FIG. 6.109 COHESION DISTRIBUTION ALONG SLIP SURFACE AT PHASE 26 (STEP=649650) | 248 |
| FIG. 6.110 COHESION DISTRIBUTION ALONG SLIP SURFACE AT INITIAL FAILURE PHASE (STEP=939103) | 248 |
| FIG. 6.111 COHESION DISTRIBUTION ALONG SLIP SURFACE AT FINAL FAILURE PHASE (STEP=1018000) | 248 |
| FIG. 6.112 FRICTION DISTRIBUTION ALONG SLIP SURFACE AT PHASE 23 (STEP=587500)..... | 249 |
| FIG. 6.113 FRICTION DISTRIBUTION ALONG SLIP SURFACE AT PHASE 26 (STEP=649650)..... | 249 |
| FIG. 6.114 FRICTION DISTRIBUTION ALONG SLIP SURFACE AT INITIAL FAILURE PHASE (STEP=939103). | 249 |
| FIG. 6.115 FRICTION DISTRIBUTION ALONG SLIP SURFACE AT FINAL FAILURE PHASE (STEP=1018000) . | 250 |
| FIG. 6.116 SHEAR STRESS DEVELOPMENT ALONG FAILURE SURFACE FROM PHASE 23 TO FINAL FAILURE | 250 |
| FIG. 6.117 POSITIONS OF WEAK LAYERS AND MATERIAL GROUPS..... | 252 |
| FIG. 6.118 SHEAR STRAIN RATE AT THE END OF SIMULATION..... | 254 |
| FIG. 6.119 ACCUMULATED PLASTIC SHEAR STRAIN AT THE END OF SIMULATION | 255 |
| FIG. 6.120 SOFTENING OF COHESION WITH PLASTIC SHEAR STRAIN FOR BLUE CLAY MASS..... | 256 |
| FIG. 6.121 SOFTENING OF FRICTION ANGLE WITH PLASTIC SHEAR STRAIN FOR BLUE CLAY MASS..... | 257 |
| FIG. 6.122 MATERIAL GROUPS IN NUMERICAL MODEL | 257 |
| FIG. 6.123 SHEAR STRAIN RATE DEVELOPMENT OF AZNALCÓLLAR DAM FAILURE | 259 |
| FIG. 6.124 SHEAR STRAIN INCREMENT DEVELOPMENT OF AZNALCÓLLAR DAM FAILURE | 260 |
| FIG. 6.125 VELOCITY DEVELOPMENT OF AZNALCÓLLAR DAM FAILURE | 261 |
| FIG. 6.126 TOTAL DISPLACEMENT DEVELOPMENT OF AZNALCÓLLAR DAM FAILURE..... | 262 |
| FIG. 6.127 HORIZONTAL DISPLACEMENT AT PHASE 35P6..... | 262 |
| FIG. 6.128 DEFORMED GRID WITH MAGNIFICATION=5..... | 262 |
| FIG. 6.129 PORE WATER PRESSURE DEVELOPMENT OF AZNALCÓLLAR DAM FAILURE | 265 |
| FIG. 6.130 DEVELOPMENT OF ACCUMULATED PLASTIC SHEAR STRAIN OF AZNALCÓLLAR DAM FAILURE | 266 |
| FIG. 6.131 EVOLUTION OF COHESION IN AZNALCÓLLAR DAM FAILURE (CONTOUR INTERVAL=5 kPa) . | 268 |
| FIG. 6.132 EVOLUTION OF FRICTION ANGLE IN AZNALCÓLLAR DAM FAILURE (CONTOUR INTERVAL=1.5°) | 270 |
| FIG. 6.133 FINAL SLIP SURFACE PREDICTED ACCORDING TO PLASTICITY POINTS..... | 270 |
| FIG. 6.134 SLIP SURFACE OBTAINED DIRECTLY FROM PLASTICITY POINTS..... | 270 |
| FIG. 6.135 SLIP SURFACE: COMPARISON OF <i>FLAC ANALYSES L-M, FEM, LEM</i> AND FIELD BORINGS..... | 271 |
| FIG. 6.136 LOCATION OF SLIP SURFACE AND REPRESENTATIVE POINTS | 271 |
| FIG. 6.137 HORIZONTAL DISPLACEMENT DEVELOPMENT ALONG DOWNSTREAM DAM EMBANKMENT ... | 271 |
| FIG. 6.138 DEVELOPMENT OF PORE PRESSURE AT POINTS (A-E) ALONG PROFILE ABCDE..... | 272 |

| | |
|---|-----|
| FIG. 6.139 DISTRIBUTION OF PORE PRESSURE JUST AT FAILURE ALONG PROFILE A-E..... | 273 |
| FIG. 6.140 REPRESENTATIVE POINTS I-P ALONG SLIP SURFACE | 273 |
| FIG. 6.141 STRESS PATH OF POINT I..... | 274 |
| FIG. 6.142 STRESS PATH OF POINT J..... | 274 |
| FIG. 6.143 STRESS PATH OF POINT K | 274 |
| FIG. 6.144 STRESS PATH OF POINT L..... | 275 |
| FIG. 6.145 STRESS PATH OF POINT M..... | 275 |
| FIG. 6.146 STRESS PATH OF POINT N | 276 |
| FIG. 6.147 STRESS PATH OF POINT O | 276 |
| FIG. 6.148 STRESS PATH OF POINT P..... | 276 |
| FIG. 6.149 SHEAR STRESS VS. SHEAR STRAIN AT POINT J..... | 277 |
| FIG. 6.150 SHEAR STRESS VS. SHEAR STRAIN AT POINT L | 277 |
| FIG. 6.151 SHEAR STRESS VS. SHEAR STRAIN AT POINT O..... | 278 |
| FIG. 6.152 SHEAR STRESS VS. SHEAR STRAIN AT POINT P | 278 |
| FIG. 6.153 DEVELOPMENT OF AVERAGE STRESS RATIO ALONG SLIP SURFACE | 279 |
| FIG. 6.154 DEVELOPMENT OF EQUIVALENT MOBILISED FRICTION ANGLE..... | 279 |
| FIG. 6.155 DEVELOPMENT OF AVERAGE RESIDUAL FACTOR | 280 |
| FIG. 6.156 DEVELOPMENT OF AVERAGE BRITTLENESS ALONG SLIP SURFACE | 280 |
| FIG. 6.157 DEVELOPMENT OF AVERAGE PORE PRESSURE RATIO ALONG SLIP SURFACE..... | 281 |
| FIG. 6.158 DEVELOPMENT OF AVERAGE STRESS PATH ALONG SLIP SURFACE | 281 |
| FIG. 6.159 DISTRIBUTION OF SHEAR STRESS ALONG FAILURE SURFACE AT PHASE 23 (STEP=629502)... | 282 |
| FIG. 6.160 DISTRIBUTION OF SHEAR STRESS ALONG FAILURE SURFACE AT PHASE 26 (STEP=689858)... | 282 |
| FIG. 6.161 DISTRIBUTION OF SHEAR STRESS ALONG FAILURE SURFACE AT INITIAL FAILURE PHASE (STEP=1013304)..... | 283 |
| FIG. 6.162 DISTRIBUTION OF SHEAR STRESS ALONG FAILURE SURFACE AT PHASE 35P2 (STEP=1016304) | 283 |
| FIG. 6.163 DISTRIBUTION OF SHEAR STRESS ALONG FAILURE SURFACE AT PHASE 35P3 (STEP=1018304) | 284 |
| FIG. 6.164 DISTRIBUTION OF SHEAR STRESS ALONG FAILURE SURFACE AT FINAL FAILURE PHASE (STEP=1032857)..... | 284 |
| FIG. 6.165 SHEAR STRAIN RATE AT FINAL PHASE IN SUPPLEMENTARY ANALYSIS R..... | 285 |
| FIG. 6.166 PLASTIC ZONES FINAL PHASE IN SUPPLEMENTARY ANALYSIS R | 285 |
| FIG. 6.167 SHEAR STRAIN RATE AT FINAL PHASE IN SUPPLEMENTARY ANALYSIS S..... | 286 |
| FIG. 6.168 PLASTIC ZONES FINAL PHASE IN SUPPLEMENTARY ANALYSIS S..... | 286 |
| FIG. 7.1 SIMPLIFIED MODEL FROM TEST CURVES | 290 |
| FIG. 7.2 SKETCH OF CYLINDRICAL CAVITY EXPANSION | 291 |
| FIG. 7.3 DISPLACEMENT DISTRIBUTION | 304 |
| FIG. 7.4 RADIAL STRESS DISTRIBUTION | 304 |
| FIG. 7.5 DISPLACEMENT DISTRIBUTION | 305 |
| FIG. 7.6 RADIAL STRESS DISTRIBUTION | 306 |



List of figures



| | |
|---|-----|
| FIG. 7.7 DISPLACEMENT DISTRIBUTION | 307 |
| FIG. 7.8 RADIAL STRESS DISTRIBUTION | 307 |
| FIG. 7.9 DISPLACEMENT DISTRIBUTION | 308 |
| FIG. 7.10 RADIAL STRESS DISTRIBUTION | 309 |
| FIG. 7.11 DISPLACEMENT DISTRIBUTION | 310 |
| FIG. 7.12 RADIAL STRESS DISTRIBUTION | 310 |
| FIG. 7.13 RADIAL STRESS DISTRIBUTION | 311 |
| FIG. 7.14 MODEL GEOMETRY | 312 |
| FIG. 7.15 EXPANSION CURVE WITH ZERO INITIAL STRESS | 313 |
| FIG. 7.16 $q - p$ STRESS PATH CURVE WITH ZERO INITIAL STRESS | 314 |
| FIG. 7.17 EXPANSION CURVE WITH 100 kPa INITIAL STRESS..... | 315 |
| FIG. 7.18 $q - p$ STRESS PATH CURVE WITH 100 kPa INITIAL STRESS | 315 |

List of tables

| | |
|--|-----|
| TABLE 2.1 COLLECTED DATA OF POST-PEAK SHEAR STRENGTHS OF STIFF CLAYS | 32 |
| TABLE 2.2 RELEVANT INDEX PROPERTIES OF THE STIFF CLAYS IN TABLE 2.1 | 36 |
| TABLE 2.3 FAILURE DEVELOPMENT IN STIFF CLAYS | 39 |
| TABLE 3.1 EXAMPLE OF PIECE-WISE LINEAR DEFINITION OF SOFTENING PROPERTIES..... | 72 |
| TABLE 3.2 <i>FISH</i> FUNCTION COMBINED WITH BUILT-IN MODEL | 74 |
| TABLE 3.3 DERIVED SOFTENING MODEL CLASS | 75 |
| TABLE 3.4 RUN CLASS FUNCTION | 76 |
| TABLE 4.1 BASIC MODEL PARAMETERS..... | 82 |
| TABLE 4.2 VARIATIONS OF c AND ϕ WITH PLASTIC SHEAR STRAIN γ | 82 |
| TABLE 4.3 DIFFERENT VALUES FOR DILATION..... | 83 |
| TABLE 4.4 DIFFERENT MESH SIZES | 83 |
| TABLE 4.5 PARAMETER ADJUSTMENTS FOR DIFFERENT MESH SIZE (SCHEME I)..... | 84 |
| TABLE 4.6 PARAMETER ADJUSTMENTS FOR DIFFERENT MESH SIZE (SCHEME II) | 84 |
| TABLE 4.7 DIFFERENT VALUES FOR DILATION..... | 85 |
| TABLE 4.8 CLAY PROPERTIES ASSUMED IN NUMERICAL ANALYSES..... | 97 |
| TABLE 4.9 DIFFERENT SCHEMES FOR INITIAL STRESS | 99 |
| TABLE 4.10 MATERIAL PARAMETERS..... | 104 |
| TABLE 4.11 ELASTIC PARAMETERS OF SHEAR BOX..... | 104 |
| TABLE 4.12 INTERFACE CONFIGURATION | 107 |
| TABLE 5.1 MODEL PARAMETERS ASSUMED IN NUMERICAL ANALYSES..... | 121 |
| TABLE 5.2 FOS CALCULATION RESULTS | 127 |
| TABLE 5.3 RESULTS OF NON-SOFTENING AND ONE-STAGE SOFTENING MODELLING | 128 |
| TABLE 5.4 RESULTS OF TWO-STAGE SOFTENING MODELLING | 142 |
| TABLE 5.5 RESULTS OF TWO-STAGE SOFTENING MODELLING WITH DIFFERENT SOFTENING RATE | 159 |
| TABLE 5.6 STRENGTH PARAMETERS OF DIFFERENT SOFTENING ANALYSES AND RELEVANT RESULTS ... | 159 |
| TABLE 5.7 STRENGTH PARAMETERS FOR SOFTENING ANALYSES WITH INTACT PEAK STRENGTH | 163 |
| TABLE 5.8 RESULTS OF STABLE SLOPE HEIGHT OF SOFTENING ANALYSES WITH INTACT PEAK STRENGTH | 164 |
| TABLE 5.9 CALCULATION SCHEMES FOR SOFTENING ANALYSES WITH BULK PEAK STRENGTH | 177 |
| TABLE 5.10 RESULTS OF STABLE SLOPE HEIGHT OF SOFTENING ANALYSES WITH BULK PEAK STRENGTH | 177 |
| TABLE 6.1 SHEAR STRENGTHS FOR GUADALQUIVIR BLUE CLAY | 192 |
| TABLE 6.2 GENERAL MODELLING PROCEDURE..... | 198 |
| TABLE 6.3 MODELLING PHASES (FROM APRIL, 1978 TILL APRIL, 1998)..... | 198 |
| TABLE 6.4 BASIC SOIL GEOTECHNICAL PROPERTIES | 199 |
| TABLE 6.5 SOIL MODELS AND PARAMETERS..... | 199 |

| | |
|---|-----|
| TABLE 6.6 SHEAR STRENGTH PARAMETERS AND PLASTIC SHEAR STRAIN LIMITS FOR BLUE CLAY MASS | 203 |
| TABLE 6.7 SHEAR STRENGTH PARAMETERS AND PLASTIC SHEAR STRAIN LIMITS FOR WEAK LAYER..... | 203 |
| TABLE 6.8 MODELLING STEP OF PRE-FAILURE, INITIAL FAILURE AND POST-FAILURE PHASES | 205 |
| TABLE 6.9 MODEL TYPES AND STRENGTH PARAMETERS | 251 |
| TABLE 6.10 ANALYSIS SUMMARY WITH DIFFERENT COMBINATIONS OF WEAK LAYER SETTING | 251 |
| TABLE 6.11 SHEAR STRENGTH PARAMETERS AND PLASTIC SHEAR STRAIN LIMITS FOR BLUE CLAY MASS | 256 |
| TABLE 6.12 MODELLING STEP OF PRE-FAILURE, INITIAL FAILURE AND POST-FAILURE PHASES | 257 |
| TABLE 6.13 SHEAR STRENGTH PARAMETERS AND PLASTIC SHEAR STRAIN LIMITS FOR BLUE CLAY MASS | 285 |
| TABLE 6.14 SHEAR STRENGTH PARAMETERS AND PLASTIC SHEAR STRAIN LIMITS FOR BLUE CLAY MASS | 285 |
| TABLE 6.15 SHEAR STRENGTH PARAMETERS AND PLASTIC SHEAR STRAIN LIMITS FOR WEAK LAYER.... | 285 |
| TABLE 7.1 COMPUTATIONAL RESULTS | 301 |
| TABLE 7.2 DATA OF SHEAR DILATION PARAMETERS h , f and g | 302 |
| TABLE 7.3 RESULTS OF ULTIMATE PRESSURE p_u AND RADII (R_3, R_2, R_1)..... | 302 |
| TABLE 7.4 RESULTS FOR DISPLACEMENT, STRAIN AND STRESS AT R_3 | 303 |
| TABLE 7.5 RESULTS FOR DISPLACEMENT, STRAIN AND STRESS AT R_2 | 303 |
| TABLE 7.6 RESULTS FOR DISPLACEMENT, STRAIN AND STRESS AT R_1 | 303 |
| TABLE 7.7 DATA OF SOFTENING PARAMETER β | 305 |
| TABLE 7.8 RESULTS OF ULTIMATE PRESSURE p_u AND RADII (R_3, R_2, R_1)..... | 305 |
| TABLE 7.9 DATA OF SOFTENING PARAMETER ω | 306 |
| TABLE 7.10 RESULTS OF ULTIMATE PRESSURE p_u AND RADII (R_3, R_2, R_1)..... | 306 |
| TABLE 7.11 DATA OF INITIAL STRESS p_0 | 307 |
| TABLE 7.12 RESULTS OF ULTIMATE PRESSURE p_u AND RADII (R_3, R_2, R_1)..... | 308 |
| TABLE 7.13 DATA OF E and ν | 309 |
| TABLE 7.14 RESULTS OF ULTIMATE PRESSURE p_u AND RADII (R_3, R_2, R_1)..... | 309 |
| TABLE 7.15 DATA OF E and ν | 310 |
| TABLE 7.16 RESULTS OF ULTIMATE PRESSURE p_u AND RADII (R_3, R_2, R_1)..... | 311 |
| TABLE 7.17 MODEL AND PARAMETER CONFIGURATION | 312 |

Chapter 1. Introduction

1.1 General

The definition of stiff clays generally applies to clays with a liquidity index (IL) lower than 0.5 in their natural state (Terzaghi, 1936). This definition identifies just a limit for the water content, below which the clays can be defined stiff. Stiff clays can have different degrees of overconsolidation ratio, but usually they are heavily overconsolidated, brittle and plastic, sometimes fissured and jointed. In this Thesis, stiff clays specifically imply stiff overconsolidated clays.

Stiff clays are also a kind of material with highly inelastic and nonlinear mechanical properties involving strain hardening and strain softening. When samples of stiff clays are subjected to shear or compression tests, a loss of overall shear resistance of specimen with increasing deformation is observed after reaching the peak value (Alonso & Gens, 2006a; Bishop et al., 1971; Burland, 1990; Burland et al., 1996, Calabresi & Manfredini, 1973; Cividini & Gioda, 1992; Georgiannou & Burland, 2001 and 2006; Lupini et al., 1981; Skempton, 1964, 1966 and 1970; Stark & Eid, 1997). This particular mechanical instability is normally referred to as strain softening. For several decades, many papers have studied the shear strength parameters of stiff clays, which are mainly related to peak and residual strengths, but they still remain inconclusive because of the extremely complicated post-peak softening behaviour. It is well known that the mobilised shear strength parameters of stiff clays, especially at post-peak stage, are difficult to determine for engineers while assessing geotechnical engineering stability problems.

1.1.1 Post-peak softening behaviour of stiff clays

As observed in many laboratory tests, the peculiar aspect of the behaviour of stiff clays is the relatively rapid shear strength reduction after peak. Bishop et al. (1965), Calabresi (1980), Burland (1990) and Burland et al. (1996) observed very brittle shearing behaviour in triaxial compression on intact samples of natural stiff clays at low to intermediate confining pressures. This behaviour results from the formation of very thin slip surfaces at around peak strength with an associated rapid drop in shear strength and thereafter approximately rigid block sliding along the resulting slip surface.

Calabresi (1980) observed the same phenomenon. He used the results of direct shear tests on intact Todi clay to distinguish two stages of post-peak strength reduction: the first occurs immediately after peak for a relative displacement of less than 1 mm; the second takes place gradually as the relative displacement increases, tending towards residual strength conditions. He also stated:

- (1) After the peak has been reached, the particle bonds are completely destroyed, so that the effective cohesion disappears and the shear strength corresponds to the value along a fresh surface, with strength parameters given as:

$$c' = 0, \phi' = \phi'_{peak} \quad (1.1)$$

- (2) Only after large relative displacements, with soil particles well reorientated parallel to the discontinuity surface, does the shear strength attain its residual value, the strength parameters now being:

$$c' = 0, \phi' = \phi'_{res} < \phi'_{peak} \quad (1.2)$$

Calabresi found that the immediate post-peak strength envelope lies above the residual strength envelope and had a friction angle corresponding approximately to the intrinsic critical friction angle ϕ_{cs} . He postulated that the immediate post-peak strength is representative of the initial strength along a recently formed pre-existing discontinuity.

The aforementioned immediate post-peak strength by Calabresi is close to the so-called fully softened strength, which is first introduced by Skempton (1970) and defined as the critical-state strength of reconstituted material. Reconstituted clay is formed after an intact clay specimen is thoroughly mixed at between 1.0 and 1.5 times the liquid limit and preferably consolidated one-dimensionally. In this document, fully softened strength is also denoted as critical state strength. Skempton also stated that the initially rapid softening only reduces the effective cohesion component of Mohr-Coulomb shear strength parameters but does not cause orientation of clay particles or reduction in friction angle. Skempton (1977) suggested that shear strength in a fissure corresponds to the fully softened value.

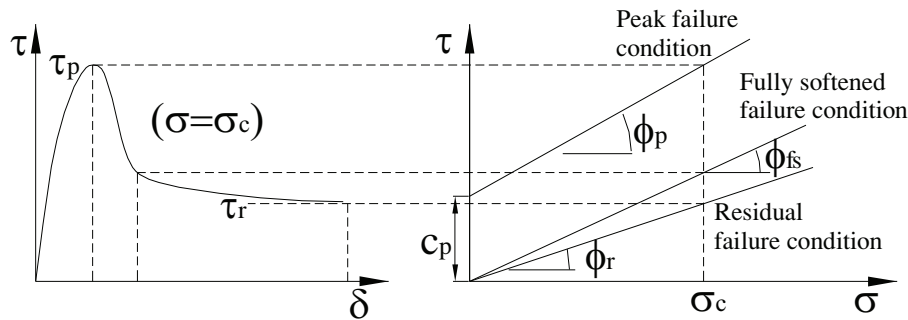


Fig. 1.1 Schematic representation of $\tau - \delta$ and relevant $\tau - \sigma$ relationship for direct shear tests on stiff clays (after Cividini & Gioda, 1992)

Cividini & Gioda (1992) performed the numerical modelling of direct shear tests on stiff clays. In their study, they summarized the observations presented by Simpson et al. (1979) and Calabresi et al. (1990) on the results of direct shear tests on stiff clays which are natural clays with an undrained shear strength greater than 75 kPa, or a liquidity index smaller than 0.5. These stiff clays are usually found in relatively deep, heavily overconsolidated deposits and frequently present, owing to their formation process, particular mechanical characteristics such as non-isotropy, swelling and strain-softening behaviour. They provided a qualitative description of the results of a direct shear test on a stiff clay sample, under constant average vertical stress σ_c , in terms of a diagram relating the average shear stress τ and the horizontal displacement δ (Fig. 1.1).

Cividini & Gioda (1992) subdivided the $\tau - \delta$ curve into three main parts. In the first part, the average shear stress increases till the peak value corresponding to the peak failure envelope indicated by peak cohesion c_p and peak friction angle ϕ_p in the average normal stress—shear stress ($\tau - \sigma$) plane. Afterwards, a reduction of the shear resistance accompanied by an almost complete loss of the peak cohesion occurs just after relatively small additional increments of displacement. This leads to so-called fully softened shear strength—a second failure condition which is characterized by c_{fs} and ϕ_{fs} . In the final part, after further large increments of the horizontal displacement, the friction angle decreases to the residual value ϕ_r while the residual cohesion c_r is approximately equal to zero.

Much attention has also been devoted to the strength on the slip surfaces shortly after their formation (e.g. Burland, 1990; Burland et al., 1996; Georgiannou & Burland, 2001 and 2006). As observed in oedometer and triaxial tests on stiff clays such as Todi Clay, London Clay, Pietrafitta clay and Vallericca clay (Burland, 1990; Burland et al., 1996), the complete destruction of particle bonds is not reached in the first softening stage. Usually a small value of cohesion remains. Burland (1990) noted that initially intact natural samples of London clay and Todi clay exhibit brittle behaviour at low to intermediate confining stresses, with the formation of rupture surfaces at peak intact strength and thereafter rigid body sliding along the surfaces. The strength on a rupture surface drops rapidly to a reasonably constant value after a relative displacement of only a few millimeters. He firstly called it post-rupture strength. For these two clays, the post-rupture strength lines are close to the intrinsic critical state failure lines. In addition, for the London clay at Ashford Common, it was shown that the shear strengths of samples containing pre-existing fissures plot closely around the post-rupture envelope of initially intact samples and are bounded by a lower limit fissured strength line lying a little below the post-rupture envelope. These results give experimental support to the hypothesis assumed by Calabresi (1980) mentioned above and to some extent relate post-rupture strength to the mobilised strength of clays containing pre-existing structures such as fissures, bedding planes and the like. Burland et al. (1996) obtained similar results.

In the 39th Rankine lecture, Leroueil (2001) summarized that Calabresi (1980), Burland (1990) and Burland et al. (1996) observed that shear tests on stiff clays give a peak with formation of rupture surfaces, followed by a rapid drop in strength towards post-rupture strength reached after a displacement along the shear surface of 1 to a few millimeters. They also found that the post-rupture strength envelope lies close to the critical state line obtained on the reconstituted soil. As further displacements take place, there is a progressive orientation of clay particles and a reduction of the angle of shearing resistance towards its residual value.

Moreover, Georgiannou & Burland (2001) designed elaborate test procedures and made a systematic analysis on post-rupture strength properties. Based on the experimental study, they described the factors influencing the post-rupture strength of initially intact samples of Vallericca Clay and Corinth Marl. They have also shown that the post-rupture strength envelope for intact natural stiff clays is well defined, repeatable and insensitive to stress history (both pre- and post-rupture) or to the rotation of principal stresses. These results are believed to be important in understanding the formation of slip surfaces and fissures in stiff clays and in

evaluating their operational strength. Recently, Georgiannou & Burland (2006) made a laboratory study of slip surface formation in an intact natural stiff clay—Corinth Marl. They stated that most of the reduction in shear strength takes place for relative displacements of less than 0.5 mm, after which stable post-rupture strength is reached. In addition, the rapid reduction in strength in stiff clays is believed to be due mainly to the breaking of interparticle bonds, particularly at low to intermediate confining pressures.

The shear strength of stiff clays involving post-rupture strength will be described in detail in Chapter 2.

1.1.2 Progressive failure in stiff clays

As described above, in stiff clays that exhibit distinct peak and residual strength, the shear resistance reduces progressively with increasing strain, and the final product will be progressive failure which is closely connected to geotechnical engineering problems involving strain-softening materials, such as slope stability, dam construction, underground excavation, and so on.

The mechanism of progressive failure was firstly recognized by Terzaghi & Peck (1948) and Taylor (1948). Skempton (1964) emphasized the significance in stability problems of the different peak and residual strengths of soils by introducing a residual factor R as a measure of the difference between the average field strength at collapse and the strengths measured in the laboratory. The residual factor is defined as:

$$R = \frac{\bar{\tau}_p - \bar{\tau}}{\bar{\tau}_p - \bar{\tau}_R} \quad (1.3)$$

where $\bar{\tau}$ is the average shear stress at collapse and $\bar{\tau}_p$ and $\bar{\tau}_R$ are the average peak and residual shear strengths at the current normal effective stress along the eventual rupture surface.

Bjerrum (1967) considered that progressive failure is a type of failure involving nonuniform straining of a strain-weakening material, which results in nonuniform mobilisation of shear strength along potential slip surface at failure. He concluded that soil brittleness and non-uniform straining are the two necessary conditions for progressive failure to play a role in the collapse of slopes. Furthermore, he particularly emphasized the importance of bonds and weathering, and of the possible release of stored energy, in the process of progressive failure.

Leroueil (2001) gave a quite clear description of the mechanisms for progressive failure. If shear stresses locally reach the peak shear strength of the material, there is local failure. If soil presents some strain-softening behaviour, the failed soil elements will support a decreasing shear stress as strain increases. The part of the shear stress that is no longer supported by the failed elements is then transferred to the neighbouring soil elements, which can fail in turn. The process, which may be accompanied by local variations in water content, continues until the equilibrium between shear stresses and strains has been reached. At that time, along a potential failure surface, part of it can exceed the peak, with possibly some elements at large deformation or residual strength, whereas another part of the potential surface has not reached the peak yet. If such equilibrium cannot be obtained, the process will continue until failure conditions extend along the entire failure surface.

Leroueil (2001) also summarized the complete conditions necessary to the development of progressive failure as:

- (a) brittleness of soil;
- (b) non-uniformity in the distribution of shear stresses;
- (c) local shear stresses that exceed the peak strength of the soil;
- (d) boundary conditions such that strains exceeding that at failure may develop.

So far, there have been many case studies on progressive failure in stiff clays, such as Carsington dam, Senise landslide, Aznalcóllar dam, Selborne cut slope, etc. Recent significant contributions with experimental tests and numerical modelling have been presented by Skempton (1970), Dounias et al. (1988, 1996), Yoshida et al. (1991), Chen et al. (1992), Skempton & Vaughan (1993), Potts et al. (1990, 1997), Bromhead et al. (1998), Cooper (1996), Cooper et al. (1998), Georgiannou (2003), Mesri & Shahien (2003), Troncone (2005) and Gens & Alonso (2006).

Mesri & Shahien (2003) stated that, in a first-time slope failure in stiff clays and clay shales, part or all of the global slip surface is unsheared prior to the occurrence of the landslide; however, part of the slip surface may be at the residual condition.

Potts et al. (1997) showed that, in first-time slides in stiff fissured London clay, peak and residual states and a state between them exist simultaneously along the slip surfaces. They also predicted that residual conditions existed along the horizontal part of the eventual slip surface. They thought progressive failure refers to the non-uniform mobilisation of shear strength along a potential rupture surface. If a brittle soil is loaded non-uniformly, some elements of soil will reach peak strength before others and a rupture surface will begin to develop. With further loading the post-peak strains along the rupture surface increases, and the strength reduces from peak towards residual. Final collapse of the soil mass can occur before the rupture surface has fully developed. At collapse, part of the rupture surface has formed and lost strength to post-peak strength, and a part has not yet formed. Thus, the average strength of the soil mass at collapse (the operational strength) must be less than the peak strength and greater than the residual strength.

As indicated by these studies, in the analyses of progressive failure, the mobilised shear strength, i.e. operational shear strength, is the critical controlling parameter. But the operational effective strength envelope for stiff fissured clays en masse is notoriously difficult to determine.

Back-analysis of many first-time slides in stiff fissured clays (e.g. Skempton, 1970 and 1977; Chandler, 1984b) gives operational strengths that are close to, but slightly above, the critical-state strength of the reconstituted material (often called the fully softened strength, i.e. critical state strength). Although there seems to be no obvious a priori reason for this, the observed close agreement between the post-rupture strength envelope and the intrinsic critical-state strength envelope at low confining pressures offers a rational explanation for this puzzle (Georgiannou & Burland, 2001).

Because of their brittle properties and the rapid drop from peak to a well-defined post-rupture strength, most natural stiff clays can be expected to develop fissures and joints during geological unloading and mild tectonic activity. The initial strength along these discontinuities like fissures formed in stiff clays will be controlled by the post-rupture strength envelope and is likely to be close to the post-rupture strength, as suggested

by Calabresi (1980). Therefore, provided significant displacements have not taken place along these discontinuities, then the first-time effective strength of the mass will be close to the post-rupture strength, which in turn has been shown in a number of cases to be close to the critical-state strength at low to medium pressures. In addition, Burland (1990) showed that the in-situ horizontal effective stresses in London Clay at Ashford Common appear to be controlled by the post-rupture strength.

All the results presented above demonstrate that, for stiff clays, post-rupture strength should be taken as an important parameter in softening analysis related to progressive failure and at least as a limit to distinguish intact natural clays and stiff fissured clays. As mentioned above, it will be of great significance to find the relationship between post-rupture strength and the mobilised operational strength of stiff clays, which will provide a way to deduce the operational strength of stiff clays. However, so far, there has not been general detailed data of post-rupture strength. In this Thesis, all the data from tests and numerical analyses related with post-rupture strength is collected and analysed in order to verify the existence of post-rupture strength and shed light on its principal properties.

1.1.3 Solution schemes of softening

As for the causes of softening initiation, two alternative hypotheses are available. Cividini & Gioda (1992), Sterpi (1999, 2000), Sterpi & Cividini (2004) referred to them as structural softening and material, i.e. intrinsic softening.

In the first case, structural instability occurs when a bifurcation point is reached for a given increment of the external actions, i.e. when the uniqueness of solution of the equations governing the stress analysis problem is lost, regardless the particular constitutive model adopted. Because in this case softening can be encountered also for ideally plastic, or even positive hardening materials if the plastic flow rule is non-associated, and it is not specifically related to a loss of its intrinsic shear resistance (Hill, 1958; Rudnicki & Rice, 1975; Rice, 1976; Vermeer, 1982; De Borst, 1988; Vardoulakis & Sulem, 1995).

The second case, referred to as material softening, assumes that the initiation of softening depends on the accumulated plastic strains (Desai, 1974; Desai et al., 1986; Cividini & Gioda, 1992). The reduction of the shear strength with increasing deformation initiates when a given condition on the strain state is attained. That is to say, it is assumed that strain softening is an intrinsic characteristic of the constitutive law which presents a descending branch of the stress-strain diagram. This implies local instability of the material (Hill, 1958), since along this descending branch the increments of stresses and strains satisfy the condition

$$\dot{\epsilon}^T \dot{\sigma} < 0 \quad (1.4)$$

The above local condition can progressively lead to irreversible strain localization and eventually to global instability.

In this paper, only material softening is considered.

1.1.4 Setting up of modified constitutive model incorporating post-rupture strength for stiff clays

Furthermore, Cividini & Gioda (1992), Dounias et al. (1988, 1996), Potts et al. (1987, 1990 and 1997), Sterpi (1999, 2000), Schuller & Schweiger (2002), Sterpi & Cividini (2004) and Troncone (2005) used a generalised non-linear strain-hardening and strain-softening elastoplastic model to make numerical modelling of slope stability such as progressive failure.

Cividini & Gioda (1992) stated that the intrinsic loss of shear strength of the material with increasing shear deformation can be interpreted at the constitutive model level as a particular type of elastic-plastic behaviour with negative hardening, i.e. strain softening.

Troncone (2005) adopted Mohr–Coulomb plastic law in which the strain-softening behaviour of the materials is simulated by reducing the strength parameters with the accumulated deviatoric plastic strains, as suggested by Potts and his coworkers (Dounias et al., 1988, 1996; Potts et al., 1990, 1997; Potts & Zdravkovic, 1999, 2001). The numerical study also confirms the progressive failure mechanism.

The aforementioned generalised non-linear strain-hardening and strain-softening elastoplastic model based on improved Mohr-Coulomb model can describe the mobilised soil strength between peak and residual states by assuming linear decay or exponential decay of strength parameters such as cohesion c' and frictional angle ϕ' with strain. But this model only embodies one-stage post-peak softening behaviour and is unable to distinguish the two-stage softening feature of stiff clays. However, for stiff overconsolidated clays, the curve between peak strength and residual strength should be considered as bilinear due to the existence of the characteristic post-rupture strength. Therefore, for stiff clays with well-defined post-rupture strength, a generalised modified bilinear softening model should be established based on the existing model mentioned above. The theoretical formulation of this new model is to be described in detail and then implemented into a finite difference program (*FLAC*).

1.1.5 Verification and application of new modified constitutive model for stiff clays

Afterwards the new model will be applied to simulate laboratory tests such as triaxial compression tests and direct shear box tests to examine the reasonableness of the new model by comparison with test data.

In addition, the new model will be used to simulate realistic engineering problems among which progressive failure is an important one. A series of analyses of delayed progressive failure of cut slopes in stiff clays similar to those conducted by Potts et al. (1997) will be performed using the two-stage softening model incorporating post-rupture strength. The comparison between the numerical results of the new model with those obtained with the one-stage softening model are then used to confirm the validity of the new model and demonstrate, through parametric analyses, the general influence of post-rupture strength.

In the next step, both the post-rupture strength concept and the two-stage softening model are applied to model a practical geotechnical case. In this thesis, a well known case, the Aznalcóllar dam failure (Olalla & Cuéllar, 2001; Alonso & Gens, 2006a;

Gens & Alonso, 2006) has been shown to involve progressive failure and it is therefore suitable to be taken as a realistic application of the new two-stage softening model. This new modelling can be considered as the continuation of the numerical simulation performed by Gens & Alonso (2006).

Besides the Aznalcóllar dam failure, the post-rupture strength can also be introduced to obtain analytical solutions of cylindrical cavity expansion in stiff overconsolidated clay. This method can be applied especially with stiff overconsolidated clays and overcome the defects in the classical theory about the expansion of elastoplastic cylindrical cavity. Moreover, numerical solutions may be compared with those from analytical method to verify further the performance of the two-stage softening model incorporating post-rupture strength.

1.2 Objectives of research

The aim of this Thesis is mainly to study the delayed and progressive failure in stiff clays via an appropriate constitutive model incorporating the post-rupture strength concept in order to improve the predictions of the softening behaviour of overconsolidated stiff clays. Generally, the main objectives of the thesis are:

- (1) to verify the existence and reliability of post-rupture strength from field tests, laboratory experiments and numerical analysis data.
- (2) to collect comprehensive data for shear strength, especially post-rupture strength, in stiff overconsolidated clays and to make analysis of the collected data to characterise the principal properties of post-rupture strength.
- (3) to establish the constitutive model to predict the two-stage softening feature of stiff overconsolidated clays by modifying the generalised non-linear strain-hardening/softening model based on improved Mohr-Coulomb model.
- (4) to formulate and implement the constitutive model into numerical programs such as *FLAC*, which is capable of analysing geotechnical engineering boundary value problems.
- (5) to examine the reasonableness of the new model by applying it to the simulation of laboratory tests such as triaxial compression tests and direct shear box test via comparison with test data.
- (6) to apply the new model to analyse delayed progressive failure of cut slopes in stiff clays, confirm the validity of the new model by comparison of the numerical results from the new model with those from one-stage softening model and demonstrate the general influence of post-rupture strength on progressive failure through parametric analyses.
- (7) to introduce both the post-rupture strength concept and the two-stage softening model into representative progressive failure cases such as the well known one of the Aznalcóllar dam failure.
- (8) to extend the post-rupture strength concept to analytical solutions to cylindrical cavity expansion in stiff overconsolidated clay to demonstrate the generalisation of post-rupture strength concept and the relevant two-stage softening model in geotechnical engineering problems.

1.3 Thesis layout

The outline of this paper is as follows:

- Chapter 1 gives the introduction and presents the objectives and the outline of the doctoral thesis.
- Chapter 2 presents the literature review of shear strength of stiff clays covering peak strength, residual strength, fully softened strength (critical state strength), post-rupture strength and mobilised strength (operational strength). In particular, data from tests and numerical analyses related to post-rupture strength are collected and analysed to summarize the typical features of post-rupture strength of stiff clays.
- Chapter 3 firstly gives a brief description of a generalised non-linear strain-softening and strain-hardening model based on an improved Mohr-Coulomb model including the model capability and drawbacks. Then, based on the analysis of collected data in Chapter 2, a modified constitutive model is formulated to predict the observed two-stage post-peak softening behaviour of stiff overconsolidated clays. Finally the new modified strain-softening model is implemented into *FLAC*.
- Chapter 4 is mainly devoted to the simulation of triaxial tests and direct shear box test via *FLAC* with the two-stage strain-softening model to examine the performance and efficiency of the new model.
- Chapter 5 describes the application of the new two-stage softening model via *FLAC* to the modelling of delayed progressive slope failure in stiff overconsolidated clays in order to study the relevant failure mechanism. Both comparison with former published results and parametric analyses are conducted to examine the general influence of post-rupture strength on failure mode, failure time and failure height.
- Chapter 6 presents simulations of the Aznalcóllar dam failure using a two-stage softening model incorporating the post-rupture strength concept under both inhomogeneous and homogeneous hypotheses with different softening rates.
- Chapter 7 extends the post-rupture strength concept to the analytical solutions of cylindrical cavity expansion in stiff overconsolidated clays including limit pressure, stress and strain distributions, and displacement fields.
- Chapter 8 gives a summary of the work and the conclusions are drawn.



Chapter 2. Theoretical background of softening behaviour of stiff clays

This chapter firstly presents the literature review of shear strength of stiff clays covering peak strength, residual strength and fully softened strength (critical state strength) with emphasis on post-rupture strength and mobilised strength (operational strength). Then all the data from tests and numerical analyses related to post-rupture strength is collected and analysed to summarize the typical features of post-rupture strength of stiff clays.

2.1 Peak strength

Burland (1990) concluded that, for stiff intact natural clays, the formation of the slip surface was initiated close to peak strength.

Georgiannou & Burland (2006) presented the results of drained constant- p' tests on natural undisturbed specimens of Corinth Marl using local strain gauges. The relationship between deviator stress and overall axial strain is characterized by a flat peak and a subsequent steep drop in strength, resulting in the formation of a thin slip surface. The results indicate that strain localization initiates after peak strength but before the commencement of the steep drop in deviator stress.

However, Viggiani et al. (1993, 1994) concluded that the onset of strain localization occurs before peak strength at the maximum stress ratio q/p' .

Synthetically, Atkinson (2000) describes triaxial tests on a variety of different soils using four axial strain gauges. He concludes that initiation of a shear band occurs a little before peak deviator stress and a little after peak stress ratio.

However, no matter when the strain localization happens, it is close to the peak point. In this Thesis, the peak strength indicates approximately the beginning of failure.

The peak strength parameters are denoted as c_p and ϕ_p which represent individually the cohesion and frictional angle of shearing resistance at peak state.

Generally, a nonlinear envelope for peak strength has been obtained through Mohr stress circles obtained in triaxial tests. Stress level is very important to determine the exact peak strength value for the same overconsolidated clay. The average peak strengths in different ranges of stress level can be determined by fitting $\tau - \sigma'$ curve drawn from laboratory tests.

2.2 Residual strength

2.2.1 Definition of residual strength

Skempton (1985) defined that residual strength is the minimum constant value attained (at slow rates of shearing) at large displacements. Leroueil (2001) stated that the residual strength is reached after large displacements and reorientation of platy particles in a direction parallel to the direction of shearing. Lupini et al. (1981) stated that residual shear strength τ_r is used for shear stress operating after shear to the residual state and the residual friction angle ϕ_r is determined by $\tan \phi_r = \tau_r / \sigma_n'$ where σ_n' is the normal effective stress operating on the failure surface because the residual cohesion c_r has a very small value close to 0. τ_r / σ_n' is termed residual friction coefficient. Generally, τ / σ_n' is called stress ratio and represents the friction angle of shear resistance.

2.2.2 Characteristics of residual strength of clays

Residual strength has been studied in many papers (Skempton, 1964, 1966, 1970 and 1985; Skempton & Petley, 1967; Bishop et al., 1971; Chandler & Skempton, 1974; Chandler, 1977, 1984a, b; Kenney, 1977; Lupini et al., 1981; Leroueil, 2001; Stark & Eid, 1994 and 1997; Tika et al., 1996; Mesri & Shahien, 2003, etc). Among these studies, the study by Lupini et al. (1981) is the most representative one.

Lupini et al. (1981) studied drained residual strength of cohesive soils containing both rotund and platy particles through ring shear tests and optical and scanning electronic microscope examinations of different types of soils including sand-mica mixtures, Happisburgh clay-London clay mixtures and sand-bentonite mixtures that exhibited similar behaviour to stiff clay properties under overconsolidation. In the paper, they divided the mechanism of residual strength into three types based on that residual strength behaviour is influenced by the proportions of platy, low friction particles and rotund particles. They are described as:

- (1) Turbulent (rolling) mode occurs for soils containing mainly rotund particles or high interparticle friction platy particles. In this case, residual friction angle ϕ_r of residual strength is usually high and typically greater than 25° . Higher proportion of platy particles, which may act as separation of contacts between rotund particles, results in strength reduction without preferred particle orientation. Brittleness is only due to dilatancy. It is noteworthy that the residual state in this case is reached at small shear displacements.
- (2) Sliding mode occurs for soils mainly constituted by platy, low friction particles. A well-formed, polished low strength shear surface of strongly orientated clay is well established. The residual friction angle is primarily dependent on mineralogy, pore water chemistry and the coefficient of interparticle friction. However, residual friction angle ϕ_r is slightly higher than the coefficient of interparticle friction ϕ_μ , which indicates that it is not a pure sliding. Brittleness in

first shearing is mainly due to preferred particle orientation. The shear surface, once formed, is unaffected by subsequent stress history.

- (3) Transitional mode occurs when there is no dominant particle shape involving both turbulent and sliding behaviour in different parts of a shear zone. Residual friction angle ϕ'_r is sensitive to small changes in grading of soils and the change in grading to cross the whole transitional range is typically small.

Simply speaking, turbulent shear is for a low content of platy clay minerals while sliding shear corresponds to a high content of platy clay minerals, which is the case studied in this thesis.

It could be seen that the three shearing types are significantly related to post-peak behaviour of soils. The shearing mode can be determined by examining brittleness with a special sequence of loading and by examining the post-peak structure of soils. When it comes to stiff clays, sliding mode seems generally applicable though clay fraction should be strictly measured.

The three shearing type can be typically illustrated by Fig. 2.1 that presents the residual friction angle ϕ'_r and the critical state friction angle ϕ'_{cr} of sand-bentonite mixtures. When the percentage of platy particles (bentonite) is small, there is no reorientation of particles, shear can be described as turbulent shear or rolling shear, and ϕ'_r is only slightly smaller than ϕ'_{cr} . When the percentage of platy particles is large, there is reorientation of these particles, shear is described as sliding shear, and ϕ'_r is significantly smaller than ϕ'_{cr} . In between, the behaviour is transitional, with rotund particles preventing the development of a continuous and perfectly smooth shear surface.

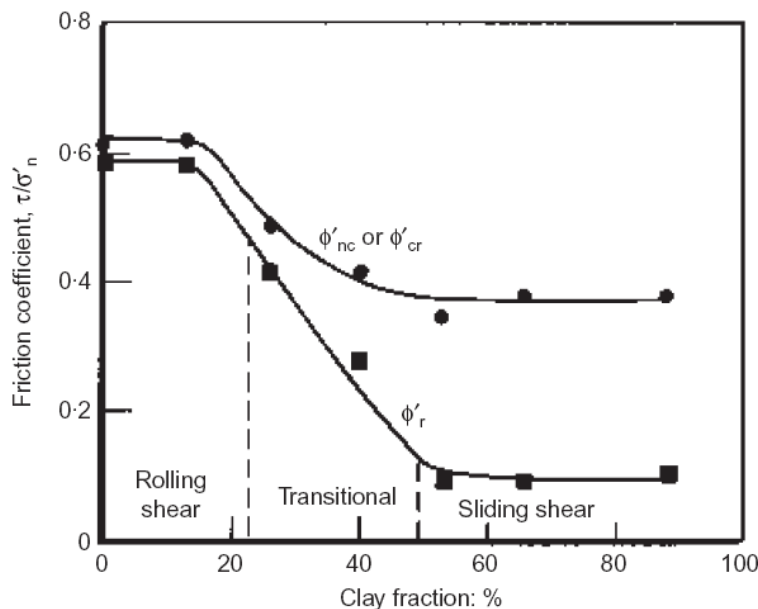


Fig. 2.1 Ring shear tests on sand-bentonite mixtures (after Lupini et al., 1981, and Skempton, 1985)

It is most noticeable that Lupini et al. (1981) investigated that mechanism of post-failure in clays through visual examination on the structure of failure zone with optical and scanning electron microscope. The results are summarized in Fig. 2.2.

Changes in structure of the failure zone were consistent with changes in behaviour observed in ring shear tests.

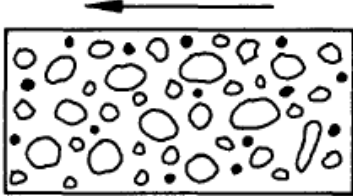
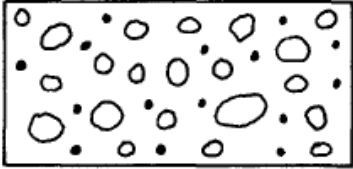
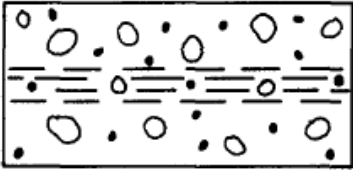
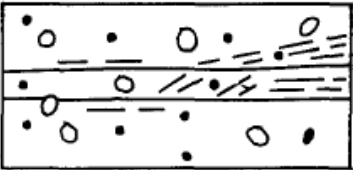

| Test no. | Clay fraction: % | Thin section | Description |
|----------|------------------|---|--|
| 2 | 20 |  | No separation on shear zone. Thin section showed no preferred orientation of the clay matrix (Figs 19, 20) |
| 3 | 27 |  | No separation on shear zone. Thin section showed no preferred orientation of the clay matrix |
| 4 | 34 |  | No separation on shear zone. Thin section showed shear zone about 1.5 mm thick containing discontinuous shear surfaces parallel to the direction of shear |
| 5 | 40 |  | Specimen separated on heavily striated (slickensided) shear surface. Thin section showed two continuous shear surfaces, undulating in the direction of shear, about 2.5 mm apart. Clay particles between them orientated 0-45° to direction of shear (Fig. 23) |
| 6 | 48 |  | Specimen separated on shear surface, more polished than test 5, with less well developed striations and no undulations in direction of shear. This surface bounded one side of zone of strongly orientated clay 0.5-2.0 mm thick; other side bounded by less well developed shear surface. Clay on either side of this zone showed partial orientation (Figs 21, 22) |

Fig. 2.2 Summary of post-failure structure of Happisburg-London clay mixtures in ring shear test (After Lupini et al., 1981)

Skempton (1985) made a further study on the post-peak strength drop. It is of paramount importance that the displacements required to cause a strength drop to the residual value are usually greater than those corresponding to the development of peak strength and the fully softened (critical state) strength in stiff overconsolidated clays.

He also stated that residual strength is not relevant to previously unsheared clays in first-time slides. However, the mobilised strength of clays will be at or close to the residual strength when pre-existing shear surfaces occur. This is in agreement with the conclusions given by Skempton (1964, 1977) that slopes undergoing 1-2 m of shear displacement should be designed using the drained residual strength.

He stated that after much larger displacements the strength falls to the residual value owing to reorientation of platy clay minerals parallel to the direction of shearing, especially when the clay fraction is 50% or more and sliding mode is prevalent.

2.2.3 Summary from examination of residual strength

- (1) The residual strength is independent of the stress history, i.e. undisturbed and remoulded soil samples have the same residual strength envelope (Bishop et al., 1971).
- (2) The residual strength value may be correlated to the clay fraction and the plasticity index.
- (3) The residual strength parameters c_r and ϕ_r can be determined by ring shear test or direct shear box test.
- (4) The difference between peak strength and residual strength, i.e. brittleness (see Eq. (2.6)), is a very important factor in the stability analysis of progressive failure.
- (5) Significantly, the laboratory test data and microstructure examination show two-stage post-peak softening of stiff overconsolidated clays. The post-peak strength of stiff overconsolidated clays is due to both interbonding between particles and particle reorientation.
- (6) In this Thesis, the residual strength parameters are denoted as c_r and ϕ_r which represent individually the cohesion and frictional angle of shearing resistance at residual state. Usually, the value of c_r at residual state with large displacement is very small or equal to zero.

2.3 Fully softened strength (critical-state strength)

Before moving to talk about post-rupture strength, it is worthwhile to discuss the concept of fully softened strength.

Skempton (1970) firstly introduced fully softened strength, which is numerically equal to the drained peak strength of a reconstituted normally consolidated specimen. He mentioned that softening only reduces the effective cohesion component of shear strength parameters but does not cause orientation of clay particles or reduction in friction angle. He also defined the fully softened strength as the critical-state strength of reconstituted material. Georgiannou and Burland (2001) also considered the fully softened strength as the same as the critical-state strength.

Skempton et al. (1969) and Skempton (1977) found that fissure development can result in softening of surrounding overconsolidated clay. Consequently, Skempton (1977) suggested that shear strength in a fissure corresponds to the fully softened value. However, this is not always true as demonstrated in progressive failure.

Stark & Eid (1997) conducted a comprehensive study on the effects of clay mineralogy, clay fraction and effective normal stress on the fully softened shear strength of cohesive soils. He found that the fully softened shear strength is stress dependent and controlled by the type of clay mineral and quantity of clay-size

particles. An empirical fully softened shear strength relationship is presented as a function of liquid limit, clay fraction and effective normal stress. The relation is shown in Fig. 2.3. It is suggested that reduction in fully softened friction angle with increasing effective normal stress is caused by an increase in face-to-face interaction among the platy clay particles.

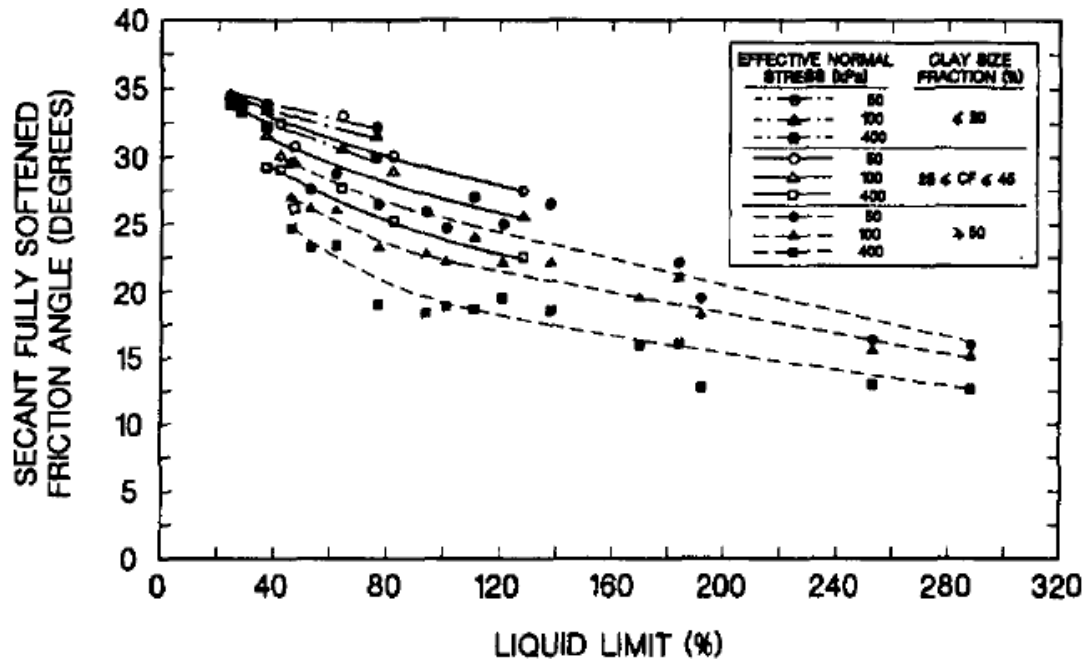


Fig. 2.3 Relationship between drained fully softened friction angles and liquid limit for triaxial compression mode of shear (Stark & Eid, 1997)

In addition, Skempton (1970) emphasized that the displacement required to drop in strength from peak value to fully softened condition is not large compared with that from peak to residual state (Fig. 2.4).

As stated by Gens & Alonso (2006), the issue of progressive failure is often associated with the concept of fully softened strength (Skempton, 1970, 1977). Skempton (1977) proposed that the fully softened shear strength could be used for designing in first-time slides in stiff fissured clay, which is usually accompanied by small magnitude of strains. Chandler (1984a) and Cancelli (1981) obtained a similar conclusion. But Chandler (1984a, b) also questioned the agreement between the field shear strength and the fully softened strength. There seems to be no obvious *a priori* reason for this agreement (Georgiannou & Burland, 2001).

Stark & Eid (1997) reviewed 14 first-time landslides in stiff fissured clay with liquid limit between 50% and 130%, reported the value of the mobilised strength at failure, and compared it with the fully softened and the residual value. Such a comparison is shown in Fig. 2.4 and Fig. 2.5. It can be seen that in most instances the mobilised strength at failure lies about midway between the fully softened strength and the residual strength. The authors explained that softening, which is a reduction in the available drained strength resulting from an increase in water content under constant effective stress, reduces the shear strength to the fully softened value. After reaching the fully softened shear strength, progressive failure reduces further the average shear strength along the failure surface to a value between the fully softened and residual shear strength values.

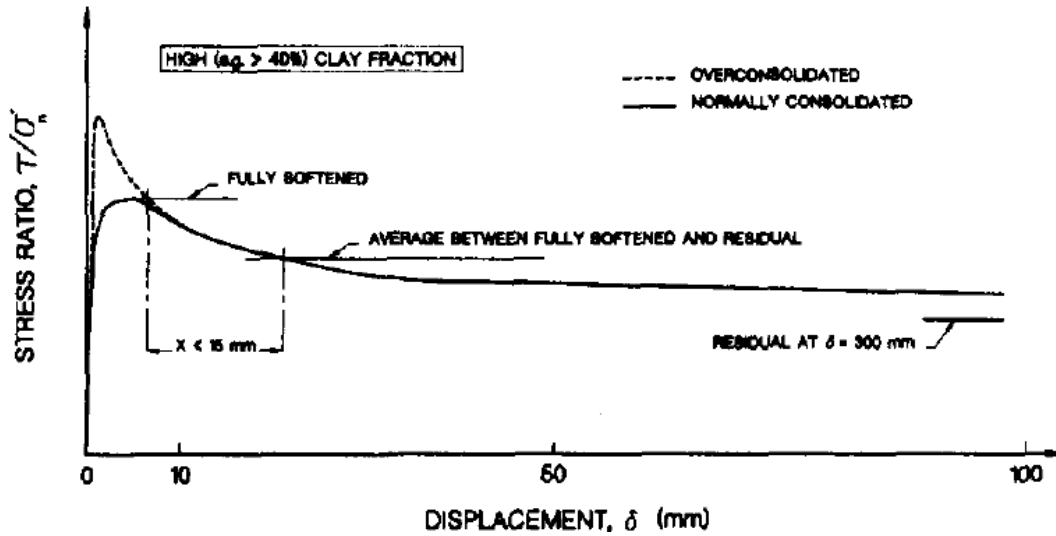


Fig. 2.4 Stress ratio-displacement curve at constant σ'_n (Stark & Eid, 1997)

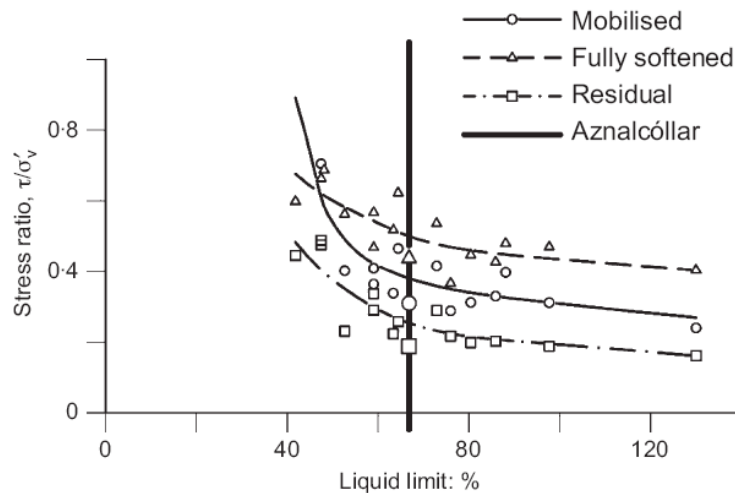


Fig. 2.5 Mobilised, fully softened, and residual stress ratios for field case histories (Stark & Eid, 1997). Also plotted are calculated values for Aznalcóllar dam failure (Gens & Alonso, 2006)

Gens & Alonso (2006) used Fig. 2.5 to plot the fully softened strength, mobilised and residual stress ratios in Aznalcóllar dam failure for the corresponding liquid limit of Guadalquivir blue clay (shown in Fig. 2.5 with black bold line). They also emphasized that one should be careful while using the average value in design because a number of factors control the development of progressive failure.

It is noticeable that Mesri and Shahien (2003) back-analysed a number of first-time slope failures in stiff fissured clays. They also commented that the mobilised shear strength of fissured clays may be at an intermediate value between the fully softened strength and residual strength (James, 1970; Chandler 1984a; Mesri & Abdel-Ghaffar 1993; Potts et al. 1997; Stark & Eid 1997). This possibility had been examined by Bishop (1971) in terms of residual factors along the slip surface. Concerning the shear strength mobilised at failure, Mesri and Shahien (2003) concluded as follows:

- (a) in non-fissured plastic clays, an average mobilised shear strength significantly higher than the fully softened strength may not be available because progressive



failure along a global slip surface may occur (Peck, 1967). Skempton (1970) recommended a mobilised strength equal to the fully softened shear strength for slopes excavated in homogeneous stiff fissured clays in which there has been no previous sliding (Henkel, 1957). Following Skempton (1970) it was widely assumed that the fully softened strength is the lower bound for first-time slides in homogeneous stiff fissured clays (James 1970; Skempton 1977, Cancelli 1981; Chandler 1984b). Skempton (1977) assumed that displacements preceding first-time slides are sufficient to cause some progressive failures, which reduce the mobilised strength toward the fully softened value, but the movements are not sufficient to reduce the strength to the residual condition.

- (b) On reactivated slip surfaces of landslides in stiff clays and clay shales the residual condition has been reached, and the mobilised shear strength is equal to the residual shear strength from laboratory reversal direct shear or ring shear tests, independently of time after initial failure.
- (c) The fully softened shear strength is the lower bound for mobilised strength in first-time slope failures in homogeneous soft to stiff clay slopes and on the part of the slip surface cutting across bedding planes and laminations in stiff fissured clays and shales.

Cividini & Gioda (1992) performed a numerical modelling of direct shear tests on stiff clays using elastoplastic softening soil model based on the concept of fully softened strength.

In summary, the mobilised shear strength for first-time slide in stiff clays is extremely complex and it may be greater or lower than, or equal to the fully softened strength, i.e. the critical-state strength according to the fundamental properties of clays.

In this Thesis, the fully softened strength parameters are denoted as c_{fs} and ϕ_{fs} (or c_{cs}^* and ϕ_{cs}^*) which represent individually the cohesion and frictional angle of shearing resistance at fully softened state.

2.4 Post-rupture strength of stiff overconsolidated clays

2.4.1 Introduction and definition of post-rupture strength

As presented in section 1.1, post-peak behaviour, i.e. softening, of stiff clays has been reported by many researchers.

Bishop et al. (1965) observed very brittle shearing behaviour in triaxial compression on intact natural stiff clays at low to intermediate confining pressures.

Calabresi (1980) distinguished two-stage post-peak strength reduction through the results of direct shear tests on intact Todi clay and gave some suggestion on the shear strength parameters.

Significantly, Burland (1990) firstly introduced post-rupture strength and defined it as a reasonably constant value to which the strength on a rupture surface rapidly drops after only a relative displacement of only a few millimeters. Burland (1990) and Burland et al. (1996) also found the similarity between post-rupture strength envelope

and the fully softened strength envelope, i.e. critical state line obtained on the reconstituted soil.

Moreover, Georgiannou & Burland (2001) made a systematic analysis on post-rupture strength of stiff clays, including the relevant influential factors, based on experimental tests. They concluded that the post-rupture strength envelope for intact natural stiff clays is well defined, repeatable and insensitive to stress history or to the rotation of principal stresses. In addition, Georgiannou & Burland (2006) made a laboratory study of slip surface formation in intact natural stiff clays. They verified further the post-rupture robustness and its typical characteristics.

In this paper, the terminology ‘post-rupture’ indicating the end point of steep rapid strength reduction is distinguished from ‘post-peak’ which is denoted to describe the whole softening course from peak state to residual state.

2.4.2 Laboratory test observations of post-rupture strength

2.4.2.1 Results from Burland (1990)

Burland (1990) made tests on intact samples of Todi clay which is a low to medium plasticity lacustrine clay of Pleistocene age at Imperial College by Dr Rampello and Dr Georgiannou. The test device included local strain transducers (Burland & Symes, 1982; Burland, 1989) and a local pore pressure probe (Hight, 1982). For all the tests, failure took place abruptly along a single slip surface, which passed outside both of the local strain transducers and close to the pore pressure probe. This provides a detailed and reliable study of the process of rupture.

A typical deviator force versus strain curve is shown in Fig. 2.6. Based on the test, the following important observations can be made:

- (a) formation of failure plane coincides with peak strength
- (b) prior to peak strength the local strains are less than the overall strains
- (c) excess pore pressure changes cease abruptly shortly after peak strength
- (d) after peak the curve of deviator force versus notional overall strain falls steeply to a well defined plateau
- (e) after peak, the local axial strains decrease due to the unloading process which indicates that post-peak deformation consists of near-rigid body sliding on the failure plane with very slight axial extension in the surrounding clay.

Fig. 2.6b shows curves of shear stress versus overall strain and relative displacement up to rupture. It can be seen that shear stress drops rapidly at first but reaches a nearly constant value after a small relative displacement of about 1 mm. The strength corresponding to the post-peak plateau is defined as the post-rupture strength.

Fig. 2.7 shows the post-rupture failure envelope for Todi Clay. It can be seen that the envelope is nonlinear and may be approximately described as bi-linear with a transition between low and high pressures at a normal effective stress of about 1500 kPa. At high normal effective stresses, the post-rupture strength parameters are given by $c'_{pr} = 0$ and $\phi'_{pr} = 20.2^\circ$ where c'_{pr} is the post-rupture cohesion and ϕ'_{pr} is the post-rupture friction angle. The post-rupture failure angle envelope is seen to lie well below the intact line and a little above the residual failure line for which c'_r is about

17° (Calabresi, 1990). While at low to intermediate stresses $c'_{pr} = 23$ kPa and $\phi'_{pr} = 23.7^\circ$. Slightly wavy failure plane may induce the cohesive intercept. For the intrinsic failure line representing reconstituted normally consolidated samples, ϕ_{cs}^* is equal to 28° at origin and then decreases to 24° at $\sigma'_n = 600$ kPa. Over the range of $\sigma'_n = 100$ kPa to 1000 kPa the post-rupture and intrinsic failure envelopes lie very close to each other.

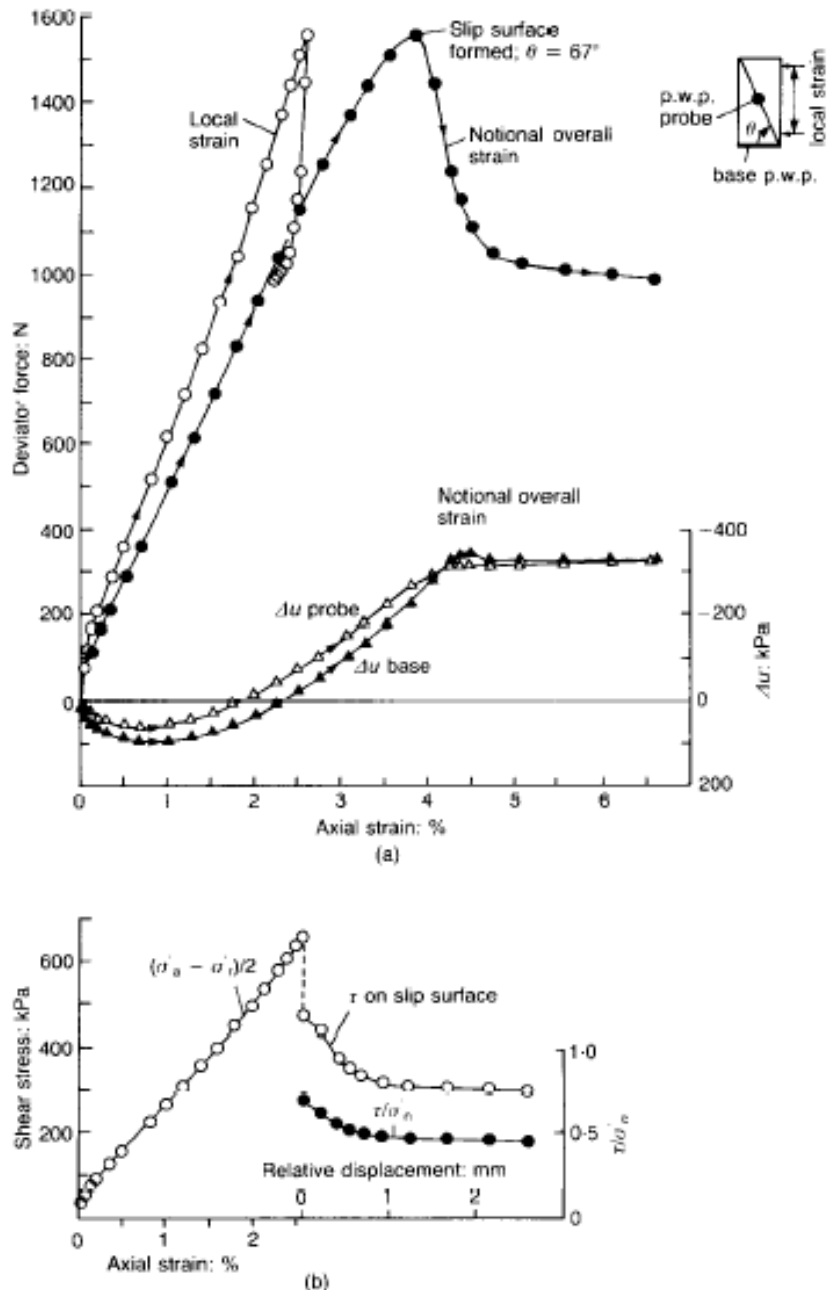


Fig. 2.6 Todi Clay: unconsolidated undrained triaxial test with pore pressure measurement showing post-rupture behaviour (Burland, 1990)

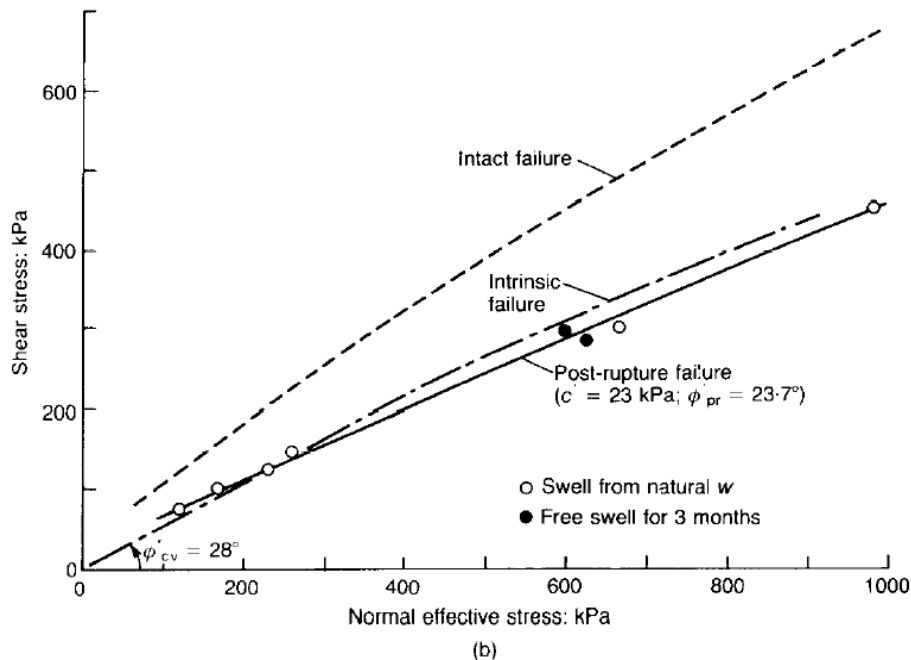
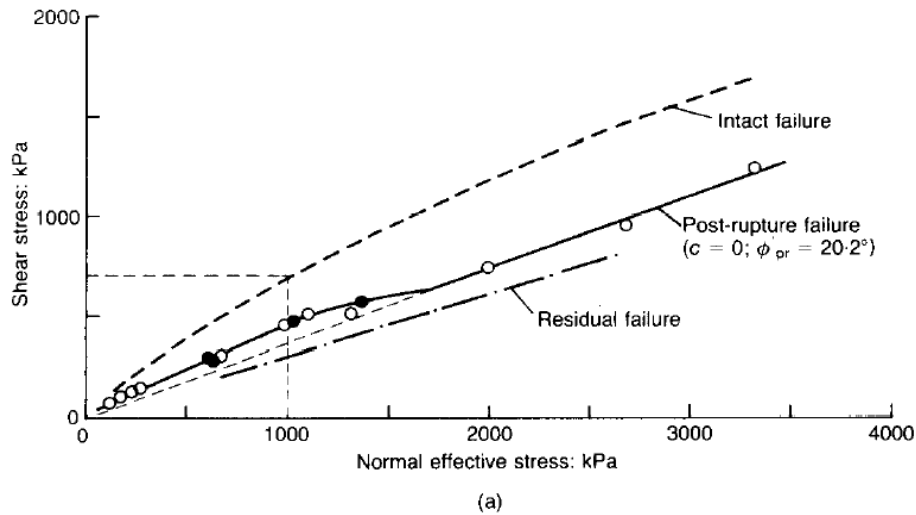


Fig. 2.7 Todi Clay: post-rupture envelope for (a) high pressures (b) low to medium pressures compared with intact, intrinsic and residual failure lines (Burland,1990)

Ninis (1990) conducted test on anisotropically and normally consolidated aged kaolin and observed the formation of rupture planes. Here again the ratio τ/σ'_n on the slip surface drops to a stationary value of about 0.27 and a post-rupture strength with $\phi'_{pr} = 15.1^\circ$ less than ϕ'_{cs} , which is 18.2° , is reached after approximately 5 mm relative displacement.

In addition, three types of tests (quick undrained triaxial compression test, drained and undrained effective stress compression tests on vertical and horizontal specimens) on Ashford Common London Clay which reported by Ward et al. (1965), Bishop et al. (1965), Webb (1964) and Wroth (1972), have been conducted at Imperial College. Most of the tests at low to moderately high confining pressure exhibited brittle behaviour with a well-defined slip surface forming at peak strength (Bishop et al., 1965). A similar post-rupture behaviour to Todi Clay under undrained and drained

conditions was observed. The shear stresses on the slip surfaces drop to a minimum after relative displacements of about 1 mm and 3 mm. Burland (1990) concluded that in general the overall notional strain between peak and post-rupture strength seldom exceeded 5%.

The corresponding post-rupture failure envelopes are shown in Fig. 2.8. The intrinsic failure line lies below the post-rupture failure line at low stresses and above it at higher stresses. At high normal effective stresses, the post-rupture strength parameters are given by $c'_{pr} = 0$ and $\phi'_{pr} = 15.2^\circ$ which is higher than residual friction angle 12° . At low stresses, intrinsic strength parameters are given by $c' = 0$ kPa and $\phi_{cs}^* = 20.1^\circ$. The post-rupture failure line has a slightly higher friction angle and $c'_{pr} = 10$ kPa. However, as normal effective stresses increase, it bends over and drops below the intrinsic failure line at about 750 kPa.

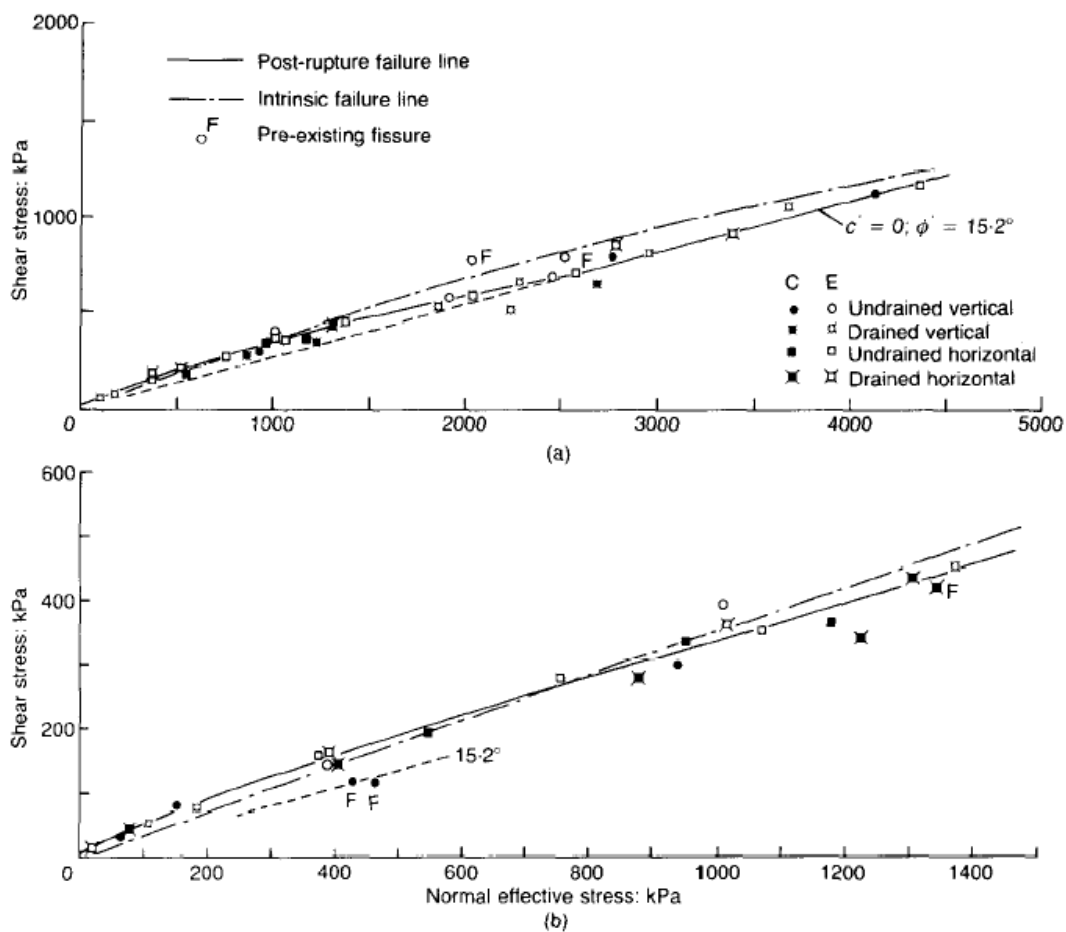


Fig. 2.8 London clay at Ashford Common: post-rupture envelope for (a) high pressures (b) low to medium pressures compared with intrinsic failure lines (Burland,1990)

2.4.2.2 Results from Burland et al. (1996)

Stiff plastic cohesive clays such as Todi clay (CF=43%) and Pietrafitta clay (CF=44%) of lacustrine origin and Vallericca clay (CF=42%) of marine origin have been studied by Burland et al. (1996) through oedometer and triaxial tests.

Results of CIU (isotropically consolidated undrained test) tests on the normally consolidated reconstituted samples all show well-defined critical states at failure. CID

(isotropically consolidated drained test) tests on overconsolidated reconstituted samples show sharp reductions in post-peak strength with the formation of slip planes.

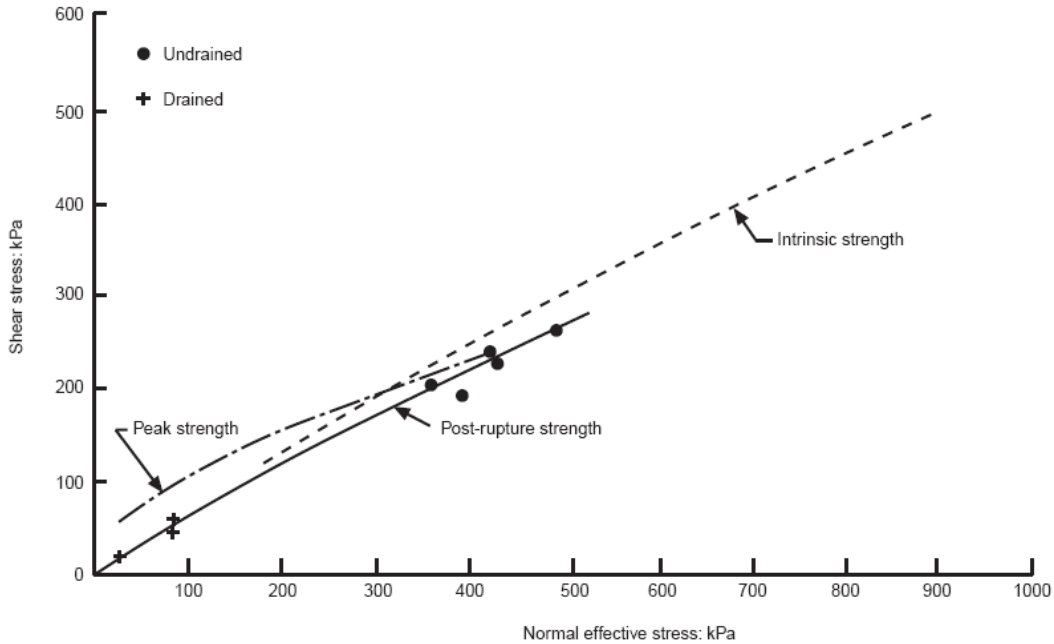


Fig. 2.9 Pietrafitta clay: post-rupture Coulomb strength envelope compared with peak intact and intrinsic failure lines (Burland et al., 1996)

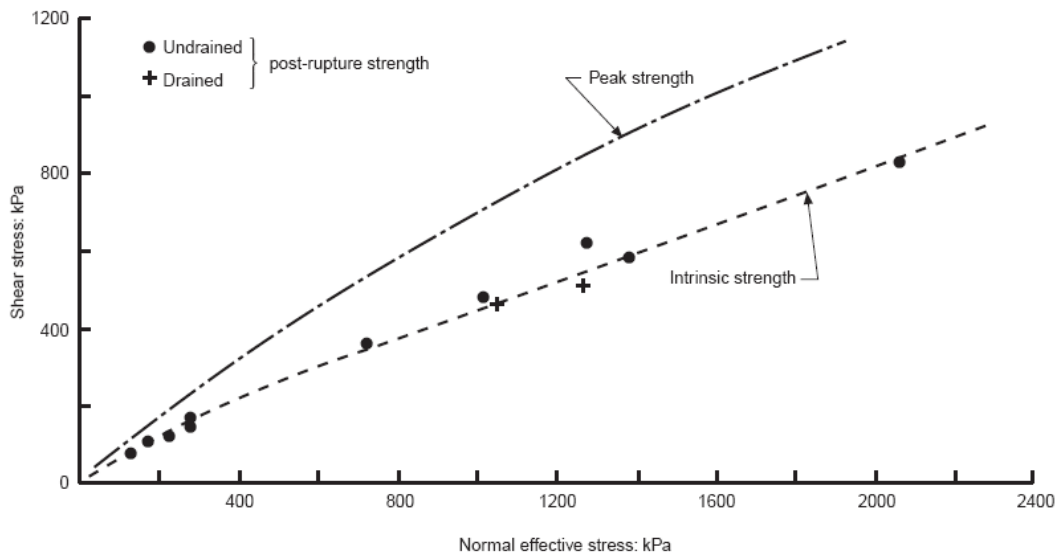


Fig. 2.10 Todi clay: post-rupture strengths compared with peak intact and intrinsic failure lines (Burland et al., 1996)

For Pietrafitta clay, post-rupture strength have been analysed in terms of the effective normal and shear stresses acting on the rupture planes, making the appropriate area corrections. For both the undrained and drained tests it was found that the post-peak strengths fall to reasonably constant values after a few millimeters of relative displacement. In Fig. 2.9 the post-rupture failure line for the natural material coincides with the intrinsic failure line for effective stresses up to 100 kPa while at higher stresses it lies slightly below it.

For Todi clay, post-rupture strengths are well defined and close to the intrinsic line as shown in Fig. 2.10.

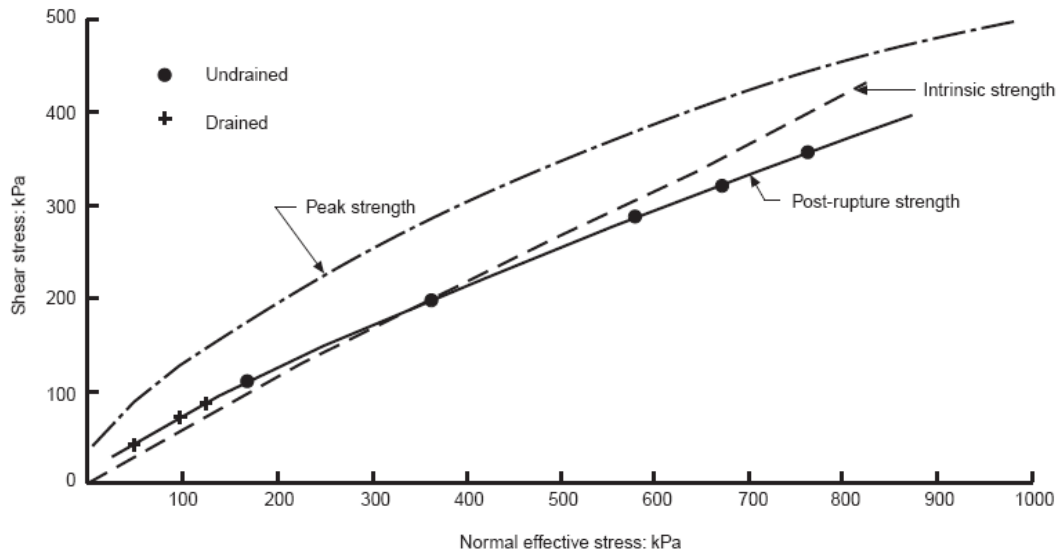


Fig. 2.11 Vallericca clay: post-rupture strength envelope compared with peak intact and intrinsic failure lines (Burland et al., 1996)

For Vallericca clay, post-rupture strengths are well defined (Fig. 2.11). At low effective pressures the post-rupture failure line lies just above the intrinsic failure line whereas, at higher stresses, it lies below the intrinsic failure line. At very low stresses, the post-rupture friction angle ϕ'_{pr} is approximately equal to ϕ'_{cs} with $c'_{pr} = 10$ kPa.

In summary, all the three stiff plastic clays exhibit brittle behaviour at low stresses with the formation of slip surfaces or shear bands at peak strength followed by, in some cases, extremely rapid reductions in strength. For all soils tested, well-defined post-rupture strengths on slip planes were obtained after relative displacements of a few millimeters. At low confining pressures the post-rupture envelope tends to lie on, or slightly above, the intrinsic critical state Mohr-Coulomb failure lines for the reconstituted materials while at higher confining pressures it tends to lie below it. Burland (1990) also observed similar behaviour in London clay.

2.4.2.3 Results from Georgiannou & Burland (2001)

Georgiannou & Burland (2001) designed elaborate test procedures and made a systematic analysis on post-rupture strength properties. Based on their experimental study, they described the influence of a number of factors on the post-rupture strength of initially intact samples of Vallericca Clay.

Georgiannou & Burland (2001) also stated that the properties of a reconstituted soil (termed intrinsic properties) form a useful frame of reference for interpreting the behaviour of the associated natural undisturbed soil (Burland, 1990; Leroueil & Vaughan, 1990; Chandler, 2000). In particular, such a frame of reference can be used to discern the influence of structure, i.e. fabric and bonding, in the natural material, and its progressive breakdown during loading and shearing. Thus, the intrinsic critical-state strength line should be regarded as a convenient reference line.

The results from Georgiannou & Burland (2001) are shown in Fig. 2.12. The chain dotted line is the peak intact failure envelope, which is tangential to the Mohr's stress circles at peak strength; the full line is the post-rupture strength envelope drawn through the points obtained by resolving the shear and normal effective stresses on the

slip surface of each specimen; the broken line is the intrinsic critical-state failure envelope for the reconstituted material, which is tangential to the Mohr's stress circles at well-defined critical states.

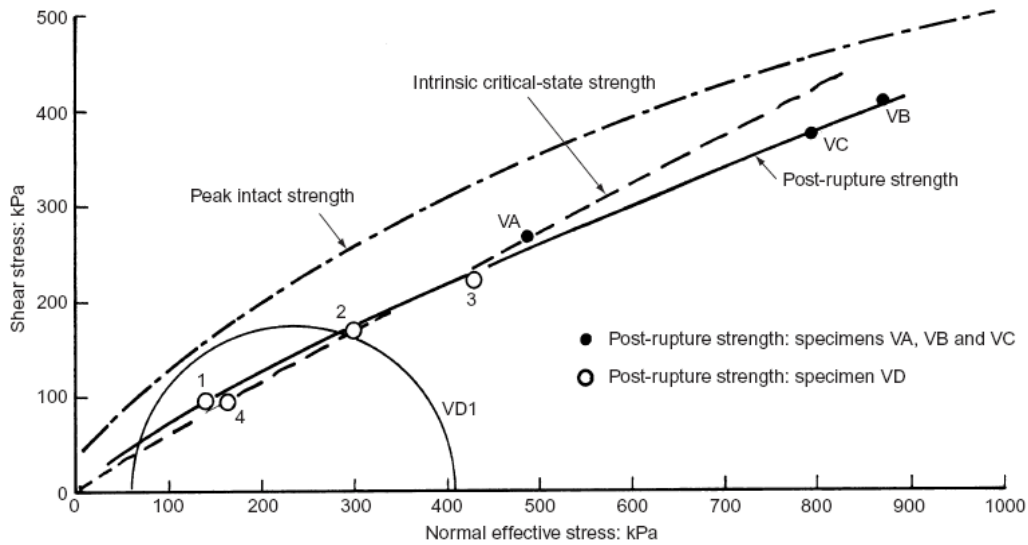


Fig. 2.12 Mohr-Coulomb strength envelopes for compression tests on Vallericca Clay (Georgiannou & Burland, 2001)

In tests on Vallericca Clay, a significant and rapid reduction in strength occurs after peak, resulting in the formation of a single slip surface, after which a plateau is reached such that the deviator stress remains approximately constant for increasing axial strain. Significant dilation occurs up to peak, but thereafter the rate of dilation reduces sharply.

Meanwhile, no further local axial strain occurs just beyond peak strength, indicating the beginning of rigid-body sliding. The slip surface was just visible once the deviator stress had reached its post-rupture value.

In addition, the relationship between the stress ratio on the slip plane, τ / σ'_n , and the relative displacement, taking the onset of rigid body sliding as the zero, shows that the stress ratio drops from its maximum value to an approximately constant value (the post-rupture strength) after a relative displacement of less than 1 mm.

The total relative displacement across the slip plane is approximately 7 mm. Examination of the slip surface showed it to be slightly wavy and slickensided, with signs of some polish. This is consistent with that observed by Lupini et al. (1981) as shown in Fig. 2.2.

In Fig. 2.12, it can also be seen that the strength values for the tests are in excellent agreement with the previously obtained post-rupture strength envelope.

At the same time, drained extension tests have also been performed to make a further attempt to observe the post-rupture strength in extension. A sharp post-peak reduction in strength occurred, which coincided with the formation of a single, shallow slip plane within the reduced section of the specimen. The test was terminated at a relative displacement across the slip surface of about 7 mm. The appropriate post-rupture point was taken as the one reaching the minimum value of τ / σ'_n .

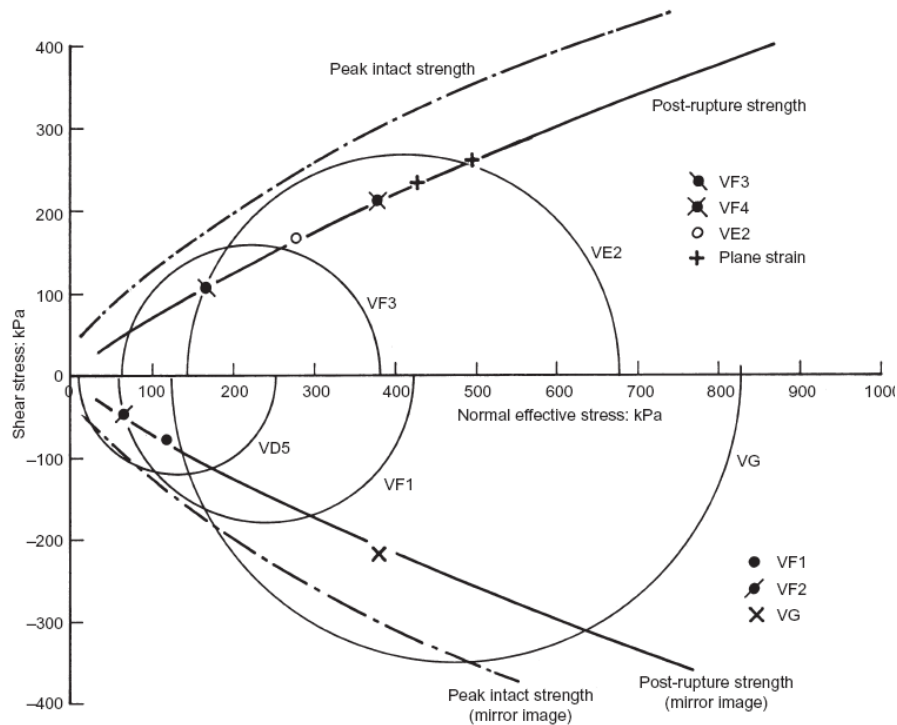


Fig. 2.13 Mohr-Coulomb strength envelopes for extension and compression tests on Vallericca Clay (Georgiannou and Burland, 2001)

Fig. 2.13 shows the Mohr diagram in which, for the purposes of comparison, the intact and post-rupture strength lines for triaxial compression have been reproduced as mirror images in triaxial extension. It shows that the post-rupture strengths in extension are in excellent agreement with the mirror image of the post-rupture strength line from the compression tests. Meanwhile, Georgiannou & Burland (2001) also mentioned that although the history of failure and dilation in extension has significantly affected the stiffness and peak strength in compression, it does not appear to have affected the corresponding post-rupture strengths.

2.4.2.4 Results from Georgiannou & Burland (2006)

Georgiannou & Burland (2006) made a laboratory study of slip surface formation in an intact natural stiff clay—Corinth Marl with initial states different from those in previous studies (Burland et al., 1996; Georgiannou & Burland, 2001).

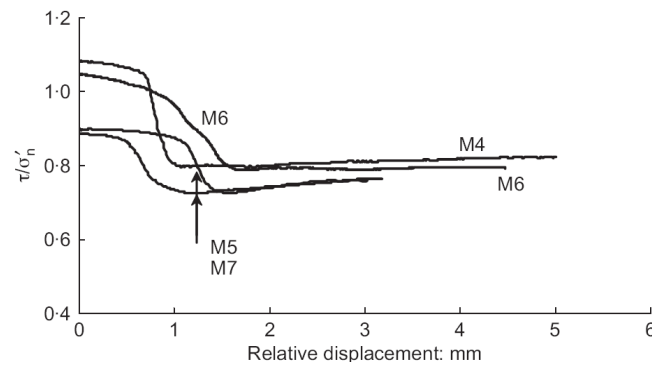


Fig. 2.14 Relationships between τ / σ'_n and displacement across slip surface for initially intact Corinth Marl specimens (Georgiannou & Burland, 2006)

Fig. 2.14 shows the relationship between the stress ratio, i.e. τ/σ'_n , on each slip plane and the relative displacement across it, taking the onset of rigid body sliding as zero. It can be seen that the stress ratio drops from its maximum value to an approximately constant value after a relative displacement of less than 2mm (the post-rupture strength). All four specimens attained a post-rupture stress ratio τ/σ'_n equal to about 0.78.

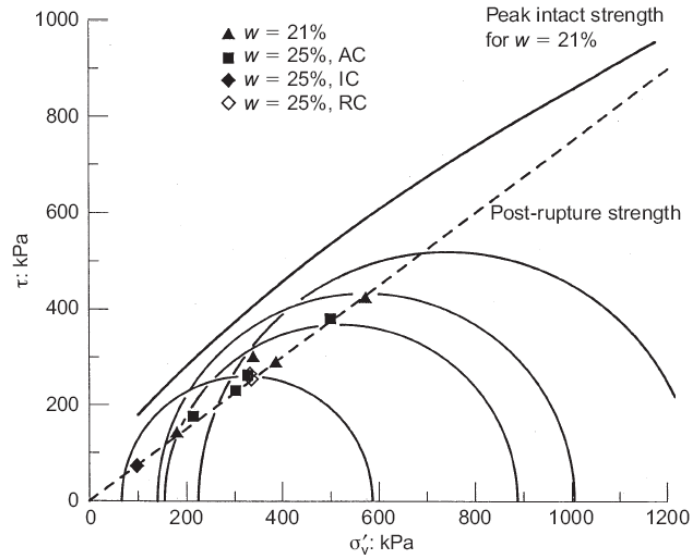


Fig. 2.15 Peak strengths and post-rupture strengths for constant- p' tests on Corinth Marl (Georgiannou & Burland, 2006)

Fig. 2.15 shows a Mohr diagram of shear stress τ against effective normal stress σ'_n for the Corinth Marl. The full line is the peak intact Mohr–Coulomb failure envelope obtained from previous studies on the material having an initial moisture content of 21–22% (Burland et al., 1996; Georgiannou & Burland, 2001). The studies made by Georgiannou & Burland (2006) are on a material with somewhat higher initial moisture content (25–26%) indicating that the new material is slightly softer than the one previously tested. The Mohr's circles corresponding to peak strength are shown in Fig. 2.15, and can be seen to lie a little below the full line. The broken line represents the post-rupture strength envelope obtained from the earlier studies on specimens that had been isotropically consolidated. The post-rupture strengths from the study by Georgiannou & Burland (2006), in which the specimens were anisotropically consolidated, are shown as squares and are seen to be in very good agreement with the previous studies. The triangles are for tests carried out with lubricated ends, and the open diamonds are for specimens that have been retested at a higher confining pressure following the formation of a slip surface in a previous test. On the basis of these results, it would appear that the post-rupture strength for Corinth Marl is not sensitive to initial moisture content, end restraint or stress history. These conclusions are in substantial agreement with those drawn by Georgiannou & Burland (2001) for Vallericca clay.

In Fig. 2.15, Mohr's circles correspond to peak intact strengths for $w = 25\%$. Post-rupture strengths are identified for reconsolidated specimens with initial water contents $w = 21\%$ and $w = 25\%$ after formation of slip surface.

2.4.3 Data collection of post-peak strength parameters of stiff clays

From all the literature related to post-rupture strength reviewed above, typical post-peak strength parameters of stiff clays are listed in Table 2.1 combined with clay index properties given in Table 2.2. The strength parameter data is based on laboratory tests, field experiments or numerical analyses. Some data is given just as reported in the original articles and other data is calculated by regression analysis of strength envelopes.

When data for post-rupture strength is absent, it is replaced by the fully softened strength parameters. In some cases, average peak strength parameters and peak strength at low normal effective stress are selected.

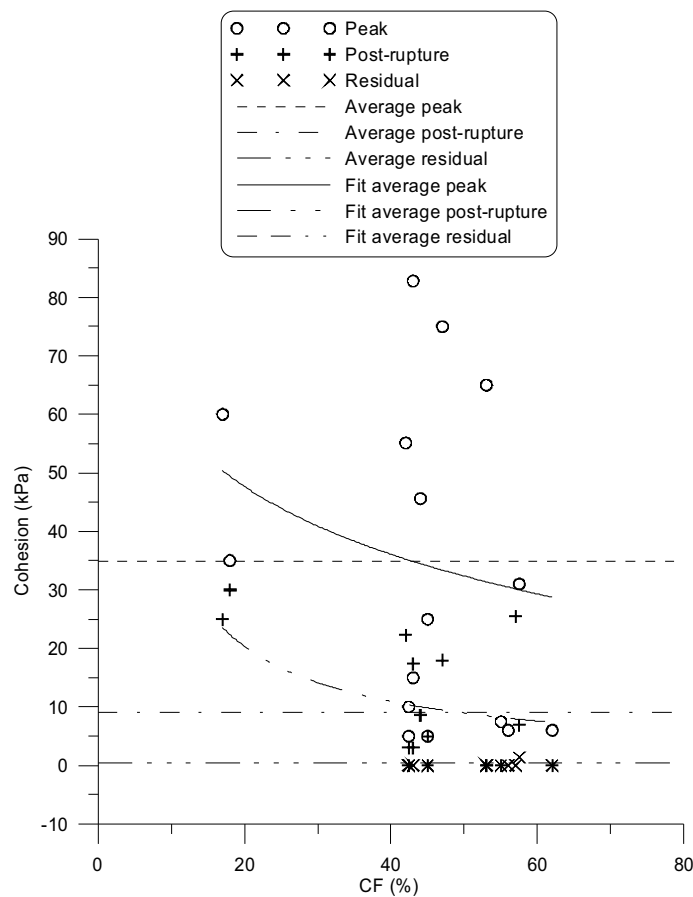


Fig. 2.16 Variation of cohesion with clay fraction

The collected data yields the relationships between strength parameters and clay fraction and activity illustrated in Fig. 2.16, Fig. 2.17, Fig. 2.18 and Fig. 2.19. In these figures, the very high strength parameters are excluded because these values are normally consistent with those for clay shales but not for clay. Activity A is defined as

$$A = IP / CF \quad (2.1)$$

where IP is the plasticity index and CF denotes clay fraction.

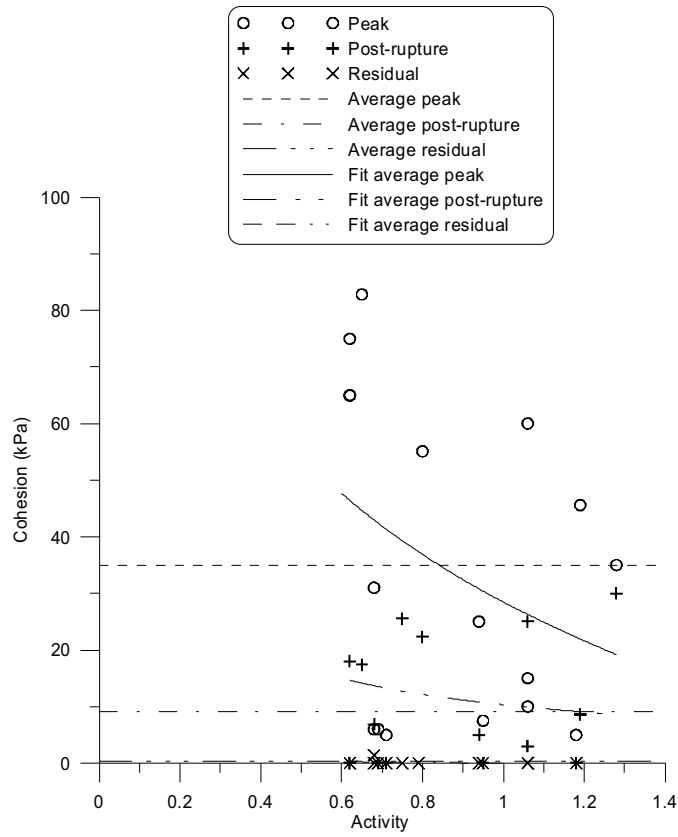


Fig. 2.17 Variation of cohesion with activity

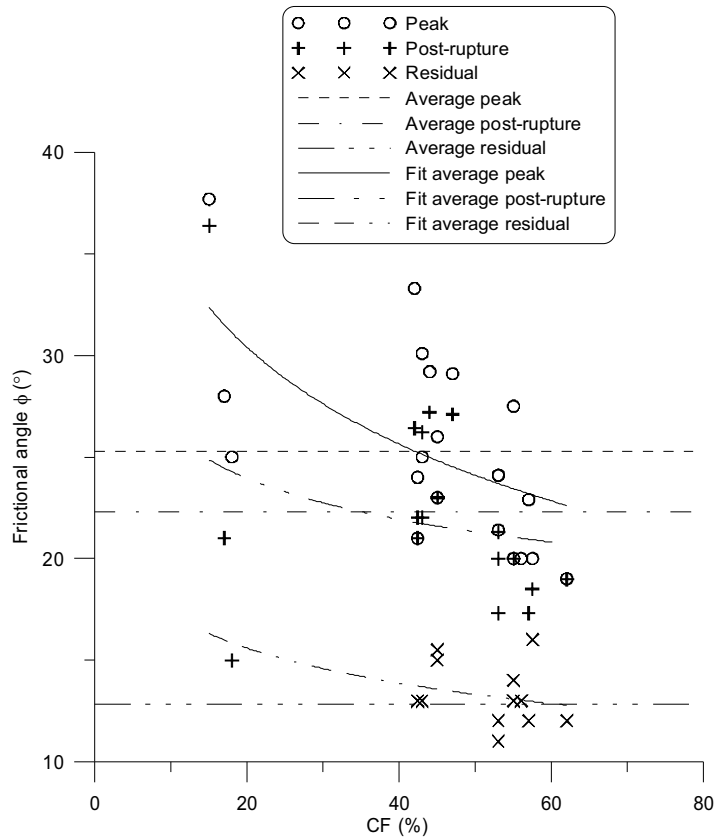


Fig. 2.18 Variation of frictional angle with clay fraction

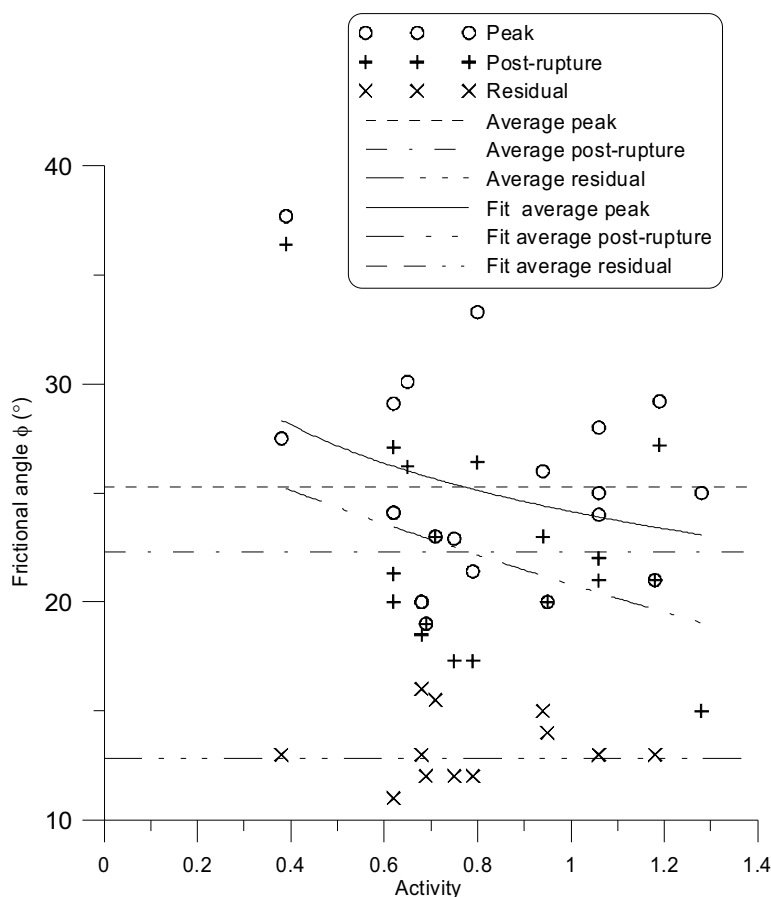


Fig. 2.19 Variation of frictional angle with activity

In Fig. 2.16, it can be seen that the difference between average post-rupture cohesion and the average residual cohesion is not large. Generally the peak and post-rupture cohesions decrease with clay fraction whereas the residual value keeps relatively stable and small. Fig. 2.17 exhibits the same tendency.

In Fig. 2.18 and Fig. 2.19, it can be seen that the difference between average peak frictional angle and average post-rupture value is small. Meanwhile, the peak and post-rupture values of frictional angle reduce with clay fraction whereas the residual value keeps relatively stable.

As shown in Table 2.1, Fig. 2.16, Fig. 2.17, Fig. 2.18 and Fig. 2.19, stiff clays generally exhibit two-stage softening characteristics in the post-peak process. Combined with the aforementioned results this feature can be described as the following:

- (1) a rapid sudden reduction of shear resistance, usually associated with loss of the cohesive component of strength—this stage is called ***cementation loss***.

This is also confirmed by Chen et al. (1992) who demonstrated that more than 95% of cohesion is lost with a development of small plastic axial strain (nearly 2%) after peak.

At low normal effective stress, the loss is remarkable and a typical small cohesive intercept between 0 and 10 kPa has been reported (Burland, 1996). While at high stress level the loss is relatively small. However, as seen in Table 2.1, Fig. 2.16,

Fig. 2.17, Fig. 2.18 and Fig. 2.19, the values of cohesive intercept could also be larger depending on the index properties of the clays.

Meanwhile, the friction angle of shear resistance also reduces but the reduction is quite small compared with that of cohesion.

Here, ‘rapid’ means small relative displacement after peak strength. Burland (1990) stated that generally the overall notional strain between peak and post-rupture strength seldom exceeded 5%.

- (2) a gentler shear stress reduction to residual strength induced by a gradual realignment, i.e. reorientation of clay particles—this stage can be named **gradual frictional resistance loss**.

The friction angle of shear resistance decreases to a relatively small value which is approximately equal to residual value after large displacement.

At the same time, the cohesive intercept drops gradually to a small value close to zero which is usually the relevant residual value after large displacement.

Based on studies by Alonso & Gens (2006a) and Georgiannou & Burland (2001), a modified shear stress τ versus shear displacement δ curve (Fig. 2.20) is used to illustrate the two-stage softening process.

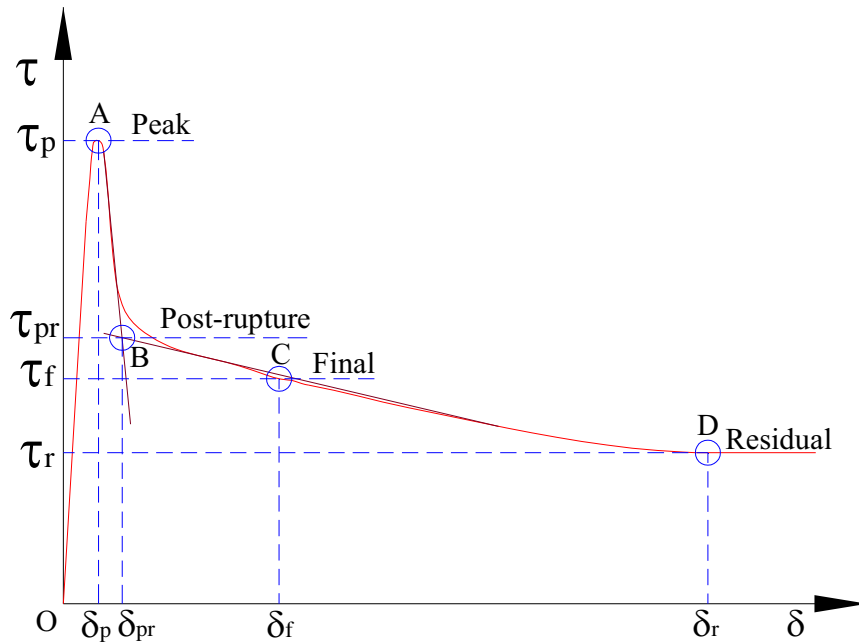


Fig. 2.20 Schematic $\tau - \delta$ curve (based on Alonso & Gens, 2006a)

In Fig. 2.20, the post-rupture strength can be represented by point B, which is the intersection of the rapid falling branch just after peak point A and the more gradually descending branch after point B (Georgiannou & Burland, 2001). δ_p , δ_{pr} , δ_f and δ_r represent the shear displacements individually at peak, post-rupture, final and residual states. It should be noted that here ‘final’ means the end of test.



Table 2.1 Collected data of post-peak shear strengths of stiff clays

| No. | Clay Name | Peak strength | | Fully softened (Critical state) strength | | Post-rupture strength | | Normal effective stress for post-rupture strength σ'_n (kPa) | Residual strength | | Operational (Mobilised) strength | | Relative disp. or deviator plastic strain to residual | Reference |
|-----|---|----------------|-----------------|--|-----------------|-----------------------|-------------|---|-------------------|--------------------------------------|----------------------------------|--------------|---|---|
| | | c_p | ϕ_p | c_{fs} | ϕ_{fs} | c_{pr} | ϕ_{pr} | | c_r | ϕ_r | c_{mob} | ϕ_{mob} | | |
| 1 | Brown London Clay | | | 0 | 20 | 0* | 20* | | 1 | 13 | 1 | 20 | | Jardine et al., 2004 |
| 2 | Numerical Material Similar to Brown London Clay | 7 | 20 | | | | | | 2 | 13 | 1 | 20 | 20% | Potts et al., 1997 |
| 3 | Brown London Clay | 7.5 | 20 | 0 | 20 | 0* | 20* | | 0 | 14 | 1 | 20 | | Chandler, 1984b |
| 4 | Weathered Upper Lias | 5 | 23 | 0 | 23 | 0* | 23* | | 0 | 15.5 | 1.5 | 23 | | Chandler, 1984a |
| 5 | London Clay | 7.5 | 20 | | | | | | | | 1 | 20 | | Chandler, 1984a |
| 6 | Upper Lias | 5 | 23 | | | | | | | | 1.5 | 23 | | Chandler, 1984a |
| 7 | Oxford Clay at Saxon Pit | 172 | 27.5 | | | | | | 3.5 | 13 | | | | Chandler, 1984a |
| 8 | Soliflucted Gault Clay | 5 | 21 | 0 | 21 | 0* | 21* | | 0 | 13 ^s 12.5 ^r | | | | Cooper et al., 1998 |
| 9 | Upper Weathered Gault Clay | 10 | 24 | 3 | 22 | 3* | 22* | | 0 | 13 ^s 12.0 ^r | | | | Cooper et al., 1998 |
| 10 | Lower Weathered Gault Clay | 15 | 25 | 5 | 22 | 5* | 22* | | 0 | 14 ^s 13.3 ^r | | | | Cooper et al., 1998 |
| 11 | Unweathered Gault Clay | 25 | 26 | 5 | 23 | 5* | 23* | | 0 | 15 ^s 14.1 ^r | | | | Cooper et al., 1998 |
| 12 | Yellow Clay at Carsington Dam | 6 ^s | 19 ^s | 0 ^y | 19 ^y | 0* | 19* | | 0 | 12 | 0 | 16 | 70% | Skempton and Vaughan, 1993; Potts et al., 1990; Dounias et al., 1988; Chen et al., 1992 |

Chapter 2 Theoretical background of softening behaviour of stiff clays

| | | | | | | | | | | | | | | | | |
|----|---|--------------------|-------------------|------------------|-------------------|------|------|-------|-----|------|------|-----|----|--------|-----|---|
| 13 | Core Fill at Carsington Dam | 6 ^s | 20 ^s | | | | | | | 0 | 13 | 1.5 | 19 | | 35% | Skempton and Vaughan, 1993; Potts et al., 1990; Dounias et al., 1988; Chen et al., 1992 |
| 14 | Todi Clay | 59.1 [♀] | 32.6 [♀] | 0 | 28 | 0 | 20.2 | >1700 | 0 | 17 | 17 | | | 1 mm | | Burland, 1990 |
| 15 | Normally Consolidated Aged Kaolin | | | 0 | 19.8 | 0 | 15.1 | | 0 | 12.4 | 12.4 | | | 5 mm | | Burland, 1990 |
| 16 | Ashford Common London Clay Level C | 185.7 [♀] | 21.4 [♀] | 0 | 20.1 | 0 | 15.2 | >2500 | 0 | 12 | 12 | | | 1 mm | | Burland, 1990 |
| 17 | Ashford Common London Clay Level E | 153.2 [♀] | 22.9 [♀] | 0 | 20.1 | 25.5 | 17.3 | <2500 | 0 | 12 | 12 | | | 1 mm | | Burland, 1990 |
| 18 | London Clay with Pre-existing Fissures | | | 0 | 20.1 | 25.5 | 17.3 | >2500 | 0 | 12 | 12 | | | 3 mm | | Burland, 1990 |
| 19 | Blue London Clay with Fissures and Joints at Wraybury | 31 | 20 | 6.9 [◇] | 18.5 [◇] | 6.9 | 18.5 | <400 | 1.4 | 16 | 16 | | | 3 mm | | Skempton et al., 1969 |
| 20 | Stiff Clays at Δ3-2 of Tunnel S2 in North-west Greece | 60 | 28 | | | 25 | 21 | <600 | | <15 | <15 | | | | | Georgiannou, 2003 |
| 21 | Stiff Clays at Δ3-5 of Tunnel S2 in North-west Greece | 35 | 25 | | | 30 | 15 | <600 | | <15 | <15 | | | | | Georgiannou, 2003 |
| 22 | Vallericca Clay | 75 [∞] | 29.1 [∞] | 0 | 28.6 | 18 | 27.1 | <400 | | | | | | <10 mm | | Georgiannou and Burland, 2001 |

Chapter 2 Theoretical background of softening behaviour of stiff clays

| | | | | | | | | | | | | | | | |
|----|---|-------------------|-------------------|-----------------|-------------------|-------------------|--------------------|------|---|------|--|----------|--------|--|-------------------------|
| 23 | London Clay from Ashford Common | 81 [∞] | 29.8 [∞] | 0 | 19.2 | 16.6 | 18.4 | <740 | 0 | 12.9 | | | | | Burland, 1996 |
| 24 | Pietrafitta | 45.6 [∞] | 29.2 [∞] | 34 [∞] | 27.6 [∞] | 8.6 | 27.2 | <600 | | | | | | | Burland, 1996 |
| 25 | Todi Clay | 82.8 [∞] | 30.1 [∞] | 51.1 | 21.1 | 17.4 | 26.2 | <600 | | | | | | | Burland, 1996 |
| 26 | Vallericca Clay | 55.1 [∞] | 33.3 [∞] | 7.3 | 27.3 | 22.3 | 26.4 | <350 | | | | | | | Burland, 1996 |
| 27 | Corinth Marl | 133 | 37.7 | 0 | 36.4 | 0 | 36.4 | | | | | | | | Burland, 1996 |
| 28 | Guadalquivir Blue Clay at Aznalcollar Dam | 65 [∞] | 24.1 [∞] | 0 | 24.1 | 28.8 [#] | 21.3 [#] | | 0 | 11 | | 1 mm | >60 mm | | Alonso & Gens, 2006a |
| | | | | | | 0 ^f | 18~20 ^f | | 0 | 11 | | 6 mm | >60 mm | | Alonso & Gens, 2006a |
| 29 | Soil A Correspondent to Brown London Clay | 7 | 20 | | | 0 ^e | 20 ^e | | | | | | | | Law, 1981 |
| 31 | Soil B Correspondent to Champlain Sea Clay | 9 | 45 | | | 0 ^e | 40 ^e | | | | | | | | Law, 1981 |
| 31 | Stiff Fissured Champlain Sea Clay | 5.5 | 48 | | | 0 ^e | 40 ^e | | | | | | | | Law, 1981 |
| 32 | Silty Clay | | | | | 70 | 40 | | | | | 4.5~7.5% | | | Cunningham et al., 2003 |

Note:

* The post-rupture strength parameters are assumed to be equal to critical-state strength parameters when post-rupture strength parameters are absent.

Δ The strain required for post-rupture strength is considered to be the same as that for peak strength.



- s Shear box test.
 - r Ring shear test.
 - \$ Peak strength with shears.
 - ¥ Assumption made on empirical grounds as safe for strength of plastic clays.
 - ♀ Low stress level.
 - ◇ Values for fissure and joint surfaces.
 - € So called post-peak strength referring to the strength at moderate strain where the stress-strain curves stabilise beyond the peak. It is assumed to be equal to post-rupture strength.
 - ∞ General average strength value.
 - # Average post- peak strength with relative displacement equaling to 1 mm.
 - £ Post-peak strength value with relative displacement equaling to 6 mm.
- Unit for cohesion is kPa.
- Unit for frictional angle of shearing resistance is degree, °.



Table 2.2 Relevant index properties of the stiff clays in Table 2.1

| No. | Clay Name | Initial or Natural Water content (%) | Liquidity limit (%) | Plasticity limit (%) | Plasticity Index (%) | Liquidity Index | Clay Fraction (%) | Activity | Test Methods | Reference |
|-----|---|--------------------------------------|---------------------|----------------------|----------------------|---------------------|-------------------------|----------|--|--|
| | | | | | | | | | | |
| 1 | Brown London Clay | w | | | | | | | Back analysis | Jardine et al., 2004 |
| 2 | Numerical Material Similar to Brown London Clay | | | | | | | | Back analysis, undrained triaxial compression tests and ring shear tests | Potts et al., 1997 |
| 3 | Brown London Clay | 31 | 82 | 30 | 52 | 0.02 | 55 | 0.95 | Triaxial tests with large samples and back analysis | Chandler, 1984b |
| 4 | Weathered Upper Lias | 28 | 60 | 28 | 32 | 0 | 45 | 0.71 | Triaxial tests with large samples and back analysis | Chandler, 1984a |
| 5 | London Clay | | | | | | | | | |
| 6 | Upper Lias | | | | | | | | Laboratory tests | Chandler, 1984a |
| 7 | Oxford Clay at Saxon Pit | 21 | 55 | 24 | 21 | -0.14 | 55 | 0.38 | Triaxial tests, drained shear box tests, and ring shear tests | Cooper et al., 1998 |
| 8 | Soliflucted Gault Clay | | 70~75 | 22 | 48~53 | | | 1.18 | Triaxial tests, drained shear box tests, and ring shear tests | Cooper et al., 1998 |
| 9 | Upper Weathered Gault Clay | | | 22 | | Variable with depth | | | Triaxial tests, drained shear box tests, and ring shear tests | Cooper et al., 1998 |
| 10 | Lower Weathered Gault Clay | Variable with depth | 65~70 | 22 | 43~48 | | 38~48 42.4 (Mean) | 1.06 | Triaxial tests, drained shear box tests, and ring shear tests | Cooper et al., 1998 |
| 11 | Unweathered Gault Clay | | 60~65 | 22 | 38~43 | | | 0.94 | Triaxial tests, drained shear box tests, and ring shear tests | Cooper et al., 1998 |
| 12 | Yellow Clay at Carsington Dam | 38 | 75 | 32 | 43 | 0.14 | 62 | 0.69 | Triaxial compression and limit equilibrium analysis | Skempton and Vaughan, 1993; Potts et al., 1990; Dounias et al., 1988; Chen et al., 1992 |

| | | | | | | | | | | |
|----|---|-------|-------|------|-------|-------|-------|------|---|--|
| 13 | Core Fill at Carsington Dam | 34 | 69 | 31 | 38 | 0.08 | 56 | 0.68 | Triaxial compression and limit equilibrium analysis | Skempton and Vaughan, 1993; Potts et al., 1990; Dounias et al., 1988; Chen et al., 1992 |
| 14 | Todi Clay | | | | | | | | UU triaxial compression tests | Burland, 1990 |
| 15 | Normally Consolidated Aged Kaolin | | | | | | | | CAU triaxial compression | Burland, 1990 |
| 16 | Ashford Common London Clay Level C | 24.82 | 70.6 | 28.9 | 41.7 | -0.10 | 53 | 0.79 | Consolidated drained and undrained triaxial compression | Burland, 1990 |
| | | | | | | | | | Consolidated drained and undrained triaxial compression | Burland, 1990 |
| 17 | Ashford Common London Clay Level E | 23.89 | 70 | 27 | 43 | -0.07 | 57 | 0.75 | Consolidated drained and undrained triaxial compression | Burland, 1990 |
| | | | | | | | | | Consolidated drained and undrained triaxial compression | Burland, 1990 |
| 18 | London Clay with Pre-existing Fissures | | | | | | | | | Webb, 1964 |
| 19 | Blue London Clay with Fissures and Joints at Wraybury | 30 | 62~76 | 30 | 32~46 | 0 | 55~60 | 0.68 | Triaxial tests | Skempton et al., 1969 |
| 20 | Stiff Clays at A3-2 of Tunnel S2 in North-west Greece | 18.1 | 40.5 | 22.5 | 18 | -0.24 | 17 | 1.06 | Direct shear | Georgiannou , 2003 |

| | | | | | | | | | | |
|----|---|-------|-------|-------|-------|-------------|-------------------|------|--|-------------------------------|
| 21 | Stiff Clays at Δ3-5 of Tunnel S2 in North-west Greece | 21.9 | 53 | 30 | 23 | -0.35 | 18 | 1.28 | Direct shear | Georgiannou , 2003 |
| 22 | Vallericca Clay | 26.4 | 53.9 | 24.7 | 29.2 | 0.06 | 47 | 0.62 | Triaxial compression and extension tests | Georgiannou and Burland, 2001 |
| 23 | London Clay from Ashford Common | | | | | | | | Triaxial tests | Burland, 1996 |
| 24 | Pietrafitta | 41.9 | 87.0 | 34.5 | 52.5 | 0.14 | 44 | 1.19 | Triaxial tests | Burland, 1996 |
| 25 | Todi Clay | 17.5 | 67.2 | 39.1 | 28.1 | -0.77 | 43 | 0.65 | Triaxial tests | Burland, 1996 |
| 26 | Vallericca Clay | 28.6 | 60.2 | 26.8 | 33.4 | 0.05 | 42 | 0.80 | Triaxial tests | Burland, 1996 |
| 27 | Corinth Marl | 21.1 | 27.5 | 21.7 | 5.8 | -0.10 | 15 | 0.39 | Triaxial tests | Burland, 1996 |
| 28 | Guadalquivir Blue Clay at Aznalcóllar Dam | 30~35 | 62~67 | 31~32 | 31~35 | 0.03 (Mean) | 47~58 53(Mean) | 0.62 | Direct shear, ring shear tests | Alonso & Gens, 2006a |
| 29 | Soil A Correspondent to Brown London Clay | 31 | 82 | 30 | 52 | 0.02 | | | Triaxial tests | Law, 1981 |
| 30 | Soil B Correspondent to Champlain Sea Clay | 70 | 60 | 25 | 35 | 1.29 | | | Triaxial tests | Law, 1981 |
| 31 | Stiff Fissured Champlain Sea Clay | 65~70 | | | | | | | Triaxial tests | Law, 1981 |
| 32 | Silty Clay | 20.5 | 28 | 10 | 18 | 0.58 | | | Triaxial tests | Cunningham et al., 2003 |

2.4.4 Summary of post-peak shear strength of stiff clays

2.4.4.1 General feature of post-peak softening behaviour of stiff clays

As discussed above, a representative schematic full-course shear stress vs. shear displacement i.e. $\tau-\delta$ curve for stiff clays can be drawn with large shear displacements and is shown in Fig. 2.21. It is similar to stress-strain curves obtained from triaxial tests.

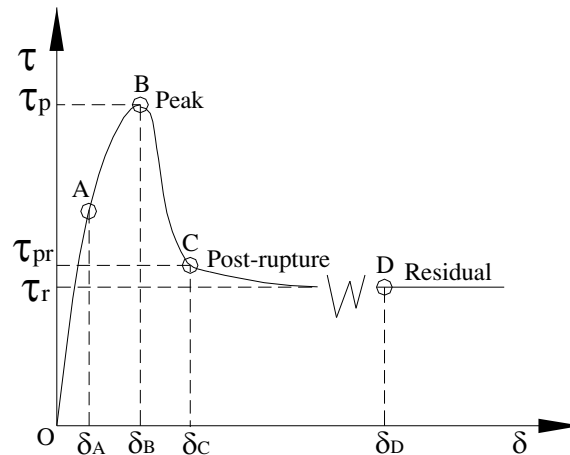
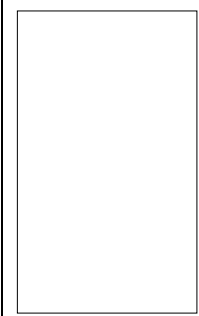
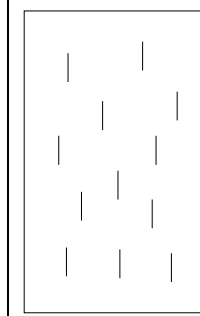
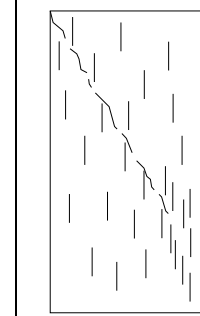
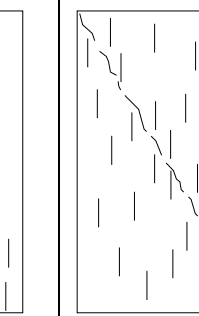
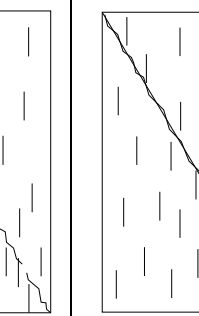


Fig. 2.21 Schematic stress-strain curve for stiff clays

In Fig. 2.21, Point A represents yield point, which distinguishes elastic and plastic stages for stiff clays. Point B indicates failure point associated with peak strength. After a relative small shear displacement, the peak strength drops rapidly to post-rupture strength, which is represented by point C. After C, residual state is reached at point D usually after large displacement. δ_A , δ_B , δ_C are normally much smaller than δ_D for stiff clays.

Table 2.3 Failure development in stiff clays

| 1 O-A | 2 A-B | 3 B-C | 4 C-D | 5 D--- |
|---|---|---|--|---|
| Intact | Pre-peak Mildly fissured | Post-peak Failure with mild fractures | Post-peak Highly fractured | Residual Continuous failure plane |
|  |  |  |  |  |

Meanwhile, the schematic failure process in stiff clays is shown in Table 2.3.

According to Fig. 2.21 and Table 2.3, it is easy to observe the five-stage $\tau-\sigma$ relationship for stiff clays which is outlined below:

- (1) a steep shear stress rise in shear stress with strain till A in elastic domain. The stiff clays keep intact.
- (2) a mild rise in shear stress until reaching the peak strength B at small relative displacement. After A plastic strain begins to develop and it is known as strain-hardening course from A to B. Only slight fissures begin to show up.
- (3) In natural stiff clays, some slight fissures may have already existed. The strain-hardening course of A-B is very short. Then O-A-B becomes continuously steep and can be merged smoothly into one elastic stage. In this Thesis, only linear elastic stage before B is considered (as seen in Fig. 2.20).
- (4) a quite rapid reduction of shear stress to post-rupture strength at C with very small relative displacement, usually associated with loss of interbonding between particles, i.e. deterioration of cohesive component of strength. Microcracks i.e. fissures in soil mass begins to form at B and then strain-softening process initiates. The stiff clays become highly fissured and the formation of fractures at a macroscopic scale is thought to be reached at point C.
- (5) a gentler shear stress reduction to residual strength at D induced by a gradual realignment, i.e. reorientation of clay particles at large displacements, which indicates the degradation of frictional angle of clays. This softening process is also due to the strain energy redistribution during the formation of fractures and a process of stress self-adjustment in clays. At this stage, clays are highly fractured.
- (6) no change in shear stress with deformation indicating the residual state. The residual strength is reached and there is not any volumetric strain. A continuous failure plan forms at this stage with purely frictional behaviour and only rigid block sliding happens along the failure plane.

In this paper, emphasis will be laid on the softening process involving post-rupture strength, i.e. stages (3)-(5).

2.4.4.2 General phenomena and observation of post-rupture strength

Georgiannou & Burland (2006) stated that it has been well established that intact natural stiff clays exhibit very brittle shearing behaviour at low to intermediate confining pressures. This behaviour results from the formation of very thin slip surfaces with an associated rapid drop in shear strength and subsequent rigid block sliding along these surfaces (e.g. Bishop et al., 1965; Calabresi, 1980; Burland, 1990).

Much attention has been devoted to the strength on the slip surfaces shortly after their formation (e.g. Burland, 1990; Burland et al., 1996; Georgiannou & Burland, 2001 and 2006). During and after the formation of a slip surface in these materials, the strength along it drops rapidly to a reasonably constant value, known as the post-rupture strength, after a relative displacement across the slip surface of only a few millimeters. The rapid reduction in strength in natural stiff materials is believed to be due mainly to the breaking of interparticle bonds, particularly at low to intermediate confining pressures.

Georgiannou & Burland (2006) reached the following conclusion based on drained tests on natural intact Corinth Marl: the steep reduction in shear stress is accompanied by the formation of a steeply inclined thin slip surface that becomes visible only as

post-rupture strength is approached. Most of the reduction in strength takes place for less than 0.5 mm relative displacement along the slip surface.

Georgiannou & Burland (2001) verified the robustness of post-rupture strength. They concluded that all the tests show equally well-defined post-rupture strengths at low to intermediate effective confining pressures. However, results obtained by Georgiannou and Burland (2001) and Burland et al. (1996) also show that at effective confining pressures in excess of about 400 kPa the post-rupture strength is often not so easily defined, as the strength continues to drop gradually after the formation of the slip plane. In such cases, the post-rupture strength is defined as the intersection of the extensions of the rapidly falling and more gently falling curves (Fig. 2.20). This implies the dependency of post-rupture strength on stress level and explains the curvature of post-rupture strength envelop. The suggestion of adopting the intersection as post-rupture point can be utilised as a general determining method for the post-rupture strength point in shear stress versus shear displacement or shear strain curve.

In brief, it can be concluded from the experimental studies:

- (1) the post-rupture strength envelope for the slip surfaces formed during the failure of initially intact stiff clay is well defined, repeatable, not sensitive to stress history or softening due to dilation and distortion, and not influenced by the rotation of the principal stresses but dependent on the stress level.
- (2) Little reduction in shearing resistance takes place for relative displacements across the slip surfaces up to about 10 mm. However, for larger relative displacements the strength will progressively reduce from the initial post-rupture value, ultimately reaching the residual value.
- (3) In this Thesis, the post-rupture strength parameters are denoted as c_{pr} and ϕ_{pr} which represent individually the cohesion and frictional angle of shearing resistance at post-rupture state.

2.4.4.3 Relationship between post-rupture and critical-state strengths

It is necessary to distinguish the difference between the critical-state strength, i.e. the fully softened strength, and post-rupture strength. Skempton (1970) explained that softening reduces the shear strength to the fully softened value. After reaching the fully softened shear strength, progressive failure reduces the average shear strength along the failure surface to a value between the fully softened and residual shear strength values. He also mentioned that softening only reduces the effective cohesion component of shear strength parameters but does not cause orientation of clay particles or reduction in friction angle.

In addition, Skempton (1970) stated that before arriving at fully softened condition, a complex of minor shears such as the Riedel, thrust and displacement shears (Skempton, 1966) forms but are not linked into a smooth continuous surface (Fig. 2.2). However, as demonstrated by Morgenstern & Tchalenko (1967), particle reorientation will have occurred along these minor shears. So the fully softened condition is just an approximate one not a precise one to be related with strength of natural stiff clays with obvious fractures because both softening and particle reorientation have happened before the formation of fractures. But, as implied by the former results, post-rupture state results from both the two processes—softening and particle



reorientation, especially at high confining pressure under which the relative small displacement may include some small degree of particle reorientation after complete softening. Therefore, post-rupture strength seems to be more reasonable to represent the strength in stiff fissured clays. Meanwhile, this explains the difference between the intrinsic strength envelope, i.e. critical-state strength envelope, and the post-rupture strength envelope at high confining pressures (Georgiannou & Burland, 2001).

Hight, Bond & Legge (1992) confirmed that natural materials frequently have microstructures which give enhanced strength and resistance to compression compared with the reconstituted material owing to interparticle bonding. Continued shearing or compression results in a degradation of the microstructure so that the state of the natural material tends towards that of the equivalent reconstituted or unstructured material. Furthermore, Burland et al. (1996) also suggested that the material in the rupture plane has a fabric similar to that of the reconstituted material. However, this may not always be the case and there still exists some confusion concerning the coincidence between the field strength and the critical-stage strength, i.e. the fully softened strength (Chandler, 1984a, b). In any case, the critical-state strength, which corresponds to the intrinsic properties of a soil, can be considered as a basic useful frame of reference for interpreting the behaviour of its natural counterpart (Georgiannou & Burland, 2001).

Burland (1990) and Burland et al. (1996) have shown that, for the natural stiff intact clays having been tested, the post-rupture strength line tends to lie on or slightly above the critical-state strength envelope at low stresses. In this case, the rapid post-peak loss of strength results largely from changes in microstructure due mainly to the breaking of interparticle bonds accompanied by local dilation, in agreement with results presented by Viggiani et al. (1993, 1994).

However, at higher confining pressures the post-rupture strength envelope drops below the intrinsic failure envelope—a result that was observed by Burland (1990) for both Todi Clay and London Clay. Burland et al. (1996) attributed this to the onset of progressive particle reorientation during the rupturing process under the influence of higher normal stresses, thereby accounting for the curvature of the post-rupture strength envelope. Moreover, as mentioned previously, the strength continues to reduce gradually after the formation of the slip surface, which implied continuing particle reorientation.

As a whole, the critical-state (fully softened) strength is best used as an intrinsic reference to consider the initial structure of natural intact stiff clays, whereas the post-rupture strength has a more realistic role in explaining the post-peak softening behaviour of stiff clays.

2.4.4.4 Relationship between operational and post-rupture strengths

As demonstrated by Burland et al. (1996), the operational effective strength envelope for stiff fissured clay en masse is notoriously difficult to determine from laboratory tests on undisturbed samples. The back-analysis of many first-time slides in stiff fissured clays (e.g. Skempton, 1970 and 1977; Chandler, 1984b) gives operational strengths that are close to, but slightly above, the critical-state strength of the reconstituted material (often called the fully softened strength). The observed close agreement between the post-rupture strength envelope and the intrinsic critical-state strength envelope at low confining pressures offers a rational explanation for this.

Meanwhile, there is some evidence to suggest that the intrinsic critical state friction angle ϕ_{cs}^* , which is relatively easy to determine from reconstituted soil, is a relevant parameter to determine the operational strength of stiff clays (Skempton, 1977; Chandler 1984b). The near coincidence of ϕ_{pr}' and ϕ_{cs}^* at low stresses, gives support to this hypothesis and provides an explanation based on microstructure behaviour. In many cases, the inclusion of a small cohesion is appropriate, as also confirmed by the back-analysis of first-time slides (Chandler, 1984b). However, for intensely fissured clays, the operational friction angle can be lower than ϕ_{cs}^* , and in the limit may be as low as ϕ_r' for pre-existing slides and slip surfaces.

Moreover, as emphasized by Burland et al. (1996), for highly contorted or tectonically sheared soils the operational strengths may be significantly less than the post-rupture strength, and can approach residual values (Skempton, 1985; Picarelli & Olivares, 1998). Hence, when assessing the operational strength of stiff clays, as well as carrying out laboratory tests on undisturbed and reconstituted samples, careful visual examination of the structure of the soil (in particular the fissure surfaces) is essential, together with a thorough knowledge of the genesis of the deposit.

Skempton et al. (1969) and many others have emphasized the importance of joints and fissures in determining the mass strength of stiff clays. The brittle shearing properties of natural intact stiff clays, and the very rapid reduction in strength from peak to post-rupture with the associated development of slip planes, are believed to be major factors in the formation of joints and fissures. Therefore, studies of the failure of intact clays and the subsequent post-rupture behaviour are thought to be of importance in developing a greater understanding of the formation of fissures and joints and of the factors controlling the strength and deformation properties of fissured materials.

The initial strength on these discontinuities will be controlled by the post-rupture strength envelope. Calabresi (1980) suggested that the initial strength along the fissures formed in stiff clays is likely to be close to the post-rupture strength. Therefore, provided significant displacements have not taken place along these discontinuities, then the first-time effective strength of the mass will be close to the post-rupture strength, which in turn has been shown in a number of cases to be close to the critical-state strength at low to medium pressures.

Gens & Alonso (2006) summarized that the operational strength must be a function of peak, post-rupture and residual strengths, the rate of strength degradation and the non-homogeneous patterns of strain development along the failure surface.

2.4.4.5 Application of post-rupture strength in geotechnical engineering

2.4.4.5.1 Application of post-rupture strength to in-situ stresses

Burland (1990) showed that the in-situ horizontal effective stresses in London Clay at Ashford Common appear to be controlled by the post-rupture strength which limits the magnitude of the horizontal effective stresses in heavily over-consolidated fissured clays since the fissures probably result from the brittle nature of the intact material.

2.4.4.5.2 Application of post-rupture strength to bearing capacity

Tarzi et al. (1982) and Chan & Morgenstern (1989) shows strain softening substantially reduces the bearing capacity. Even quite moderate rates of strain softening reduce the bearing capacity significantly and the effect is more pronounced for strain softening with localised slip surfaces. Burland (1990) demonstrated that post-rupture strength forms a very reasonable lower bound for the bearing capacity of a footing even when the material is initially intact.

2.4.4.5.3 Application of post-rupture strength to tunnel excavation

Georgiannou (2003) described a good example of application of post-rupture strength to tunnel excavation. Georgiannou (2003) made experimental study on stiff sedimentary clays underlying heavily fractured limestone from tunnel S2 of Egnatia Motorway in north-west Greece. The shear behaviour of the clays was examined in direct shear tests. The peak and post-rupture strength of the intact clay as well as the part of the clay in contact with the limestone are shown in Fig. 2.22. The peak intact strength is reached after approximately 1–1.5 mm displacement, and as a rupture surface is formed, the strength drops rapidly to a nearly constant value (post-rupture strength) after a relative displacement of approximately 1.5 mm. The slope of the peak strength envelope of the intact clay for the stress range considered in this study is $\phi' = 28^\circ$ and the cohesion intercept is approximately 60 kPa, whereas the corresponding peak values for the same clay at the interface between stiff clay and fractured limestone are $\phi' = 25^\circ$ and $c' = 35$ kPa.

The specimens in the vicinity of the limestone when tested in direct shear show a gradual drop in strength after peak. The difference between the latter and the intact clay is probably due to differences in bonding. This has also been found by Burland (1996) and Georgiannou & Burland (2001).

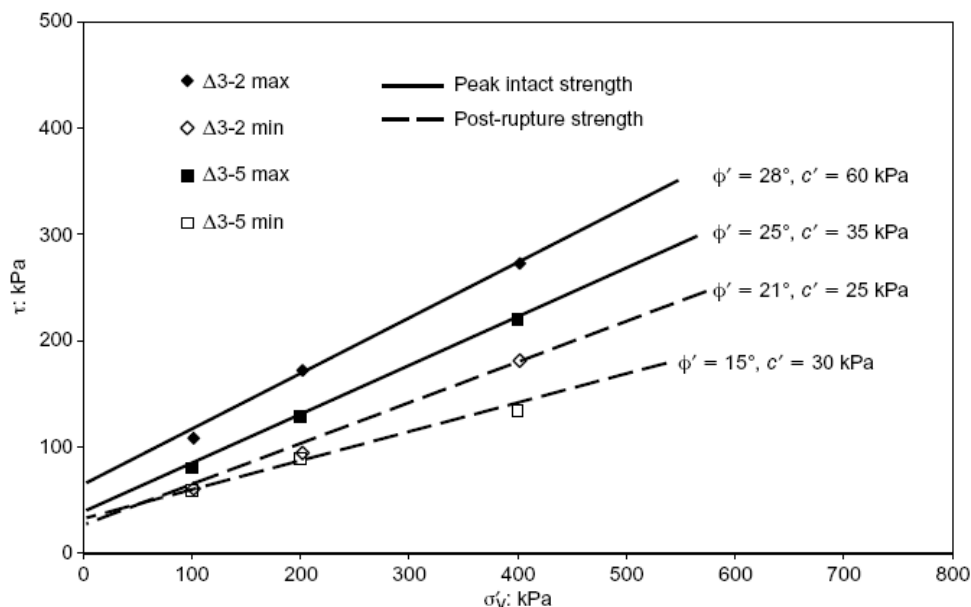


Fig. 2.22 Intact and post-rupture strength envelopes for direct-drained shear tests on stiff clay (Georgiannou, 2003)

The post-rupture strength envelopes, as shown in Fig. 2.22, fall below the peak strength envelopes for both states of clay. The post-rupture strength envelope for the intact material has a slope $\phi' = 21^\circ$ and a cohesive intercept $c' = 25$ kPa, whereas the

post-rupture strength envelope for the same material in the vicinity of the limestone appears to be flatter, with $\phi' = 15^\circ$ and $c' = 30$ kPa. Unfortunately, the residual value has not been defined, but it is expected to be lower than 15° .

Significantly, Georgiannou (2003) stated that the post-rupture strength probably results from a combination of the presence of fissures and progressive failure due to the brittle nature of the intact material. Careful visual examination of the fissure surfaces indicated that the post-rupture strength would control the behaviour of the clay under consideration. In fact, the post-rupture strength appears to form a very reasonable lower bound for the operational strength of the clay mass. Hence, the post-rupture strength parameters deduced from the laboratory tests were used in the numerical analyses performed for the design of primary support and excavation sequences of the tunnel.

Testing of block samples in the laboratory has shown that these overconsolidated clay sediments (OCR=10) appear to possess structural bonding, which is progressively disrupted in the process of loading. Whereas the intact clay shows an abrupt drop to post-rupture strength when tested in direct shear, the samples in contact with the overlying limestone show a gradual drop in strength after peak. Considering the strength envelopes the latter one is weaker compared with the intact clay. The post-rupture strengths for the intact clay and the clay in contact with the overlying limestone form a reasonable lower bound for the operational strength of the clay mass and were used as the design parameters.

2.4.4.6 Generalised descriptive indices based on post-rupture strength

2.4.4.6.1 Residual factor R

Gens & Alonso (2006) stated that a useful parameter for characterising progressive failure is the residual factor defined by Skempton (1964) and given in Eq. (1.3). R measures the degree of development of residual strength along the failure surface and the difference between the average operational strength and the strength measured in the laboratory.

According to Eq. (1.3), a generalised residual factor can be defined as

$$R_{GB} = \frac{\bar{\tau}_P - \bar{\tau}_{mob}}{\bar{\tau}_P - \bar{\tau}_R} \quad (2.2)$$

where τ_{mob} is the mobilised shear stress at collapse.

If $\tau_{mob} = \tau_{pr}$, it becomes as

$$R_{GB-pr} = \frac{\bar{\tau}_P - \bar{\tau}_{pr}}{\bar{\tau}_P - \bar{\tau}_R} \quad (2.3)$$

at post-rupture state.

2.4.4.6.2 Brittleness Index

Brittleness, which constitutes a major factor in the development of progressive failure, has been characterised by the brittleness index. Alonso & Gens (2006a) put up two brittleness indices defined as

$$I_f = (\tau_p - \tau_f) / \tau_p \quad (2.4)$$

and

$$I_B = (\tau_p - \tau_{res}) / \tau_p \quad (2.5)$$

where τ_p denotes peak strength; τ_f is the shear strength at the end of laboratory test at small displacement; τ_{res} is the residual strength.

I_B is the definition of brittleness index proposed by Bishop (1967). It is clear that $I_B > I_f$.

D'Elia et al. (1998) proposed a generalised brittleness index, I_{GB} , defined as

$$I_{GB} = \frac{\tau_p - \tau_{mob}}{\tau_p} \quad (2.6)$$

in which τ_{mob} is the mobilised shear stress at the considered strain or displacement. I_{GB} thus varies with strain or displacement from 0 at the peak to a value equal to I_B at large displacements, i.e. residual state.

Specifically, when the mobilised shear stress τ_{mob} equals to the post-rupture shear strength τ_{pr} , I_{GB} is could be defined as

$$I_{GB-pr} = \frac{\tau_p - \tau_{pr}}{\tau_p} \quad (2.7)$$

following the rapid decrease of shear strength after peak at relative small displacements.

Chen et al. (1992) defined the alternative brittleness index as

$$I_{GB} = \frac{k_p - k_r}{k_p} \quad (2.8)$$

where k may be state parameter such as c or ϕ .

Similarly, the alternative generalised brittleness index is given as

$$I_{GB} = \frac{k_p - k_{mob}}{k_p} \quad (2.9)$$

and the corresponding value for post-rupture state could be obtained by setting $k_{mob} = k_{pr}$.

In a later Chapter, Fig. 6.10 and Fig. 6.11 provide good references for of I_f and I_B values.

2.4.4.6.3 Cementation loss index

As shown in Fig. 6.7, Alonso & Gens (2006a) introduced two *cementation loss indices* defined as

$$CL_f = \Delta\tau_b / (\tau_p - \tau_f) \quad (2.10)$$

and

$$CL_B = \Delta\tau_b / (\tau_p - \tau_{res}) \quad (2.11)$$

These two *cementation loss indices* are used to measure the rapid sudden drop of shear strength. They are useful parameters to characterize the post-rupture strength.

2.4.4.7 Representative descriptive curves for post-rupture behaviour

2.4.4.7.1 Shear stress versus shear strain or displacement ($\tau - \varepsilon_s$ or $\tau - \delta$)

According to studies of Bishop et al. (1971), Calabresi & Manfredini (1973), Lupini et al. (1981), Skempton (1964, 1985), Burland (1990), Burland et al. (1996), Stark & Eid (1997), Georgiannou & Burland (2001 and 2006) and Alonso & Gens (2006a), the typical diagram for post-peak behaviour can be shown in schematic curves as shown in Fig. 2.21. All the figures show the rapid strength loss at very small relative displacement after peak. In addition, the relevant softening model parameters can be determined from $\tau - \delta$ curve obtained from direct shear tests. This will be described in subsequent section of this thesis.

2.4.4.7.2 Deviatoric force versus notional axial strain in triaxial tests ($\tau - \varepsilon_a$)

As demonstrated by Burland (1990) and Burland et al. (1996), a rapid reduction of deviatoric stress or load can be depicted by a curve with deviatoric stress versus notional axial strain acquired in triaxial tests as shown in Fig. 2.6.

2.4.4.7.3 Stress Ratio τ / σ_n' versus displacement or strain

Triaxial tests on kaolin (Ninis, 1990), Todi clay and London clay (Burland, 1990 and Burland et al., 1996) and Vallericca clay (Georgiannou and Burland, 2001) show the relationship between τ / σ_n' and axial strain and relative displacement across slip surface. A representative one is shown in Fig. 2.6. During post-peak stage, $\tau / \sigma_n' - \delta_{relative}$ curve exhibits a similar change trend as $\tau - \varepsilon_a$. To some extent, τ / σ_n' is approximately equal to the tangent of friction angle of shear resistance provided that cohesion is very small.

2.4.4.7.4 Shear stress versus normal effective stress ($\tau - \sigma_n$)

According to Burland (1990), Burland et al. (1996), Georgiannou (2003) and Georgiannou & Burland (2001 and 2006), the relationship between shear stress and normal effective stress, i.e. shear strength envelopes, of stiff clays can be plotted as curves shown in Fig. 2.23, which are normally drawn from triaxial tests and direct shear tests.

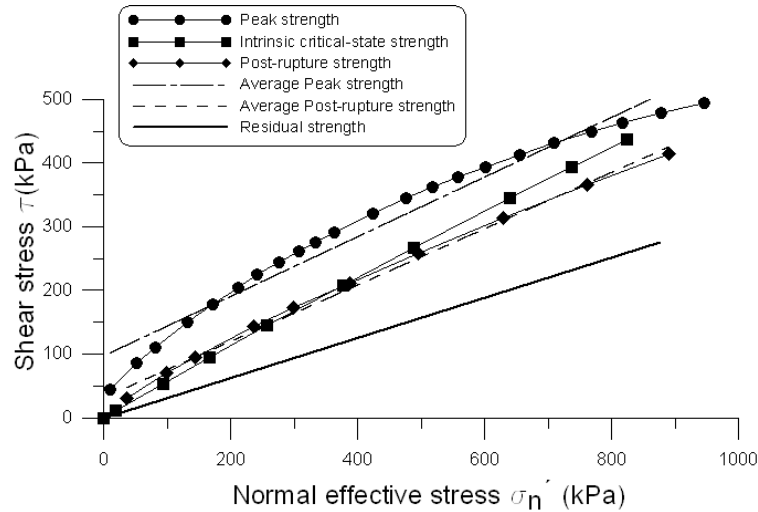


Fig. 2.23 Sketch diagram of shear strength envelopes of stiff clay

According to Fig. 2.23, the shear strength envelopes are stress-dependent and show apparent nonlinearity. As normal effective stress increases, the difference between peak and post-rupture strength becomes smaller indicating a reduction in brittleness.

The post-rupture strength envelope can be roughly divided into two parts compared with intrinsic critical-state strength. To some extent, intrinsic critical-state strength can be used as an approximation to post-rupture strength at low stress.

Chapter 3. Formulation and implementation of two-stage softening constitutive model for stiff clays

3.1 Introduction

Many constitutive models for soils have been developed using the framework of elastoplasticity (Yu, 2006). This chapter firstly gives a brief description of the classical theory of elastoplastic constitutive models. Then some representative models involving strain softening are presented. In particular, a generalised non-linear strain-softening and strain-hardening model based on an improved Mohr-Coulomb yield criterion is described in detail including the model capabilities and drawbacks.

Afterwards, in line with the collected data for post-rupture strength parameters acquired in Chapter 2, the modified constitutive model is introduced to predict the observed two-stage post-peak softening behaviour of stiff overconsolidated clays. The relevant formulation for this new modified model is illustrated at length and then the new model is implemented into an explicit finite difference program *FLAC* (ITASCA) based on an embedded strain-hardening/softening model.

3.2 Classical theory of elastoplasticity

This section describes the basic concepts of the theory and the formulation of the elastoplastic constitutive matrix. A more detailed description can be found in Potts and Zdravkovic (1999).

3.2.1 Basic concepts

To formulate an elastoplastic constitutive model, four essential ingredients need to be defined: yield surface, flow rule, hardening/softening rules and elastic response.

3.2.1.1 Yield surface

A yield surface separates purely elastic behaviour from elastoplastic behaviour. The yield function, F , is defined as one of stress state, $\{\sigma\}$, and state (also called hardening) parameters, $\{k\}$:

$$F(\{\sigma\}, \{k\}) = 0 \quad (3.1)$$

With stress states remaining within the yield surface, i.e. $F < 0$, purely elastic behaviour occurs. Whereas for stress states on the yield surface, i.e. $F = 0$, elastoplastic behaviour occurs. $F > 0$ signifies impossible states.

3.2.1.2 Flow rule

The flow rule specifies the direction of plastic strain increments. It is usually related to the plastic potential surface, whose outward normal vector at the current stress state represents the plastic strain increment vector. The flow rule can be expressed as follows:

$$\{d\varepsilon^p\} = \Lambda \left\{ \frac{\partial P(\{\sigma\}, \{m\})}{\partial \sigma} \right\} \quad (3.2)$$

where $\{d\varepsilon_p\}$ is the plastic strain increment vector, $P(\{\sigma\}, \{m\}) = 0$, is the plastic potential function and Λ is a scalar multiplier. $\{m\}$ are a vector of state parameters because only the differentials of the plastic potential function with respect to the stress components are required in the flow rule.

In Eq. (3.2) the plastic potential function just defines the relative magnitude of the plastic strain increments and the scalar multiplier, Λ , which will be discussed later, determines the actual magnitude.

If the plastic potential function is assumed to be the same as the yield function, i.e. $P(\{\sigma\}, \{m\}) = F(\{\sigma\}, \{k\})$, the flow rule is said to be associated and a normality condition applies; whereas, in the general case, where the plastic potential function is different from the yield function, i.e. $P(\{\sigma\}, \{m\}) \neq F(\{\sigma\}, \{k\})$, the flow rule is said to be non-associated.

3.2.1.3 Hardening/softening rule

The hardening/softening rule describes the evolution of the yield surface in the course of plastic deformation. It defines how the hardening parameters $\{k\}$ change with plastic strain. For perfectly plastic elastoplastic model, the hardening parameters $\{k\}$ are constant and no hardening occurs. Generally, the hardening parameters are usually assumed to be dependent on either the plastic work or the plastic strains, resulting in work-hardening and strain-hardening formulations respectively. In particular, for the strain-softening case, the rule can be expressed as a piecewise function capable of simulating both hardening and softening phenomena.

3.2.1.4 Elastic response

The elastic response encompasses two parts. One is the purely elastic behaviour, when the stress state remains within the yield surface, and the other is the elastic deformation occurring as part of the elastoplastic behaviour, when the stress state is on the yield surface.

3.2.1.5 Determination of the scalar multiplier, Λ

The scalar multiplier, Λ , is determined by applying the consistency condition which requires the stress state to remain always on the yield surface, i.e. $dF = 0$ while the soil is yielding. As mentioned above, the yield function depends on the stress state,

$\{\sigma\}$, and the hardening parameters, $\{k\}$, so the chain rule of differentiation of yield function gives:

$$dF = \left\{ \frac{\partial F}{\partial \sigma} \right\}^T \{d\sigma\} + \left\{ \frac{\partial F}{\partial k} \right\}^T \{dk\} = 0 \quad (3.3)$$

The hardening parameters can be considered as a function of the plastic strains as follows:

$$\{dk\} = \left[\frac{\partial k}{\partial \varepsilon^p} \right] \{d\varepsilon^p\} \quad (3.4)$$

Then Eq. (3.3) becomes:

$$dF = \left\{ \frac{\partial F}{\partial \sigma} \right\}^T \{d\sigma\} + \left\{ \frac{\partial F}{\partial k} \right\}^T \left[\frac{\partial k}{\partial \varepsilon^p} \right] \{d\varepsilon^p\} = 0 \quad (3.5)$$

Substitution of the flow rule in the above equation leads to:

$$dF = \left\{ \frac{\partial F}{\partial \sigma} \right\}^T \{d\sigma\} + \left\{ \frac{\partial F}{\partial k} \right\}^T \left[\frac{\partial k}{\partial \varepsilon^p} \right] \Lambda \left\{ \frac{\partial P(\{\sigma\}, \{m\})}{\partial \sigma} \right\} = 0 \quad (3.6)$$

So, the scalar quantity, Λ , can be written as:

$$\Lambda = \frac{1}{A} \left\{ \frac{\partial F}{\partial \sigma} \right\}^T \{d\sigma\} \quad (3.7)$$

where A denotes the hardening modulus (or otherwise called plastic modulus) given as:

$$A = - \left\{ \frac{\partial F}{\partial k} \right\}^T \left[\frac{\partial k}{\partial \varepsilon^p} \right] \left\{ \frac{\partial P}{\partial \sigma} \right\} \quad (3.8)$$

Therefore, the plastic strains can then be calculated by Eq. (3.2).

3.2.2 Formulation of the elastoplastic constitutive matrix

Elastoplastic constitutive matrix $[D^{ep}]$, which defines the relationship between the changes in stresses and strains, can be formulated in terms of the basic ingredients described in the previous section. The relationship is expressed as:

$$\{d\sigma\} = [D^{ep}] \{d\varepsilon\} \quad (3.9)$$

The changes in total strains are assumed to be composed of two components, the elastic strains and the plastic counterparts as given by:

$$\{d\varepsilon\} = \{d\varepsilon^e\} + \{d\varepsilon^p\} \quad (3.10)$$

where $\{d\varepsilon^e\}$ and $\{d\varepsilon^p\}$ are the changes in elastic and plastic strains respectively.

The changes in stresses can be expressed by the changes in elastic strains via the elastic constitutive matrix $[D]$ as follows:

$$\{d\sigma\} = [D] \{d\varepsilon^e\} \quad (3.11)$$

Substituting Eq. (3.10) into Eq. (3.11) gives:

$$\{d\sigma\} = [D] \left(\{d\varepsilon\} - \{d\varepsilon^p\} \right) \quad (3.12)$$

Substitution of the flow rule in the above equation gives:

$$\{d\sigma\} = [D] \{d\varepsilon\} - [D] \Lambda \left\{ \frac{\partial P}{\partial \sigma} \right\} \quad (3.13)$$

Substitution of Eq. (3.13) in Eq. (3.7) let the scalar multiplier, Λ , become:

$$\Lambda = \frac{\left\{ \frac{\partial F}{\partial \sigma} \right\}^T [D] \{d\varepsilon\}}{\left\{ \frac{\partial F}{\partial \sigma} \right\}^T [D] \left\{ \frac{\partial P}{\partial \sigma} \right\} + A} \quad (3.14)$$

Substitution of the above equation in Eq. (3.13) gives:

$$\{d\sigma\} = [D] \{d\varepsilon\} - \frac{[D] \left\{ \frac{\partial P}{\partial \sigma} \right\} \left\{ \frac{\partial F}{\partial \sigma} \right\}^T [D] \{d\varepsilon\}}{\left\{ \frac{\partial F}{\partial \sigma} \right\}^T [D] \left\{ \frac{\partial P}{\partial \sigma} \right\} + A} \quad (3.15)$$

Eq. (3.15) presents a relationship between changes in stresses and strains. According to Eq. (3.9) the elastoplastic constitutive matrix is given by:

$$[D^{ep}] = [D] - \frac{[D] \left\{ \frac{\partial P}{\partial \sigma} \right\} \left\{ \frac{\partial F}{\partial \sigma} \right\}^T [D]}{\left\{ \frac{\partial F}{\partial \sigma} \right\}^T [D] \left\{ \frac{\partial P}{\partial \sigma} \right\} + A} \quad (3.16)$$

3.3 Basic Mohr-Coulomb model

The yield criterion is expressed in terms of effective stress invariants. The mean effective stress invariant, p' , the deviatoric stress invariant, J and Lode's angle, θ are defined in Appendix I.

The Coulomb failure criterion can be expressed as:

$$\tau_f = c' + \sigma_{nf}' \tan \phi' \quad (3.17)$$

where τ_f and σ_{nf}' are the shear and normal effective stresses on the failure plane, and the material parameters c' and ϕ' represent the cohesion and the angle of shearing resistance respectively.

The Mohr-Coulomb failure criterion can be written as:

$$\sigma_1' - \sigma_3' = 2c' \cos \phi' + (\sigma_1' + \sigma_3') \sin \phi' \quad (3.18)$$

In terms of the effective stress invariants, the Mohr-Coulomb yield surface is defined as:

$$F(\{\sigma'\}, \{k\}) = J - \left(\frac{c'}{\tan \phi'} + p' \right) g(\theta) = 0 \quad (3.19)$$

where

$$g(\theta) = \frac{\sin \phi'}{\cos \theta + \frac{\sin \theta \sin \phi'}{\sqrt{3}}} \quad (3.20)$$

where $\{k\} = \{c', \phi'\}^T$ is assumed to be constant, i.e. independent of plastic strain or plastic work. $g(\theta)$ is a function defining the shape of the yield surface in the deviatoric plane and the gradient of the yield surface in the $J - p'$ plane (see Fig. 3.1 and Fig. 3.2).

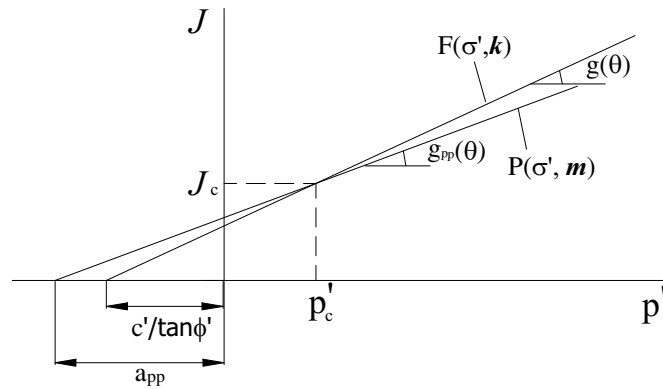


Fig. 3.1 Mohr-Coulomb failure criterion in $J - p'$ plane

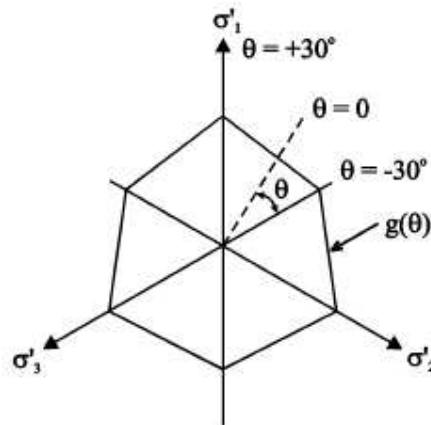


Fig. 3.2 Mohr-Coulomb failure criterion in deviatoric plane

As shown in Fig. 3.2, for triaxial compression $\theta = 30^\circ$ ($b = 0$), and for triaxial extension $\theta = -30^\circ$ ($b = 1$). b is defined by Eq. (I.14).

If an associated flow rule is adopted, the plastic potential function can be given by:

$$P(\{\sigma'\}, \{m\}) = F(\{\sigma'\}, \{k\}) \quad (3.21)$$

where $\{k\} = \{c', \psi'\}^T$ because of $\phi' = \psi'$.

The plastic strain increment vector is then inclined at an angle ϕ' to the vertical and indicates negative direct plastic strains. This results in the angle of dilation, ψ' being equal to the angle of shearing resistance, ϕ' . The angle of dilation is defined as:

$$\psi' = \sin^{-1} \left(-\frac{d\varepsilon_1^p + d\varepsilon_3^p}{d\varepsilon_1^p - d\varepsilon_3^p} \right) \quad (3.22)$$

where

$$d\varepsilon_1^p = \Lambda \frac{\partial P(\{\sigma'\}, \{m\})}{\partial \sigma_1'} \quad (3.23)$$

$$d\varepsilon_3^p = \Lambda \frac{\partial P(\{\sigma'\}, \{m\})}{\partial \sigma_3'} \quad (3.24)$$

Using an associated flow rule has two problems. Firstly, the magnitude of the plastic volumetric strains (i.e. dilation) predicted is much larger than that observed in real soil behaviour. Secondly, once the soil yields it will dilate forever. Real soil may dilate initially on meeting the failure surface but often reaches a constant volume condition (i.e. zero incremental plastic volumetric strains) at large strains.

The first problem can be overcome by using a non-associated flow rule in which the angle of dilation is different from the angle of shearing resistance. In this case the plastic potential function is similar to Eq. (3.19) with the angle of shearing resistance, ϕ' , replaced by the angle of dilation, ψ' . This can be written as:

$$P(\{\sigma'\}, \{m\}) = J - (a_{pp} + p') g_{pp}(\theta) = 0 \quad (3.25)$$

where

$$g_{pp}(\theta) = \frac{\sin \psi'}{\cos \theta + \frac{\sin \theta \sin \psi'}{\sqrt{3}}} \quad (3.26)$$

and a_{pp} is the distance of the apex of the plastic potential cone from the origin in $J - p'$ plane as shown in Fig. 3.1.

In Fig. 3.1, p_c' , J_c and θ_c (not shown in Fig. 3.1) are stress invariants at the current stress state on the yield surface. Combining Eq. (3.19) and Eq. (3.25) leads to:

$$a_{pp} = \left(\frac{c'}{\tan \phi'} + p_c' \right) \frac{g(\theta_c)}{g_{pp}(\theta_c)} - p_c' \quad (3.27)$$

Substitution of the above equation in Eq. (3.25) gives:

$$P(\{\sigma'\}, \{m\}) = J - \left(\left(\frac{c'}{\tan \phi'} + p_c' \right) \frac{g(\theta_c)}{g_{pp}(\theta_c)} - p_c' + p' \right) g_{pp}(\theta) = 0 \quad (3.28)$$

If $\psi' = \phi'$, an associated flow rule results.

If $\psi' < \phi'$, non-associate conditions arise and as ψ' reduces, less dilation is generated. For example, if $\psi' = 0$, no plastic volumetric strain (i.e. zero plastic dilation) occurs.

Therefore, the predicted plastic volumetric strains can be controlled by prescribing the angle of dilation, ψ' .

The basic Mohr-Coulomb model is assumed to be perfectly plastic which indicates that no hardening/softening law is required and the state parameters, $\{k\}$ are constant. This basic model requires 5 parameters which are c' , ϕ' and ψ' controlling the plastic behaviour and E' and μ' predicting the elastic response. For associated conditions, only 4 parameters are needed since $\psi' = \phi'$.

By applying the equations given in Section 3.2, the partial derivatives of the yield surface and plastic potential surface can be written as:

$$\frac{\partial F}{\partial \sigma'} = \frac{\partial F}{\partial p'} \frac{\partial p'}{\partial \sigma'} + \frac{\partial F}{\partial J} \frac{\partial J}{\partial \sigma'} + \frac{\partial F}{\partial \theta} \frac{\partial \theta}{\partial \sigma'} \quad (3.29)$$

$$\frac{\partial P}{\partial \sigma'} = \frac{\partial P}{\partial p'} \frac{\partial p'}{\partial \sigma'} + \frac{\partial P}{\partial J} \frac{\partial J}{\partial \sigma'} + \frac{\partial P}{\partial \theta} \frac{\partial \theta}{\partial \sigma'} \quad (3.30)$$

where the values of $\frac{\partial p'}{\partial \sigma'}$, $\frac{\partial J}{\partial \sigma'}$, and $\frac{\partial \theta}{\partial \sigma'}$, are model independent and are presented in Appendix II., and

$$\frac{\partial F}{\partial p'} = -g(\theta) \quad (3.31)$$

$$\frac{\partial F}{\partial J} = 1 \quad (3.32)$$

$$\frac{\partial F}{\partial \theta} = \left(\frac{c'}{\tan \phi'} + p' \right) \frac{\sin \phi'}{\left(\cos \theta + \frac{\sin \theta \sin \phi'}{\sqrt{3}} \right)^2} \left(\sin \theta - \frac{\cos \theta \sin \phi'}{\sqrt{3}} \right) \quad (3.33)$$

$$\frac{\partial P}{\partial p'} = -g_{pp}(\theta) \quad (3.34)$$

$$\frac{\partial P}{\partial J} = 1 \quad (3.35)$$

$$\frac{\partial P}{\partial \theta} = (a_{pp} + p') \frac{\sin \psi'}{\left(\cos \theta + \frac{\sin \theta \sin \psi'}{\sqrt{3}} \right)^2} \left(\sin \theta - \frac{\cos \theta \sin \psi'}{\sqrt{3}} \right) \quad (3.36)$$

It is possible to replace the linear elastic behaviour with nonlinear elastic behaviour by allowing the elastic constants to vary with stress and/or strain level.

3.4 One-stage softening model

3.4.1 General concept of softening of strength parameters

Although the application of a non-associated flow rule can restrict the magnitude of the incremental plastic volumetric strains, the model still predicts increasing volumetric strains, no matter how far the soil is sheared. This is unrealistic and can give unreasonable predictions in some boundary value problems. One solution method is to allow model parameters such as the friction angle of shearing resistance and the angle of dilation to vary with plastic strain.

Potts et al. (1987, 1990 and 1997), Dounias et al. (1988 and 1996), Cividini and Gioda (1992) and Troncone (2005) used a generalised non-linear strain-softening and strain-hardening soil model shown in Fig. 3.3 and Fig. 3.4 for progressive failure analysis. This is an elastoplastic model in which softening behaviour is accounted for by allowing the angle of shearing resistance, ϕ' , and the apparent cohesion intercept, c' , to vary with the deviatoric plastic strain invariant, ε_D^P . That is to say, in this model, the mobilised shear strength along slip surfaces in a strain-softening material is dependent on the amount of plastic straining. Meanwhile, the angle of dilation may also vary with ε_D^P .

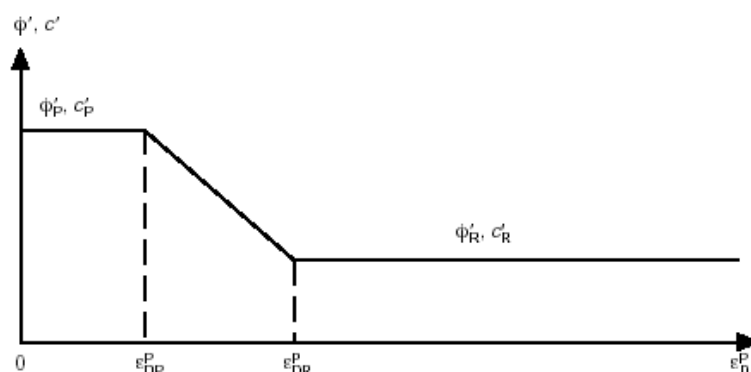


Fig. 3.3 Variation of the angle of shearing resistance ϕ' , and the cohesion intercept c' , with the deviatoric plastic strain invariant ε_D^P (Potts et al., 1990)

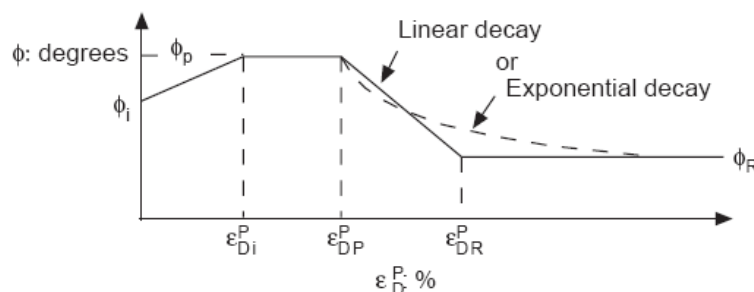


Fig. 3.4 Variation of the angle of shearing resistance with plastic deviatoric strain ε_D^P (Dounias et al., 1988 & 1996)

Based on the idea, a one-stage softening Mohr-Coulomb model can be formulated and the softening of strength parameters is shown in Fig. 3.5.

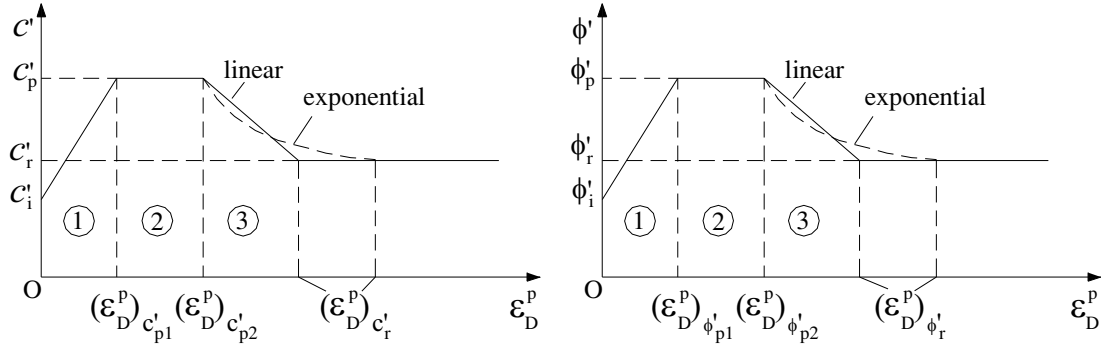


Fig. 3.5 Variations of state parameters with plastic strains

As shown in Fig. 3.5, state parameters, c' and ϕ' vary with accumulated deviatoric plastic strain, ε_D^p , which is given as

$$\varepsilon_D^p = \sqrt{\frac{2}{3}} \left[(\varepsilon_1^p - \varepsilon_2^p)^2 + (\varepsilon_2^p - \varepsilon_3^p)^2 + (\varepsilon_3^p - \varepsilon_1^p)^2 \right]^{1/2} \quad (3.37)$$

There are three zones:

- (1) In zone 1, c' and ϕ' are assumed to increase linearly from initial values, c'_i and ϕ'_i , to peak values, c'_p and ϕ'_p . This means strain hardening occurs.
- (2) In zone 2, c' and ϕ' remain constant and equal to peak values, c'_p and ϕ'_p and this implies perfect plasticity.
- (3) In zone 3, c' and ϕ' reduce from peak values, c'_p and ϕ'_p to residual values, c'_r and ϕ'_r , in a linear or exponential way. Obviously, strain softening happens.

The variation of the angle of dilation, ψ' , is assumed to be proportional to the angle of shearing resistance, ϕ' , in zones 1 and 2. This can be expressed by:

$$\psi' = \nu \phi' \quad (3.38)$$

where ν is a constant.

While in zone 3, ψ' is assumed to reduce from the peak value, ψ'_p , to a residual value ψ'_r , in the same way as ϕ' reduces.

Generally, the model requires the input parameter as follows:

- (1) Elastic parameters: E' and μ' or parameters for a nonlinear elastic model.
- (2) Plastic parameters: c'_i , c'_p , c'_r , ϕ'_i , ϕ'_p , ϕ'_r , $(\varepsilon_D^p)_{c'_{p1}}$, $(\varepsilon_D^p)_{c'_{p2}}$, $(\varepsilon_D^p)_{\phi'_{p1}}$, $(\varepsilon_D^p)_{\phi'_{p2}}$, ν and either $(\varepsilon_D^p)_{c'_r}$, $(\varepsilon_D^p)_{\phi'_r}$ for linear softening, or a_c , a_ϕ for exponential softening.

The model is quite flexible since different values of input parameters can be chosen. For example, if $c'_i = c'_p = c'_r$ and $\phi'_i = \phi'_p = \phi'_r$, it reduces to the perfectly plastic Mohr-Coulomb model mentioned previously. Likewise, if $c'_i = c'_p$ and $\phi'_i = \phi'_p$ and

$(\varepsilon_D^p)_{c_{p1}}' = (\varepsilon_D^p)_{\phi_{p1}}' = (\varepsilon_D^p)_{c_{p2}}' = (\varepsilon_D^p)_{\phi_{p2}}' = 0$, only the softening part of the model, i.e. zone 3, is activated.

Actually, hardening/softening rules can be expressed in a piecewise way because respective mathematical expressions can be assigned to the variations of c' and ϕ' with ε_D^p in the three zones.

By combining the theory presented in Section 3.2, the hardening/softening modulus, A , can be obtained as:

$$A = - \left(\frac{\partial F}{\partial c'} \frac{\partial c'}{\partial \varepsilon_D^p} + \frac{\partial F}{\partial \phi'} \frac{\partial \phi'}{\partial \varepsilon_D^p} \right) \frac{\partial P}{\partial J} \quad (3.39)$$

where

$$\frac{\partial P}{\partial J} = 1 \quad (3.40)$$

$$\frac{\partial F}{\partial c'} = - \frac{g(\theta)}{\tan \phi'} \quad (3.41)$$

$$\frac{\partial F}{\partial \phi'} = \frac{g(\theta)}{\sin^2 \phi'} \left[c' - \left(\frac{c'}{\tan \phi'} + p' \right) g(\theta) \cos \theta \cos \phi' \right] \quad (3.42)$$

The piecewise derivatives of ϕ' and c' are given as:

(1) Zone 1: linear

$$\frac{\partial \phi'}{\partial \varepsilon_D^p} = \frac{\phi_p' - \phi_i'}{(\varepsilon_D^p)_{\phi_{p1}}'} ; \quad \frac{\partial c'}{\partial \varepsilon_D^p} = \frac{c_p' - c_i'}{(\varepsilon_D^p)_{c_{p1}}'} \quad (3.43)$$

(2) Zone 2: Constant

$$\frac{\partial \phi'}{\partial \varepsilon_D^p} = 0 ; \quad \frac{\partial c'}{\partial \varepsilon_D^p} = 0 \quad (3.44)$$

(3) Zone 3:

a. Linear

$$\frac{\partial \phi'}{\partial \varepsilon_D^p} = \frac{\phi_r' - \phi_p'}{(\varepsilon_D^p)_{\phi_r'} - (\varepsilon_D^p)_{\phi_{p2}}'} \quad (3.45)$$

$$\frac{\partial c'}{\partial \varepsilon_D^p} = \frac{c_r' - c_p'}{(\varepsilon_D^p)_{c_r'} - (\varepsilon_D^p)_{c_{p2}}'} \quad (3.46)$$

b. Exponential

$$\frac{\partial \phi'}{\partial \varepsilon_D^p} = a_\phi (\phi_r' - \phi_p') \exp \left\{ -a_\phi \left[\varepsilon_D^p - (\varepsilon_D^p)_{\phi_{p2}}' \right] \right\} \quad (3.47)$$

$$\frac{\partial c'}{\partial \varepsilon_D^p} = a_c (c'_r - c'_p) \exp \left\{ -a_c \left[\varepsilon_D^p - (\varepsilon_D^p)_{c_{p2}} \right] \right\} \quad (3.48)$$

3.4.2 Other basic model parameters

The elastic parameters vary according to the following equations (Potts et al., 1990 and Dounias et al., 1988 & 1996):

$$E = E_i(1 - ABS)/(1 + BS) \quad (3.49)$$

where

$$E_i = E_0 [((p' + p_\alpha) / p_\alpha)^C + Dp'] \quad (3.50)$$

$$\mu = \{I - L \log_{10} [(p' + p_\alpha) / p_\alpha]\} \times \{1 - S\} + 0.49S \quad (3.51)$$

where E is Young's modulus, μ is Poisson's ratio, p_α is atmospheric pressure, E_0 is the initial Young's modulus at zero average stress, A , B , C , D , I and L are constants, and p' is mean effective stress. Shear stress level, S , is defined below and in Fig. 3.6. It represents the proportion of the shear strength mobilised, varying from zero at isotropic stress to unity at failure (plastic yielding). It remains at unity during strain softening.

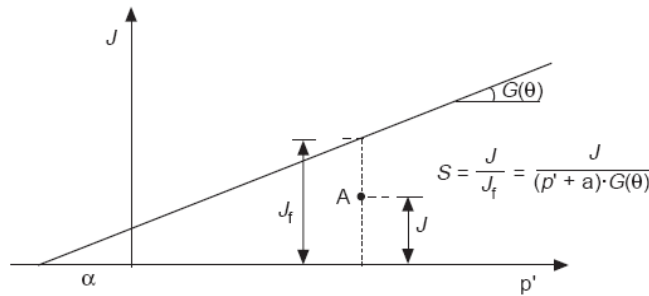


Fig. 3.6 Mohr-Coulomb yield surface on the $p' - J$ plane, definition of stress level S (Potts et al., 1990 and Dounias et al., 1988 & 1996)

Eq. (3.49) is a form of hyperbolic variation. Different values of A , B , C , D can be chosen. For example, $A = B = 0$ leads to:

$$E = E_i = E_0 [((p' + p_\alpha) / p_\alpha)^C + Dp'] \quad (3.52)$$

And $A = B = D = 0$ further gives:

$$E = E_0 ((p' + p_\alpha) / p_\alpha)^C \quad (3.53)$$

$A = B = C = D = 0$ results in a linear elastic response prior to yield which is given by:

$$E = E_i = E_0 \quad (3.54)$$

During unloading the Young's modulus is given by:

$$E_u = HE_i \quad (3.55)$$

where H is a constant and E_i is defined in Eq. (3.50).

The model obeys Mohr-Coulomb yield criterion and the yield function is defined as:

$$F(\{\sigma'\}, \{k\}) = S - 1 \quad (3.56)$$

and

$$S = J / [(p' + \alpha)G(\theta)] \quad (3.57)$$

where $G(\theta)$ is the same as $g(\theta)$ which has been defined in Eq. (3.20); p' , J and θ are presented in Appendix I. ; and α is the intercept of the yield surface on the p' axis (Fig. 3.6) and is given by:

$$\alpha = c' / G(\theta = 0) = c' / \sin \phi' \quad (3.58)$$

where c' is the cohesion intercept with Lode angle $\theta = 0$, i.e. $\sigma_2' = (\sigma_1' + \sigma_3')/2$. Since α is kept constant, c' varies with Lode angle and the intermediate principal stress to a limited extent.

For the associated conditions, the plastic potential can be also defined by Eq. (3.56) and Eq. (3.57) but with the angle of shearing resistance, ϕ' , replaced by the angle of dilation, ψ' , i.e. $\phi' = \psi'$. This results in:

$$P(\{\sigma'\}, \{m\}) = J / [(p' + \alpha) \frac{\sin \psi'}{\cos \theta + \frac{\sin \theta \sin \psi'}{\sqrt{3}}}] - 1 = 0 \quad (3.59)$$

For the non-associated conditions, $\phi' \neq \psi'$ and usually $\psi' < \phi'$.

This model has been incorporated into numerical programs such as finite element program—*ICFEP* developed by Imperial College. This program with this model has been used to predict progressive failure. The most representative cases are analyses of progressive failure of Carsington dam (Potts et al., 1990), the delayed collapse of cut slopes in stiff clays (Potts et al., 1997) and a landslide in clays with strain-softening behaviour (Troncone, 2005).

Also, Cividini and Gioda (1992) used the model to simulate direct shear test in stiff clays; Sterpi (2000) performed numerical modelling of a plain strain test and stability of a cantilever sheet wall; Sterpi (1999), Schuller and Schweiger (2002) and Sterpi and Cividini (2004) analysed stability of tunneling excavation with the same one-stage softening model; and Alonso et al. (2003) and Guan et al. (2007) applied this model to cavity excavation in order to predict the ground reaction in tunneling excavation in soils and rocks exhibiting strain-softening behaviour.

3.5 Two-stage softening model

3.5.1 General concept of two-stage strength parameter softening

Potts et al. (1987, 1990 and 1997) and Dounias et al. (1988 and 1996) used a generalised non-linear strain-softening soil model shown in Fig. 3.3 and Fig. 3.4 with

linear or exponential decay of strength parameters, which only indicates one-stage post-peak softening behaviour but not two-stage characteristics.

In the analysis of Potts et al. (1990), the cohesion and friction angle soften with same rate. However, as demonstrated in Section 2.4.3, the softening rates of cohesion and friction angle for stiff clays are different in the two-stage softening model and have more physical meaning. For stiff overconsolidated clays, the branch of $\tau - \sigma$ curve between peak strength and residual strength should be considered as bilinear owing to the existence of the characteristic post-rupture strength. This should be taken into account while simulating the behaviour of stiff clays. Therefore, for stiff clays with well-defined post-rupture strength, a modified bilinear model should be established.

The general concept of this kind of model can be offered in Fig. 3.7 and is similar to that presented by Alonso et al. (2003). For both friction angle and cohesion, the model is similar, but the slopes of bilinear section will be different and depend on index properties of stiff clays.

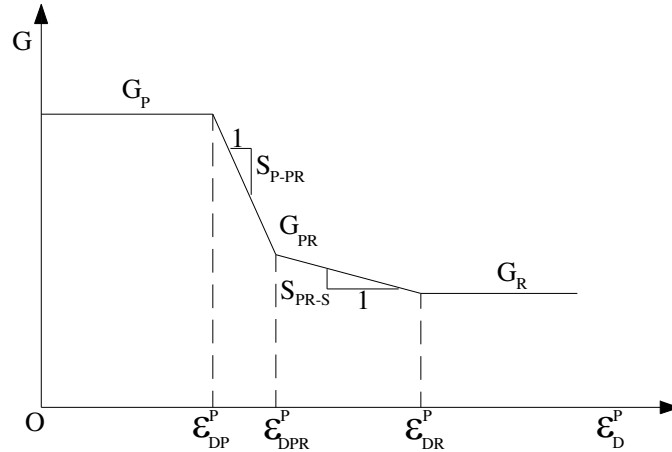


Fig. 3.7 Conceptual two-stage post-peak softening model for stiff clays

The generalised two-stage post-peak model can be defined mathematically as below:

$$G(\varepsilon_D^P) = \begin{cases} G_P & , \quad \varepsilon_D^P \leq \varepsilon_{DP}^P \\ G_P - S_{P-PR}(\varepsilon_D^P - \varepsilon_{DP}^P) & , \quad \varepsilon_{DP}^P < \varepsilon_D^P \leq \varepsilon_{DPR}^P \\ G_{PR} - S_{PR-S}(\varepsilon_D^P - \varepsilon_{DPR}^P) & , \quad \varepsilon_{DPR}^P < \varepsilon_D^P \leq \varepsilon_{DR}^P \\ G_R & , \quad \varepsilon_D^P > \varepsilon_{DR}^P \end{cases} \quad (3.60)$$

where $G(\varepsilon_D^P)$ represents friction angle of shearing resistance, ϕ , or cohesion, c ; it is a segmented function of deviatoric plastic strain invariant ε_D^P ; G_P , G_{PR} and G_R are peak, post-rupture and residual values; ε_{DP}^P , ε_{DPR}^P and ε_{DR}^P are peak, post-rupture and residual values of deviatoric plastic strain invariant; S_{P-PR} and S_{PR-S} are positive slopes for the segment from peak point to post-rupture point and the segment from post-rupture point to residual point respectively. They represent the strain-softening rates at different stages.

G_P , G_{PR} , G_R , S_{P-PR} and S_{PR-S} are all associated with specific properties of stiff overconsolidated clays and can be determined by laboratory tests.

3.5.2 Detailed two-stage softening of frictional angle and cohesion

As presented in Section 2.4.3, the developments of frictional angle and cohesion in the two post-peak stages are different. So it is necessary to establish distinct models for cohesion and friction angle (shown in Fig. 3.8).

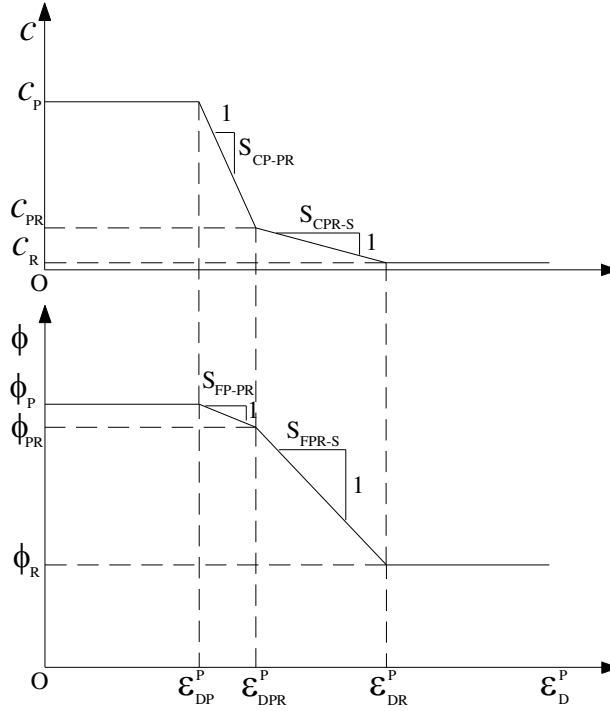


Fig. 3.8 Distinct two-stage models for frictional angle and cohesion

The model for cohesion can be defined as below:

$$c(\varepsilon_D^P) = \begin{cases} C_P & , \quad \varepsilon_D^P \leq \varepsilon_{DP}^P \\ C_P - S_{CP-PR}(\varepsilon_D^P - \varepsilon_{DP}^P) & , \quad \varepsilon_{DP}^P < \varepsilon_D^P \leq \varepsilon_{DPR}^P \\ C_{PR} - S_{CPR-S}(\varepsilon_D^P - \varepsilon_{DPR}^P) & , \quad \varepsilon_{DPR}^P < \varepsilon_D^P \leq \varepsilon_{DR}^P \\ C_R & , \quad \varepsilon_D^P > \varepsilon_{DR}^P \end{cases} \quad (3.61)$$

where $c(\varepsilon_D^P)$ represents cohesion c , it is a segmented function of deviatoric plastic strain invariant ε_D^P ; C_P , C_{PR} and C_R are peak, post-rupture and residual values respectively; ε_{DP}^P , ε_{DPR}^P and ε_{DR}^P are peak, post-rupture and residual values of deviatoric plastic strain invariant; S_{CP-PR} and S_{CPR-S} are positive slopes for the segment from peak to post-rupture and the segment from post-rupture to residual respectively.

The model for friction angle can be similarly defined as below:

$$\phi(\varepsilon_D^P) = \begin{cases} \phi_P & , \quad \varepsilon_D^P \leq \varepsilon_{DP}^P \\ \phi_P - S_{FP-PR}(\varepsilon_D^P - \varepsilon_{DP}^P) & , \quad \varepsilon_{DP}^P < \varepsilon_D^P \leq \varepsilon_{DPR}^P \\ \phi_{PR} - S_{FPR-S}(\varepsilon_D^P - \varepsilon_{DPR}^P) & , \quad \varepsilon_{DPR}^P < \varepsilon_D^P \leq \varepsilon_{DR}^P \\ \phi_R & , \quad \varepsilon_D^P > \varepsilon_{DR}^P \end{cases} \quad (3.62)$$

where $\phi(\varepsilon_D^P)$ represents friction angle ϕ , it is a piecewise function of deviatoric plastic strain invariant ε_D^P ; ϕ_P , ϕ_{PR} and ϕ_R are peak, post-rupture and residual value; ε_{DP}^P , ε_{DPR}^P and ε_{DR}^P are peak, post-rupture and residual values of deviatoric plastic strain invariant; S_{FP-PR} and S_{FPR-S} are positive slopes individually for the segment from peak state to post-rupture state and the segment from post-rupture state to residual state respectively.

3.5.3 Formulation of the new model

The formulation of the new model can be performed on the basis of the generalised non-linear strain-softening and strain-hardening model incorporating Mohr-Coulomb yield criterion discussed in Section 3.4.

3.5.3.1 General description of two-stage softening of strength parameters

The modified model can be shown in Fig. 3.9 and Fig. 3.10 according to Section 3.4.

As shown in Fig. 3.9, state parameters, c' and ϕ' , vary with accumulated deviatoric plastic strain, ε_D^P . There are four zones. The first two zones are the same as those described in Section 3.4.

- (1) In zone 3, c' and ϕ' reduce from peak values, c'_p and ϕ'_p to post-rupture values, c'_{pr} and ϕ'_{pr} , in a linear way. Obviously, this is the first stage of strain softening.
- (2) In zone 4, c' and ϕ' reduce from post-rupture values, c'_{pr} and ϕ'_{pr} , to residual values, c'_r and ϕ'_r , in a linear way. This corresponds to the second stage of strain softening.

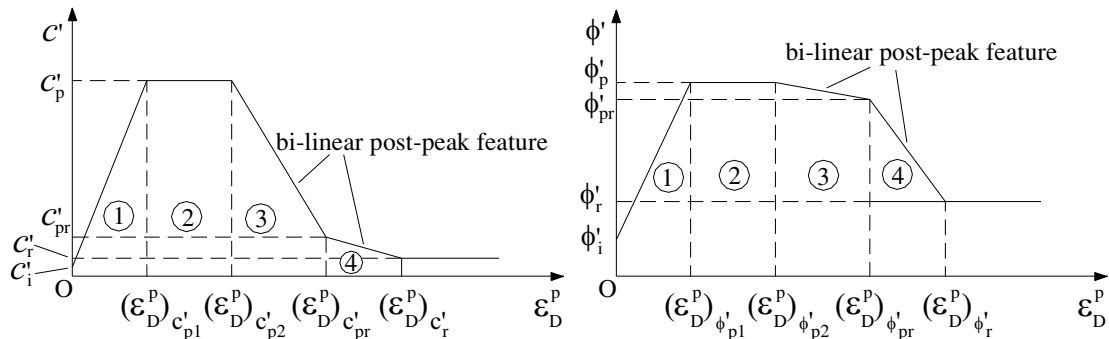


Fig. 3.9 Variations of state parameters with plastic strains

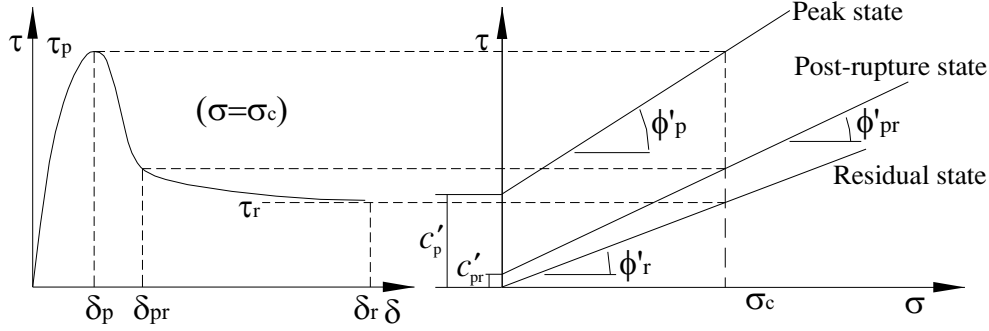


Fig. 3.10 Schematic $\tau - \delta$ curve and variations of state parameters in $\tau - \sigma'$ plane

The variation of the angle of dilation, ψ' , is assumed to be the same as that depicted in Section 3.4 in zones 1 and 2.

In zone 3, ψ' is assumed to reduce from the peak value, ψ'_p , to a post-rupture value ψ'_{pr} , in the same way as ϕ' reduces.

In zone 4, ψ' is assumed to reduce from the post-rupture value, ψ'_{pr} , to a residual value ψ'_r , in the same way as ϕ' reduces.

Generally, the model requires the following input parameters:

- (1) Elastic parameters: E' and μ' or parameters for a nonlinear elastic model.
- (2) Plastic parameters: $c'_i, c'_p, c'_r, c'_{pr}, \phi'_i, \phi'_p, \phi'_{pr}, \phi'_r, (\varepsilon_D^P)_{c'_{p1}}, (\varepsilon_D^P)_{c'_{p2}}, (\varepsilon_D^P)_{\phi'_{p1}}, (\varepsilon_D^P)_{\phi'_{p2}}, \nu$ and $(\varepsilon_D^P)_{c'_{pr}}, (\varepsilon_D^P)_{\phi'_{pr}}, (\varepsilon_D^P)_{c'_r}, (\varepsilon_D^P)_{\phi'_r}$ for bi-linear softening.

Similar to the original model in Section 3.4, the modified model is also flexible since different values of input parameters can be chosen. Here again, if $c'_i = c'_p = c'_r$ and $\phi'_i = \phi'_p = \phi'_r$, it reduces to the perfectly plastic Mohr-Coulomb model. Likewise, if $c'_i = c'_p$ and $\phi'_i = \phi'_p$ and $(\varepsilon_D^P)_{c'_{p1}} = (\varepsilon_D^P)_{\phi'_{p1}} = (\varepsilon_D^P)_{c'_{p2}} = (\varepsilon_D^P)_{\phi'_{p2}} = 0$, only the softening parts of the model, i.e. zone 3 and zone 4, are activated.

The hardening/softening modulus, A , can also be calculated by Eq. (3.39).

The hardening/softening rules can be also expressed in a piecewise way because different mathematical expressions can be assigned to the variations of c' and ϕ' with ε_D^P in the three zones.

The piecewise derivatives of ϕ' and c' are given as:

- (1) Zone 1: linear

$$\frac{\partial \phi'}{\partial \varepsilon_D^P} = \frac{\phi'_p - \phi'_i}{(\varepsilon_D^P)_{\phi'_{p1}}} ; \quad \frac{\partial c'}{\partial \varepsilon_D^P} = \frac{c'_p - c'_i}{(\varepsilon_D^P)_{c'_{p1}}} \quad (3.63)$$

- (2) Zone 2: Constant

$$\frac{\partial \phi'}{\partial \varepsilon_D^p} = 0 ; \quad \frac{\partial c'}{\partial \varepsilon_D^p} = 0 \quad (3.64)$$

(3) Zone 3: Linear

$$\frac{\partial \phi'}{\partial \varepsilon_D^p} = \frac{\phi'_{pr} - \phi'_p}{(\varepsilon_D^p)_{\phi'_{pr}} - (\varepsilon_D^p)_{\phi'_p}} \quad (3.65)$$

$$\frac{\partial c'}{\partial \varepsilon_D^p} = \frac{c'_{pr} - c'_p}{(\varepsilon_D^p)_{c'_{pr}} - (\varepsilon_D^p)_{c'_p}} \quad (3.66)$$

(4) Zone 4: Linear

$$\frac{\partial \phi'}{\partial \varepsilon_D^p} = \frac{\phi'_r - \phi'_{pr}}{(\varepsilon_D^p)_{\phi'_r} - (\varepsilon_D^p)_{\phi'_{pr}}} \quad (3.67)$$

$$\frac{\partial c'}{\partial \varepsilon_D^p} = \frac{c'_r - c'_{pr}}{(\varepsilon_D^p)_{c'_r} - (\varepsilon_D^p)_{c'_{pr}}} \quad (3.68)$$

3.5.3.2 Elastoplastic description of modified two-stage softening model

3.5.3.2.1 Elastic response and parameters

As mentioned in Section 3.4, for the elastic part, the following parameters are needed to determine E (Young's modulus) and μ (Poisson's ratio):

- (1) p_α —atmospheric pressure
- (2) A, B, C, D, I and L —5 constants
- (3) H —unloading constant to determine unloading Young's modulus.
- (4) S —shear stress level, which is defined by Eq. (3.57). It represents the proportion of the shear strength mobilised, varying from zero at isotropic stress to unity at failure (plastic yielding). It remains at unity during strain softening.

3.5.3.2.2 Yield function

The model obeys Mohr-Coulomb yield criterion and the yield function is defined as:

$$F(\{\sigma'\}, \{k\}) = J / [(p' + \alpha)G(\theta)] - 1 \quad (3.69)$$

where $G(\theta)$ is the same as $g(\theta)$ which has been defined in Eq. (3.20); p', J and θ are presented in Appendix I; and α is the intercept of the yield surface on the p' axis (Fig. 3.6) and is given by Eq. (3.58).

3.5.3.2.3 Plastic potential function

For associated conditions, the plastic potential can be also defined by Eq. (3.69) but with the angle of shearing resistance, ϕ' , replaced by the angle of dilation, ψ' , i.e. $\phi' = \psi'$:

$$P(\{\sigma'\}, \{m\}) = J / [(p' + \alpha) \frac{\sin \psi'}{\cos \theta + \frac{\sin \theta \sin \psi'}{\sqrt{3}}}] - 1 = 0 \quad (3.70)$$

For non-associated conditions, $\phi' \neq \psi'$ and usually $\psi' < \phi'$.

3.5.3.2.4 Hardening and softening rules

Hardening and softening behaviour is introduced by allowing the angle of shearing resistance, ϕ' and the cohesion intercept, c' , to vary with the deviatoric plastic strain invariant, ε_D^P , as described in Section 3.5.3.1 and shown in Fig. 3.9 and Fig. 3.10.

The angle of dilation may also be varied with ε_D^P as described in Section 3.5.3.1.

3.5.3.2.5 Plastic model parameters

Generally, the plastic model requires the following input parameters:

- (1) $c'_i, c'_p, c'_r, c'_{pr}$;
- (2) $\phi'_i, \phi'_p, \phi'_{pr}, \phi'_r$;
- (3) $(\varepsilon_D^P)_{c'_{p1}}, (\varepsilon_D^P)_{c'_{p2}}, (\varepsilon_D^P)_{\phi'_{p1}}, (\varepsilon_D^P)_{\phi'_{p2}}$;
- (4) ν ;
- (5) $(\varepsilon_D^P)_{c'_{pr}}, (\varepsilon_D^P)_{\phi'_{pr}}, (\varepsilon_D^P)_{c'_r}, (\varepsilon_D^P)_{\phi'_r}$ for bi-linear softening.

In this work, only softening parts, i.e. zone 3 and zone 4 are activated because the two-stage post-peak softening is the main research aim. This means that $c'_i = c'_p$, $\phi'_i = \phi'_p$ and $(\varepsilon_D^P)_{c'_{p1}} = (\varepsilon_D^P)_{c'_{p2}} = (\varepsilon_D^P)_{\phi'_{p1}} = (\varepsilon_D^P)_{\phi'_{p2}} = \varepsilon_{DP}^P$. Meanwhile, it is assumed that $(\varepsilon_D^P)_{c'_{pr}} = (\varepsilon_D^P)_{\phi'_{pr}} = \varepsilon_{DPR}^P$ and $(\varepsilon_D^P)_{c'_r} = (\varepsilon_D^P)_{\phi'_r} = \varepsilon_{DR}^P$. In addition, as stated in Section 2.4.4.1, the $\tau - \delta$ relation is nearly linear elastic for stiff overconsolidated clays. So only the linear elastic response is considered and only E and μ are needed for the model. Thus with these simplified conditions, only 12 parameters ($E, \mu, c'_p, c'_r, c'_{pr}, \phi'_p, \phi'_{pr}, \phi'_r, \nu, \varepsilon_{DPR}^P, \varepsilon_{DP}^P$ and ε_{DR}^P) are necessary to define the new model.

3.5.4 Determination and calibration of model parameters

3.5.4.1 Comprehensive methods

It is well known that the reasonable determination of model parameters for stiff clays is not always easy. The best way is to conduct comprehensive tests on the geotechnical properties of stiff clays just as presented by Alonso & Gens (2006a)

through basic identification, mineralogy and structure examination, such as X-ray diffraction tests and scanning electronic microscope observation, direct shear tests, ring shear tests, unconfined compression and triaxial tests, odometer tests and in-situ field investigation. However, these methods are not always available in geotechnical engineering.

3.5.4.2 Determination of elastic parameters

As implied in Section 3.4, the elastic parameters E and μ are stress dependent. This can be implemented into numerical programs such as *FLAC*. As stated by Potts et al. (1997) and Chen et al. (1992), E is normally a function of mean effective stress p' .

Although stiff soils exhibit nonlinear behaviour before peak, here a linear elastic response is assumed and, therefore, $A = B = C = D = 0$. In this case, the elastic parameters E and μ can be derived, as a suitable average, from the shear stress vs. shear strain or displacement curves obtained from laboratory tests such as triaxial or direct shear tests.

For example, Carter and Yeung (1985) explained the methods of parameter determination for one-stage strain-softening model. Results of triaxial compression tests are often represented as plots of deviator stress $\sigma_1 - \sigma_3$ versus axial strain ε_1 and volumetric strain $v = \varepsilon_1 + 2\varepsilon_3$ versus axial strain ε_1 . These plots allow values of the elastic properties K, G or E, μ to be determined from the initial slopes of the curves.

Wood (1990) also described the detailed procedure to get elastic model parameters.

3.5.4.3 Determination of shear strength parameters of stiff clays

The most general test methods to determine strength parameters are the direct shear test and the triaxial test (Skempton and Petley, 1967; Skempton, 1985; Bishop et al., 1960 and 1965; Bishop, 1971; Chandler and Skempton, 1974; Chandler, 1966; Kenney, 1977; Lupini et al., 1981; Leroueil, 2001; Stark & Eid, 1994 and 1997; Tika et al., 1996; Mesri & Shahien, 2003; Burland, 1990; Burland et al. 1996; Georgiannou and Burland, 2001 and 2006; Alonso & Gens, 2006a).

The strength parameters— c' and ϕ' can be determined from the Mohr circle plots corresponding to the actual conditions of soil samples such as peak and residual states from a series of tests (Carter & Yeung, 1985). This can also be seen in Fig. 2.23.

The average peak strength envelope is usually adopted to derive the corresponding parameters in view of the dependency of peak strength on confining pressure.

In contrast, the residual strength is relatively uninfluenced by confining pressure and normally unique parameters are obtained. It should be noted that both the ring shear test and the direct shear test yield residual strength parameters. When very large deformations are involved, the values for residual strength from ring shear test should be adopted because it normally yields lower values than direct shear test because of the greater extent of shearing of specimen at the end of the tests. In addition, the residual friction angle could also be evaluated directly from residual stress ratio τ/σ assuming that no residual cohesion exists.

As far as post-rupture strength is concerned, both shear tests and triaxial tests could be used to determine the relevant strength parameters (Alonso & Gens, 2006a; Burland,

1990; Burland et al., 1996; and Georgiannou & Burland, 2001 and 2006). The critical-state strength provides a good reference for the post-rupture strength. Sometimes strength values obtained from tests with small displacement along fissures may be taken as the approximation of those for post-rupture strength.

However, sometimes the strength parameters are unavailable and back analysis is an alternative method to derive the practical strength parameters. For example, Cividini and Gioda (1992) presented a detailed procedure to determine model parameters such as the elastic modulus and peak strength parameters through back analysis of three series of test data at peak state.

The dilation angle can be obtained from volumetric strain versus axial strain curve. The concrete numerical procedure of this method has been illustrated by Wood (1990).

3.5.4.4 Determination of deviatoric plastic strains— ε_{DPR}^P , ε_{DP}^P and ε_{DR}^P

Potts et al. (1990) pointed out that the rate at which strength drops from peak to residual with strain or displacement is also an important factor while evaluating stability problems in geotechnical engineering. Two numerical cases with different rates have been assumed to demonstrate the post-peak decrease of friction angle with plastic strain in yellow clay based on direct shear box test data. They found that decreasing the rate at which the yellow clay softens with post-peak plastic strain decreases the amount of progressive failure and increases stability. Therefore it is obvious that the decreasing rate from peak state to residual state has influence on slope stability.

By analogy with this view, the decreasing rates from peak state to post-rupture state and from post-rupture state to residual state are likewise important while analysing stability problems involving stiff clays in geotechnical engineering. Thus different strain-softening rates at different stages for the same strength parameters will induce different effects on the geotechnical problems.

Carter and Yeung (1985) described a method to determine ε_{DR}^P . They stated that the rate of dilation can be determined from the $v-\varepsilon$ curve and the onset of the residual condition can usually be determined from these plots if during testing straining is allowed to continue for long enough beyond the peak condition. From this an estimate can be made of ε_1 and ε_3 at the residual condition and hence plastic shear strain at the onset of residual state $\varepsilon_{DR}^P = \varepsilon_1^P - \varepsilon_3^P$ can be calculated.

Troncone (2005) determined the relevant threshold values of ε_{DP}^P and ε_{DR}^P for one-stage strain-softening model directly from shear stress vs. axial strain curve obtained from triaxial tests. He mentioned that the deviatoric plastic strain is close to the plastic axial strain when the soil dilatancy angle is nil (Troncone, 2004). In his analysis, ε_{DP}^P was set to zero.

Cividini and Gioda (1992) also proposed a method to calibrate the threshold values of deviatoric plastic strains via back analysis. Firstly, they performed some numerical calculations by changing these values. Then the threshold values were chosen so that the numerical results of horizontal displacements at peak and fully softened states approximate the corresponding values obtained from experimental data.

In the numerical modelling of progressive failure of Carsington dam, Potts et al. (1990) and Chen et al. (1992) obtained the softening parameters by fitting the shear stress versus shear strain curves. It is described in detail in Appendix III.

In this thesis, the method used by Potts et al. (1990) and Chen et al. (1992) is followed by making use of shear stress (τ) versus shear displacement (δ) curve obtained from direct shear test. As seen in Fig. 2.20, the difference between δ_p and δ_{pr} or δ_f or δ_r , divided by the height of specimen can be thought to be the approximate threshold value of deviatoric plastic strain.

In summary, ε_{DPR}^P , ε_{DP}^P and ε_{DR}^P can be derived from triaxial test, direct shear test or back analysis.

3.6 Implementation of two-stage softening model

3.6.1 Introduction

The new two-stage softening constitutive model should be encoded into a numerical program. In this work, the explicit finite difference code—*FLAC* (Fast Lagrangian Analysis of Continua) is utilised because less effort is likely to be required to develop a user-defined strain-softening model on the basis of its built-in strain hardening/softening model in *FLAC* and its capability of writing constitutive models via *FISH* and C++. Details can be found in *Itasca FLAC Manual* (2005).

3.6.2 Built-in strain hardening/softening model in *FLAC*

3.6.2.1 Introduction

This model is based on the *FLAC* Mohr-Coulomb model with non-associated shear and associated tension flow rules. The model allows the possibility that cohesion, friction, dilation and tensile strength may harden or soften after the onset of plastic yield. In the Mohr-Coulomb model, those properties are assumed to remain constant. Here, the user can define the cohesion, friction and dilation as piecewise-linear functions of a hardening parameter based on the plastic shear strain. A piecewise-linear softening law for the tensile strength can also be prescribed in terms of another hardening parameter measuring the plastic tensile strain. This gives a quite flexible method to control the softening parameters. Different functions of the strength softening parameters can be approximated by some piecewise-linear sections. At each time step the total plastic shear and tensile strains are calculated by incrementing the hardening parameters and then the model properties are changed accordingly via the user-defined softening functions.

The yield and potential functions, plastic flow rules and stress corrections are identical to those of the Mohr-Coulomb model.

The built-in strain hardening/softening model in *FLAC* has been widely used to simulate geotechnical engineering problems involving softening of soils and rocks (Sabzalisenjani, 1998; Collotta et al., 1999; Kwasniewski and Wang, 1999; Vinkler and Piguet, 1999; Barla et al., 2001; Dolezalová et al., 2001; Hammoud and Schafll,

2001; Yavuz et al., 2001; Alonso et al., 2003; Badr et al., 2003; Brummeq et al., 2003; Laigle, 2003; Laigle and Saitta, 2003; Souley et al., 2003; Guan et al., 2007).

3.6.2.2 Hardening/Softening Parameters

In *FLAC*, plastic shear strain is measured by the shear hardening parameter e^{ps} , whose incremental form is defined as (see Eq. 6.4 in Vermeer and de Borst, 1984)

$$\Delta e^{ps} = \left\{ \frac{1}{2} (\Delta e_1^{ps} - \Delta e_m^{ps})^2 + \frac{1}{2} (\Delta e_m^{ps})^2 + \frac{1}{2} (\Delta e_3^{ps} - \Delta e_m^{ps})^2 \right\}^{\frac{1}{2}} \quad (3.71)$$

where

$$\Delta e_m^{ps} = \frac{1}{3} (\Delta e_1^{ps} + \Delta e_3^{ps}) \quad (3.72)$$

and Δe_j^{ps} , $j = 1, 3$ are the principal plastic shear strain increments.

It can be noted that Δe^{ps} is different from the incremental form of ε_D^p defined by Eq. (3.37). After some manipulation, it can be derived that

$$\Delta e^{ps} = \frac{1}{2} \Delta \varepsilon_D^p \quad (3.73)$$

Attention should be paid to this relationship while determining the threshold values of plastic shear strains in *FLAC* which are only half of those conventional values used in *FEM* with Eq. (3.37) or obtained from conventional laboratory tests such as triaxial and direct shear tests (Alonso et al., 2003).

The tensile hardening parameter e^{pt} measures the accumulated tensile plastic strain and its increment is defined as

$$\Delta e^{pt} = \Delta e_3^{pt} \quad (3.74)$$

where Δe_3^{pt} is the increment of tensile plastic strain in the direction of the major principal stress (in *FLAC* tensile stresses are positive).

The term Δe_3^{ps} is defined as

$$\Delta e_i^{ps} = \lambda^s \frac{\partial g^s}{\partial \sigma_i} \quad i = 1, 3 \quad (3.75)$$

where g^s is the shear potential function and has the form

$$g^s = \sigma_1 - \sigma_3 N_\psi \quad (3.76)$$

where ψ is the dilation angle and

$$N_\psi = \frac{1 + \sin \psi}{1 - \sin \psi} \quad (3.77)$$

The added superscript, s , denotes that the plastic strain is related to the shear yield surface. Note that Δe_i^{ps} are plastic principal strain increments, not shear strain increments.

Similarly, the term Δe_i^{pt} is defined as

$$\Delta e_i^{pt} = \lambda^t \frac{\partial g^t}{\partial \sigma_i} \quad i=1,3 \quad (3.78)$$

where the superscript t denotes that the plastic strain is related to the tensile yield surface and g^t is the tensile potential function which is defined as

$$g^t = -\sigma_3 \quad (3.79)$$

3.6.2.3 User-defined functions for strength parameters

A simplified one-dimensional stress-strain curve, e.g. $\sigma - e$ curve, which softens upon yield and attains some residual strength, is shown in Fig. 3.11. The curve is linear to the point of yield; in that range, the strain is elastic only: $e = e^e$. After yield, the total strain is composed of elastic and plastic parts: $e = e^e + e^p$. In the softening/hardening model, the user defines the cohesion, friction, dilation and tensile strength variance as a function of the plastic portion, e^p , of the total strain. Some sketches of these functions are drawn in Fig. 3.12 and may be approximated in *FLAC* as sets of linear segments (see Fig. 3.13).

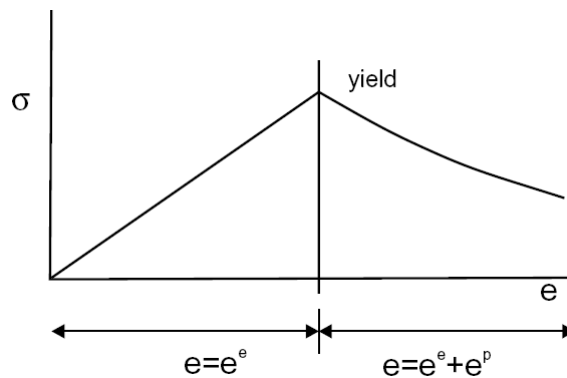


Fig. 3.11 Simplified one-dimensional stress-strain curve

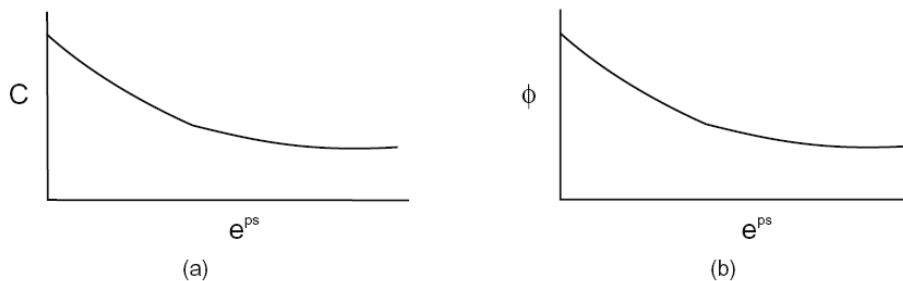


Fig. 3.12 Variation of (a) cohesion and (b) friction angle with plastic strain

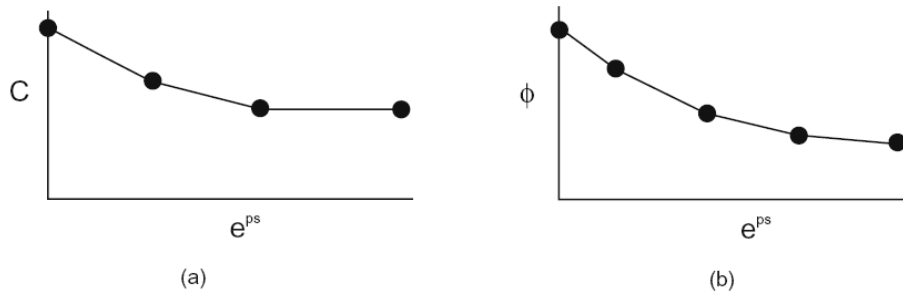


Fig. 3.13 Piece-wise linear approximation of variation of (a) cohesion and (b) friction angle with plastic strain

Hardening and softening variations for the cohesion, friction and dilation in terms of the shear parameter e^{ps} (see Eq. (3.71)) are provided by the user in the form of look-up tables. Each table contains pairs of values: one for the parameter and one for the corresponding property value. It is assumed that the property varies linearly between two consecutive parameter entries in the table. Softening of the tensile strength is described in a similar manner using the parameter e^{pt} (see Eq. (3.74)).

An example of piece-wise linear definition of softening properties with *FLAC* is given in Table 3.1. Here, the friction function is defined in table 1, the cohesion in table 2, the dilation in table 3 and the tensile strength in table 4. Note that the initial friction, cohesion, dilation and tensile strength must be defined (here, to be 40°, 20 MPa, 10° and 15 MPa, respectively). Each function consists of two linear segments, as shown in Fig. 3.14. The values remain constant for plastic strains greater than the last table value.

Similarly, the two-stage post-peak softening of stiff clays involving post-rupture strength comprises three linear segments as shown in Fig. 3.7, Fig. 3.8 and Fig. 3.9. This two-stage softening model can be expressed by a three-segment look-up table.

Table 3.1 Example of piece-wise linear definition of softening properties

```

model ss
prop s=11.5e9 b=8.62e9 d=2000 ftab=1 ctab=2 dtab=3 ttab=4
prop fric=40 coh=20e6 dil=10 ten=15e6
table 1 0, 40 .01, 30
table 2 0, 20e6 .01, 10e6
table 3 0, 10 .01, 5
table 4 0, 15e6 .01, 0.0

```

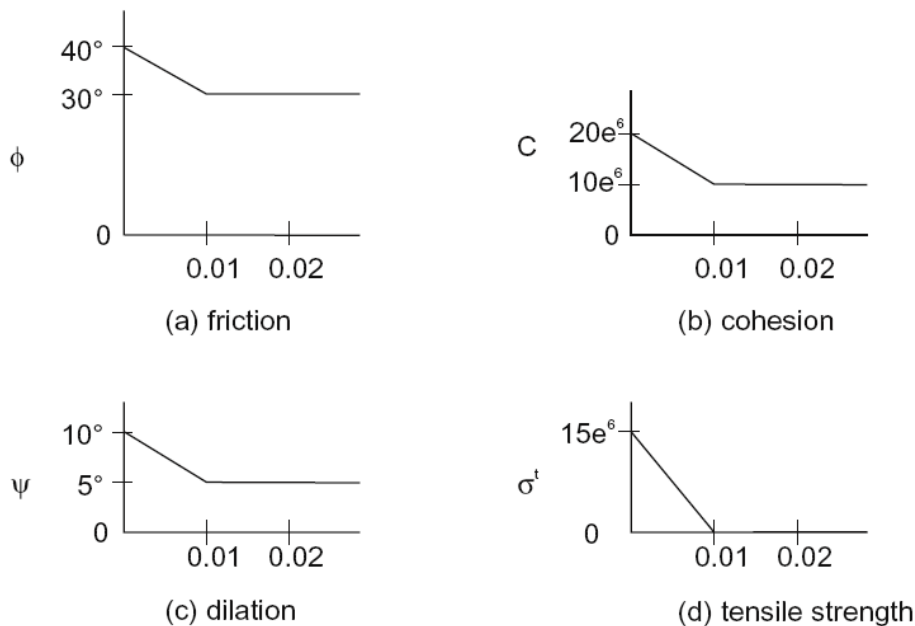


Fig. 3.14 (a) Friction (b) cohesion (c) dilation (d) tensile strength defined by two linear segments

Obviously, hardening behaviour for the cohesion, friction and dilation can be also easily produced by an increase in these properties with increasing plastic strain.

3.6.3 Implementation of two-stage softening model into *FLAC*

This section will present three methods to implement the two-stage softening model described in section 3.5 into *FLAC*:

- (1) the combination of built-in softening model and *FISH* functions;
- (2) use of *FISH* to write the two-stage softening model;
- (3) use of C++ to write the two-stage softening model.

3.6.3.1 Implementation procedure of hardening/softening model

Before discussing these three methods, it is necessary to illustrate the procedure to implement the hardening/softening model.

In the implementation of the strain-hardening/softening model, new stresses for the step are computed using the current values of the model properties. Plastic shear and tensile strain increments are evaluated from Eq. (3.75) and Eq. (3.78). Hardening increments are calculated as the surface average of values obtained from Eq. (3.71) and Eq. (3.74) for all triangles involved in the zone. The hardening parameters are updated and new model properties are evaluated by linear interpolation in the tables. These properties are stored for use in the next step. The hardening or softening of strength parameters lags one time step behind the corresponding plastic deformation. In an explicit code, this error is small because the steps are small.

3.6.3.2 Combination of *FISH* and built-in model

With this method, the elastic modulus, permeability and other parameters can vary using specific functions. The *FISH* function with *WHILE_STEPPING* statement will update these parameters automatically at the start of every *FLAC* step. However, the

use of *WHILE_STEPPING* will slow the calculation speed. This method is illustrated in Table 3.2.

Table 3.2 *FISH* function combined with built-in model

```

model ss
...
def updateEGK
  while_stepping
  loop i(1,izones)
    loop j(1,jzones)
      s1=-sxx(i,j)
      s2=-syy(i,j)
      s3=-szz(i,j)
      pv=(s1+s2+s3)/3.0
      puv=pp(i,j)
      pev=pv-puv
      youngv=2.5e4*(pev/1000.0+100)
      if youngv<4e6
        youngv=4e6
      endif
      bulkupv=youngv/3.0/(1-2*mu)
      shearupv=youngv/2.0/(1+mu)
      bulk_mod(i,j)=bulkupv
      shear_mod(i,j)=shearupv
    ...
  endloop
endloop
end
...

```

3.6.3.3 Two-stage softening model written with *FISH*

Based on the original MC softening model, the modified model is written with *FISH*. This model can not only update the model parameters such as elastic stiffness and permeability, which are stress dependent, but also includes coupling with thermal process. This model can be used in *FLAC* with the command **CALL usersoftmodel.fis**.

User-written *FISH* models execute more slowly than built-in models. After optimization, a *FISH* model will typically run somewhere between one-quarter and one-third the speed of a built-in model.

3.6.3.4 Two-stage softening model written with C++

The C++ softening model is set up by defining a derived class of constitutive model with private variables for model properties and class functions for model calculation (shown in Table 3.3 and Table 3.4). The main calculation process is manipulated in the **RUN** function.

This model has the same function as that written in *FISH*, whereas the C++ model has nearly the same speed as built-in models and it is noticeably faster than *FISH* constitutive models.

Table 3.3 Derived softening model class

```
class UserStrainSofteningModel : public ConstitutiveModel {
public:
...
virtual const char **Properties(void) const;
virtual const char **States(void) const;
virtual double GetProperty(unsigned ul) const;
virtual double ConfinedModulus(void) const { return(dBulk + d4d3*dShear); }
virtual double ShearModulus(void) const { return(dShear); }
virtual double BulkModulus(void) const { return(dBulk); }
virtual double SafetyFactor(void) const { return(10.0); }
// Manipulators
virtual void SetProperty(unsigned ul,const double &dVal);
//Initilise and Run
virtual const char *Initialise(unsigned uDim,State *ps);
virtual const char *Run(unsigned uDim,State *pst);
//Save Restore
virtual const char *SaveRestore(ModelSaveObject *mso);
private:
//properties
double dBulk,dShear,dYoung,dPoisson,dCohesion,dFriction,dDilation,dPerm,dMb,dPerm0;
double dTension,dSHP,dTHP;
int iCTab,iFTab,iDTab,iTTab;
//utility members for ease of calculation
double dE1,dE2,dG2,dNPH,dCSN,dSC1,dSC2,dSC3,dSF1,dSF3,dBisc;
unsigned uiCTab,uiFTab,uiDTab,uiTTab;
};
```

Table 3.4 Run class function

```
const char *UserStrainSofteningModel::Run(unsigned ulDim,State *ps)
{
...
//-----bulk and shear Stress dependence----
  m_p1=-(ps->stnS.d11 + ps->stnS.d22 + ps->stnS.d33)/3.0;
  dVal=2.5e4*(m_p1/1000.0+100);
  if (dVal<4e6){ dVal=4e6; }
                SetProperty(3,dVal);
//-----permeability stress dependence-----
  mdperm0=GetProperty(17);
  mdmb=GetProperty(16);
  dVal2=mdperm0*exp(-mdmb*m_p1/1000.0);
  SetProperty(15,dVal2);
  return(0);
}
```

3.6.3.5 Summary

In this section, two methods for the implementation of the two-stage softening model into FLAC have been described. For simplicity, the built-in strain hardening/softening model in combination of the specific *FISH* function has been used in the calculations although computational times are somewhat longer.

Chapter 4. Laboratory test simulation via two-stage softening model

This chapter firstly presents the performance of *FLAC* in a plastic deformation calculation compared with that using *FEM* (finite element method). Then, to check on its efficiency, triaxial compression tests and direct shear box tests are reproduced via *FLAC* using *FDM* (finite difference method) employing the two-stage strain-softening model.

Specifically, the performance of those numerical analyses allows:

- To check the accuracy of the plastic deformation using *FLAC*;
- To examine the performance of the model under various hypotheses concerning loading system, dilatancy and testing conditions;
- To observe the effect of using different degrees of mesh refinement and to explore the application of regularization schemes to reduce the mesh-dependency of the results.

4.1 Accuracy of plastic deformation calculation in *FLAC*

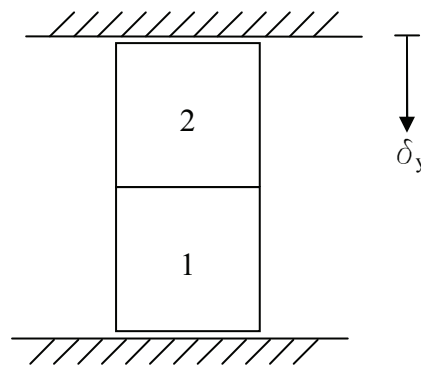


Fig. 4.1 Test model with two elements (after Cividini and Gioda, 1992)

As shown by Cividini and Gioda (1992), the numerical analysis should yield an accurate evaluation of plastic strains as they govern the variation of the shear strength parameters. However, the use of iterative *FEM* techniques to obtain elastoplastic solutions may lead to incorrect values of plastic strains because of the dependency on the size of the displacement increments used.

To demonstrate this effect, the test problem depicted in Fig. 4.1 was considered by Cividini and Gioda (1992) with two four-node quadrilateral elements subjected to a prescribed vertical displacement δ_y . Both elements are elastic-perfectly-plastic frictionless materials with the same elastic parameters but with different cohesions.

Due to the simple geometry and boundary conditions, the stress has the same value at every point within both elements. Several analyses were performed varying only the cohesion of element 2 (c_2) but keeping it larger than that of element 1 (c_1). Theoretically, the plastic deformation should develop only in the weaker element 1. But the analyses presented by Cividini and Gioda (1992) indicate non-negligible plastic deformation also in element 2 and an underestimation of the plastic strains in element 1. For this reason, a special solution technique in *FEM* was devised by Cividini and Gioda (1992) to avoid this undesired effect.

So, in order to check the accuracy of plastic strain calculation using *FLAC*, the same analyses with the same model parameters are performed. The results are shown from Fig. 4.2 to Fig. 4.7. With $c_1 = c_2$ both elements deform equally (Fig. 4.2). However, by varying the cohesion of element 2, the two elements deform differently (shown in Fig. 4.3 to Fig. 4.7). From the moment when the weaker element 1 yields, deformation of element 2 stops and plastic deformation only occurs in the weaker element 1. This is what should be theoretically obtained indicating the accuracy of plastic deformation calculation in *FLAC* and that no special solution technique is needed.

Furthermore, it can be seen from Fig. 4.3 to Fig. 4.7 that the deformations of both elements do not change for different cohesion values of element 2 given the same cohesion value kept for element 1.

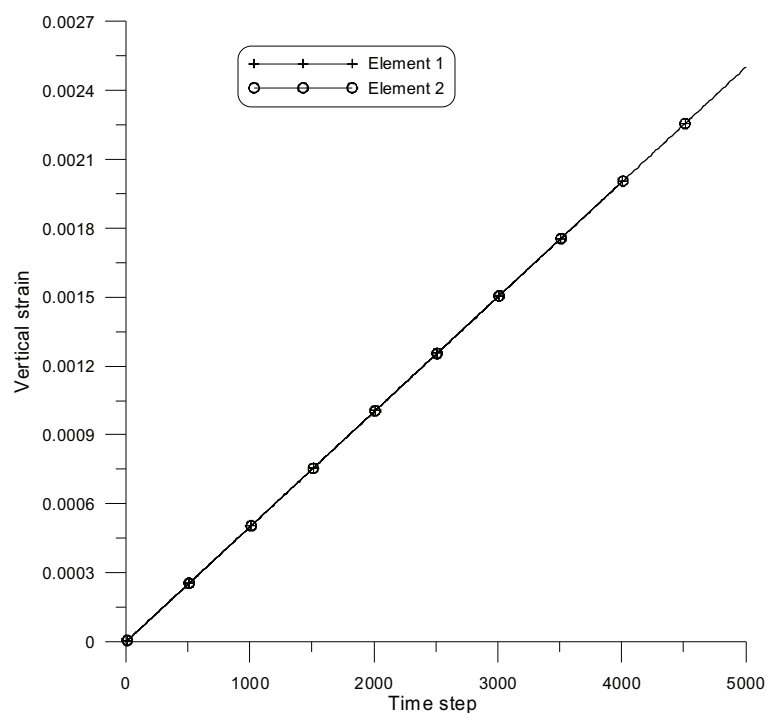


Fig. 4.2 Vertical strains of both elements with $c_1 = c_2 = 2e4$ Pa

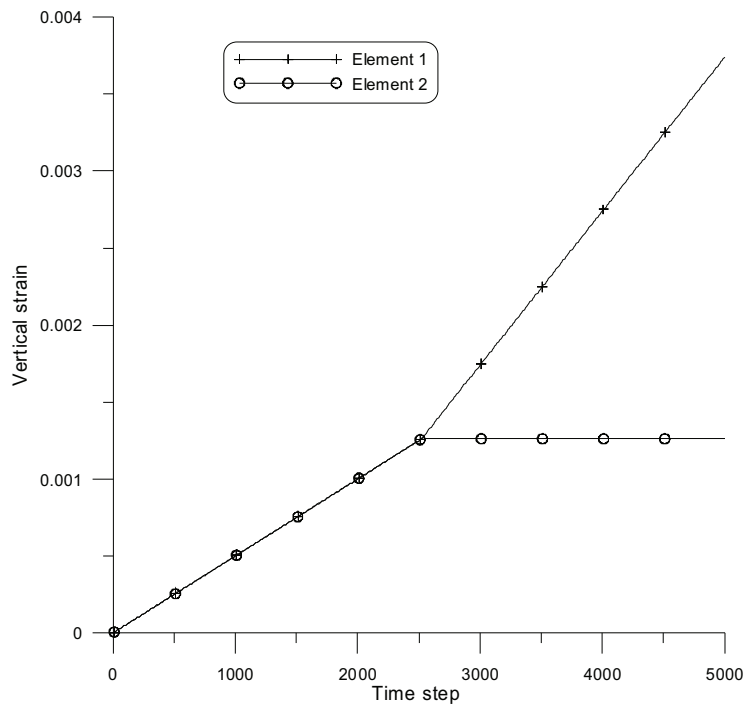


Fig. 4.3 Vertical strains of both elements with $c2 = 2.1e4$ Pa

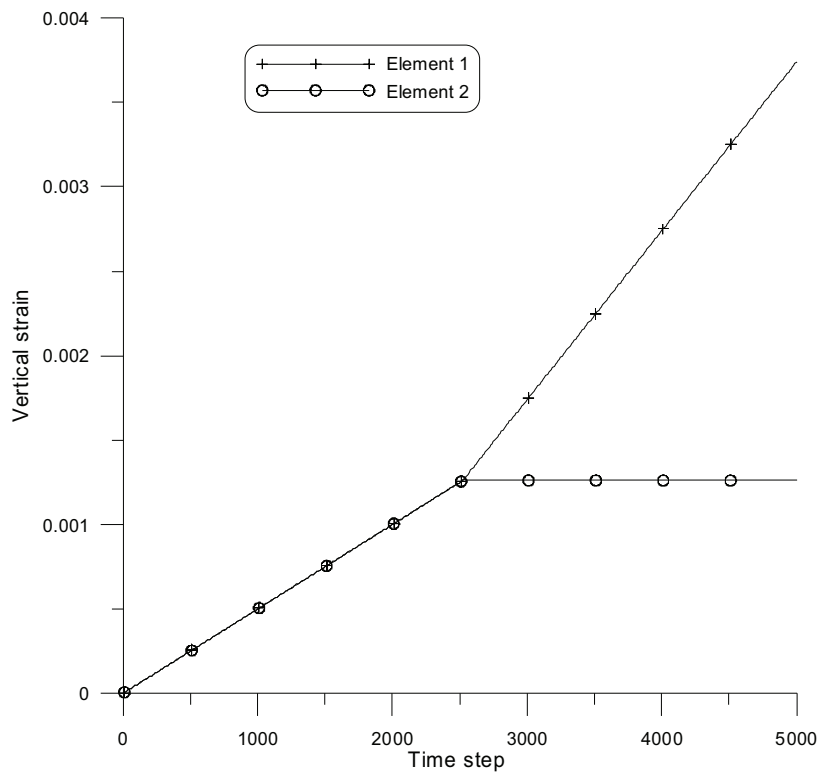


Fig. 4.4 Vertical strains of both elements with $c2 = 2.5e4$ Pa

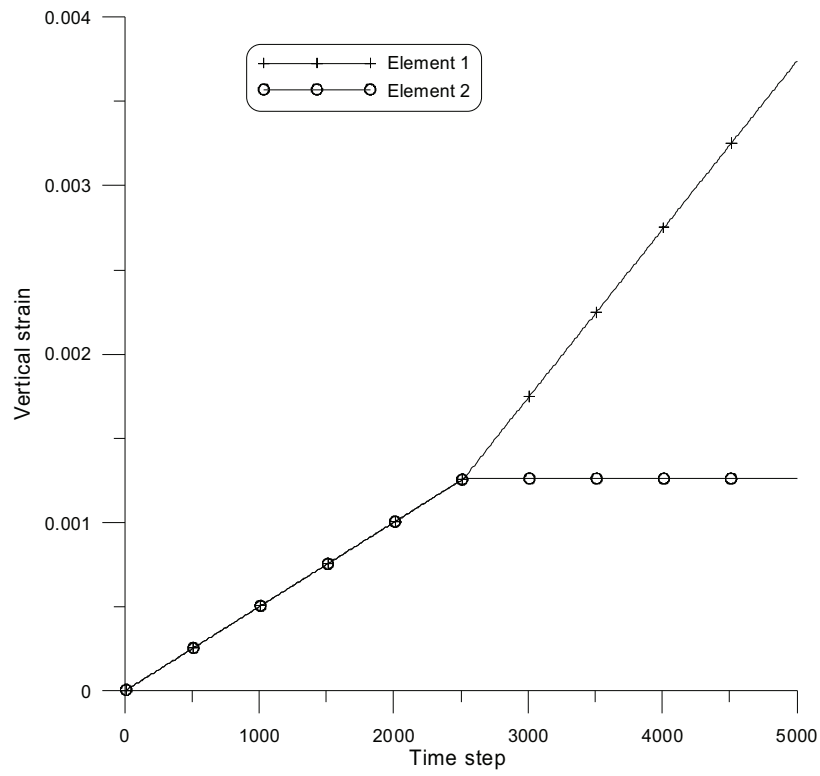


Fig. 4.5 Vertical strains of both elements with $c_2 = 3.0e4$ Pa

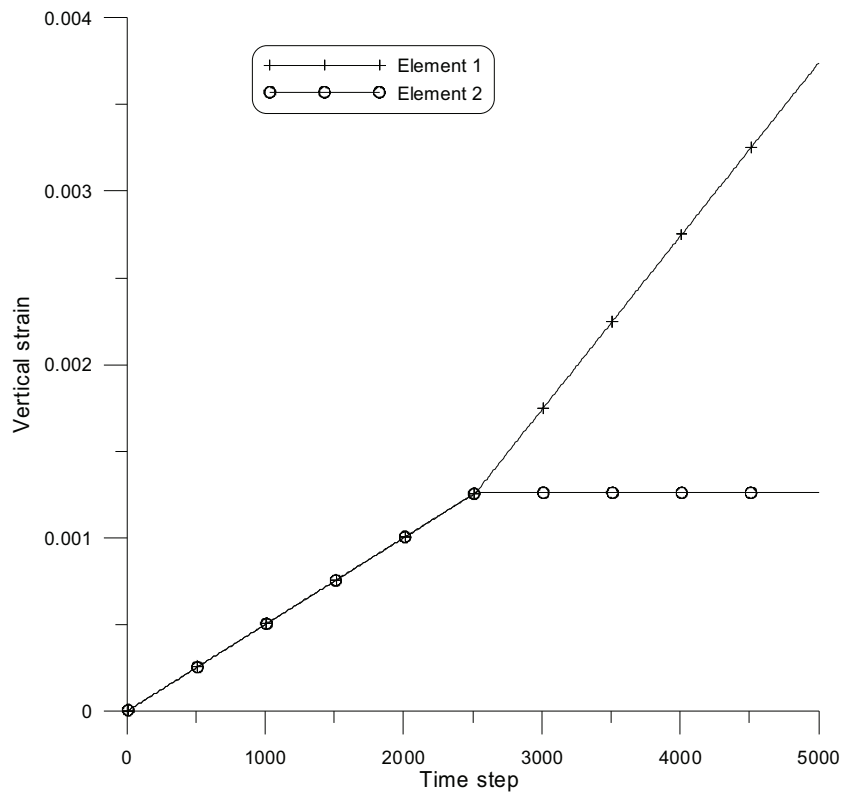


Fig. 4.6 Vertical strains of both elements with $c_2 = 4.0e4$ Pa

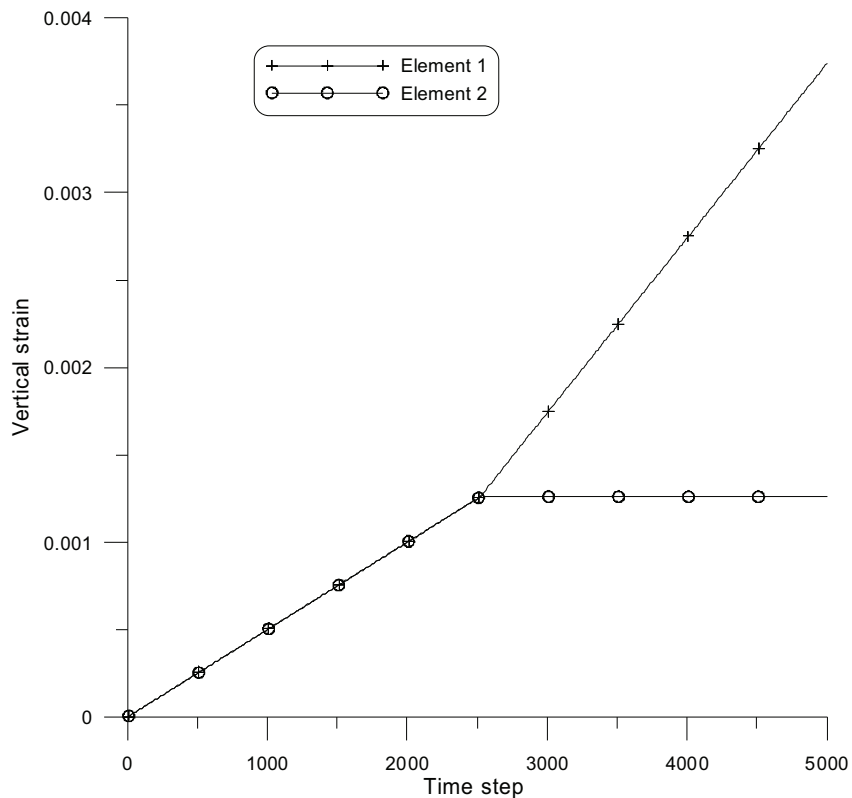


Fig. 4.7 Vertical strains of both elements with $c2 = 6.0e4$ Pa

4.2 Simulation of triaxial tests

4.2.1 Basic model configuration and simulation schemes

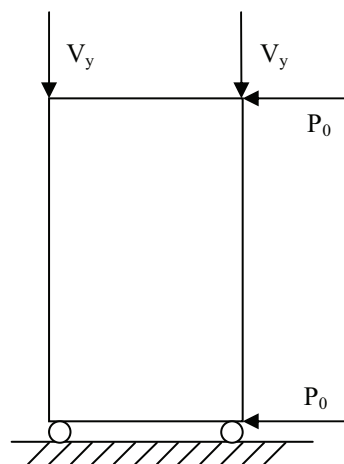


Fig. 4.8 Geometry and boundary conditions

This section simulates the triaxial compression test with the two-stage softening model. Fig. 4.8 shows the geometry and boundary conditions of the model. The dimensions of the model are $5\text{cm} \times 10\text{cm}$. An axisymmetrical configuration is adopted. The grid is fixed in the y -direction; an in-situ isotropic compressive stress is prescribed, and a constant lateral confining pressure equal to the in-situ isotropic

compressive stress, is imposed. The compression is modelled with a vertical velocity magnitude of 1.0×10^{-8} m/s applied to the top of the model. The confining pressure p_0 is set at different values (100kPa, 200kPa, 400kPa, 600kPa, 800kPa and 1000kPa) to study the corresponding influence. In the simulation, the two-stage strain-softening model presented in section 3.5 is applied.

The model parameters are listed in Table 4.1, Table 4.2, Table 4.3 and Table 4.4.

Table 4.1 Basic model parameters

| ρ (kg/m ³) | E (Pa) | ν | K (Pa) | G (Pa) | σ_{ten} (Pa) |
|-----------------------------|----------|-------|----------|----------|---------------------|
| 2000 | 5.0e7 | 0.3 | 4.17e7 | 1.82e7 | 196261 |

The basic elastic parameters are shown in Table 4.1. In Table 4.1, K and G are calculated from E and ν according to the following equations:

$$K = \frac{E}{3(1-2\nu)} \quad (4.1)$$

$$G = \frac{E}{2(1+\nu)} \quad (4.2)$$

The tensile strength σ_{ten} is taken as the limit value given by

$$\sigma_{ten} = \frac{c}{\tan \phi} \quad (4.3)$$

The variations of c and ϕ with plastic shear strain γ are listed in Table 4.2. The dilation and mesh size schemes are listed in Table 4.3 and Table 4.4.

Table 4.2 Variations of c and $\phi^{\#}$ with plastic shear strain γ

| γ_p | γ_{pr} | γ_r |
|------------|---------------|------------|
| 0.0 | 0.0175 | 0.3 |
| c_p (Pa) | c_{pr} (Pa) | c_r (Pa) |
| 1e5 | 4e4 | 0 |
| ϕ_p | ϕ_{pr} | ϕ_r |
| 27 | 26 | 17 |

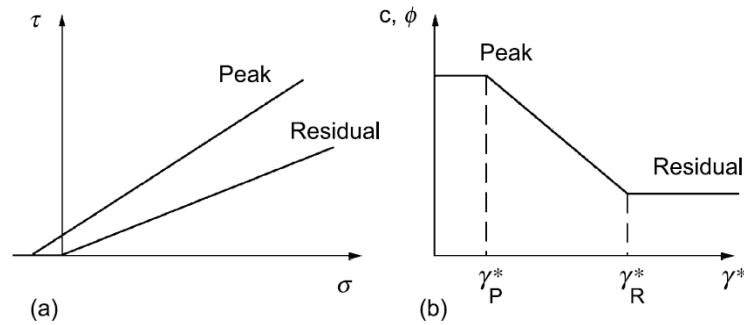
[#] In this paper, the unit for friction and dilation angles is degree and Pa for the unit of cohesion and tensile strength.

Table 4.3 Different values for dilation

| | |
|---|--|
| A | $\psi = 0$ |
| B | $\psi = \phi = 27$ |
| C | $\psi_p = 27, \psi_{pr} = 26, \psi_r = 17$ |
| D | $\psi_p = 15, \psi_{pr} = 10, \psi_r = 0$ |

Table 4.4 Different mesh sizes

| | |
|---|--------|
| 1 | 50×100 |
| 2 | 25×50 |
| 3 | 16×32 |
| 4 | 10×20 |
| 5 | 5×10 |


Fig. 4.9 (a) Peak and residual yield conditions (b) adopted variation of the shear strength parameters after the onset of localization (after Sterpi and Cividini, 2004)

As described by Pietruszczak and Mroz (1981), Cividini and Giuda (1992), Sterpi (1999, 2000) and Sterpi and Cividini (2004), a particular provision can be introduced to circumvent the marked mesh dependence. It consists of relating the slope of the softening branch (Fig. 4.9) to a characteristic dimension of the elements in such a way that their ratio is kept constant. In Fig. 4.9, γ^* has the same meaning as ε_D^p shown in Fig. 3.5 and defined in Eq. (3.37).

At first, the parameters defining the strain-softening behaviour, γ_p^* , γ_R^* (Fig. 4.9) and $\Delta\gamma^* = \gamma_R^* - \gamma_p^*$ are determined on the basis of laboratory tests and set to be the reference parameters for a certain numerical model with representative mesh size. Then, when different mesh sizes are adopted, the previously determined parameter $\Delta\gamma^*$ is adjusted depending on the current element size.

Therefore, the parameter $\Delta\gamma^*$, which governs the rate of decrease of the shear strength, does not only depend on material mechanical properties, but also mesh

discretization, since the results of softening analyses are markedly influenced by the size of the adopted finite elements. This drawback can be alleviated by keeping constant the product between the mean size S of the elements and the parameter $\Delta\gamma^*$,

$$\Delta\gamma_1^* S_1 = \Delta\gamma_2^* S_2 \tag{4.4}$$

With this criterion, the numerical solution of some benchmark problems in two dimensions (e.g. Cividini and Giuda, 1992; Sterpi, 2000) demonstrates that this provision reduces the mesh dependence of softening analyses.

The aforementioned method to limit mesh effect is also applicable to the two-stage softening model. The difference is that there are two differences— $\Delta\gamma_A^* = \gamma_{PR}^* - \gamma_P^*$ and $\Delta\gamma_B^* = \gamma_R^* - \gamma_{PR}^*$. Both adjustments for parameters γ_{PR}^* and γ_R^* should be made. The calculation procedure is described as below:

- (1) obtain γ_{PR2}^* according to Eq. (4.4) with $\Delta\gamma^* = \Delta\gamma_A^*$ by keeping γ_P^* unchanged;
- (2) calculate γ_{R2}^* by applying again Eq. (4.4) with $\Delta\gamma^* = \Delta\gamma_B^*$ and using the new value γ_{PR2}^* from (1).

Table 4.5 Parameter adjustments for different mesh size (Scheme I)

| Mesh size | γ_P | γ_{pr} | γ_r |
|-----------|------------|---------------|------------|
| 50×100 | 0 | 0.0175 | 0.93 |
| 25×50 | 0 | 0.0175 | 0.47 |
| 16×32 | 0 | 0.0175 | 0.30 |
| 10×20 | 0 | 0.0175 | 0.189 |
| 5×10 | 0 | 0.0175 | 0.115 |

Table 4.6 Parameter adjustments for different mesh size (Scheme II)

| Mesh size | γ_P | γ_{pr} | γ_r |
|-----------|------------|---------------|------------|
| 50×100 | 0 | 0.04297 | 0.975 |
| 25×50 | 0 | 0.02148 | 0.4875 |
| 16×32 | 0 | 0.0175 | 0.30 |
| 10×20 | 0 | 0.00859 | 0.195 |
| 5×10 | 0 | 0.0043 | 0.0975 |

Here two schemes of parameter adjustment are carried out. The first scheme is to keep γ_{PR}^* unchanged and only to modify γ_R^* based on mesh size whereas the second one

involves the modification of both γ_{pr}^* and γ_r^* as described. Two sets of strain threshold parameters are provided in Table 4.5 and Table 4.6 based on the method described above to study the mesh dependency. The reference mesh size of simulation is taken as 16×32 .

In order to check the effect of dilation, two more schemes—E and F (Table 4.7) are performed. In addition, schemes—G and H (Table 4.7) with new softening parameters are used to investigate their influence.

Table 4.7 Different values for dilation

| | |
|---|--|
| E | $\psi_p = 15, \psi_{pr} = 10, \psi_r = 2$ |
| F | $\psi_p = 27, \psi_{pr} = 20, \psi_r = 5$ |
| G | $\gamma_p = 0, \gamma_{pr} = 0.015, \gamma_r = 0.15$ $\phi_p = 27, \phi_{pr} = 25, \phi_r = 17$ $c_p = 1e5, c_{pr} = 1e4, c_r = 0$ $\psi_p = 10, \psi_{pr} = 8, \psi_r = 0$ |
| H | γ, ϕ, ψ are the same as G $c_p = 3e4, c_{pr} = 3e3, c_r = 0$ |

4.2.2 Theoretical solution with 1×1 grid

The analysis with 1×1 grid in axisymmetric configuration is conducted to examine the performance of the constitutive model. The vertical velocity value is 5.0×10^{-8} m/s.

In Fig. 4.10 it can be seen the characteristic bilinear softening process—rapid reduction with subsequent relatively slower decrease. As the dilation angle becomes larger, the vertical stress decreases more quickly. The reduction of cohesion (scheme H) is accompanied by a reduction in peak stress. The reduction of γ_{pr} and γ_r (scheme G) accelerates the stress reduction to residual state.

Fig. 4.11 indicates the enhancement of dilation with dilation angle. As ψ_r drops (scheme D and E), the final volumetric strain decreases until reaching the ultimate residual state which corresponds to zero volumetric strain increment.

In addition, the influence of confining pressure is presented in Fig. 4.12. The increase of p_0 reduces the peak of stress ratio) and therefore reduces the brittleness.

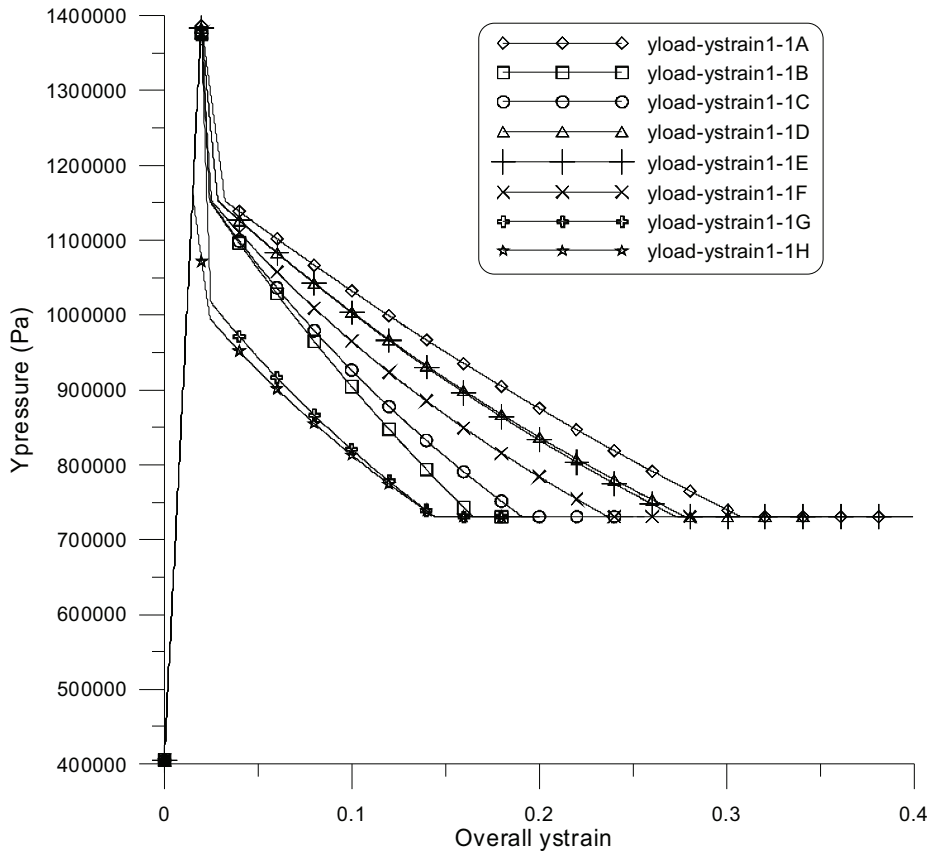


Fig. 4.10 Vertical stress vs. vertical strain for 1×1 grid

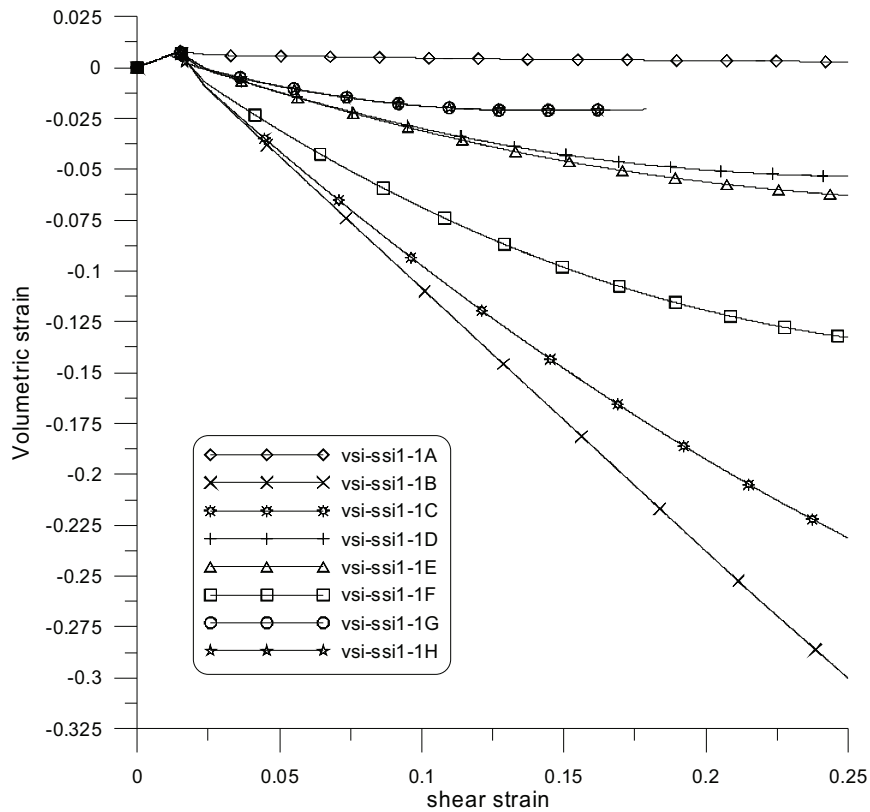


Fig. 4.11 Volumetric strain vs. shear strain $((\epsilon_1 - \epsilon_3) / 2)$ for 1×1 grid

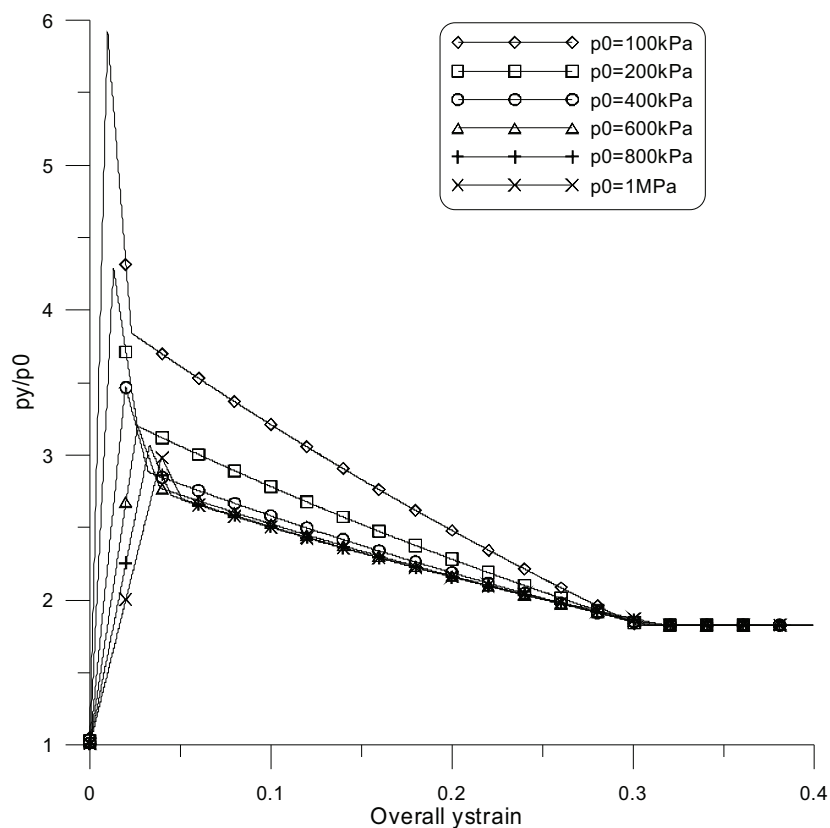


Fig. 4.12 Stress ratio vs. vertical strain for 1×1 grid

4.2.3 Simulation with different grids

After the 1×1 grid simulations, analyses with different grids (Table 4.3 and Table 4.4) have been performed. Fig. 4.13-Fig. 4.26 exhibit similar two-stage softening characteristics as described above. Again a larger dilation value leads to a faster rate of reduction of vertical stress. Similarly, as the confining pressure p_0 increases, the peak stress ratio decreases and so does the brittleness.

Fig. 4.27-Fig. 4.31 illustrate the influence of mesh size. Fig. 4.27 shows results for both simulations with original and adjusted strength parameters. It is evident that the mesh size effect can not be ignored and Scheme I diminishes efficiently the size effect on the softening behaviour. Meanwhile, results with adjusted strength parameters (Scheme II) shown in Fig. 4.28-Fig. 4.31 demonstrate that the mesh size influence is almost eliminated by using Scheme II which thus will be applied in subsequent modelling.

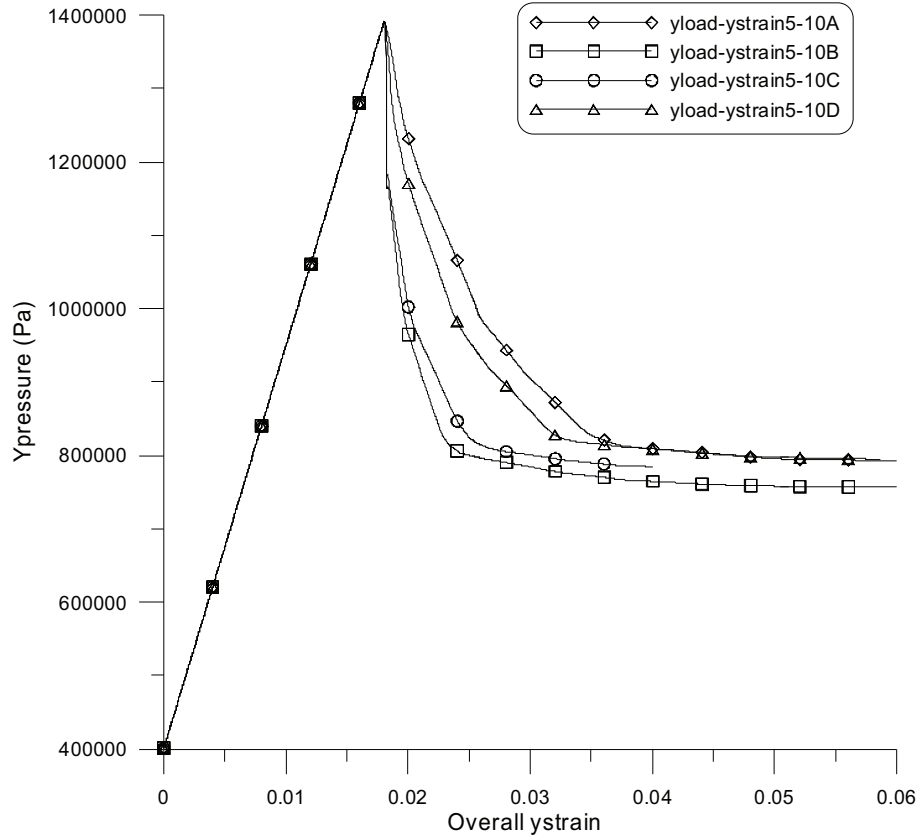


Fig. 4.13 Vertical stress vs. vertical strain with different dilation angles for 5×10 grid

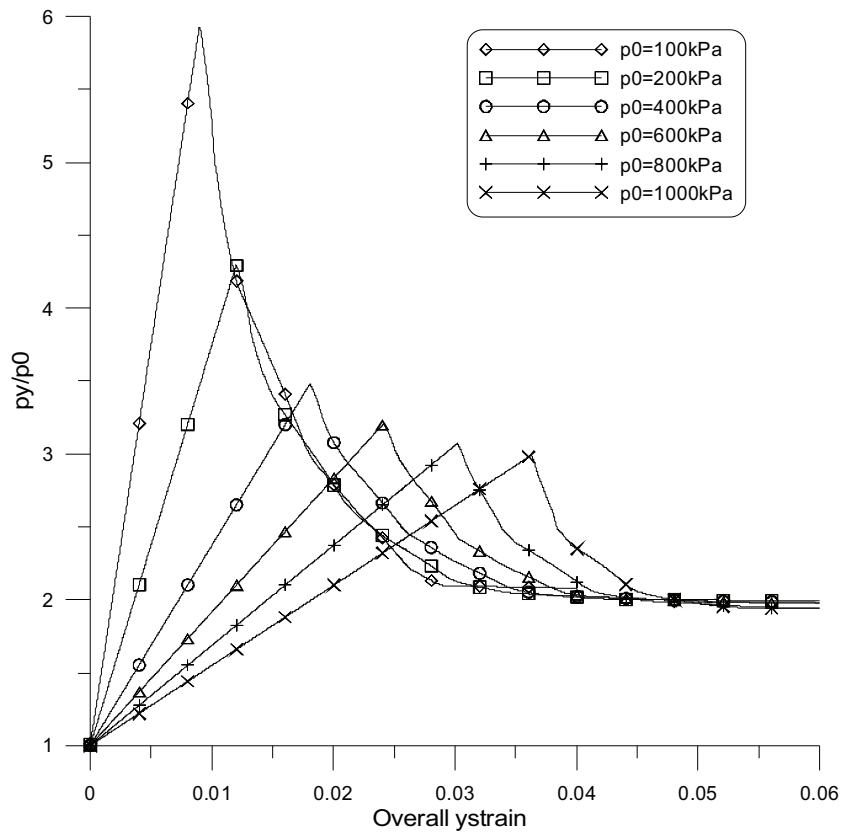


Fig. 4.14 Vertical pressure ratio vs. vertical strain with different p_0 for 5×10 grid

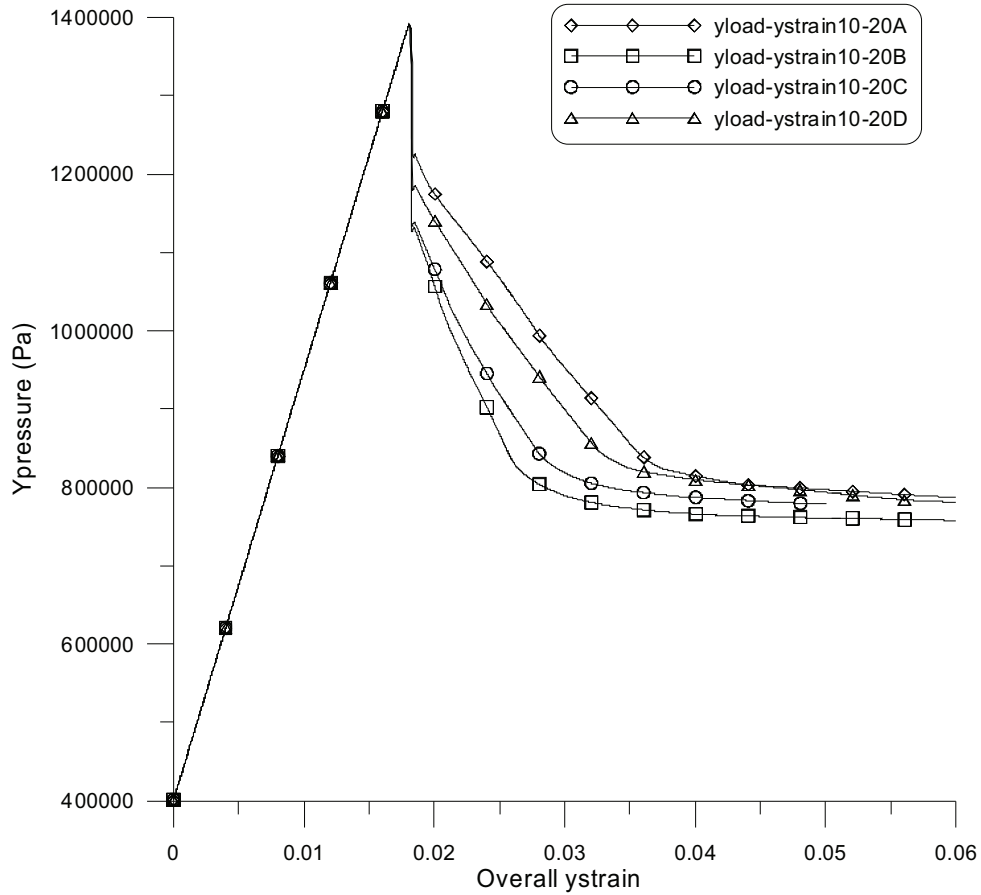


Fig. 4.15 Vertical stress vs. vertical strain with different dilation angles for 10×20 grid

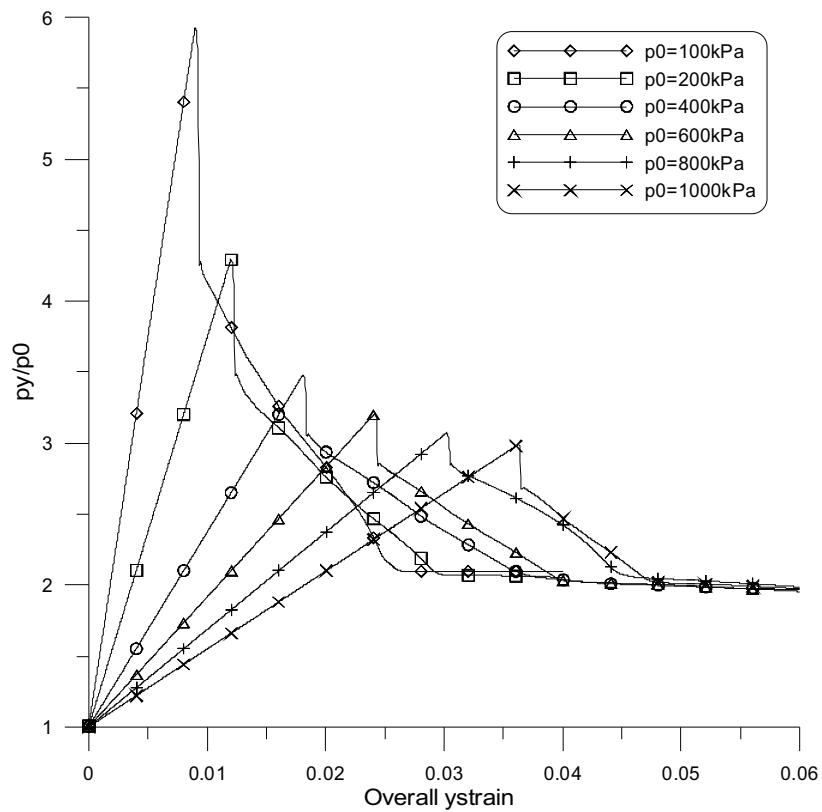


Fig. 4.16 Vertical pressure ratio vs. vertical strain with different p_0 for 10×20 grid

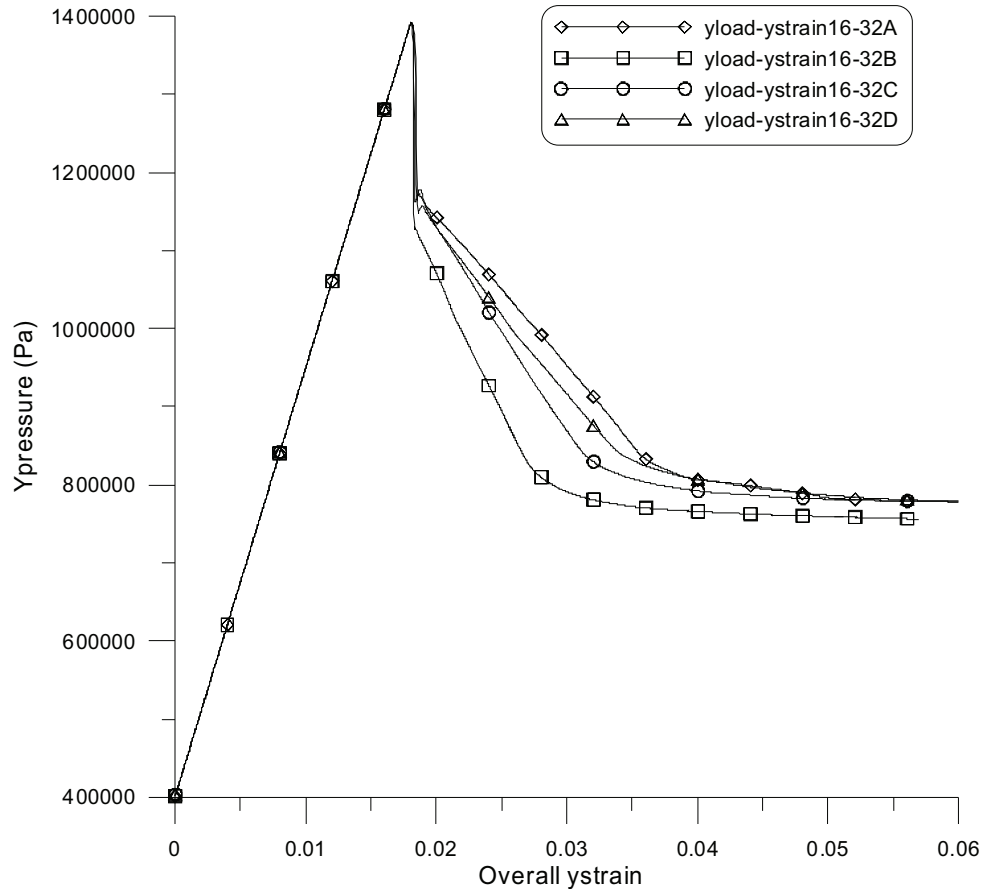


Fig. 4.17 Vertical stress vs. vertical strain with different dilation angles for 16×32 grid

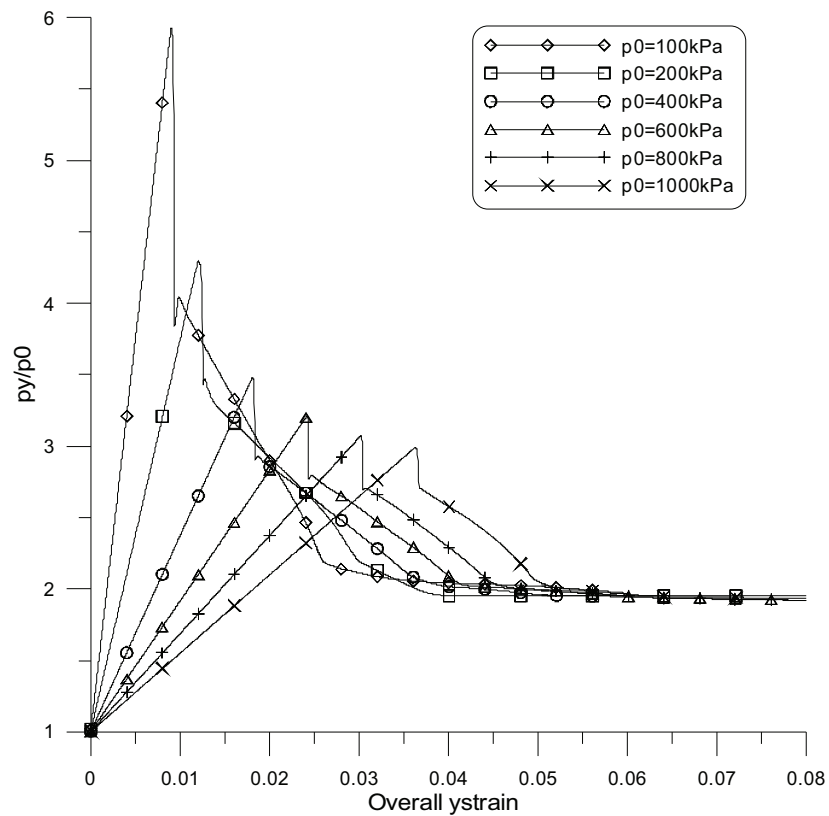


Fig. 4.18 Vertical pressure ratio vs. vertical strain with different p_0 for 16×32 grid

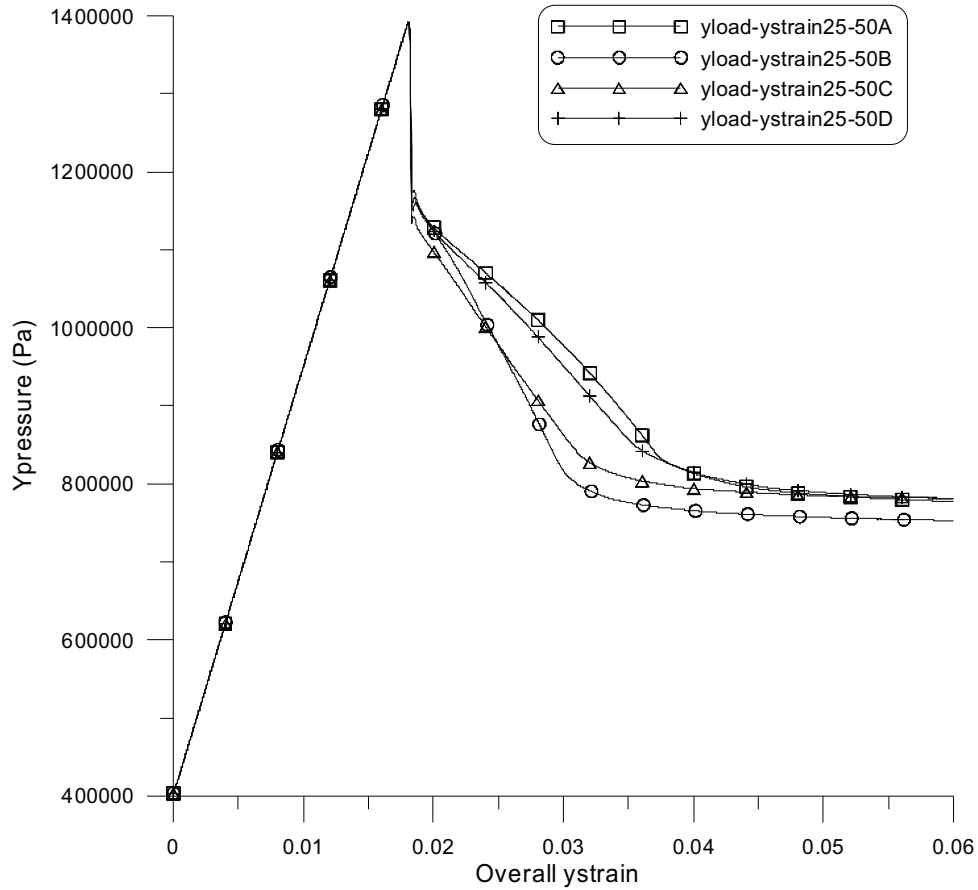


Fig. 4.19 Vertical stress vs. vertical strain with different dilation angles for 25×50 grid

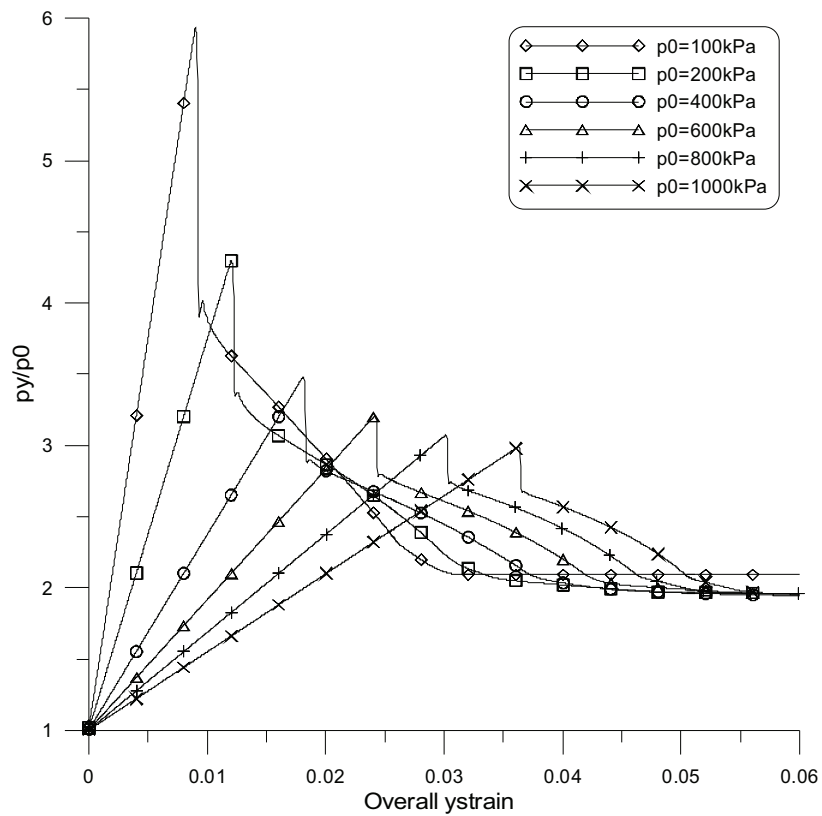


Fig. 4.20 Vertical pressure ratio vs. vertical strain with different p_0 for 25×50 grid

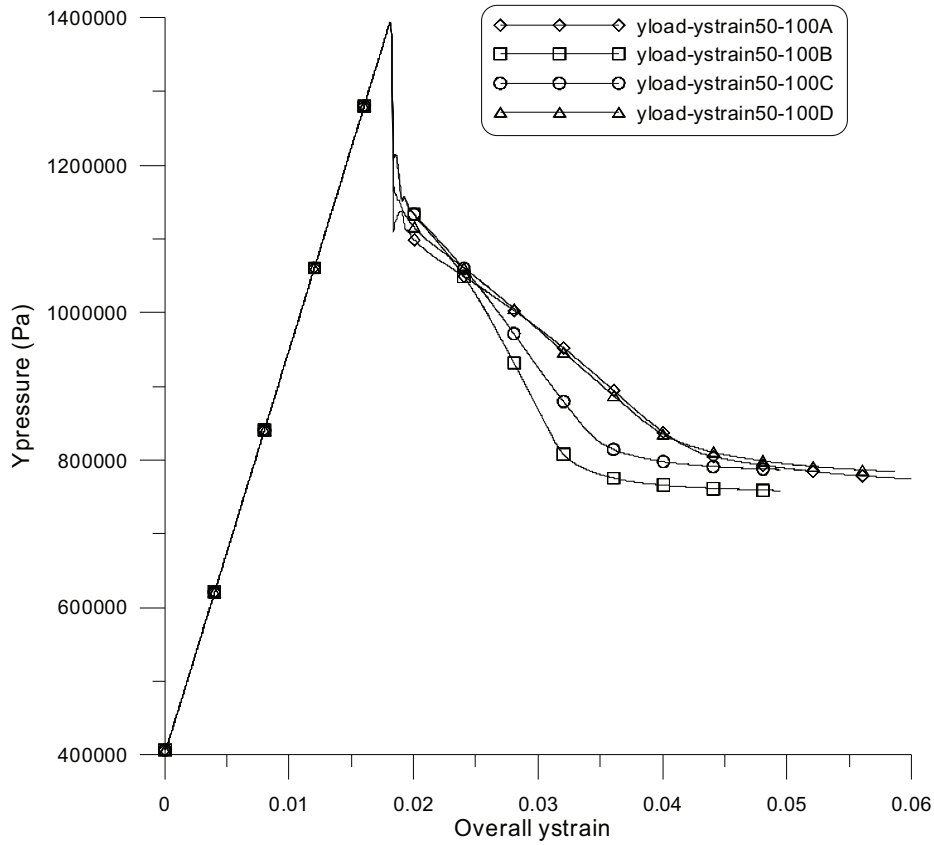


Fig. 4.21 Vertical stress vs. vertical strain with different dilation angles for 50×100 grid

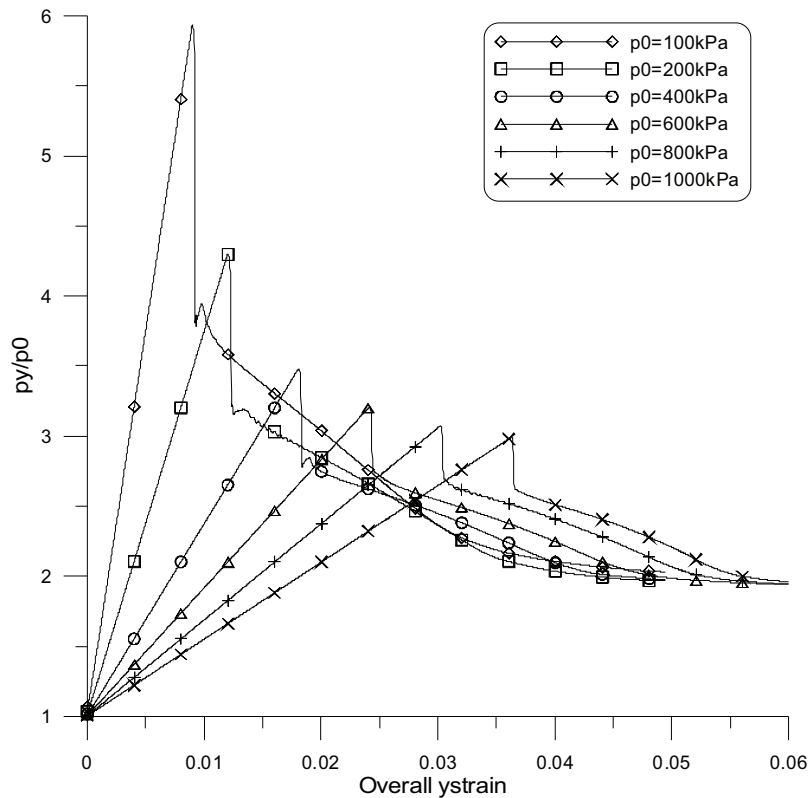


Fig. 4.22 Vertical pressure ratio vs. vertical strain with different p_0 50×100 grid

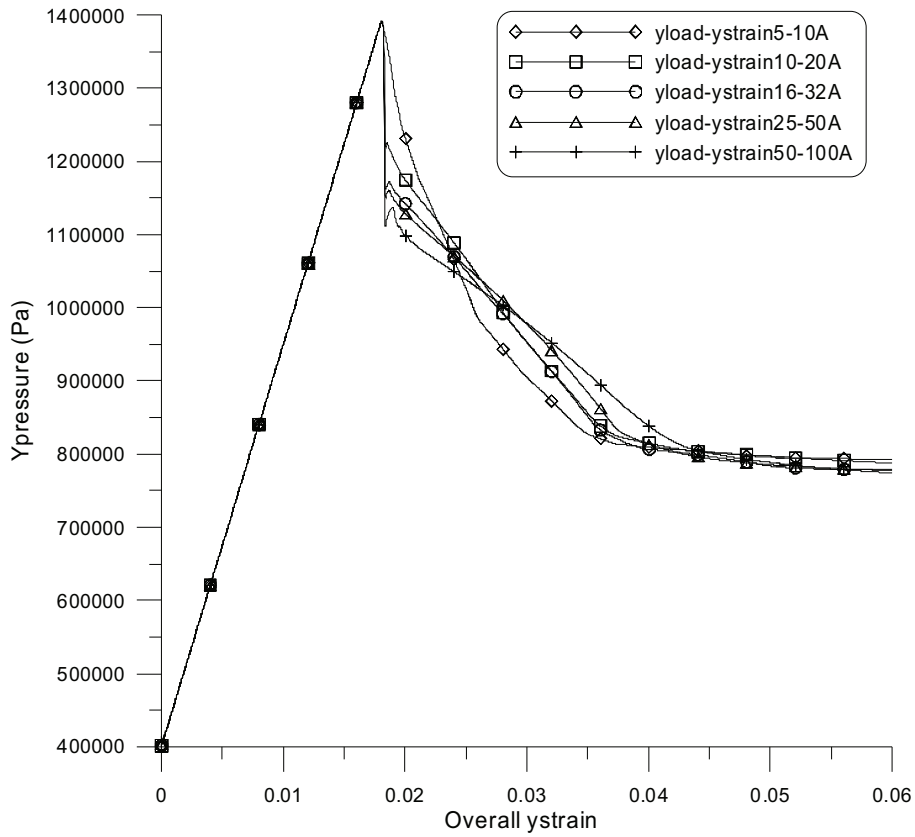


Fig. 4.23 Vertical stress vs. vertical strain for different grids with dilation scheme A

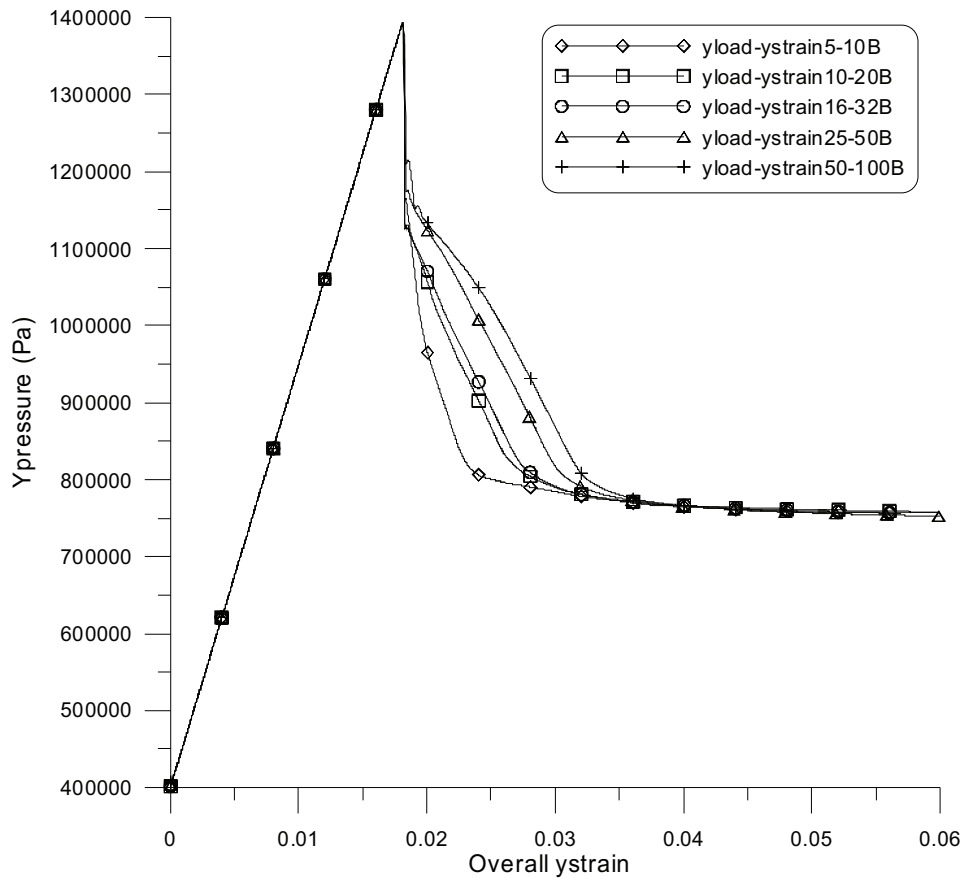


Fig. 4.24 Vertical stress vs. vertical strain for different grids with dilation scheme B

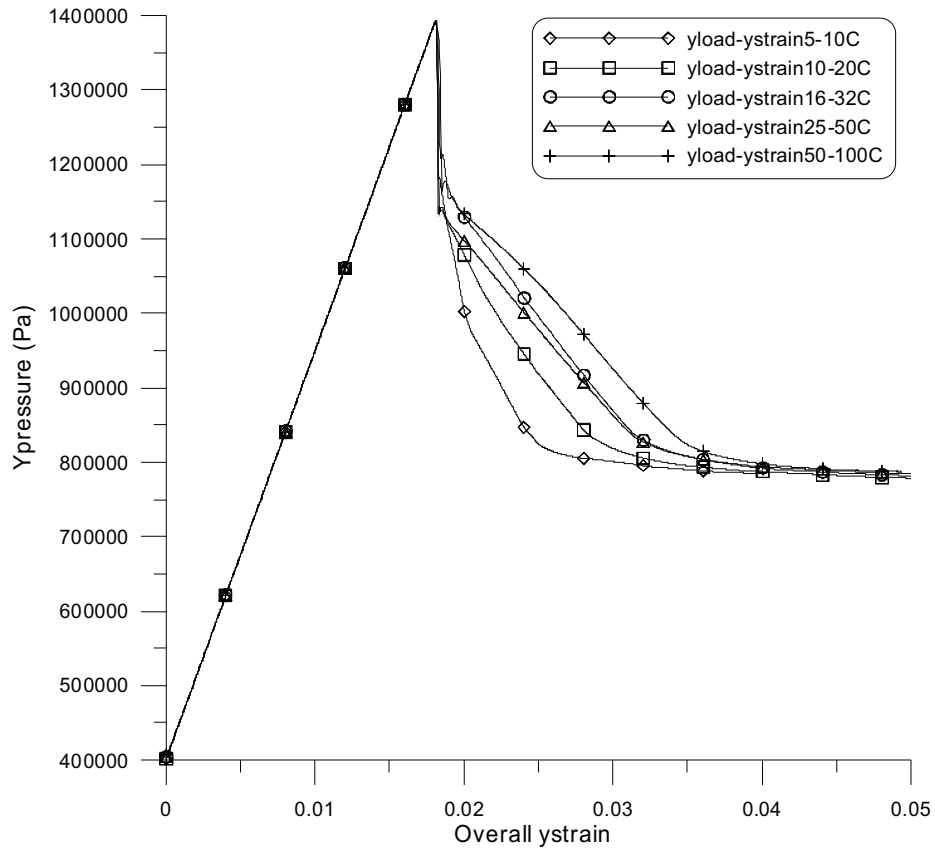


Fig. 4.25 Vertical stress vs. vertical strain for different grids with dilation scheme C

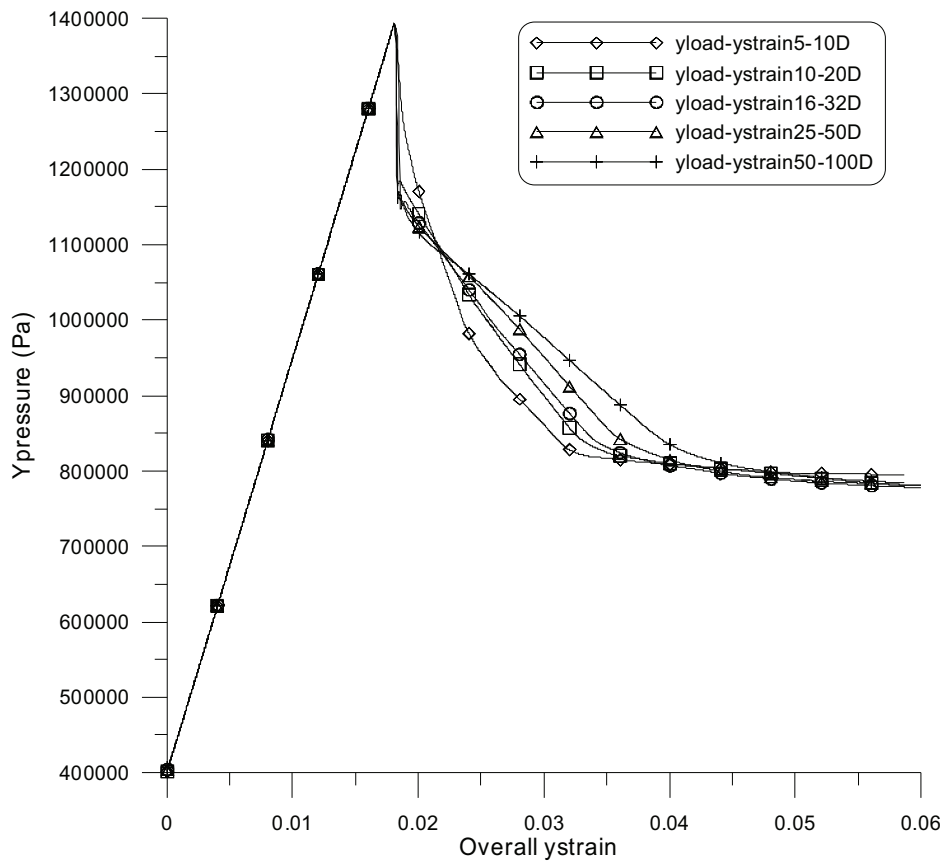


Fig. 4.26 Vertical stress vs. vertical strain for different grids with dilation scheme D

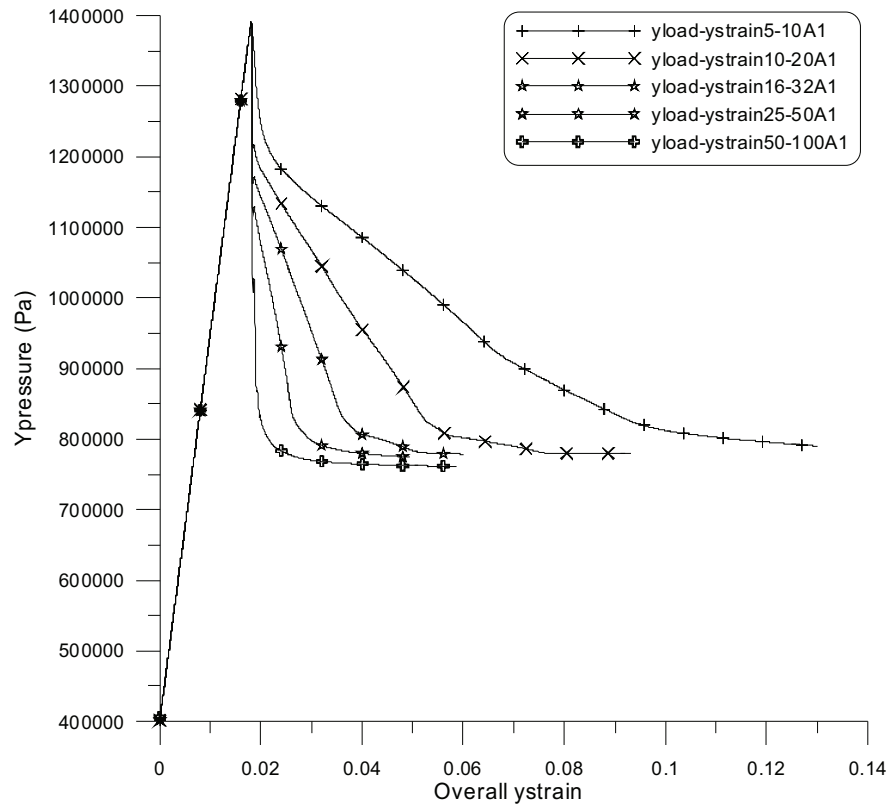


Fig. 4.27 Vertical stress vs. vertical strain for different grids with adjusted strength parameters according to mesh size (Scheme I and A)

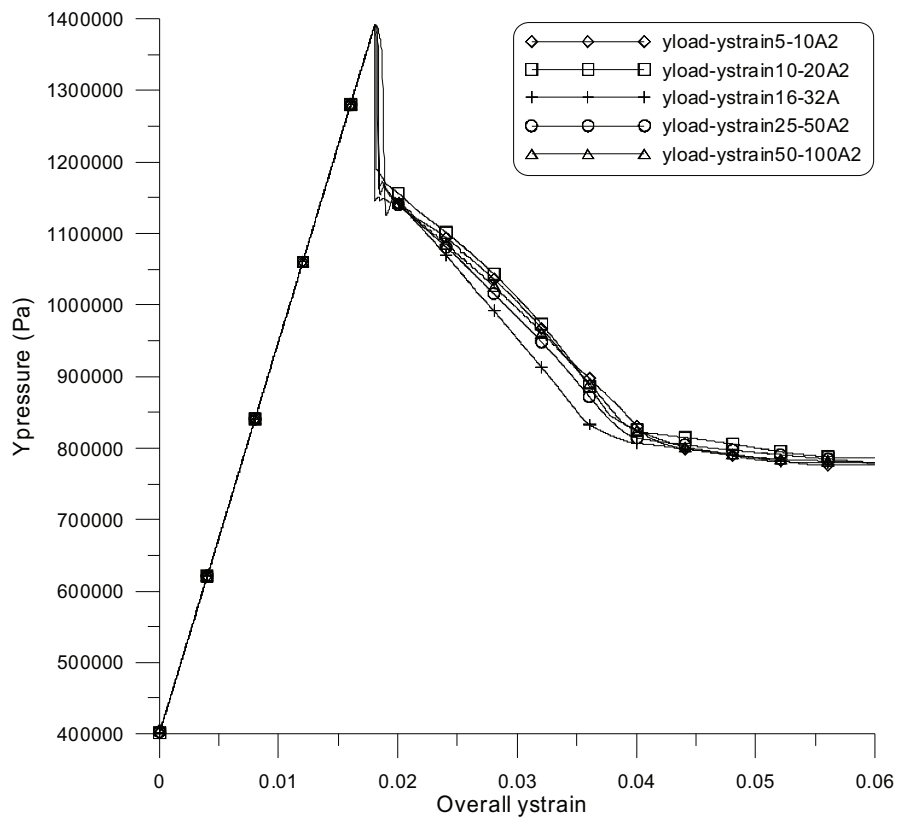


Fig. 4.28 Vertical stress vs. vertical strain for different grids with adjusted strength parameters according to mesh size (Scheme II and A)

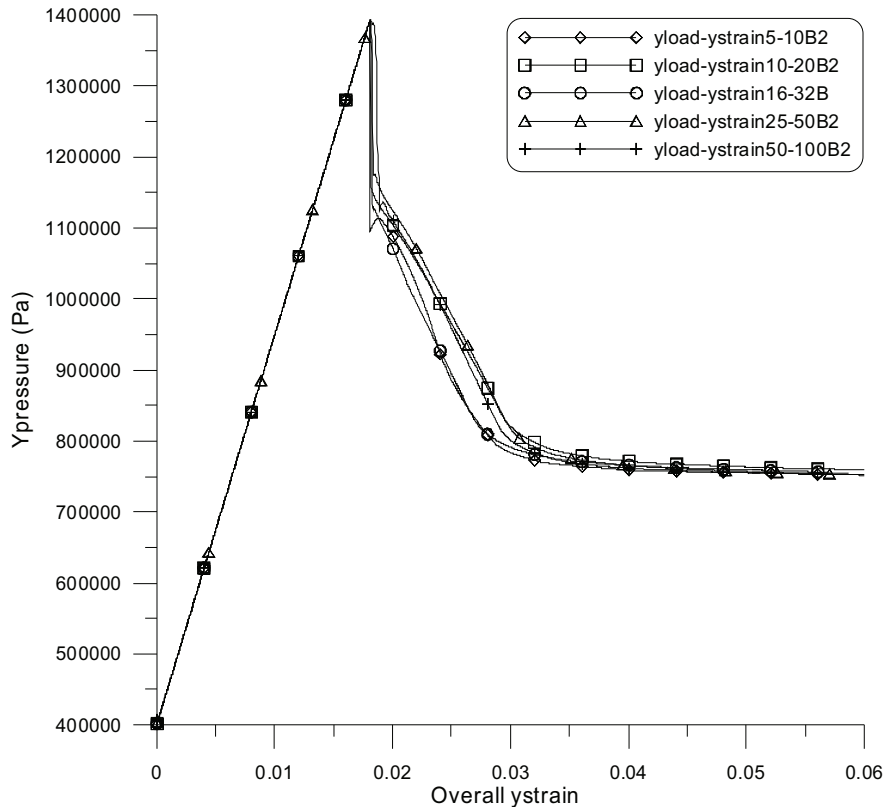


Fig. 4.29 Vertical stress vs. vertical strain for different grids with adjusted strength parameters according to mesh size (Scheme II and B)

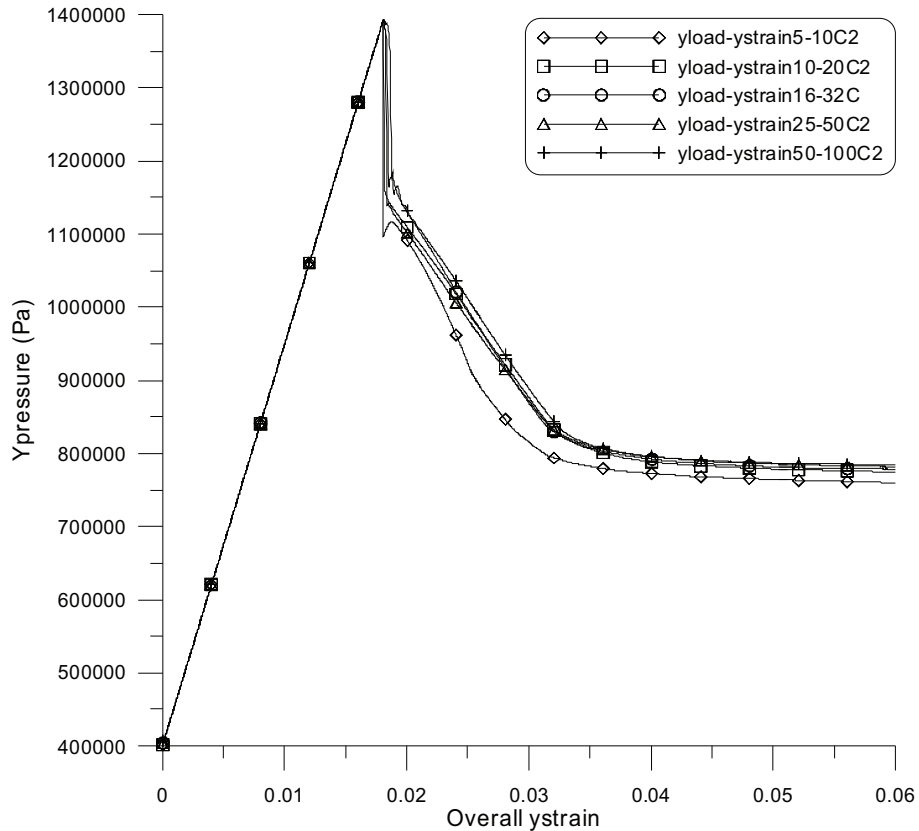


Fig. 4.30 Vertical stress vs. vertical strain for different grids with adjusted strength parameters according to mesh size (Scheme II and C)

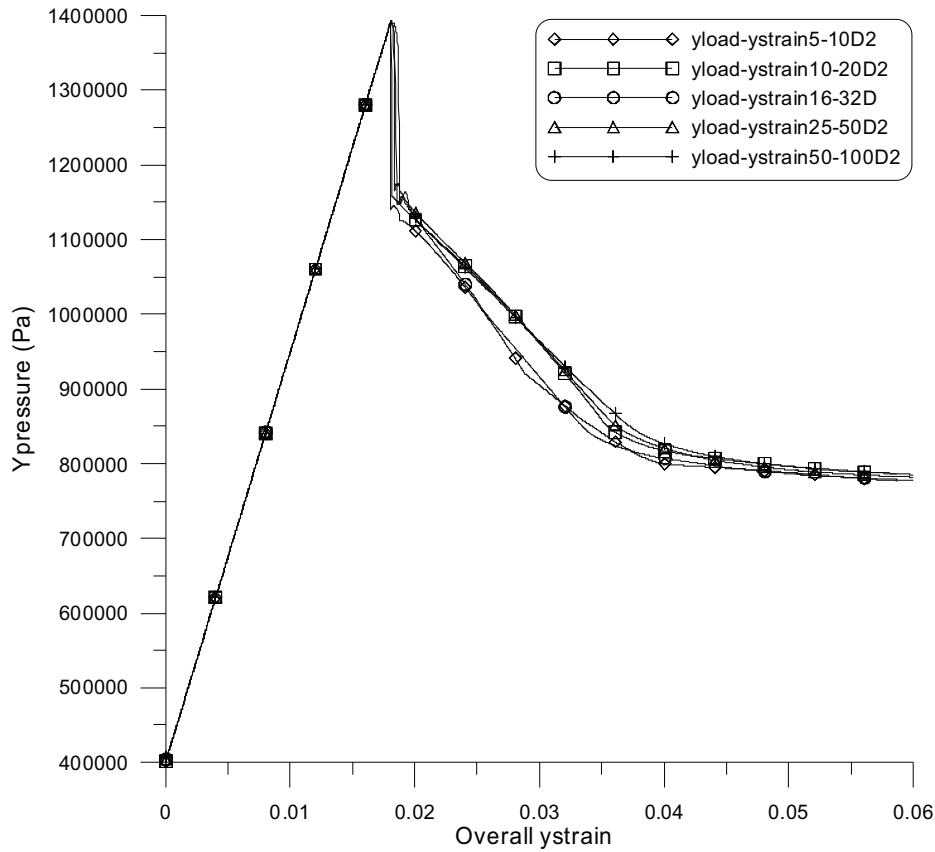


Fig. 4.31 Vertical stress vs. vertical strain for different grids with adjusted strength parameters according to mesh size (Scheme II and D)

4.2.4 Verification of undrained triaxial test simulation

Table 4.8 Clay properties assumed in numerical analyses

| Property | Assumed value |
|---------------------------------------|---|
| Bulk unit weight | 18.8 kN/m ³ |
| Bulk peak strength | $c'_p = 7\text{kPa}$, $\phi'_p = 20^\circ$ |
| Residual strength | $c'_r = 2\text{kPa}$, $\phi'_r = 13^\circ$ |
| Plastic strain at peak | $\epsilon_{DP}^P = 5\%^\#$ |
| Plastic strain at residual | $\epsilon_{DR}^P = 20\%^\#$ |
| Poisson's ratio | $\mu = 0.20$ |
| Young's modulus | $E = 25(p' + 100)$, (min. 4000 kPa) [*] |
| Angle of dilation | $\psi = 0$ |
| Coefficient of permeability | $k = 1\text{e-}6 \sim 1\text{e-}9$ m/s |
| Coefficient of earth pressure at rest | $K_0 = 1.0$ |
| Porosity | $n = 0.3$ |
| Water bulk modulus | $K_w = 2.0\text{e}9$ |

* p' is the mean effective stress in kPa ;

[#]Note: the plastic shear strain used in *FLAC* tables for softening parameters is half of ϵ_D^P .

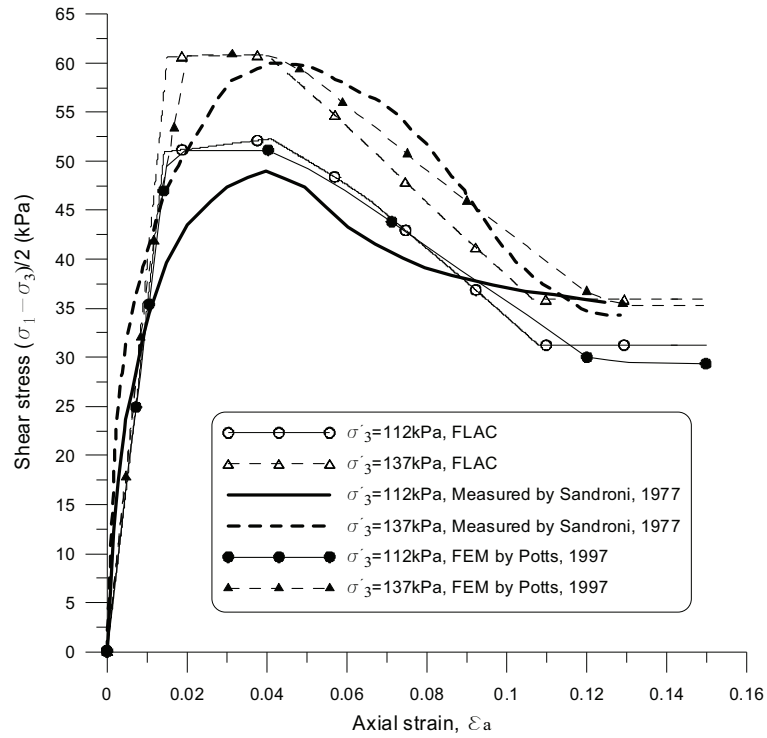


Fig. 4.32 Measured and predicted shear stress vs. axial strain curve in undrained triaxial tests on Brown London Clay

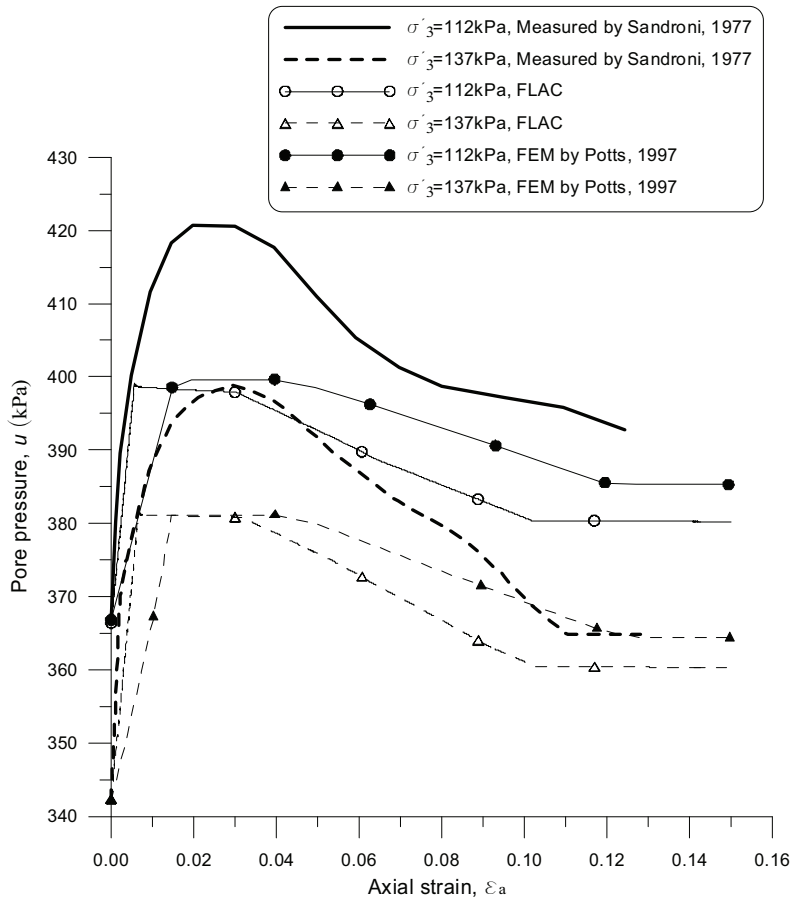


Fig. 4.33 Measured and predicted pore pressure vs. axial strain curve in undrained triaxial tests on Brown London Clay

Potts et al. (1997) used a non-linear one-stage strain-softening model to simulate the stress-strain behaviour observed in two unconsolidated undrained triaxial tests on 265 mm diameter samples of Brown London Clay (Sandroni, 1977) using the finite element method. The material properties are shown in Table 4.8. The Young's modulus varies with mean effective stress, p' and this can be easily incorporated in *FLAC* using a *FISH* function. It is noticeable that, to some extent, the bulk peak strength could be considered approximately as the post-rupture strength because the Brown London Clay is highly fissured.

Fig. 4.32 and Fig. 4.33 show the comparisons between measured results and *FEM* and *FLAC* modelling results. The comparisons are reasonable, although the generation of pore pressure during shear is underestimated by both *FEM* and *FLAC* analyses. In any case, the *FLAC* simulation yields very similar results as *FEM* does. This verifies the efficiency of *FLAC* to model softening behaviour of clay.

4.3 Simulation of direct shear box tests

The direct shear test is used most commonly to determine a drained strength envelope. A specimen of soil is placed in a shear box, and consolidated under an applied normal load. The shear box is made of two separate halves, an upper one and a lower one. After the application of the normal load, these two halves move relative to one another, shearing the soil specimen along the plane that is the separation of the two halves. The direct-shear test imposes stress conditions on the soil that force the failure plane to occur at a predetermined location. The shear strength and the vertical normal effective stress are both determined directly from the test.

4.3.1 Theoretical solution with 1×1 grid

Firstly a 1×1 grid is used to conduct theoretical numerical analyses. The geometry and boundary conditions are shown in Fig. 4.34. The bottom is fixed in both x and y directions and a horizontal velocity v_x is assigned to the top. The horizontal velocity magnitude is 1.0×10^{-6} m/s. A normal force N is also imposed on the top. W is the width and H is the height. In 1×1 grid, $W = 1$ and $H = 1$. The initial stress given by $\sigma_h = K_0 \sigma_v$ is shown in Table 4.9. K_0 is the earth pressure coefficient at rest.

Table 4.9 Different schemes for initial stress

| | | |
|---|-----------|--|
| 1 | $K_0 = 1$ | $\sigma_{xx} = -100$ kPa, $\sigma_{yy} = -100$ kPa, $\sigma_{zz} = -100$ kPa |
| 2 | $K_0 = 2$ | $\sigma_{xx} = -200$ kPa, $\sigma_{yy} = -100$ kPa, $\sigma_{zz} = -200$ kPa |
| 3 | $K_0 = 3$ | $\sigma_{xx} = -300$ kPa, $\sigma_{yy} = -100$ kPa, $\sigma_{zz} = -300$ kPa |

The material parameters and schemes are the same as those in Table 4.1, Table 4.2 (with γ_p replaced by 0) and Table 4.3. In addition, the vertical or applied normal stresses σ_n are 100 kPa, 300 kPa and 500 kPa. When checking the dilation effect with different schemes (seen in Table 4.3), K_0 is set to be 2 (scheme 2 in Table 4.9) and σ_n is set to be 100 kPa and when checking the normal stress effect with different

schemes, K_0 is kept to be 3 and the dilation angle is set to 0 (scheme A in Table 4.3). Finally while studying the influence of K_0 , σ_n is kept 100 kPa and the dilation angle is set to 0 (scheme A in Table 4.3).

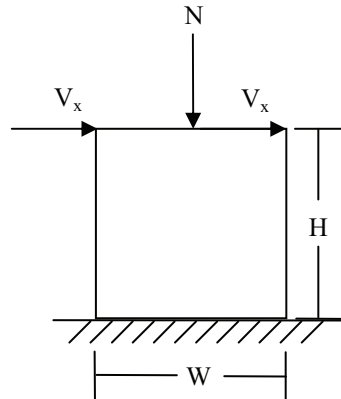


Fig. 4.34 Geometry and boundary conditions

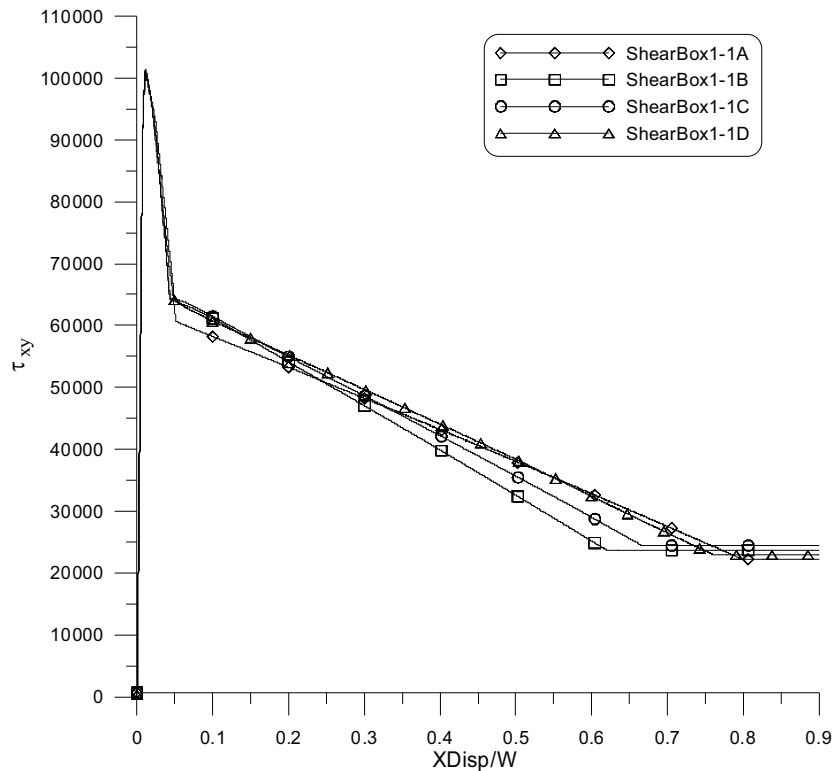


Fig. 4.35 Shear stress vs. horizontal displacement ratio with different dilation schemes ($K_0=2$ and $\sigma_n=100$ kPa)

The bilinear softening process—rapid reduction with subsequent slower decrease—can be seen from Fig. 4.35 and Fig. 4.36. Compared with results of triaxial compression tests, the dilation has a similar effect—increasing dilation angle accelerates the reduction in shear stress. However, the effect of dilation on stress is much less. However, the rate of vertical displacement increase augments as the dilation angles becomes higher (Fig. 4.36).

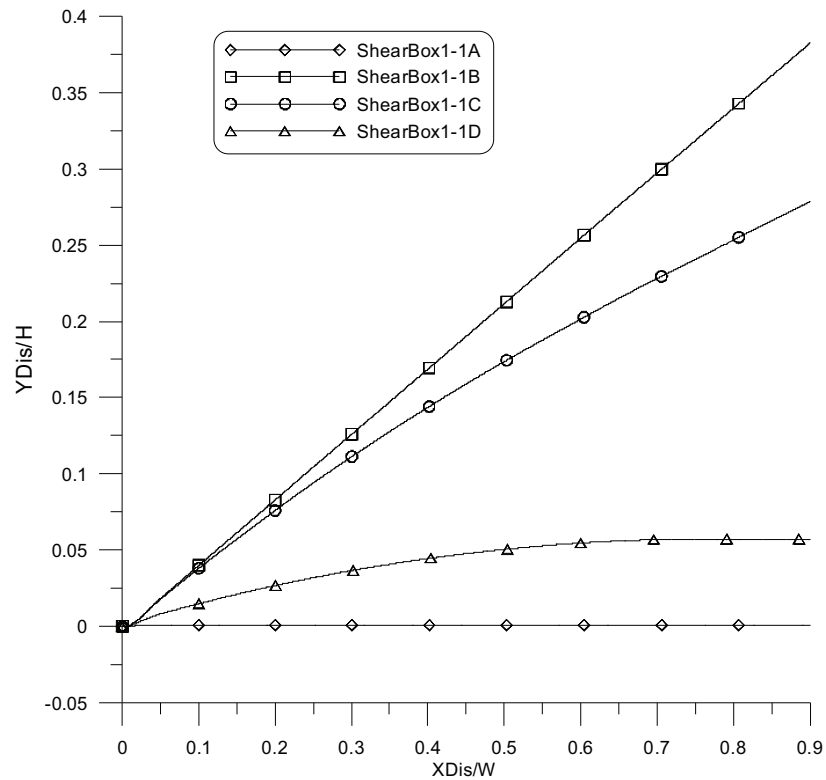


Fig. 4.36 Vertical displacement ratio vs. horizontal displacement ratio with different dilation schemes ($K_0=2$ and $\sigma_n=100$ kPa)

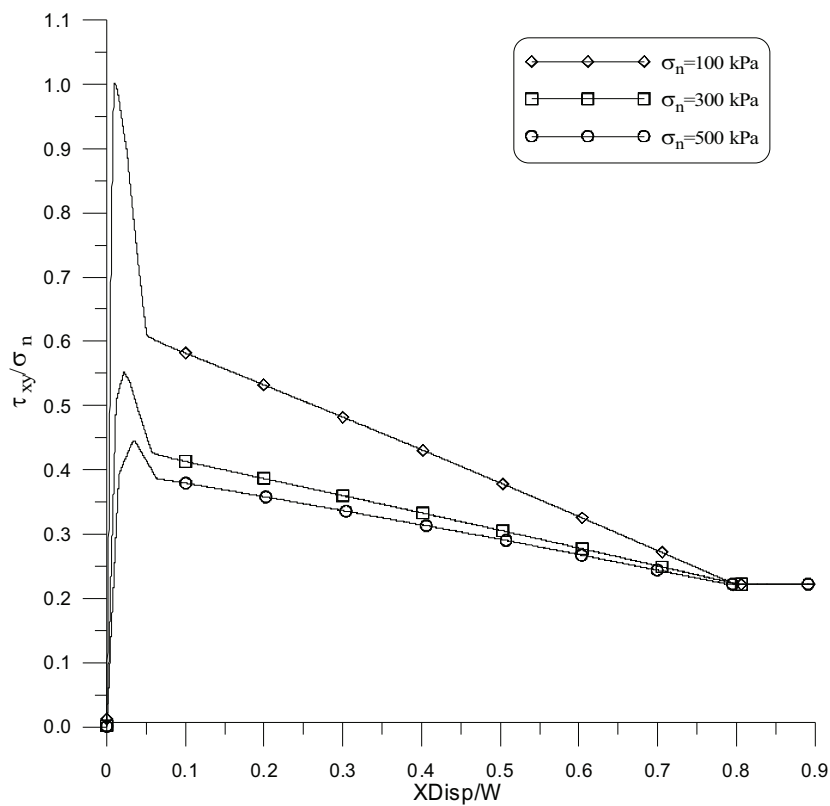


Fig. 4.37 Stress ratio vs. horizontal displacement ratio under different normal stresses ($K_0=3$ and $\psi=0$)

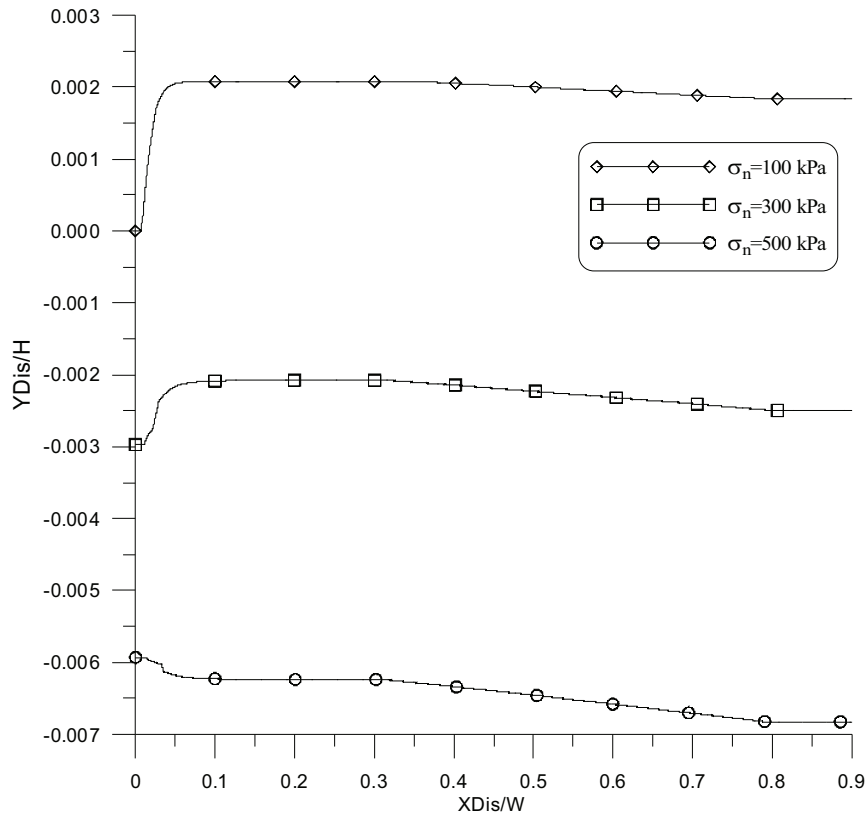


Fig. 4.38 Vertical displacement ratio vs. horizontal displacement ratio under different normal stresses ($K_0=3$ and $\psi=0$)

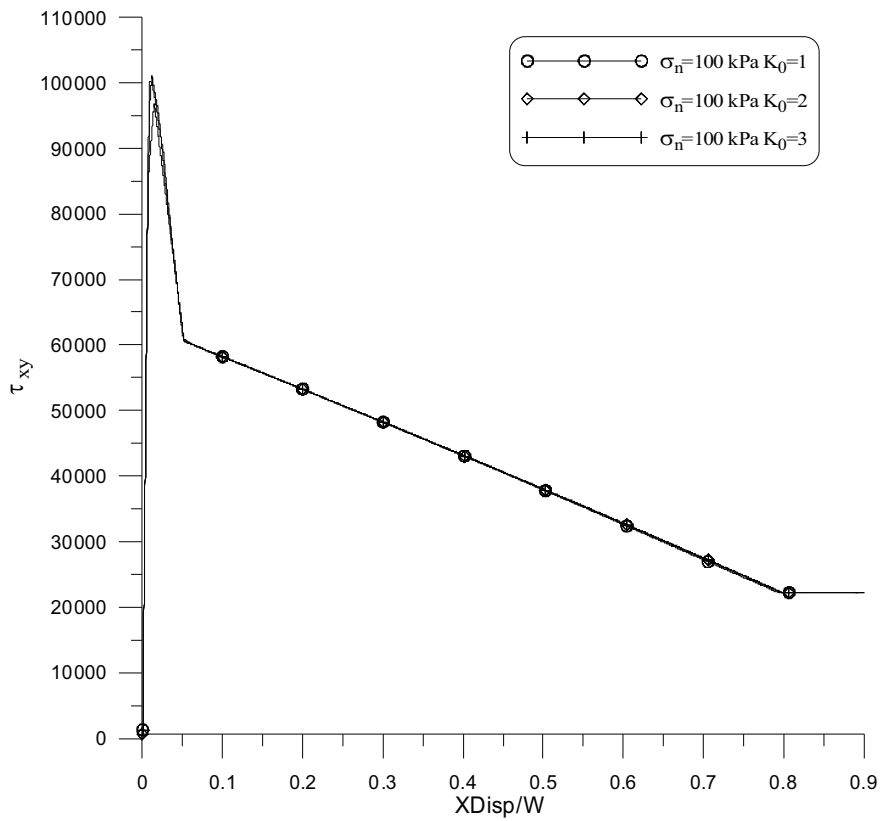


Fig. 4.39 Shear stress vs. horizontal displacement ratio under different normal stresses ($\psi = 0$)

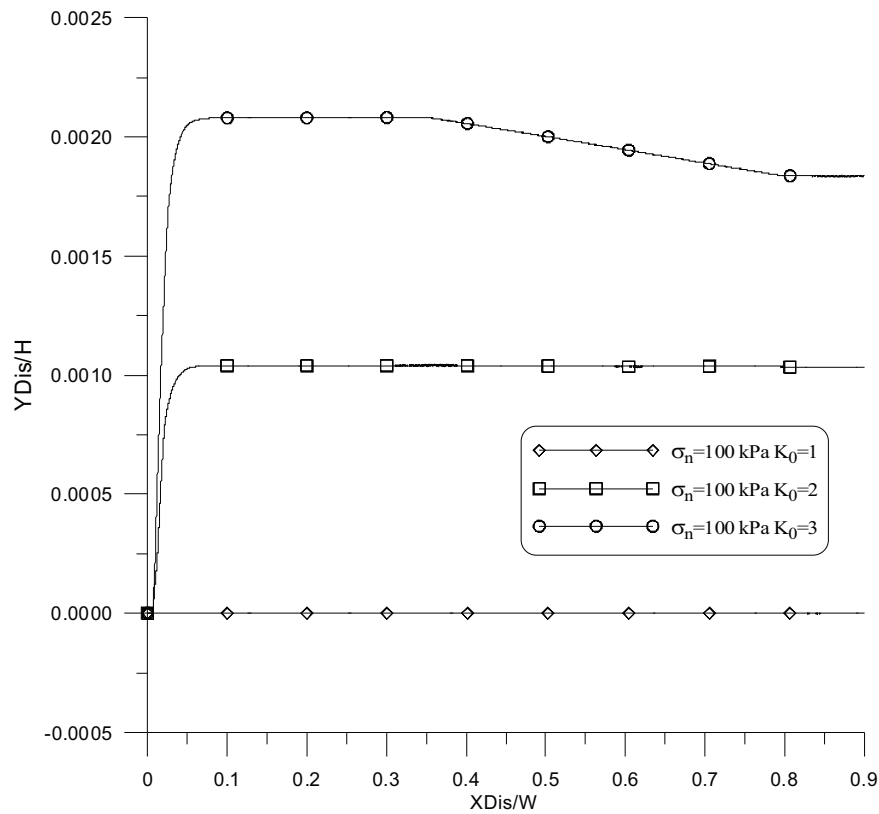


Fig. 4.40 Vertical displacement ratio vs. horizontal displacement ratio under different normal stresses ($\psi = 0$)

The influence of vertical normal stress is shown in Fig. 4.37 and Fig. 4.38. As the normal stress reduces, brittleness increases and the two-stage softening process becomes more apparent. On the other hand, the increase of vertical normal stress restrains the dilatant behaviour of specimen. Under 100 kPa normal stress, the vertical displacement increases and remains positive, indicating dilatant behaviour. Under 300 kPa normal stress, the vertical displacement decreases and keeps negative which indicates compressive displacement. Under 500 kPa normal stress, the vertical displacement increases and remains compressive.

The effect of K_0 is also demonstrated in Fig. 4.39 and Fig. 4.40. It is evident that K_0 has little influence on the shear stress except that the peak shear stress increases with higher K_0 values. However, it affects dilation behaviour significantly. With $K_0 = 1$, the dilation is almost zero. But the vertical displacement increases by almost twice as K_0 varies from 2 to 3.

4.3.2 Simulation of direct shear box test with finer grid

Potts et al. (1987) and Cividini & Giuda (1992) performed numerical modelling of direct shear box test using the finite element method. Similarly, in this section, the numerical model simulates a specimen with dimensions of $6 \times 6 \times 2$ cm subjected to a normal stress of 100 kPa. The analyses are performed in plane strain to model a shear box 6 cm long by 2 cm deep of two equal halves.

The two-stage softening model is adopted and the material parameters are similar to those used in Section 4.3.1 and the previous triaxial compression test simulations. They are listed concisely in Table 4.10.

Table 4.10 Material parameters

| | |
|---|---|
| 1 | $\gamma_p = 0, \gamma_{pr} = 0.0175, \gamma_r = 0.3$ |
| 2 | $\phi_p = 27, \phi_{pr} = 26, \phi_r = 17$ |
| 3 | $c_p = 1e5, c_{pr} = 4e4, c_r = 0$ |
| 4 | $\psi = 0$ |
| 5 | $\sigma_n = 1e5$ |
| 6 | $K_0 = 1 \quad \sigma_{xx0} = -1e5, \sigma_{yy0} = -1e5, \sigma_{zz0} = -1e5$ |

The simulation of the shear box includes lower, upper and cap loading parts. All these parts are modelled by very stiff elements with a linear elastic model. The elastic parameters are shown in Table 4.11.

Table 4.11 Elastic parameters of shear box

| ρ (kg/m ³) | E (Pa) | ν | K (Pa) | G (Pa) |
|-----------------------------|----------|-------|----------|----------|
| 7850 | 1.03e11 | 0.35 | 1.144e11 | 3.815e10 |

The geometry and boundary conditions are shown in Fig. 4.41, Fig. 4.42 and Fig. 4.43. The lower shear box is fixed in both x and y directions and a horizontal velocity v_x is assigned to the upper shear box. The horizontal velocity value is 3.0×10^{-7} m/s. A normal pressure σ_n is imposed on the top of the shear box. The initial stress is set to be $-1e5$ Pa (negative sign means compression in *FLAC*).

Two schemes are considered in simulating the contact between shear box and specimen. In Scheme I (with 62×42 grid) no interfaces are set between shear box and the specimen whereas in Scheme II (with 64×44 grid) interface elements are placed between shear box and the specimen (see Sabzalisenjani and Nikraz, 1998).

4.3.2.1 Scheme I without interfaces



Fig. 4.41 Material models

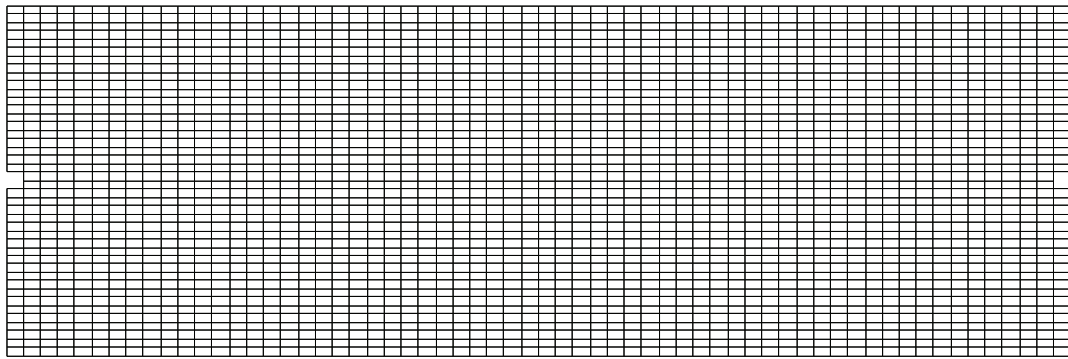


Fig. 4.42 Geometry and grid

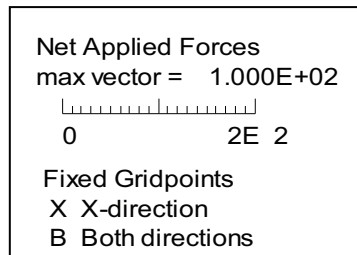
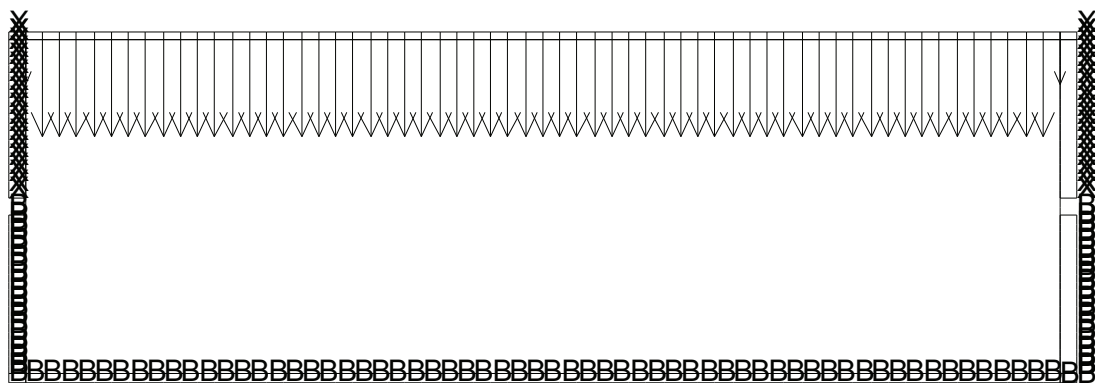


Fig. 4.43 Applied force and boundary conditions

The diagram of shear stress vs. shear strain is shown in Fig. 4.44. It is obvious that the shear stress reduces very rapidly after peak and then arrives at residual value slowly after large displacements. This is consistent with the characteristics of the two-stage softening model (Fig. 2.20).

Fig. 4.45 presents the relation between vertical and horizontal displacements. Compared with the horizontal displacement, the vertical displacements are very small and they eventually become stable.

It can be seen from Fig. 4.46 that the deformation is concentrated in a shear band and Fig. 4.47 indicates that the distribution of shear strain is almost uniform along the shear band.

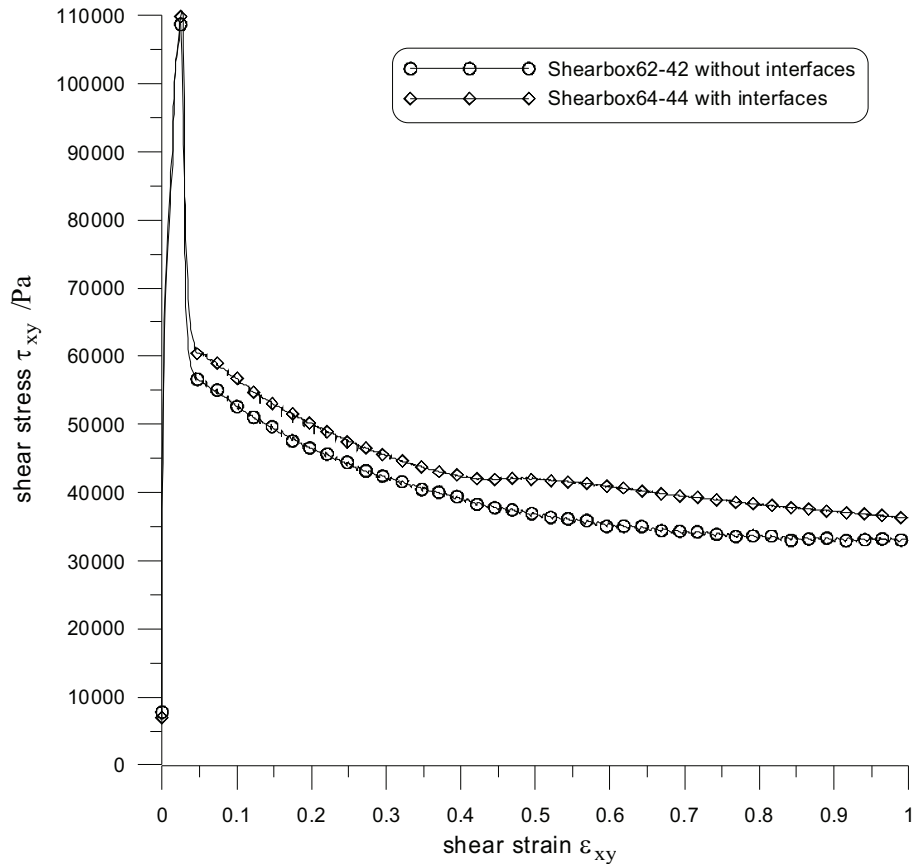


Fig. 4.44 Shear stress vs. shear strain for both schemes

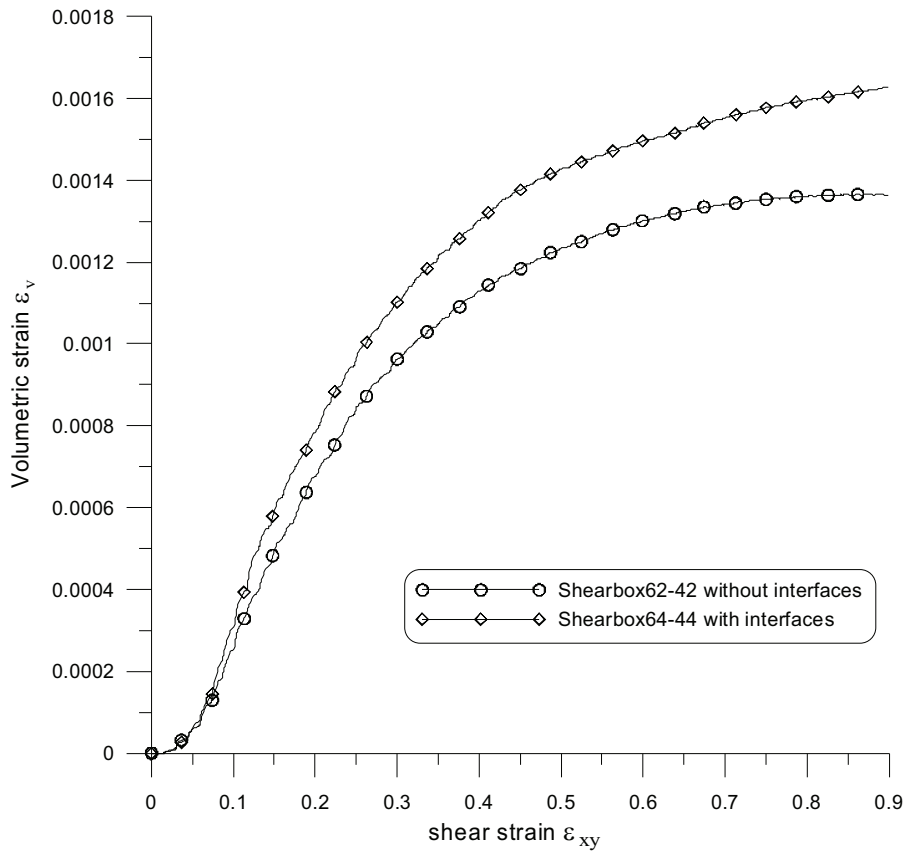


Fig. 4.45 Volumetric strain vs. shear strain for both schemes

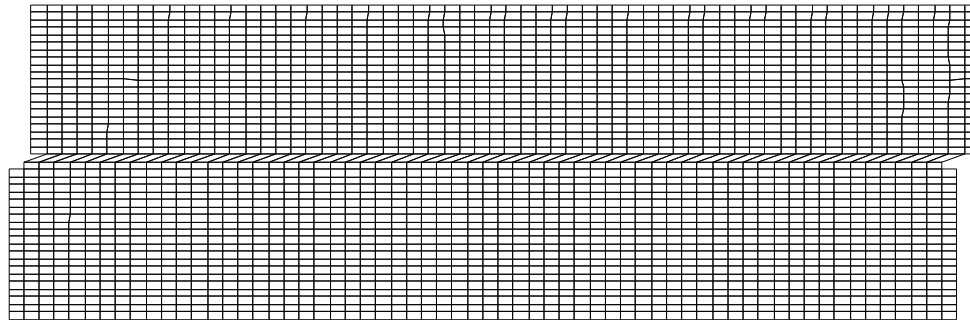


Fig. 4.46 Deformed grid without interfaces

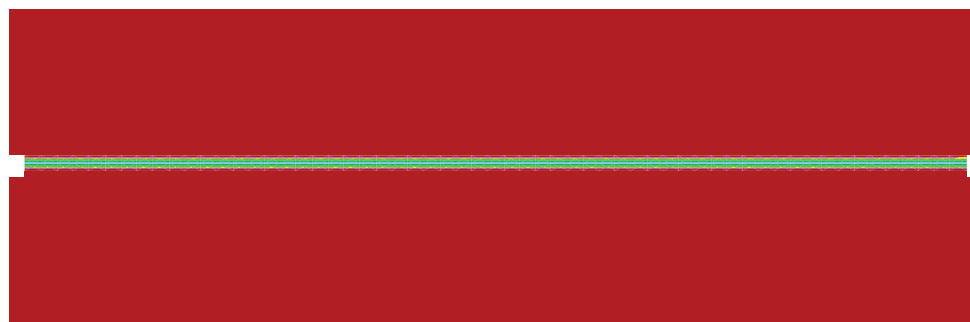


Fig. 4.47 Shear strain contour without interfaces

4.3.2.2 Scheme II with interfaces

In scheme II, six interfaces between shear box and the specimen are defined as glued to prevent any slip or separation. The shear stiffness and normal stiffness of these interfaces are determined using the method described in *Itasca FLAC Manual (2005)*. The interface configuration is given in Table 4.12.

Table 4.12 Interface configuration

| No. | Type | Normal stiffness (Pa) | Shear stiffness (Pa) |
|-----|-------|-----------------------|----------------------|
| 1-4 | glued | 6.731e11 | 6.731e11 |
| 5-6 | glued | 1.3461e11 | 1.3461e11 |

Apart from the presence of these interfaces, all the other model configurations such as material model, geometry and applied force are the same as those in scheme I.

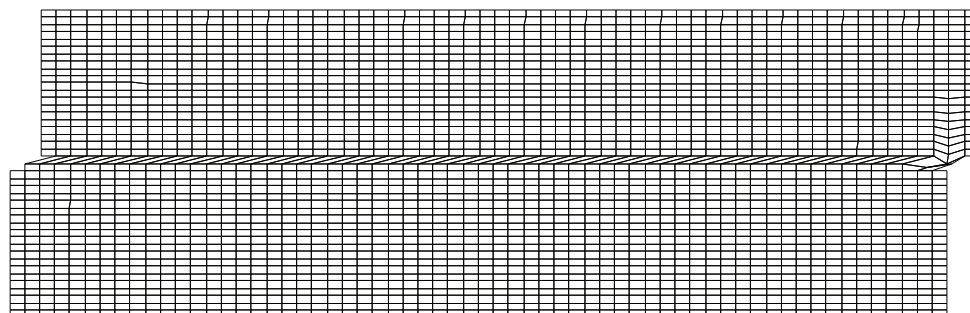


Fig. 4.48 Deformed grid with interfaces

The relationship between shear stress and shear strain is also shown in Fig. 4.44. It exhibits the same character as demonstrated in scheme I. Both curves for schemes I and II are similar before post-rupture strength and afterwards differ slightly with just a little higher shear stress in scheme II than that in scheme I.

Meanwhile, the vertical displacements shown in Fig. 4.45 are a little larger than that of scheme I but they still remain very small and become constant at large horizontal displacements. The deformation is also concentrated in a shear band as seen in Fig. 4.48 and the resulting uniform distribution of shear strain is presented in Fig. 4.49.

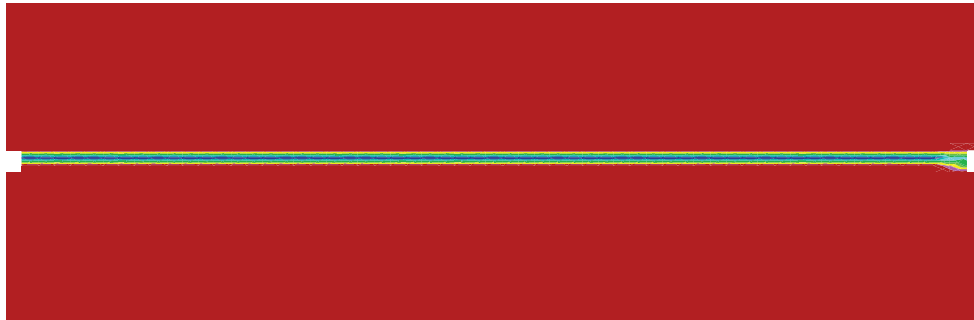


Fig. 4.49 Shear strain contour with interfaces

4.4 Summary

This chapter illustrates the accuracy of plastic deformation calculation in *FLAC* and that no special solution technique is needed in *FLAC*.

The triaxial tests and direct shear box test are reproduced using the two-stage strain-softening model. The numerical results demonstrate the capability and efficiency of the two-stage softening model via *FLAC* to simulate the softening behaviour of stiff clays.

The mesh influence can be eliminated efficiently with a special scheme that relates the slope of softening to a characteristic dimension of the elements in such a way that their ratio is kept constant.

Chapter 5. Numerical modelling of delayed progressive slope failure in stiff clays using strain-softening models

This chapter studies the general development process of progressive slope failure involving a delayed mechanism due to long term pore pressure equalization. To provide context, some representative case histories of progressive failure in stiff clays comprising both numerical and field experimental results are presented. Afterwards, simulations of delayed collapse of cut slopes in stiff clays using the one-stage softening model are performed in order to justify the validity and capability of the numerical procedure to simulate this type of behaviour. The results of Potts et al. (1997) are used as reference. The rest of the chapter is devoted to the analysis of the same problem, progressive failure in cut slopes, using the two-stage softening model. Effects of K_0 , surface suction and slope geometry are examined. Special attention is given to the effect of the softening rate on slope failure characteristics. Two main hypotheses are made concerning the selection of peak strength in the model: i) Bulk strength, i.e. the strength that incorporates the effect of existing fissures and discontinuities in the material, and ii) Strength of the intact clay. In addition, the issue of slope stability is recast in terms of the critical cutting height for the various cases considered.

5.1 Development of progressive slope failure in stiff clays

5.1.1 Developing history of slope movements

Vaunat et al. (1994) and Leroueil et al. (1996) suggested dividing slope movements into four stages:

- (1) The pre-failure stage, including all the deformation processes leading to failure. This stage is controlled mostly by deformations due to changes in stresses, creep and progressive failure;
- (2) The onset of failure, characterised by the formation of a continuous shear surface through the entire soil mass;
- (3) The post-failure stage, which includes movement of the soil mass involved in the landslide, from just after failure until it essentially stops. It is generally characterised by an increase of the displacement rate followed by a progressive decrease in velocity;
- (4) The reactivation stage, when soil mass slides along one or several pre-existing shear surfaces.

5.1.2 Transition from local soil failure to general slope failure

Pre-failure includes all movements before first-time failure, which are due to the combination of phenomena such as elastoplastic deformations associated with changes in effective stresses and strains and displacements related to progressive failure. The mechanisms of progressive failure and the relevant softening analysis methods have been illustrated in Section 1.1.2.

Urciuoli et al. (2007) demonstrated in detail the local soil failure before general slope failure involving the development process of progressive failure. This process is critical in analysing the slope failure which is strongly dependent on the deformation patterns in the pre-failure stage since they affect the mobilised shear strength.

Engineering experience shows that many natural slopes are constituted by high overconsolidated clay whose structure and overconsolidation ratio normally result in brittleness. Natural slopes are generally characterized by non-uniform initial stress field which depends on the complex geological processes that led to slope formation (Picarelli 2000). Additional stresses induced by changes in boundary conditions (surcharges, excavations, groundwater recharge, etc.) can further increase the local differences in stress level. High stress levels can induce localised plastic shear strain and formation of local shear discontinuities. Therefore, slope failure process is firstly local with formation of plastic zones and then becomes general.

Local soil failure occurs when the shear strength is mobilised in a limited zone of the soil. D'Elia et al. (1998) stated that this mechanism might involve a pre-existing discontinuity, such as a fissure or a joint. In intact highly overconsolidated clay, local failure may lead to soil destructuration (Leroueil and Vaughan 1990) due to the breaking of bonds between particles or aggregates, and causes mechanisms of strain softening and formation of shear discontinuities.

General slope failure occurs with large displacements. Slope fails as a slide when the shear strength is fully mobilised everywhere along a slip surface. If a weak surface or a discontinuity, such as a bedding surface, a joint or a shear pre-exists in the soil, general failure may cause a complete mobilisation along the discontinuity. In such a case, slope failure essentially depends on the stress state and available operational strength along the weak surface.

Riedel (1929) described the effects of localised shear strain and Skempton (1967) reported fundamental observations on the fabric induced in direct shear tests. Riedel (1929) observed that rupture is preceded by formation of short discontinuous shear fissures which are not aligned to the direction of imposed shear displacement (Stage 1 in Fig. 5.1). As the shear force increases, further shear fissures form with different orientations (Stage 2 in Fig. 5.1). According to their orientation, they are called Riedel or thrust shears, as proposed by Skempton and Petley (1967). All these fissures are referred to as minor shears, being caused by small relative displacements. Only in the final stage, a continuous shear discontinuity, the so-called principal shear (Skempton and Petley 1967), eventually forms in the direction of shear force (Stage 3 in Fig. 5.1). Thus, a shear zone develops. This has a special fabric characterized by a number of fissures bounding intact soil elements, which sometimes are referred to as shear lenses, and a continuous slip surface. Further displacements along the slip surface lead to orientation of clay particles along the slip surface causing a decrease of the shear strength towards its residual value.

In addition, the mechanism of rupture observed in direct shear tests might occur also in the field, if failure is forced by rotation of the principal stresses. In fact, field evidences of shear-induced fabric show several similarities with the fabric of specimens subjected to direct shear tests (Picarelli et al., 1997).

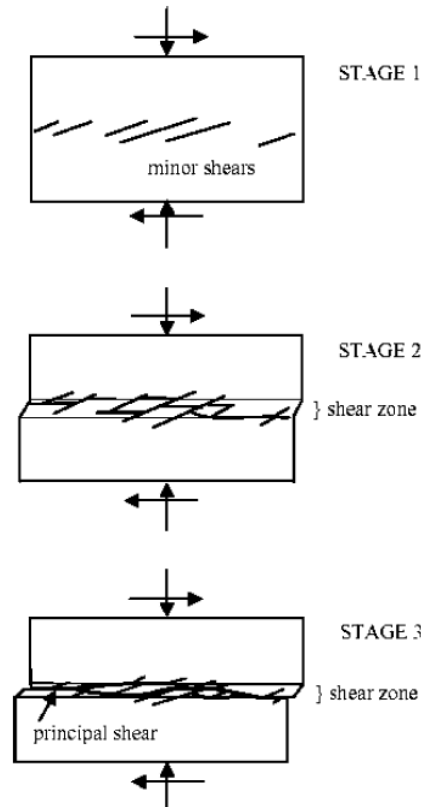


Fig. 5.1 Shear-induced fabric during a direct shear tests (Picarelli et al., 2000, adjusted after Skempton, 1967)

Leroueil (2001) also explained that slope failure is characterised by the formation of a continuous slip surface through the entire soil or rock mass. The slip surface develops within a weakened zone. Observations also show that there is an intermediate structure surrounding the slip surface which is usually called the shear zone (see Fig. 5.2).

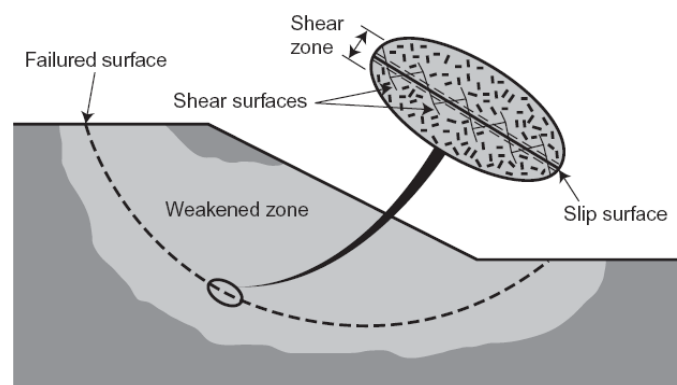


Fig. 5.2 Weakened zone, shear zone and slip surface in a slope (Leroueil, 2001)

In particular, Urciuoli et al. (2007) interpreted the process of a cut slope failure (Fig. 5.3) on the basis of considerations by Skempton and Petley (1967) and by

Morgenstern and Tchalenko (1967), suggesting a possible evolution of slope failure by localised shear strain and propagation of a slip surface in intact soils.

As seen in Fig. 5.3, local failure firstly occurs in a limited zone at the toe of the cut, where the peak strength is mobilised along directions depending on the direction of local principal stresses (Fig. 5.3a). This process may produce small shear fissures (minor shears) in the direction of failure planes (Fig. 5.3d). Such fissures are not necessarily consistent with formation of a continuous slip surface; therefore, at this stage only finite strains occur. A slip surface can develop only in a subsequent phase, as a consequence of further shear stress increase, causing a rotation of failure planes and formation of new shears, which merge into a unique principal shear (Fig. 5.3b and Fig. 5.3e). Further stress change can determine propagation of the shear zone and development of a slip surface. In this stage, the global safety factor of the slope remains larger than one, even if locally it is equal to one. A general slope failure will occur only when the slip surface reaches the ground surface, allowing for development of large displacements (Fig. 5.3c and Fig. 5.3f).

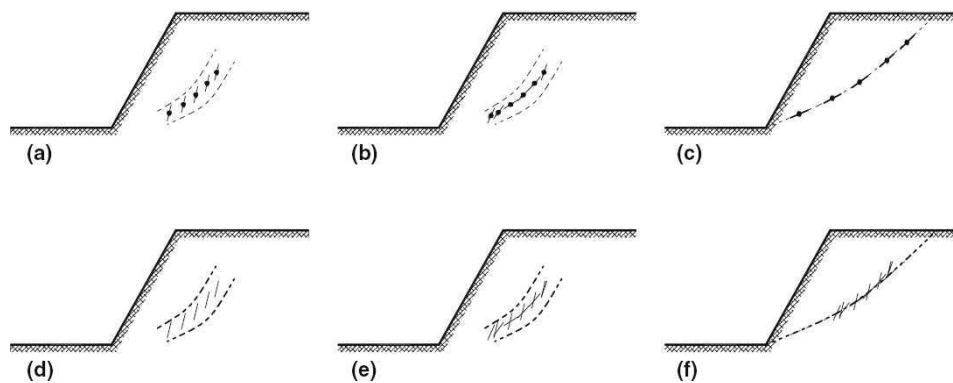


Fig. 5.3 A hypothetical process of slope failure induced by cutting (Urciuoli et al., (2007))

5.2 Representative case histories of progressive failure

It is well known that traditional limit equilibrium method with simplified assumptions does not take into account the role of pre-failure deformation on soil behaviour. Since Skempton (1964), Bishop (1967) and Bjerrum (1967) introduced progressive failure, some well documented case histories (Burland et al., 1977; Skempton, 1985), full scale experiments (Cooper et al., 1998), numerical analyses (Potts et al., 1990 and 1997) and analytical models (Gilbert et al., 1996) have confirmed that slope failure is often progressive. In this Section, some well-documented examples of progressive failure are discussed as background.

5.2.1 Progressive failure of Carsington dam

The progressive failure of Carsington dam has been studied by many authors (Dounias et al., 1988; Potts et al., 1990; Chen et al., 1992; Skempton & Vaughan, 1993). They analysed the behaviour of the Carsington dam failed in June 1984 just prior to completion. The Carsington dam was built above carboniferous mudstones, which are locally covered by about 1 m of ‘yellow clay’ that was left under the dam embankment (Fig. 5.4). In the numerical analyses, strain-softening soil behaviour was

assumed for all materials except for the mudstone foundation. Both total stress and effective stress analyses have been performed and compared.

The FEM analysis with one-stage softening model (Fig. 5.5) reproduces well the progressive development of the actual failure surface and provides reasonable agreement with observations made by instrumentation.

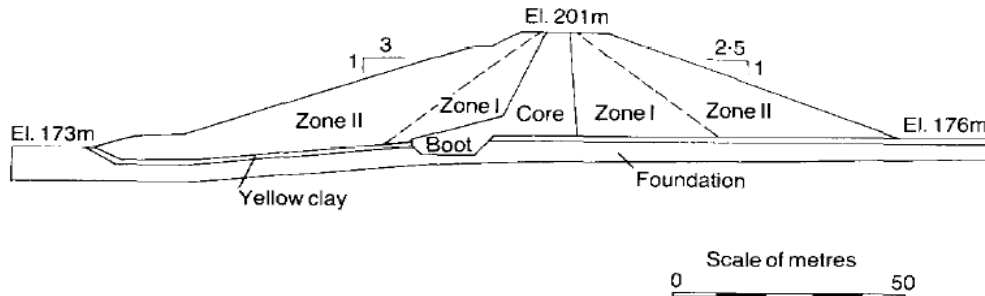


Fig. 5.4 Cross section of Carsington embankment (Potts et al., 1990)

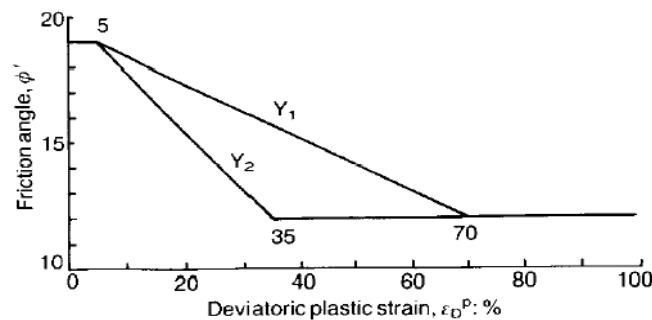


Fig. 5.5 Assumed softening of frictional angle with plastic strain for yellow clay (Potts et al., 1990)

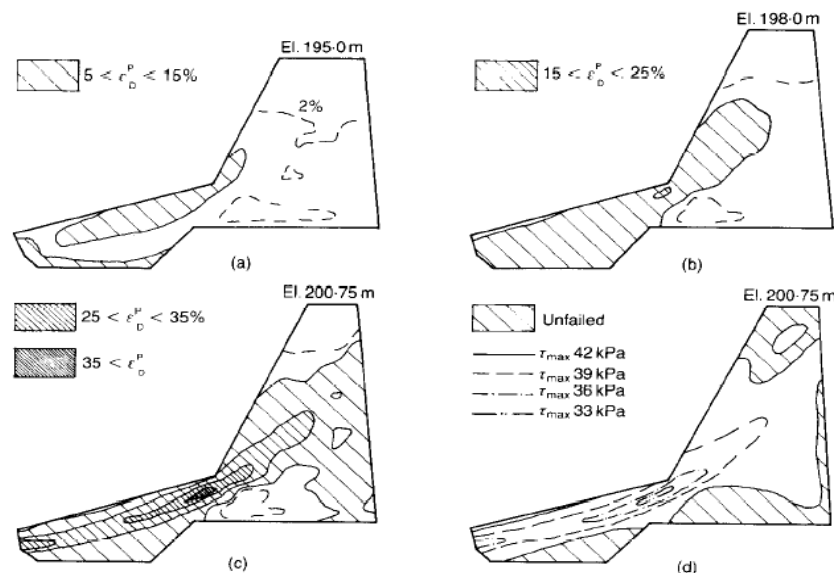


Fig. 5.6 (a)-(c) development of strains as collapse is approached; (d) strength mobilised just before failure in strain-softening zone (Potts et al., 1990)

All the results have shown that the failure of Carsington dam is due to progressive failure of the underlying yellow clay and the dam core materials. Failure was initiated in the boot area and then propagated upstream in the yellow layer and up through the

core. The major part of the core and boot reached local failure when the elevation of the embankment was at about 196 m, i.e., well before general failure, which occurred at elevation 200.75 m. This can be seen clearly in Fig. 5.6. Moreover, the progressive development of the actual surface was reproduced and abrupt collapse was observed. Skempton & Vaughan (1993) concluded that while movements prior to collapse were sufficiently large to cause concern, the measured deformation did not accelerate to indicate imminent failure until just before collapse. This suggests that when progressive failure is involved, measurements of deformation cannot be relied upon for monitoring stability.

5.2.2 Field evidence of progressive failure—Selborne cut failure

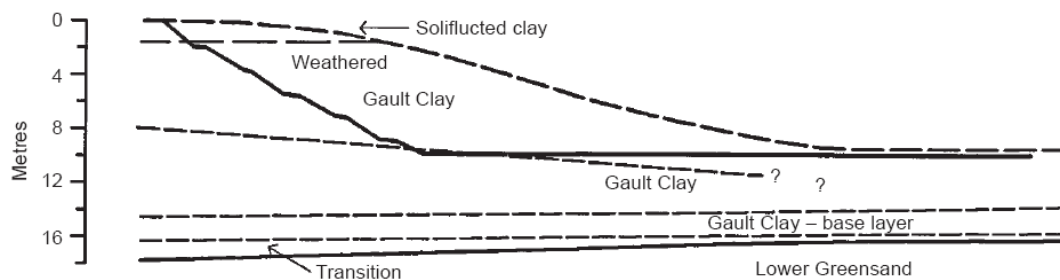


Fig. 5.7 Geological section and slope profile

A well instrumented experimental cut at Selborne, using piezometers, inclinometers and surface wire extensometer lines, has been reported by Cooper et al. (1998). The Selborne cut slope failure was caused by increasing pore pressures through some wells built within the slope. It is the first time that the development of progressive failure up to generalised failure is observed with detailed high-quality experimental data of deformation and pore pressure. Instrumentation, survey results and interpretations have been presented in papers by Muir Wood et al. (1995), Cooper (1996) and Cooper et al. (1998), as well as in a CD-ROM (Bromhead et al., 1998). This constitutes an important step forward for the analysis of progressive failure.

The Selborne cut is 9 m high, 2:1 slope in overconsolidated Gault clay which is stiff, brittle and highly plastic (Fig. 5.7). Failure occurred on 16 July 1989 (day 196 in the time scale used by Cooper et al. 1998). Results as well as observations reported by Cooper and co-workers, give interesting insights in the development of progressive failure which have been summarized in Fig. 5.8 (Leroueil, 2001).

The failure and eventual collapse of the slope took place as a result of a progressive failure mechanism, initiating rapidly at the toe of the slope and extending into the slope as pore pressures increased. At the same time a similar progressive failure is believed to have taken place starting from the slope crest. The continuous slip surface eventually forms with relative large deformations. The lower part of the slip surface, in high plasticity Gault Clay, formed as a single, highly polished, strongly striated slickenside. The upper part of the slip surface, passing through structure-less soliflucted materials and across the bedding of the upper weathered Gault Clay gave a much wider zone of shearing, estimated as being up to 2 mm across in places. The surface within this zone was much rougher, with little polishing, but striations were still clearly visible.

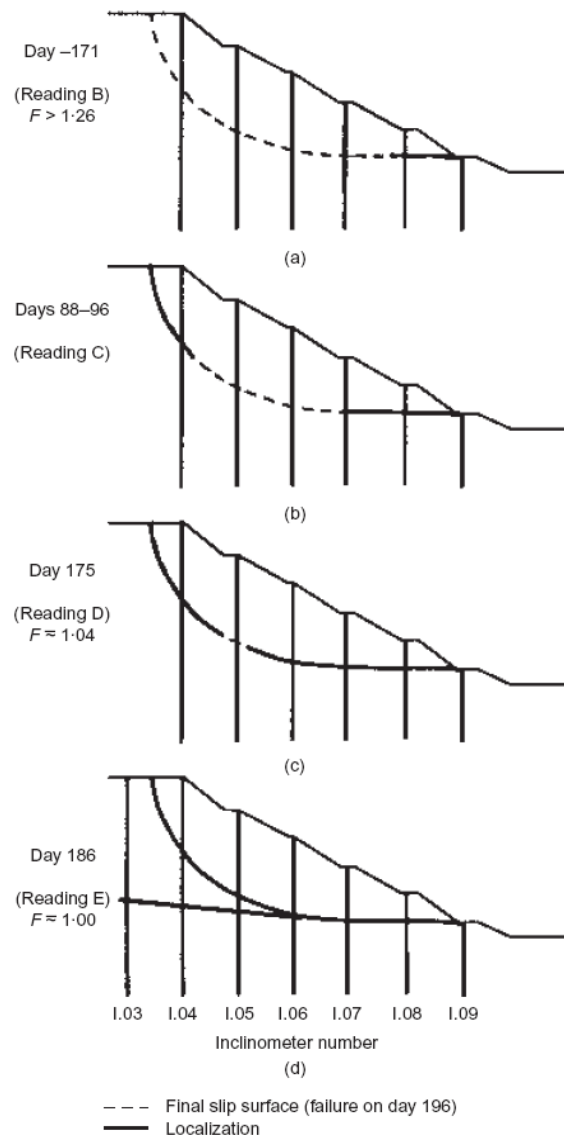


Fig. 5.8 Development of the slip surface at Selborne (after Bromhead et al., 1998)

As shown in Fig. 5.8, the progressive failure process of Selborne cut slope can be described as below:

- (a) All the inclinometers show a progressive deformation of the soil mass with occurrence of local shearing at some time. This is quite clear for inclinometer I.06, which shows continuous deformations on day 88, initiation of localization of displacement on day 175 and clear localization on day 186.
- (b) Shortly after excavation, localised shearing appeared at the toe of the cut, whereas the overall factor of safety was larger than 1.26. Localization was already evident on day 171 in inclinometer I.08, at a depth of about 2 m. Fig. 5.8a shows the part of the final slip surface on which failure had already been reached at that time.
- (c) On days 88-96, the profile in I.06 is continuous whereas localizations were observed at a depth of about 2 m in I.04 and I.08. Fig. 5.8b shows the localizations at the higher and lower parts of the final slip surface.

- (d) On day 175, localization was discernible in all the inclinometers, except inclinometer I.05 (Fig. 5.8c). According to Cooper et al. (1998), the global factor of safety was close to 1.04 at that time.
- (e) The last field reading on day 186 shows localization along the entire slip surface, and general failure occurred 10 days later (Fig. 5.8d). Another slip surface is developing, about 5 m below the first one (Fig. 5.8d).

The displacement-time curves for the critical elements of all the inclinometers affected by the failure are plotted together in Fig. 5.9. Inclinometer 9 near the toe of the slope experienced significant deflections starting immediately after slope cutting. Inclinometers 8 and 7, further into the slope, show a similar pattern but with less dramatic movements. Inclinometers 6 and 5, nearer the centre and back of the slope, show negligible movements for the first 400 days and only very small displacements during the early stages of pore pressure recharge (from around Day 0). Only with the onset of the final collapse stages did the central inclinometers show appreciable movements. It is obvious from Fig. 5.9 that the rate of displacement increased continually up to the point of collapse, illustrating the progressive reduction in the average mobilised shear strength along the slip surface with continuing displacement. In addition, by the time slip occurred, appreciable displacement (with maximum value greater than 25 mm) had taken place along an extension of the basal failure surface into the slope.

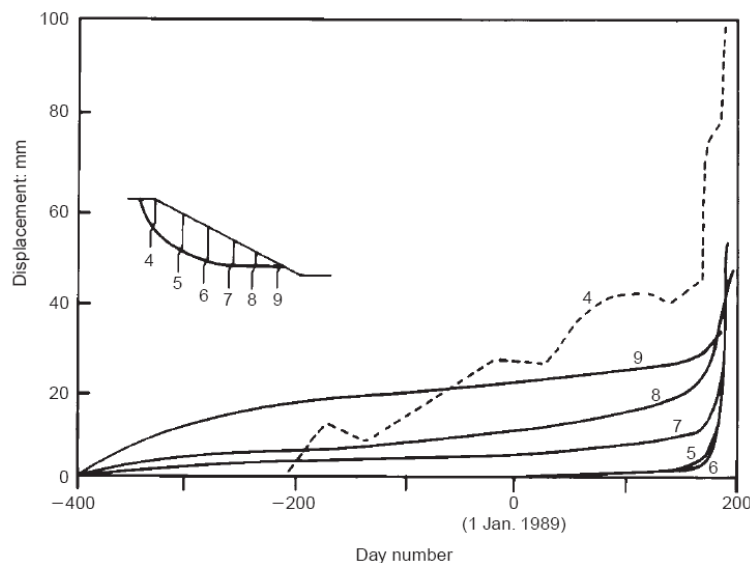


Fig. 5.9 Critical inclinometer element displacements with time (Cooper et al., 1998)

5.3 Analysis of delayed progressive slope failure in stiff clays

Progressive failure is also associated with delayed first-time failures of slopes in stiff fissured plastic clays. Discussions concerning progressive failure induced by excavation are reported by Potts et al. (1997) who related the development of general slope failure to pore pressure equilibrium.

In this section, the original results presented by Potts et al. (1997) are summarised first. Then non-softening *FLAC* analyses and *LEM* (Limit equilibrium method)

analyses are performed to study the effect of dilation. Afterwards, simulations via one-stage softening model are also performed. Comparison between original *FEM* analysis and *FLAC* modelling is made to justify the rationality and validity of the simulation of softening process using *FLAC*. Moreover, simulations via two-stage softening model are also conducted to elucidate the influence of post-rupture strength in slope failure.

Afterwards, parametric analyses to examine the effects of K_0 , surface suction and slope geometry are performed using one-stage and two-stage softening models.

In addition, a series of sensitivity analyses by varying the relevant plastic shear strain threshold values (γ_p , γ_{pr} and γ_r) are carried out to study the influence of softening strength parameters including both the strength magnitude and the softening rate.

5.3.1 Original *FEM* results from Potts et al. (1997)

Potts et al. (1997) used the same soil model as that used by Potts et al. (1990) to analyse delayed collapse in cuttings that involve unloading and swelling. This soil model has been described in section 3.4 in detail. Coupled consolidation analyses are performed that enable the history of swelling and the time to collapse to be predicted.

The parametric studies show that the occurrence of collapse is relatively insensitive to the value of K_0 . However, the value of K_0 strongly influences the location of the shear surface and the time to collapse (Fig. 5.10). There is a slight increase in the amount of progressive failure with increasing K_0 up to a critical value, after which the base rupture surface extends beyond the final inclined rupture surface, which relieves the stress in the slip prior to its final formation and reduces the amount of progressive failure.

The rupture surface has four parts (see Fig. 5.10):

- (a) the horizontal base shear, which forms early and reaches residual well before collapse;
- (b) a short transition length between peak and residual;
- (c) an inclined back surface, in which rupture has occurred but where strains are not sufficient for strain softening to start;
- (d) when K_0 is low, an inclined section near the original ground surface on which rupture only occurs post-collapse.

The deep-seated nature of slips predicted at the high values of K_0 is usually present in in-situ London Clay through field experience. At the higher values of K_0 , the rupture surface is developed by progressive failure at a greater depth than the critical surface which would be determined by limit equilibrium analysis. As a consequence the predicted operational strength on the rupture surface is less than that which would be determined for the same slope with the same pore water pressures by limit equilibrium analysis using a search technique to find the critical surface.

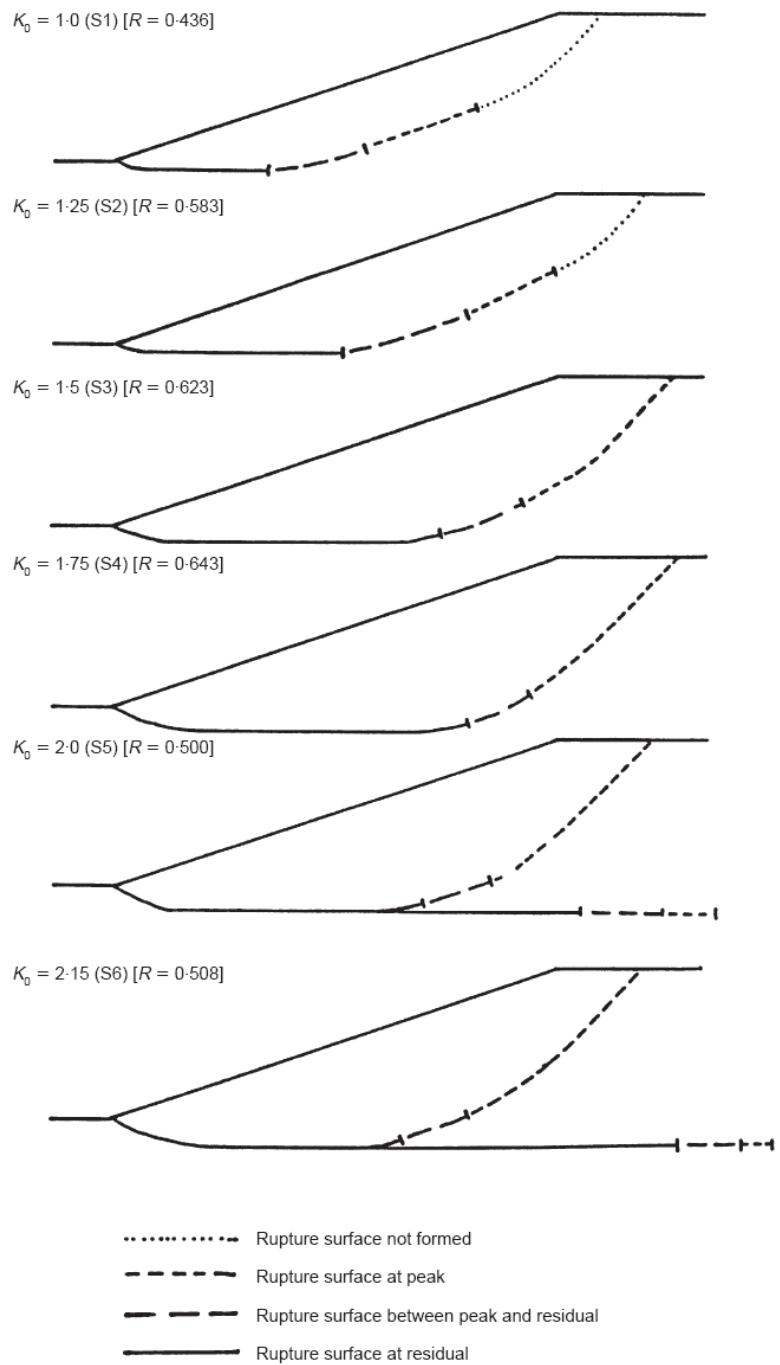


Fig. 5.10 Rupture surfaces predicted by the analyses on 3:1 slopes, 10 m high, with surface suction 10 kPa and varying K_0 (Potts et al., 1997)

Contours of deviatoric strain are given in Fig. 5.11. The 5% and 20% contours represent the start and end of strain softening. A horizontal shear zone propagates from just below the toe of the slope. This base shear rapidly drops from peak to residual as the rupture zone develops.

Fig. 5.12 shows predicted vectors of current (incremental) displacement 14.5 years after excavation, just before collapse is predicted. The vectors show the current mechanism of movement and indicate the eventual collapse mechanism. The absolute values of the displacements are of no significance.

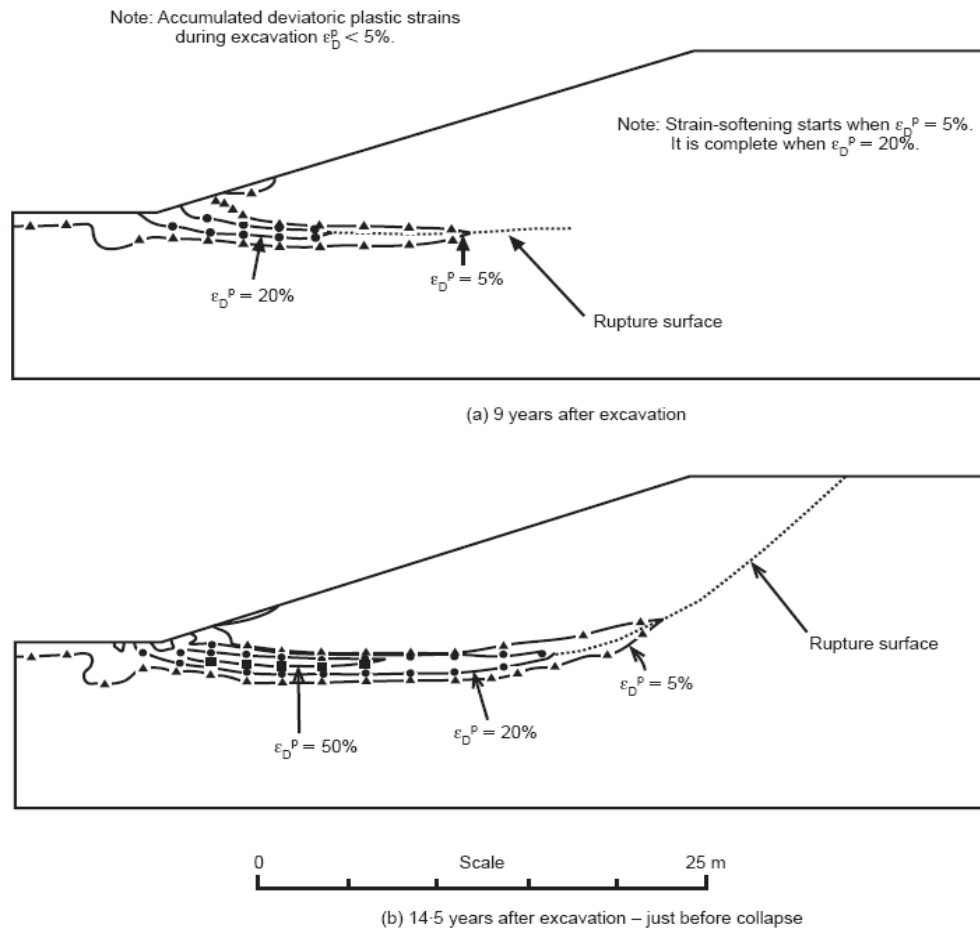


Fig. 5.11 Contours of accumulated deviatoric plastic strain (3:1 slope, 10 m high, $K_0=1.5$ and surface suction 10 kPa) (Potts et al., 1997)

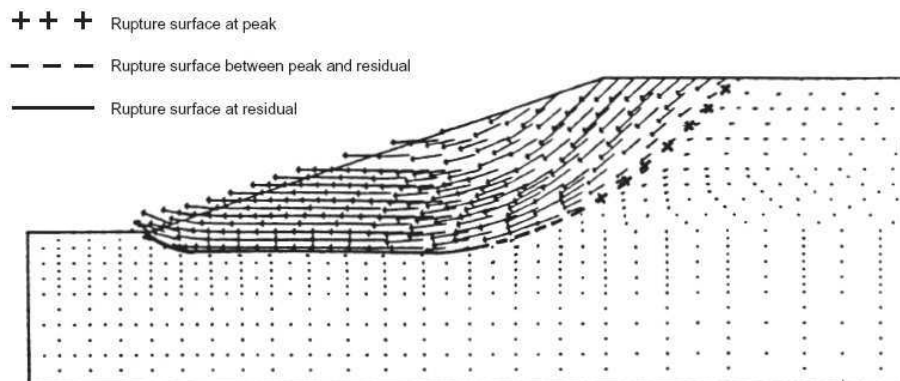


Fig. 5.12 Vectors of current displacement (14.5 years after excavation, 3:1 slope, 10 m high, $K_0=1.5$ and surface suction 10 kPa) (Potts et al., 1997)

Potts et al. (1997) concluded that the average operational strength at failure in delayed slides has been significantly less than the peak strength implying the progressive failure. Progressive failure can now be examined using the FEM results. Results of coupled finite element analyses assuming strain-softening soil with properties based on the Brown London Clay show that progressive failure is considerable, and fully explain the observed field behaviour. The failure delays experienced in the field are also reproduced by the analyses. Potts et al. (1997) also emphasized the role of the

hydraulic surface boundary condition which is controlled by climate and is important in controlling delayed collapse.

Fig. 5.13 shows the change with time of the predicted average pore pressure ratio— $r_u = u / \sigma_v$ (the ratio of the pore water pressure u to the vertical overburden pressure σ_v at a given point in soil body) on the rupture surface, and the horizontal displacement at mid-height of the slope. The average pore water pressure has got close to the value at collapse before the rupture surface at the base of the slide starts to form. The mid-height displacement then starts to accelerate. It is obvious that final collapse is quite abrupt, without significant warning from accelerating displacements or pore water pressures.

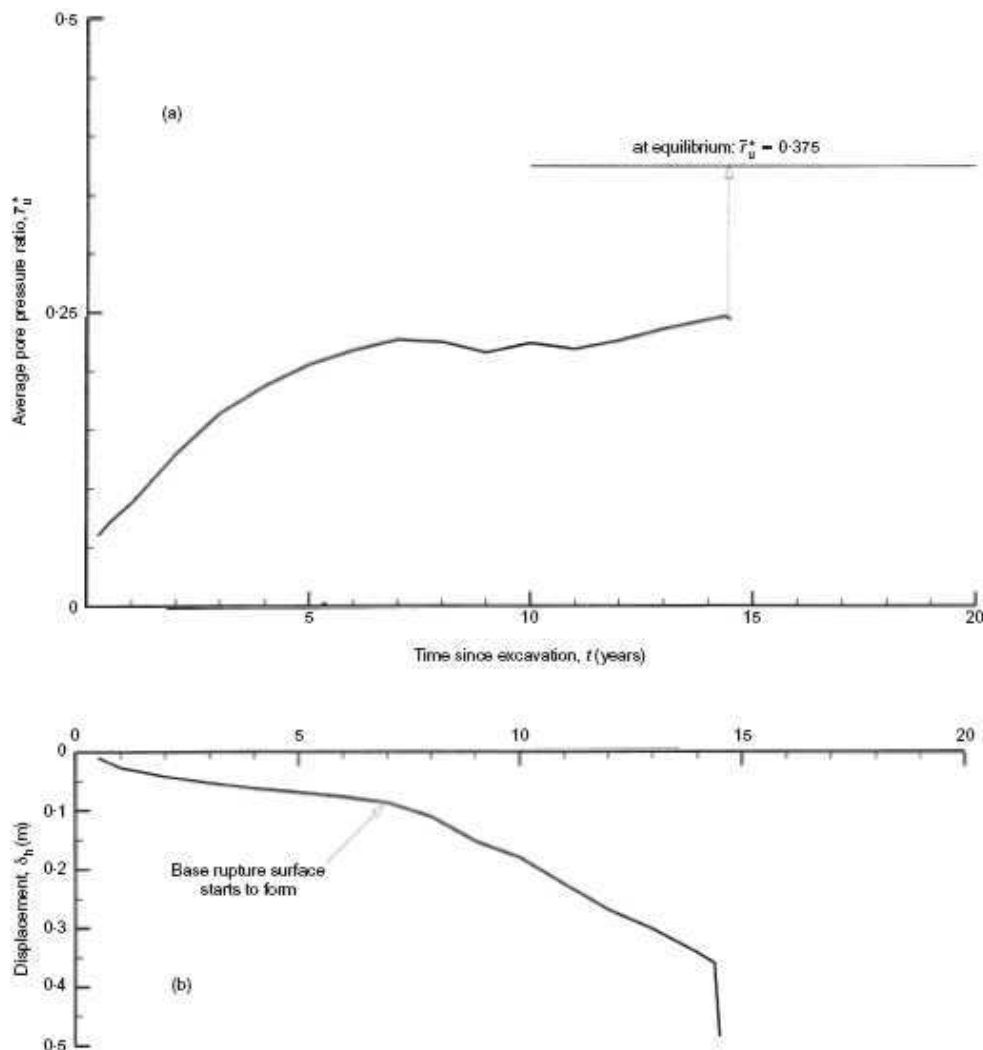


Fig. 5.13 (a) Development of average pore pressure ratio on the rupture surface, and (b) mid-slope horizontal displacement with time (14.5 years after excavation, 3:1 slope, 10 m high, $K_0=1.5$ and surface suction 10 kPa) (Potts et al., 1997)

5.3.2 General description of numerical model for delayed failures of cut slopes

A series of analyses of delayed progressive failure in cuttings have been performed using *FLAC* with both non-softening and softening models. In principle the finite

difference method may be considered similar to finite element approach, although numerical implementation differs.

The typical *FLAC* grid (mesh) is shown in Fig. 5.14 where the geometry slope is 1:2 and can vary in different modelling schemes, which is based on an initially rectangular mesh modelling the original ground with a small surface pore suction $u_b = -10$ kPa and hydrostatic variation of pore pressure with depth. No horizontal displacement was allowed on the vertical boundaries while the bottom boundary was completely fixed in both the vertical and horizontal direction. Three points indicating the top, middle and bottom of slope are also shown in Fig. 5.14 and will be used in the presentation of the results. They will remain the same for all subsequent analyses.

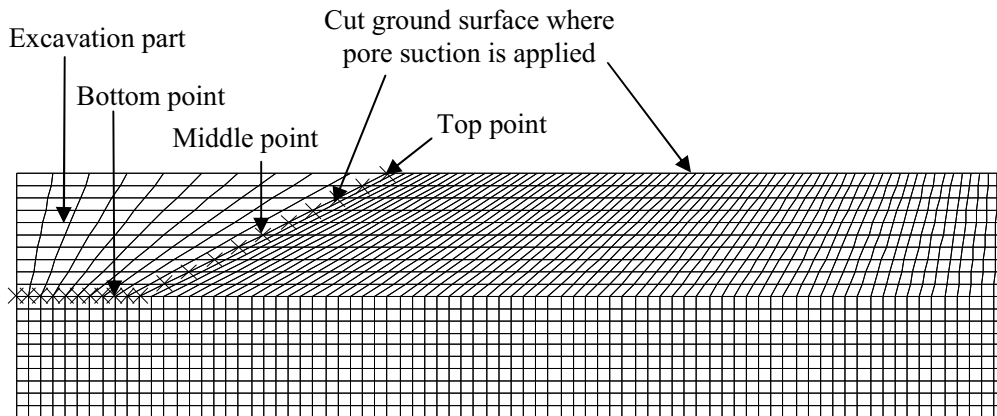


Fig. 5.14 Model geometry of slope in stiff clay

Table 5.1 Model parameters assumed in numerical analyses

| Property | Assumed value |
|---------------------------------------|--|
| Bulk unit weight | 18.8 kN/m ³ |
| Intact peak strength | $c'_p = 20$ kPa, $\phi'_p = 20^\circ$ |
| Bulk peak strength | $c'_p = 7$ kPa, $\phi'_p = 20^\circ$ |
| Residual strength | $c'_r = 2$ kPa, $\phi'_r = 13^\circ$ |
| Plastic strain at peak | $\varepsilon_{DP}^P = 5\%$ # |
| Plastic strain at residual | $\varepsilon_{DR}^P = 20\%$ # |
| Poisson's ratio | $\mu = 0.20$ |
| Young's modulus | $E = 25(p' + 100)$, (min. 4000 kPa) * |
| Angle of dilation | $\psi = 0$ |
| Coefficient of permeability | $k = 1e-6 \sim 1e-9$ m/s |
| Coefficient of earth pressure at rest | $K_0 = 1.0$ |
| Porosity | $n = 0.3$ |
| Water bulk modulus | $K_w = 2.0e9$ |

* p' is the mean effective stress in kPa ;

Note: the plastic shear strain used in *FLAC* tables for softening parameters is half of ε_D^P and may vary in different analysis.

The soil material is assumed to be entirely weathered London Clay and the relevant model parameters are listed in Table 5.1. The soil is assumed to remain completely saturated, and the prevailing groundwater table is considered to be at 1 m depth. Seasonal fluctuations in surface boundary conditions were not modelled in the analyses reported here because only the long term recovery of pore pressures after construction is relevant in the context of delayed progressive failure.

Excavation of the cutting was modelled in stages as an undrained event, by removing successive layers of elements at a uniform rate. As excavation is usually completed very quickly. It was assumed undrained in the analysis.

After excavation swelling was allowed with a surface boundary suction $u_b = -10$ kPa at the excavated slope, and maintained along the original ground surface. The vertical and bottom boundaries of the mesh were assumed to be impermeable. The swelling was allowed to proceed until failure or long term stability.

As stated in *FLAC* manual, in most practical cases of pore pressure driven systems, experience shows that the coupling between pore pressure and mechanical fields is not very strong. Therefore the numerical simulation can be performed with the flow calculation in flow-only mode (**SET flow on** and **SET mech off**), and then in mechanical-only mode (**SET mech on** and **SET flow off**), to bring the model to equilibrium. This is so-called staggered modelling

During the excavation stage, the slope undergoes mainly undrained deformation which means a mechanical driven system. Whereas in the course of swelling after excavation, the pore pressure variation is the primary driving factor. Then a pore pressure driven system is assumed and the aforementioned modelling method is used.

In this paper, the entire deformation process was simulated in five stages:

- (1) very short-time deformation just after excavation;
- (2) deformation well before collapse;
- (3) simulation of deformation with very small time increments just before collapse;
- (4) simulation of deformation with very small time increments just after collapse;
- (5) deformation after collapse.

In stages 1, 2 and 5, the time for the analysis was split into many small increments, with successive increments increased by a small ratio just a little greater than 1.0, say 1.005, in order to speed the calculation. The initial time increment is set as 1 day. However, for strain-softening analyses, as failure approaches, small changes in pore pressure will lead to large reductions in mobilised shear strength. Therefore at stages 3 and 4 the time increment was set to a small enough value (1 day) because the use of longer time increments around collapse will potentially introduce some error in the prediction of time to collapse. Each time increment gave only a small proportion of the ultimate change of pore pressure at a given point in the soil during swelling. This small divergence between the flow and mechanical states was considered acceptable.

FLAC can also model large deformation continuously even after failure, which is normally not easy to implement in finite element method because of the difficulty in monitoring convergence especially for strain softening.

Updating of material stiffness and mechanical equilibrium were carried out at the end of each time increment. The solution convergence is generally monitored via measurement of unbalanced force at grid points, which should be zero for complete equilibrium. In this paper, the ratio of unbalanced force to applied force for each grid point was used. Generally the maximum value of ratio throughout the grid was not allowed to exceed 2%, and this value was reduced to 1% at the end of every fifth time increment.

5.3.3 Non-softening analyses

Non-softening analyses are performed to investigate the effect of dilation in slope failure modelling and to determine a reasonable dilation value for the subsequent softening analyses.

Three analyses of a 10 m high and 2:1 slope were performed with non-softening soil ($c' = 7\text{kPa}$, $\phi' = 20^\circ$) (NS1 to NS3 in Table 5.3).

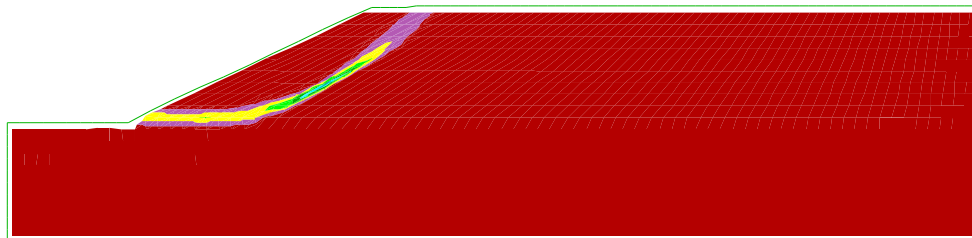


Fig. 5.15 Shear strain rate just after collapse (NS1)

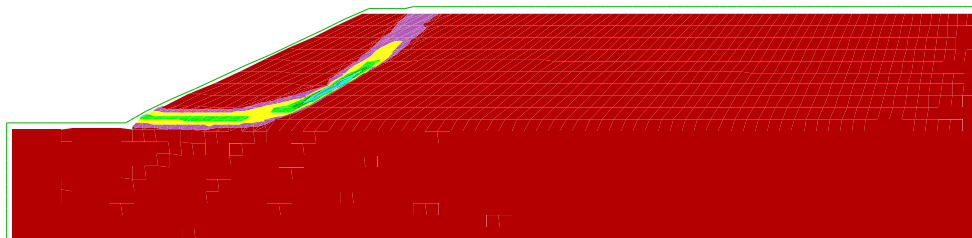


Fig. 5.16 Shear strain rate just after collapse (NS2)

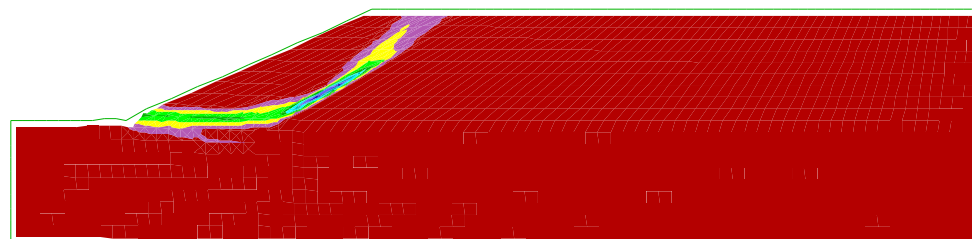


Fig. 5.17 Shear strain rate just after collapse (NS3)

In analyses NS1 and NS2 the dilation angle was assumed to be $\psi = 0$, and the initial in-situ stress was calculated by assuming $K_0 = 1.0$ and 1.5 . In each case collapse occurred during the swelling process with a well defined rupture zone of the same shape in each analysis (Fig. 5.15 and Fig. 5.16).

Analysis NS3 was similar to NS1 and NS2 except that the angle of dilation was $\psi = \phi'$. Well defined rupture surface was again predicted, but with a somewhat different shape from that predicted with $\psi = 0$ (Fig. 5.17).

Fig. 5.18 shows the change of mid-slope displacement with time. When rupture develops in NS3, the displacement does not accelerate as in NS1 and NS2. Instead there is a gradual increase in displacement with time. Two compensating effects induce this. On one hand, pore water pressures are generally increasing with time during swelling; on the other hand, in the rupture zone the clay is dilating and the pore water pressures are reducing. Hence at collapse the rate of decrease in pore water pressure in the rupture zone is matched by the increase due to swelling. The generation of negative pore water pressure is controlled by the permeability of the clay and the thickness of the rupture zone. This accounts for the gradual increase in displacement which is predicted with $\psi = \phi'$ once a rupture surface has formed. The pore water pressures generated by dilation essentially act as a partial brake on post-rupture movements. This effect is of great practical significance, since it helps to prevent rapid post-collapse movement of slides in strain-softening clays.

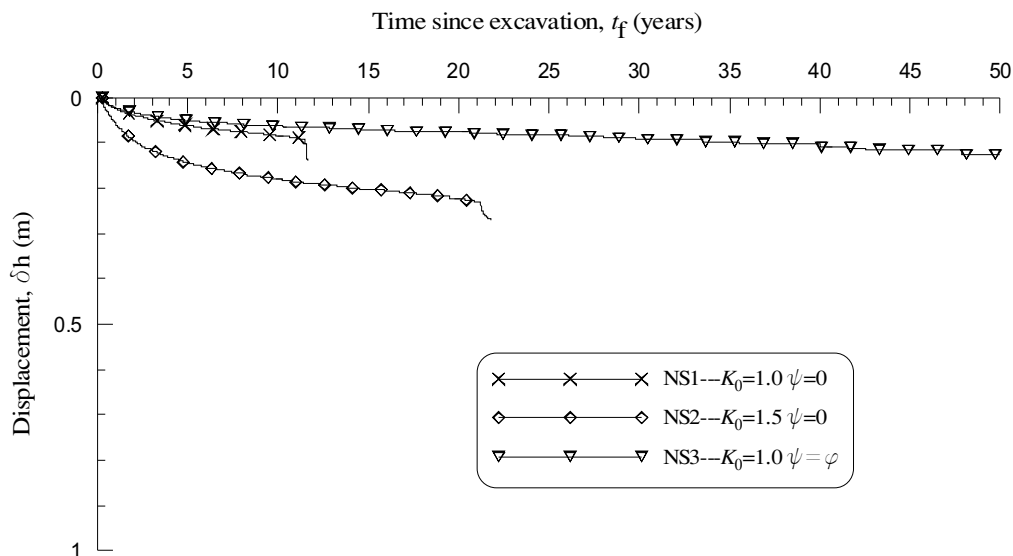


Fig. 5.18 Mid-slope horizontal displacement with time for NS1-NS3

Dilation will be restricted in the field to a much thinner rupture zone than that predicted by the analyses, where the rupture surface is approximately half an element thick (typically 0.5 m). Equilibration of pore water pressure would occur more rapidly in the field. Thus, if it is assumed that dilation occurs post-peak but only on thin shear surfaces, as occurs in laboratory tests, the analyses in which $\psi = 0$ are likely to give a better representation of undrained effects in clay in which discontinuities develop post-peak, unless an unrealistically large number of elements are used to allow a thin rupture zone to develop. Consequently, for analyses involving strain softening, an angle of dilation, $\psi = 0$, was adopted.

The angle of dilation also affects the position of the rupture surface predicted, and the stresses acting on it. The angles which the predicted rupture surfaces make with the plane on which the major principal stress acts are $\pm(45^\circ + \psi/2)$. The shear stresses acting on these rupture surfaces are given by:

$$\tau_f = \frac{c' \cos \phi' \cos \psi + \sigma'_n \sin \phi' \cos \psi}{1 - \sin \phi' \sin \psi} \quad (5.1)$$

When $\psi = \phi'$ Eq. (5.1) reduces to the Coulomb failure criterion, namely:

$$\tau_f = c' + \sigma'_n \tan \phi' \quad (5.2)$$

If $\psi \neq \phi'$ the strength on the rupture surface from Eq. (5.1) does not reduce to the Coulomb criterion. For instance, if $\psi = 0$, Eq. (5.1) reduces to:

$$\tau_f = c' \cos \phi' + \sigma'_n \sin \phi' \quad (5.3)$$

For clays the differences are small, but they need to be taken into account when comparisons are made between the results of numerical modelling and limit equilibrium calculations in which the Coulomb equation is adopted (Potts et al., 1990). If the rupture surface is kinematically constrained, then the differences are likely to be mainly in the strength on the rupture surface. If the rupture surface is not constrained, the differences are likely to be mainly in the location of the rupture surface itself.

As noted previously, the rupture surfaces predicted by the non-softening analyses depend on ψ and so does the relevant factor of safety. A series of stability analyses (Table 5.2) under drained condition using both *FLAC* and limit equilibrium method were performed to investigate the dilation effect.

5.3.3.1 LEM results

Limit equilibrium calculation using the Morgenstern-Price method is performed in this section. The boundary conditions are set the same as those described in section 5.3.2.

Fig. 5.19 to Fig. 5.21 show the FOS (Factor of safety) and predicted slip surfaces calculated by limit equilibrium method. The influence of strength parameters is obvious. With the strength decrease from peak to residual, the FOS reduces from 1.254 to 0.655. The shape of predicted slip surface changes accordingly. It is interesting to note that the FOS using post-rupture strength is close to 1.0 implying a relatively stable slope state.

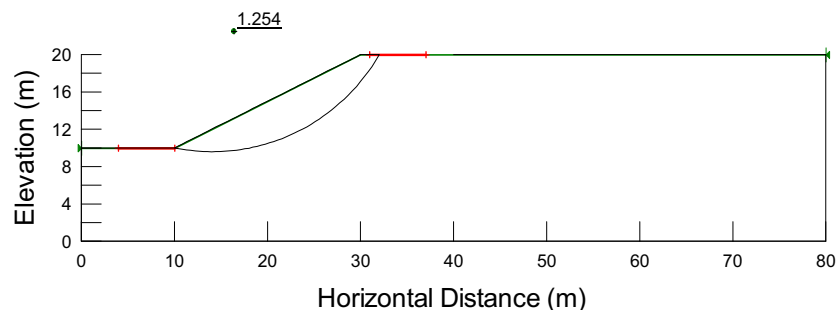


Fig. 5.19 FOS and predicted slip surface with peak strength parameters

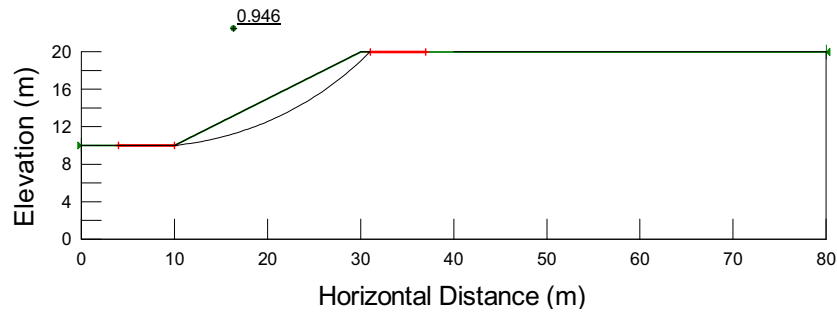


Fig. 5.20 FOS and predicted slip surface with post-strength parameters

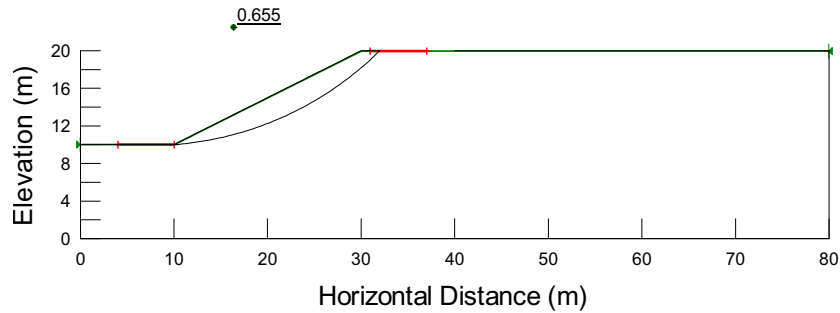


Fig. 5.21 FOS and predicted slip surface with residual strength parameters

5.3.3.2 Results of FOS analysis via FLAC

Fig. 5.22—Fig. 5.27 show the shear strain rate and the relevant FOS calculated by FLAC. The shear strain rate contours imply the rupture surfaces. Similarly, the FOS reduces as the strength decreases. In all the FLAC analyses, the FOS for $\psi = \phi'$ is a little higher than that with $\psi = 0$. This confirms further that dilation may increase the current slope stability.

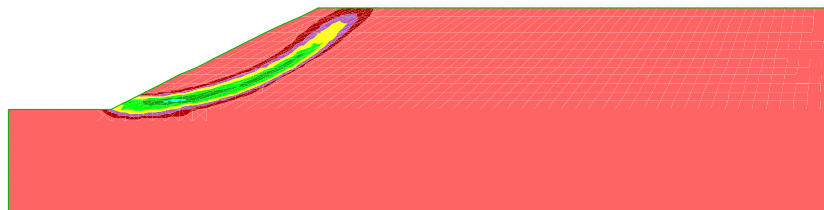


Fig. 5.22 Shear strain rate using peak strength with $\psi = 0$ (FOS=1.25)

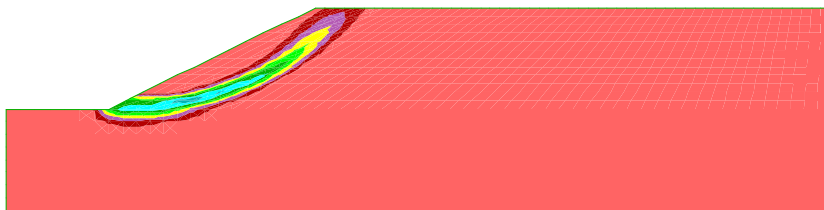


Fig. 5.23 Shear strain rate using peak strength with $\psi = \phi'$ (FOS=1.29)

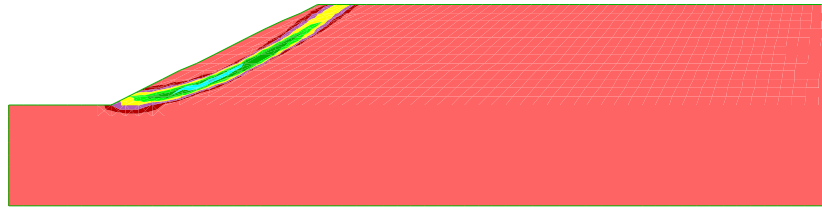


Fig. 5.24 Shear strain rate using post-rupture strength with $\psi = 0$ (FOS=0.92)

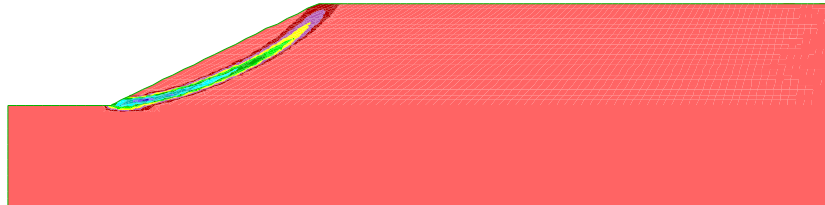


Fig. 5.25 Shear strain rate using post-rupture strength with $\psi = \phi'$ (FOS=0.96)

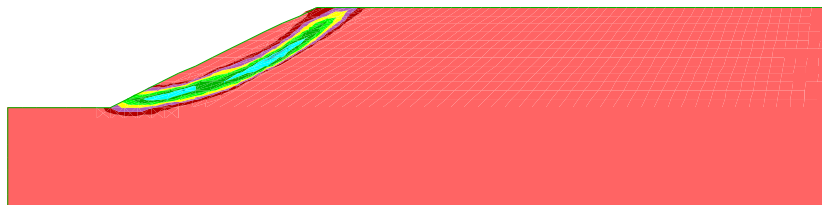


Fig. 5.26 Shear strain rate using residual strength with $\psi = 0$ (FOS=0.64)

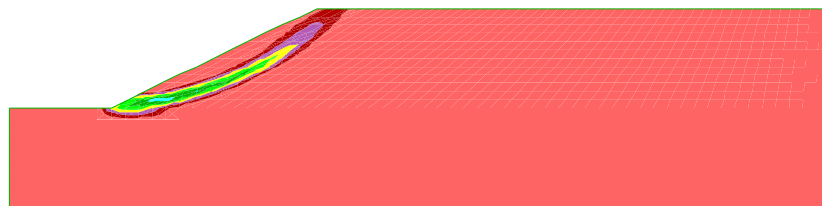


Fig. 5.27 Shear strain rate using residual strength with $\psi = \phi'$ (FOS=0.67)

5.3.3.3 Summary

All the FOS calculated by *FLAC* and *LEM* are listed in Table 5.2. It is interesting to find that the FOS calculated by *LEM* lies between the value for *FLAC* with $\psi = 0$ and that for *FLAC* with $\psi = \phi'$. This implies that *LEM* seems to calculate FOS using a ‘fictitious’ dilation angle between 0 and ϕ' .

Table 5.2 FOS calculation results

| FOS | Peak strength | Post-rupture strength | Residual strength |
|----------------------------|---------------|-----------------------|-------------------|
| <i>LEM</i> | 1.254 | 0.946 | 0.655 |
| <i>FLAC</i> $\psi = 0$ | 1.25 | 0.92 | 0.64 |
| <i>FLAC</i> $\psi = \phi'$ | 1.29 | 0.96 | 0.67 |

All the predicted failure surfaces with *FLAC* and limit equilibrium method are shown in Fig. 5.28. The critical circular slip surface was obtained from a limit equilibrium calculation using the Morgenstern-Price method. In the cut slope problem there is little kinematic restraint on the position of the rupture surface and it is evident from these plots that the rupture surfaces from the *FLAC* analyses are somewhat dependent

on ψ . It may be noted that at the soil surface the major principal effective stress is vertical and the rupture surfaces should be inclined at an angle of $(45^\circ - \psi/2)$ to the vertical. Inspection of Fig. 5.28 shows this to be so.

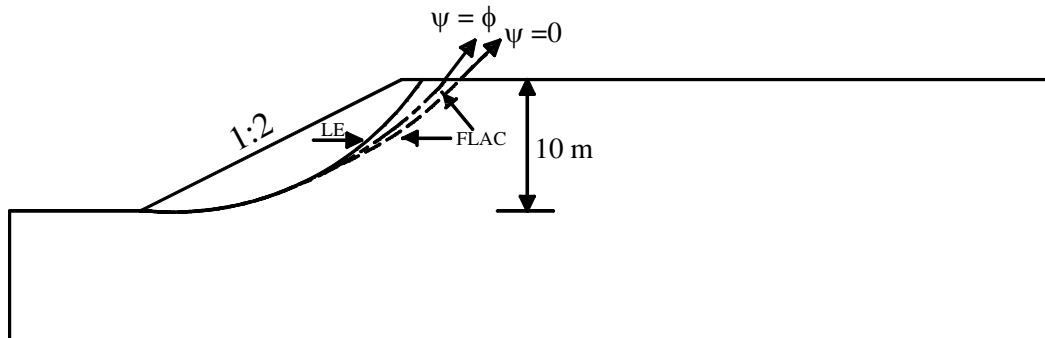


Fig. 5.28 Comparison of predicted rupture surfaces from non-softening analyses

In the softening analyses reported in this paper Eq. (5.3) is used. Since there is little apparent kinematic constraint on the rupture surfaces, and $\psi = 0$ is assumed, a small difference between the predicted slip surfaces and those in the field is likely.

5.3.4 One-stage softening analyses

FLAC can be used to analyse delayed slope failure by using the softening model. All the analysis cases with different slope and K_0 are shown in Table 5.3. The strength parameters in analyses S1-S11 are all assumed to be $c'_p = 7\text{kPa}$, $\phi'_p = 20^\circ$ (bulk peak strength), $c'_r = 2\text{kPa}$, $\phi'_r = 13^\circ$ (residual strength) and $\gamma_p = 0.025$, $\gamma_r = 0.1$.

Table 5.3 Results of non-softening and one-stage softening modelling

| Analysis | Height (m) | Slope ($\cot \beta$) | K_0 | ψ (deg) | u_b (kPa) | Middle slope X Displacement at collapse (mm) | t_f (years) |
|----------|------------|------------------------|-------|--------------|-------------|--|---------------|
| NS1 | 10 | 2 | 1.00 | 0 | -10 | 92.5 | 11.4 |
| NS2 | 10 | 2 | 1.50 | 0 | -10 | 230 | 21.2 |
| NS3 | 10 | 2 | 1.00 | 20 | -10 | >349 | >100* |
| S1 | 10 | 3 | 1.00 | 0 | -10 | 87 | 6.4 |
| S2 | 10 | 3 | 1.25 | 0 | -10 | 186 | 6.2 |
| S3 | 10 | 3 | 1.50 | 0 | -10 | 394 | 14.0 |
| S4 | 10 | 3 | 1.75 | 0 | -10 | 577 | 18.5 |
| S5 | 10 | 3 | 2.00 | 0 | -10 | 757 | 23.4 |
| S6 | 10 | 3 | 2.15 | 0 | -10 | 873 | 26.4 |
| S7 | 10 | 3 | 2.00 | 0 | -20 | >650 | >100* |
| S8 | 10 | 2 | 1.50 | 0 | -10 | 165 | 1.0 |
| S9 | 10 | 2 | 2.00 | 0 | -10 | 381 | 4.0 |
| S10 | 10 | 2.5 | 2.00 | 0 | -10 | 528 | 9.5 |
| S11 | 10 | 4 | 2.00 | 0 | -10 | >817 | >100* |

* Final calculation time

5.3.4.1 Results of representative analysis (S3)

Results are shown from a representative analysis of a 10 m high, 3:1 slope, with a value of the initial coefficient of earth pressure at rest, $K_0 = 1.5$ (analysis S3). Fig. 5.29 shows the *FLAC* model mesh.

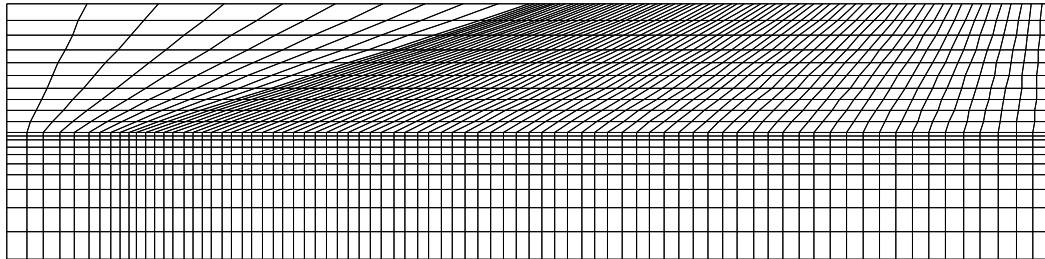
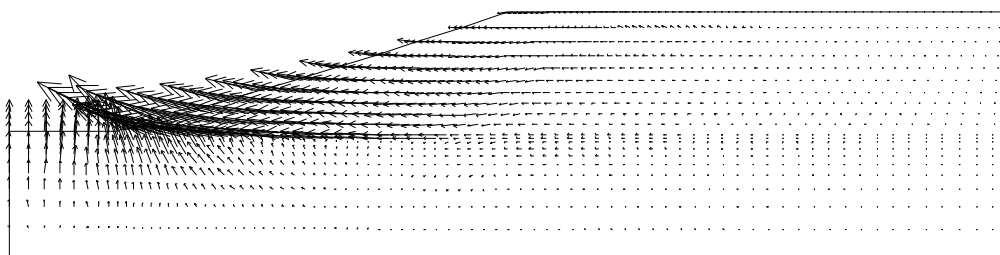
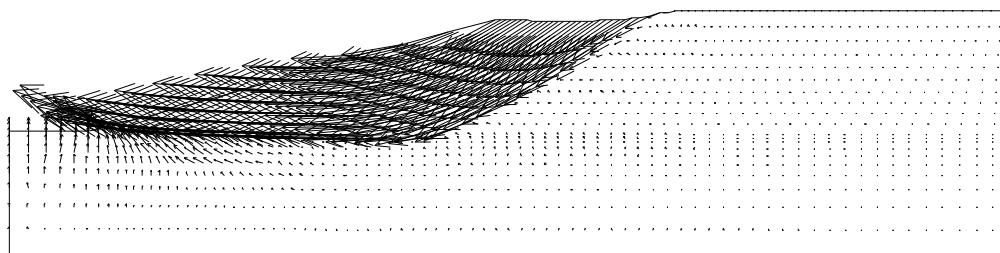


Fig. 5.29 Geometry of slope in stiff clay in typical analysis (S3)

Fig. 5.30 shows computed vectors of displacement at 9 years after excavation, and 14 years after excavation, just at the point of collapse. The vectors show the current pattern of movements and indicate the eventual collapse mechanism. At collapse, the absolute values of the displacements are of no significance. The figures show that the outer part of the slip surface has developed after 9 years, and that the complete slip surface has developed after 14 years.



(a) 9 years after excavation



(b) 14 years after excavation—just at collapse

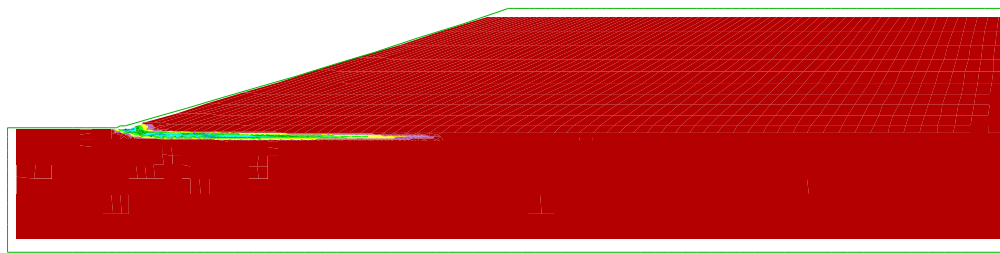
Fig. 5.30 Vectors of displacement for typical analysis (S3)

Fig. 5.31 shows the relevant accumulated plastic shear strain for typical analysis (S3) and the formation of slip surface.

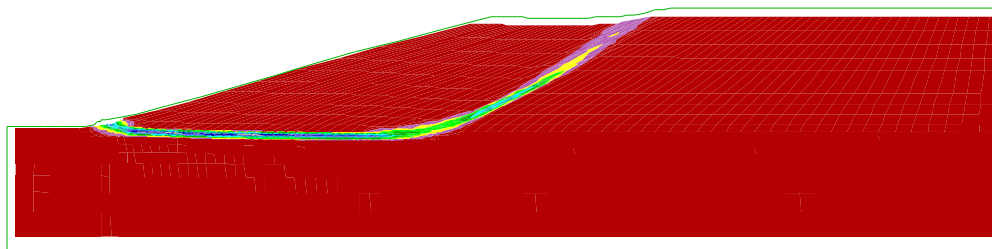
Fig. 5.32 shows the volumetric strains which develop due to swelling. The strains within the slip are quite large and the analysis predicts an abrupt change in volumetric strains across the rupture surface. This trend extends to the inner side of the slope indicating the complete formation of a slip surface.

All these results predict that a complete thin rupture zone has formed 14 years after excavation with the stresses lined up to allow rupture on a single surface. Residual

strength has been reached along all the horizontal part of the zone (Fig. 5.31). The amount of progressive failure is substantial.

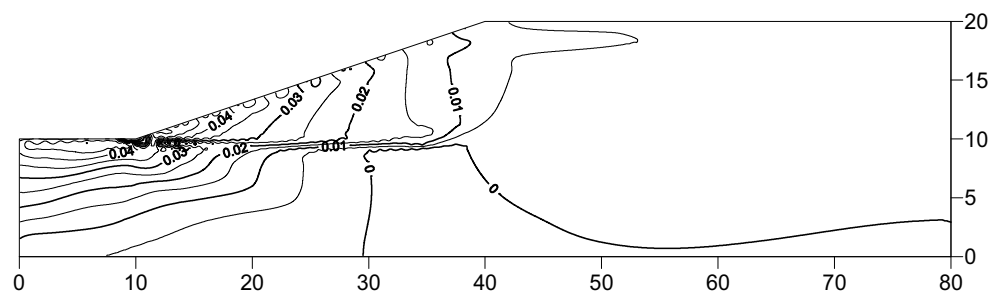


(a) 9 years after excavation

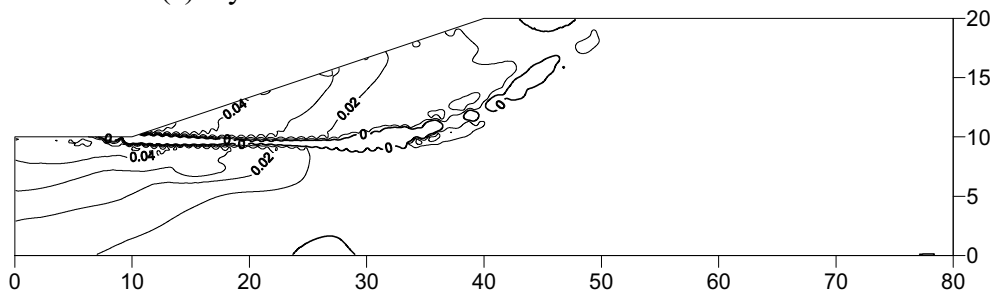


(b) 14 years after excavation—just at collapse

Fig. 5.31 Accumulated plastic shear strain for typical analysis (S3)



(a) 9 years after excavation with maximum value 5%



(b) 14 years after excavation—just at collapse with maximum value 5.5%

Fig. 5.32 Contours of volumetric strain for typical analysis (S3)

Pore water pressure development is shown as contours in Fig. 5.33 and the corresponding pore pressure change towards an equilibrium state (Fig. 5.34 and Fig. 5.35) is presented in bottom and middle profiles (Fig. 5.33a). In the middle of the slope, pore water pressures along the profile due to excavation are almost linear with depth. The pore pressure change after excavation is almost equal to the weight of soil removed from the slope above. At the toe of the slope, high lateral stresses remain after excavation. The reduction in mean total stress is smaller, and the reduction in pore water pressure is significantly less than the weight of soil removed. It is evident from these plots that the pore pressure increases as the slope deforms outwards.

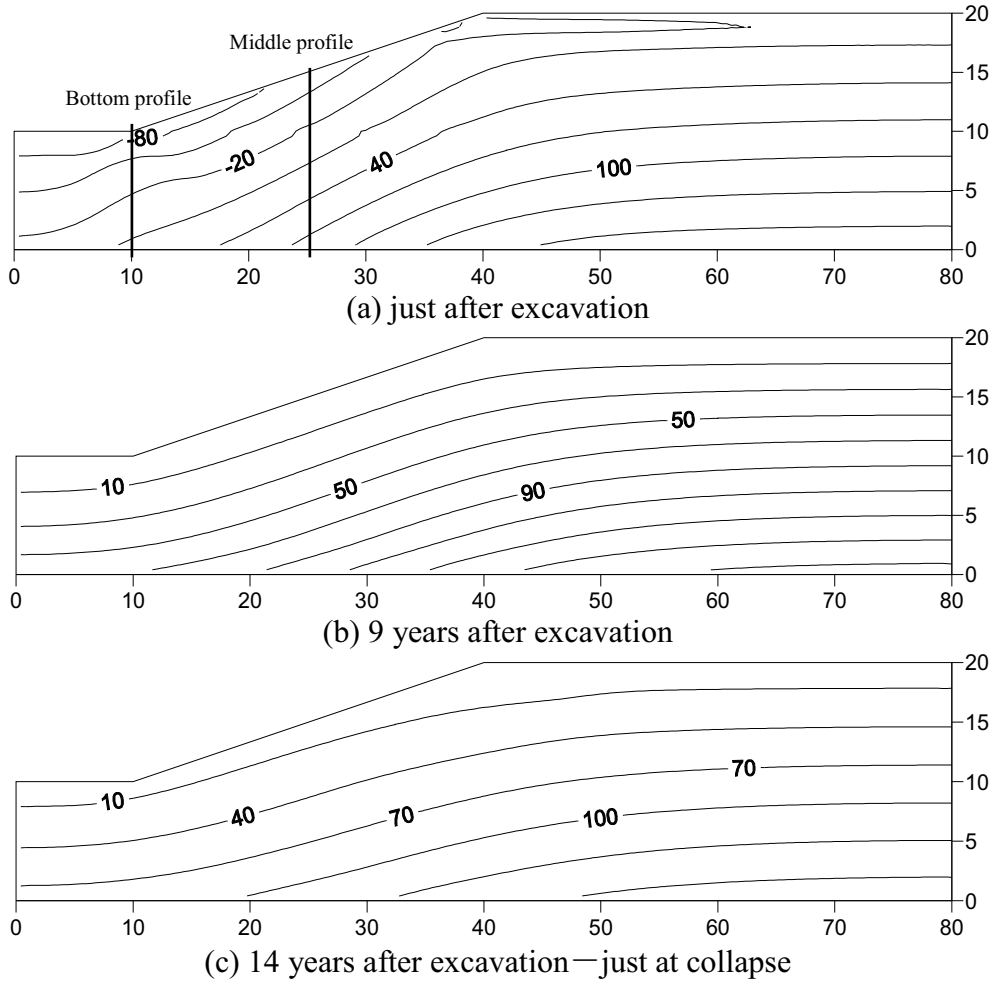


Fig. 5.33 Contours of pore pressure for typical analysis (S3) (just after excavation)

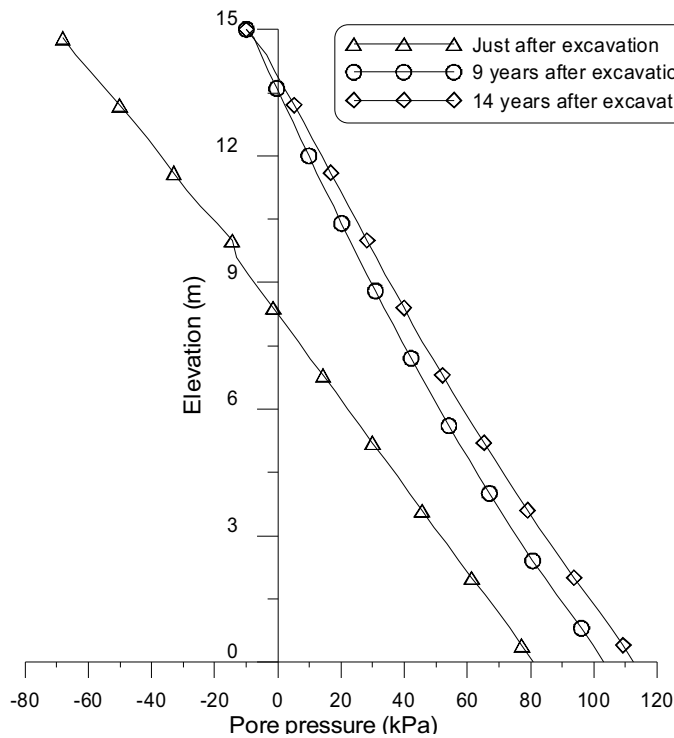


Fig. 5.34 Pore pressure change in middle profile

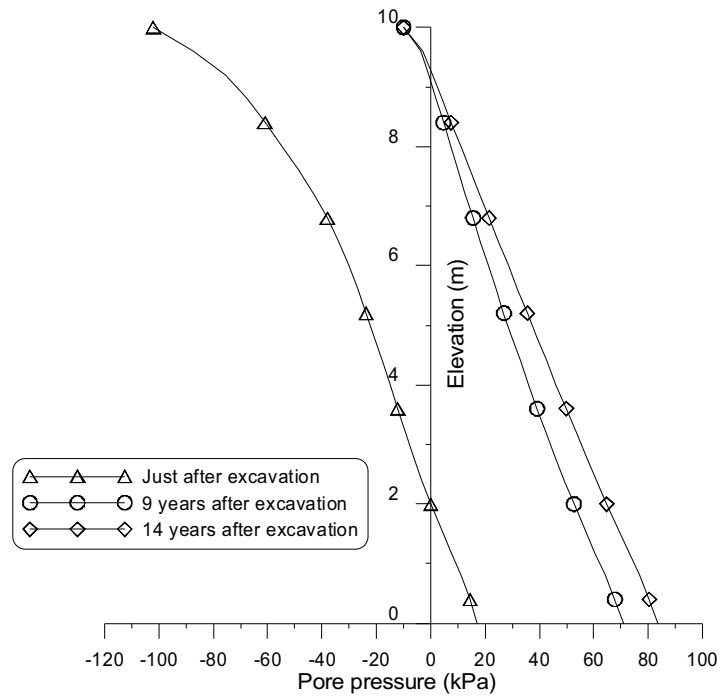


Fig. 5.35 Pore pressure change in bottom profile

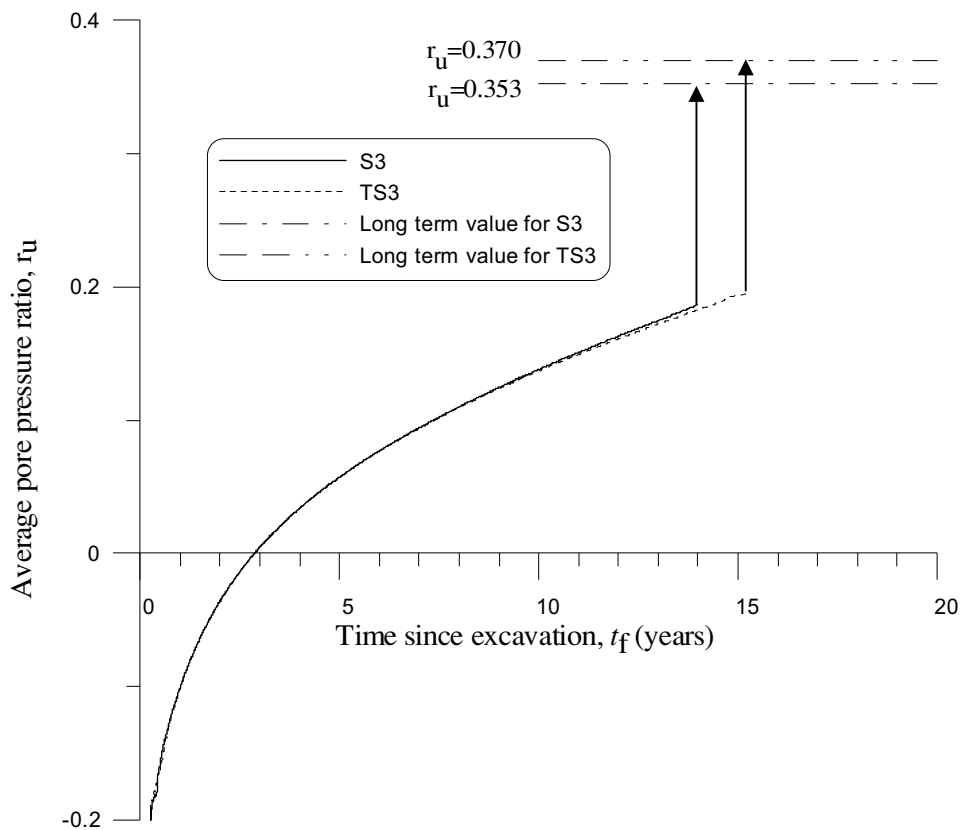


Fig. 5.36 Development of average pore pressure ratio on the rupture surface

For case S3, the average shear and normal stresses at failure are respectively 22.35 kPa and 64.96 kPa. With the use of Eq. (1.3), the residual factor R is calculated to be 0.527 indicating a substantial amount of progressive failure. This value of residual

factor R means that the average strength has dropped 52.7% of the way from peak to residual.

Fig. 5.36 shows the change with time of the predicted average pore pressure ratio on the rupture surface, defined as

$$\bar{r}_u = \sum (r_{ui} A_i) = \sum \left(\frac{u_i}{\sigma_{vi}} A_i \right) \quad (5.4)$$

where r_{ui} is the local *FLAC* zone pore pressure ratio; A_i is the zone area; u_i is zone pore pressure and σ_{vi} is the vertical overburden stress on the rupture surface. It can be seen that the average pore pressure ratio on the final rupture surface has increased from -0.195 after excavation to 0.187 at collapse. The long term equilibrium pore pressure ratio is equivalent to 0.353 . Thus, on the rupture surface, the pore water pressure has changed 69.7% of the way towards long term equilibrium.

The rate of change in pore pressure is initially high and then reduces with time. This is physically reasonable and in agreement with field observations.

The average strength at collapse predicted in S3 is shown in Fig. 5.37, together with the peak, post-rupture and residual strengths. Also shown is the operational field strength deduced from back analysis (using limit equilibrium analyses) of slips by Chandler & Skempton (1974). The strength from the *FLAC* analysis (S3) is a little lower than, but very close to the backcalculated field strength.

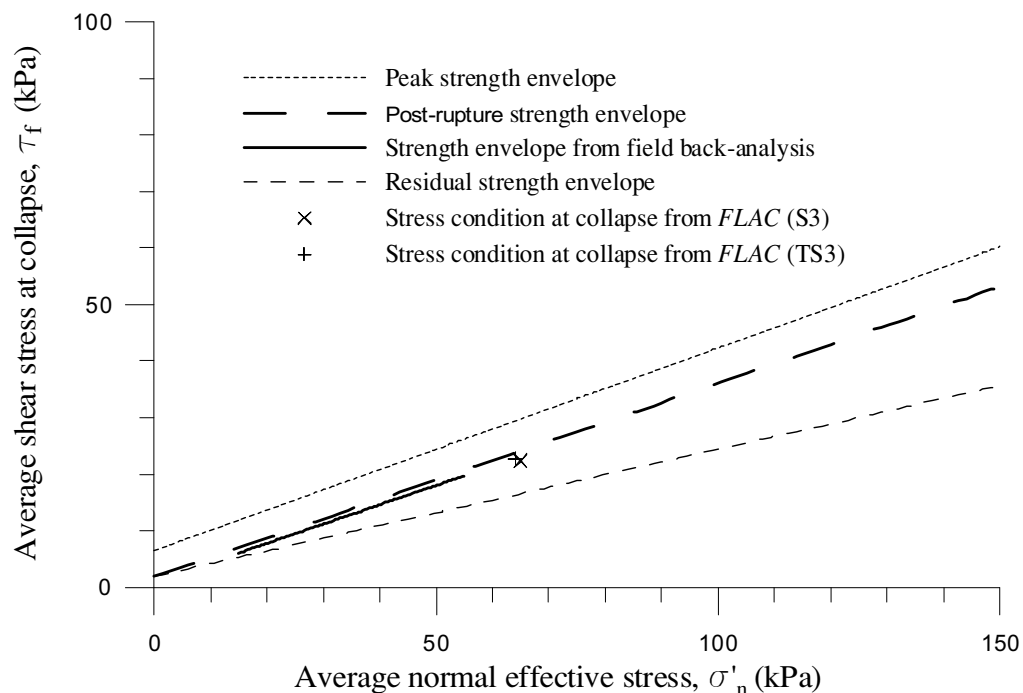


Fig. 5.37 Comprehensive shear strength envelopes

There is general consistency between *FLAC* modelling and the previous results by Potts et al. (1997). The collapse time for *FLAC* is 14.0 years after excavation which is just a little shorter than 14.5 years after excavation for *ICFEP* (Potts et al., 1997). Fig. 5.30 and Fig. 5.31 exhibit the development of rupture zone 9 years after excavation and during ongoing failure, showing the initiation of the shear surface from the toe of

the cutting, and the fully developed surface respectively. The results can be compared with plots at 9 years and just before failure, as reported by Potts et al. (1997).

Potts (2003) stated that it would not be realistic to expect precise agreement between two analyses (even with prescribed numerical parameters) based on different numerical approaches as the period as failure is approached.

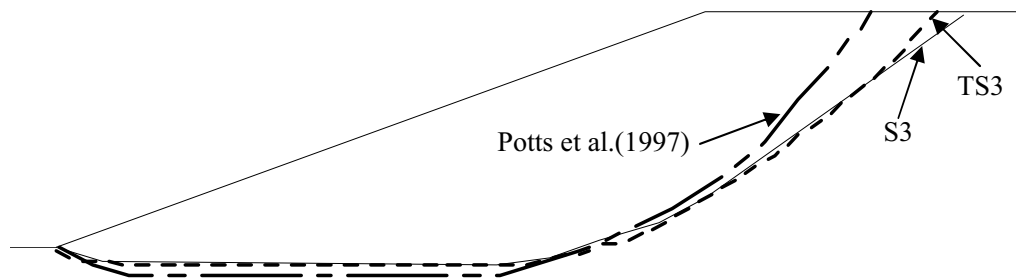


Fig. 5.38 Comparison of final slip surface with original result (Potts et al., 1997)

Fig. 5.38 compares the fully developed slip surfaces. The surface predicted by Potts et al. (1997) has a slightly deeper horizontal rupture and a back slip surface closer to the slope surface. As demonstrated in section 5.3.3.3, the slip surface angle to vertical at ground level is nearly 45° for $\psi = 0$. The *FLAC* result is in agreement with this whereas there is some difference in the original result given by Potts et al. (1997).

5.3.4.2 K_0 effect

Analyses S1–S6 were all performed for a 10 m high 3:1 slope adopting values of K_0 increasing from 1.0 to 2.15 (the last value is approximately equal to K_p , the passive coefficient of earth pressure). Fig. 5.39 shows the horizontal displacement variations at mid-height of the slope with time for the various analyses. The mid-height displacements start to accelerate after an approximate steady increase. Final collapse is quite abrupt, without significant warning from accelerating displacement. Therefore, in these cases, it is not reliable to monitor the displacement for assessing slope safety.

Collapse times are strongly dependent on K_0 and increase continuously with K_0 when $K_0 > 1.25$ (Fig. 5.40). There is little difference in collapse time for case S1 and case S2. Moreover, the mid-slope horizontal displacement at collapse increases also with K_0 (as indicated in Table 5.3).

The shapes of the rupture surface expressed by displacement vectors and accumulated plastic shear strain for each analysis are shown in Fig. 5.41 and Fig. 5.42. The rupture surfaces are strongly influenced by the value of K_0 . They become deeper as K_0 increases from 1.0 to 2.15. As K_0 increases further from 1.75, the back of the slip moves out towards the slope face. The rupture surface at the crest of the slip forms after the collapse event when K_0 is low. As shown in both Fig. 5.41 and Fig. 5.42, the length of the horizontal rupture surface which develops from the toe of the slope increases with K_0 . With high values of K_0 it extends beyond the crest of the slope. Then the back of the final rupture surface develops subsequently closer to the slope,

and the inner part of the horizontal rupture surface is not incorporated in the final rupture surface (Fig. 5.41). As a consequence part of the horizontal stress in the zone in which the back of the slip finally develops is relieved before collapse, and the amount of progressive failure is reduced.

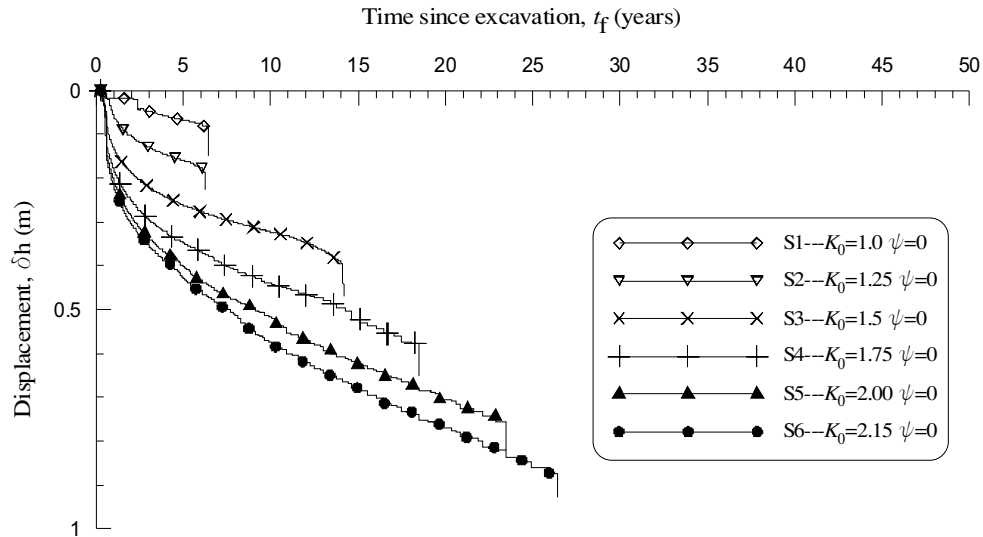


Fig. 5.39 Mid-slope horizontal displacement with time for S1-S6

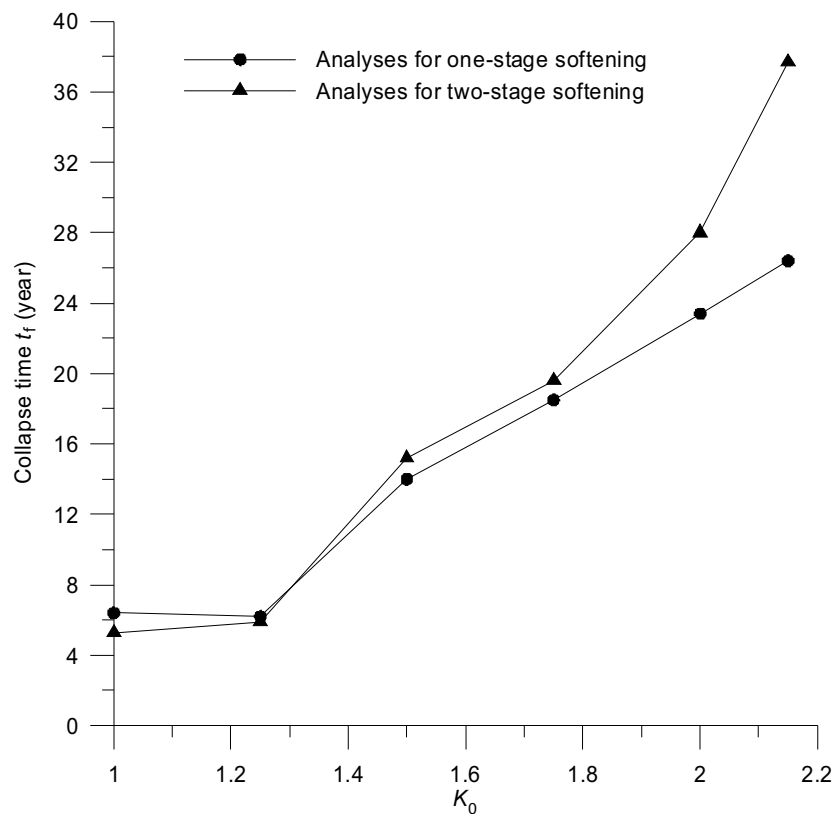


Fig. 5.40 Variation of collapse time with K_0

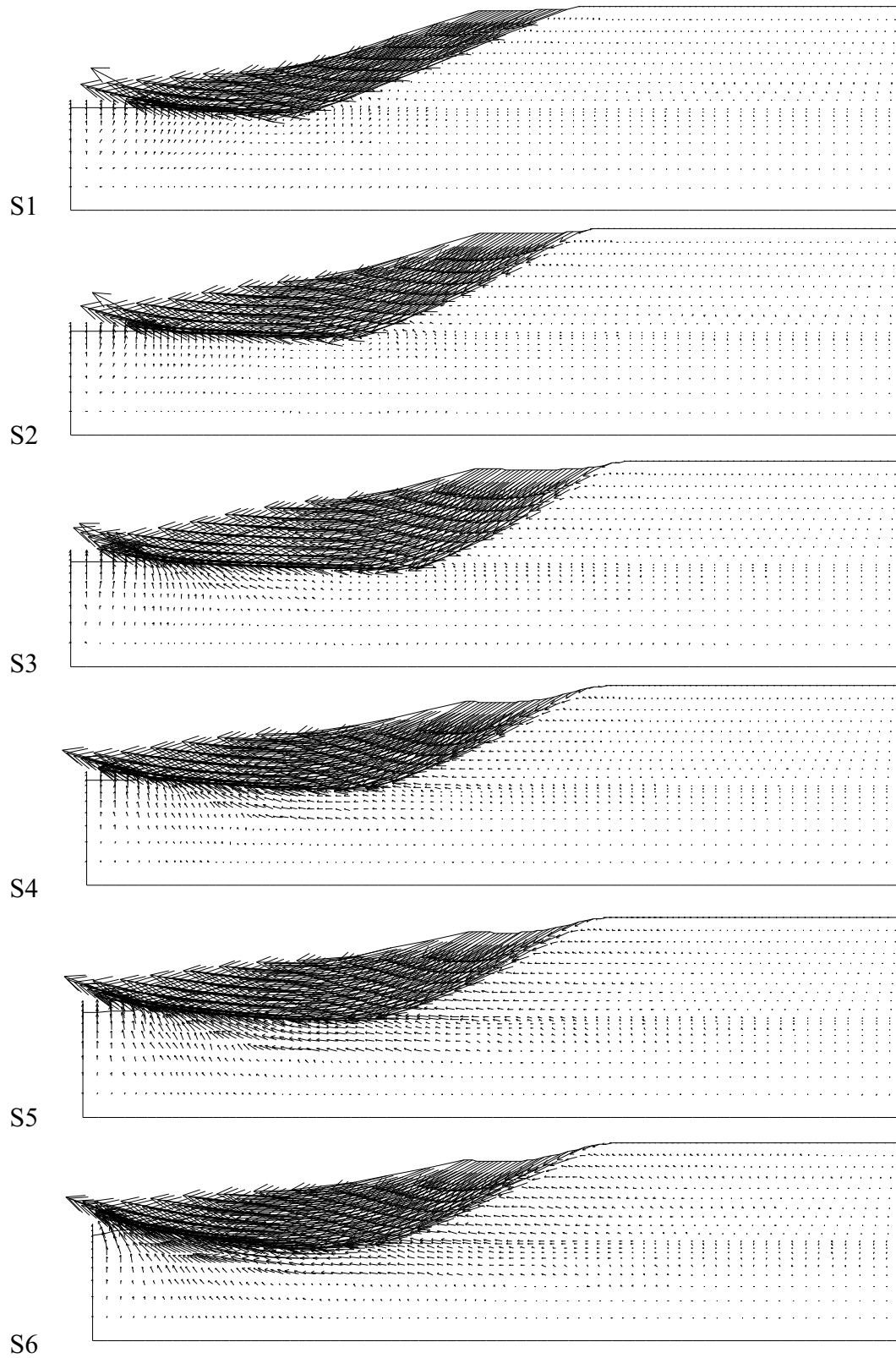


Fig. 5.41 Vectors of displacement for S1-S6

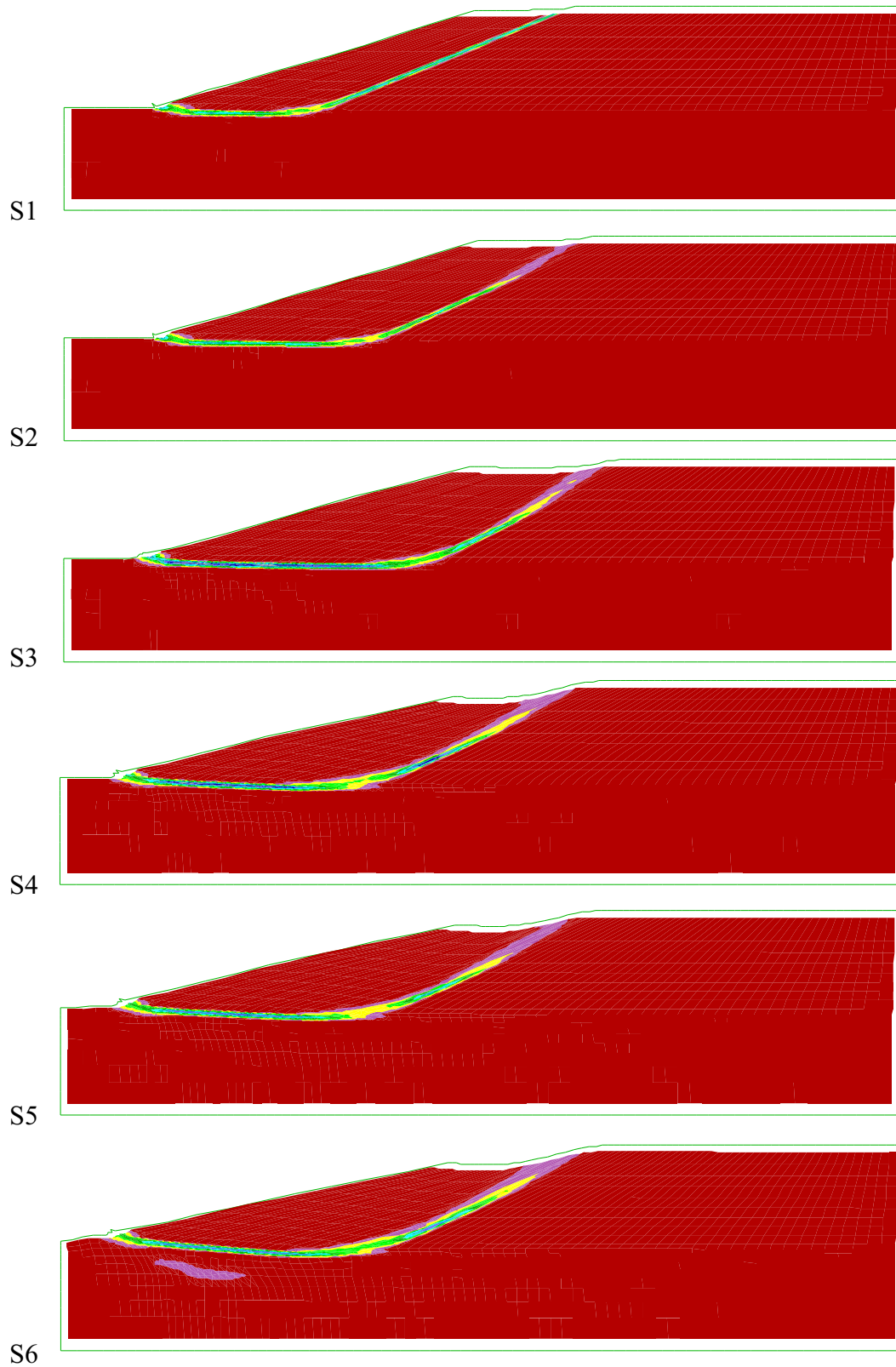


Fig. 5.42 Accumulated plastic shear strain for S1-S6

5.3.4.3 Effect of surface suction

Analysis S7 corresponds to a 3:1 slope, 10 m high, with $K_0 = 2.00$ and with a surface suction $u_b = -20$ kPa . Such an increase in suction might be produced by the management of slope vegetation. The results may be compared directly with analysis S5 in which $u_b = -10$ kPa . Fig. 5.43 shows that collapse with larger boundary suction did not occur even 100 years after excavation which is much longer than collapse time for case S5.

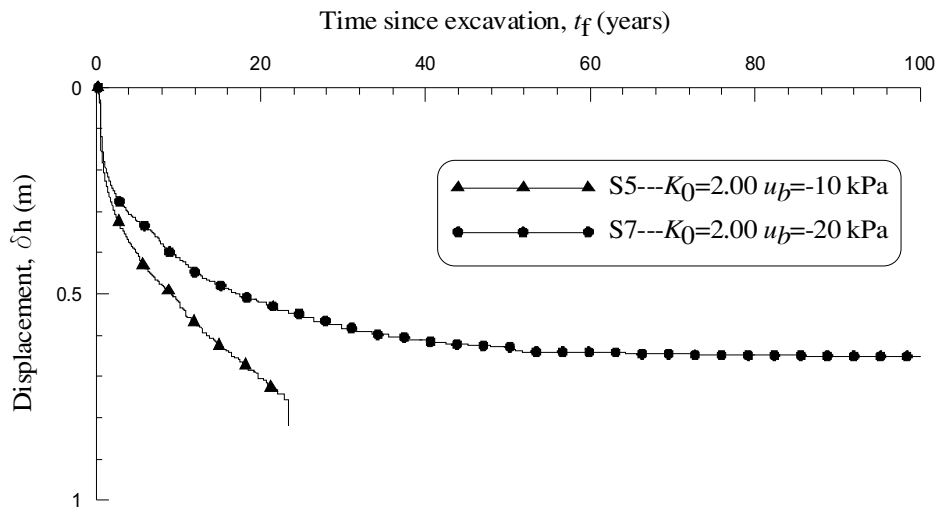


Fig. 5.43 Mid-slope horizontal displacement with time for S5 and S7

The displacement vectors and plastic shear strain are shown in Fig. 5.44 and Fig. 5.45. The rupture surface for analysis S7 was not formed completely 100 years after excavation and a slip surface bifurcation appeared indicating by a deeper surface below the horizontal rupture part. All these demonstrate that increasing surface suction (slope vegetation) even by a modest amount will improve slope stability dramatically.

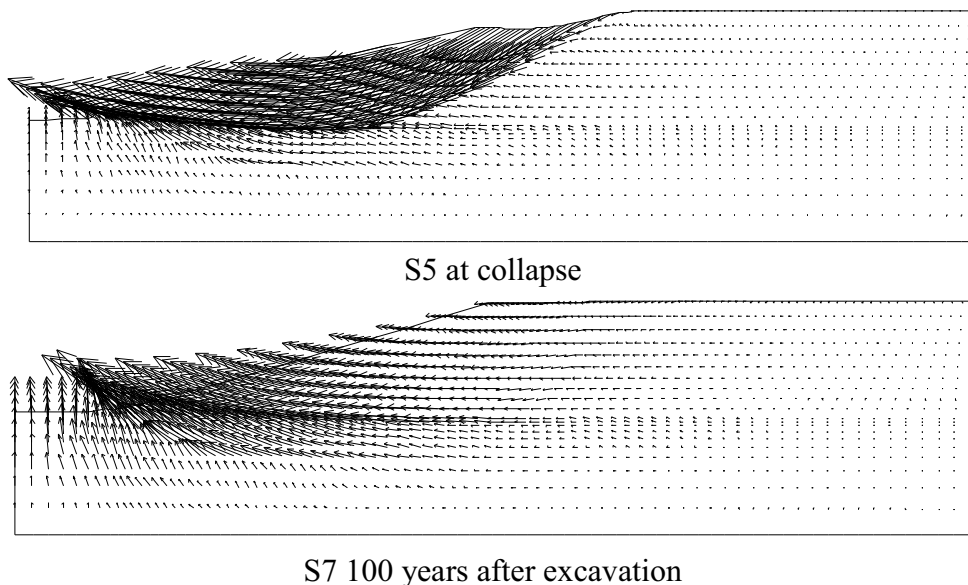


Fig. 5.44 Vectors of displacement for S5 and S7

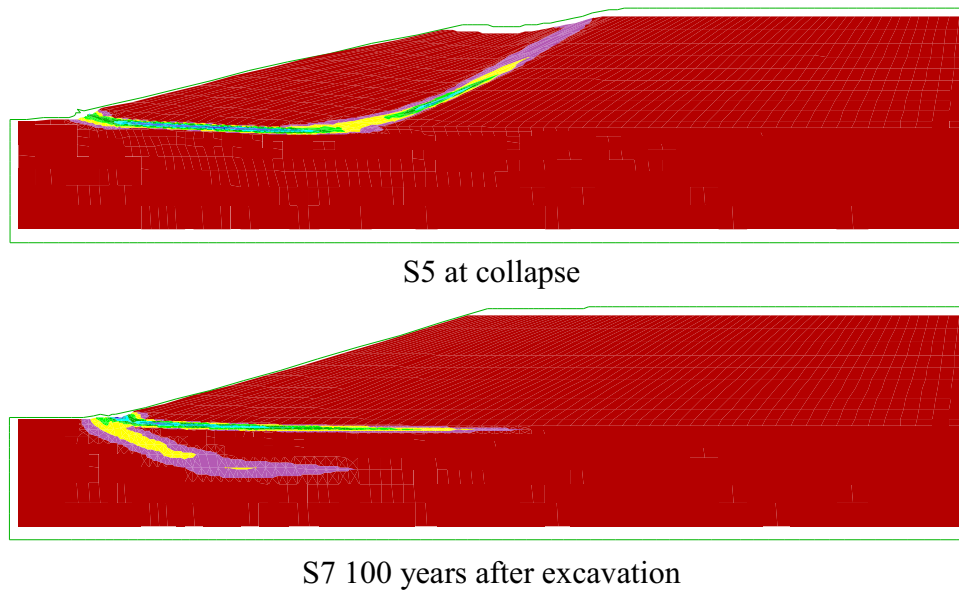


Fig. 5.45 Accumulated plastic shear strain for S5 and S7

5.3.4.4 Effect of slope geometry

Analyses S9 and S10 were performed to examine the stability of 2:1 and 2.5:1 slopes, 10 m high, with $K_0 = 2.0$. Results may be compared with analysis S5 with 3:1 slope.

The development of deformation with time is shown in Fig. 5.46. Both slopes fail in less than 10 years.

Analysis S8 was of a 2:1 slope, 10 m high, with $K_0 = 1.5$ and a surface suction $u_b = -10$ kPa. The results may be compared with analysis S3 for the 3:1 slope. Again the steeper slope failed earlier (1 year compared to 14 years).

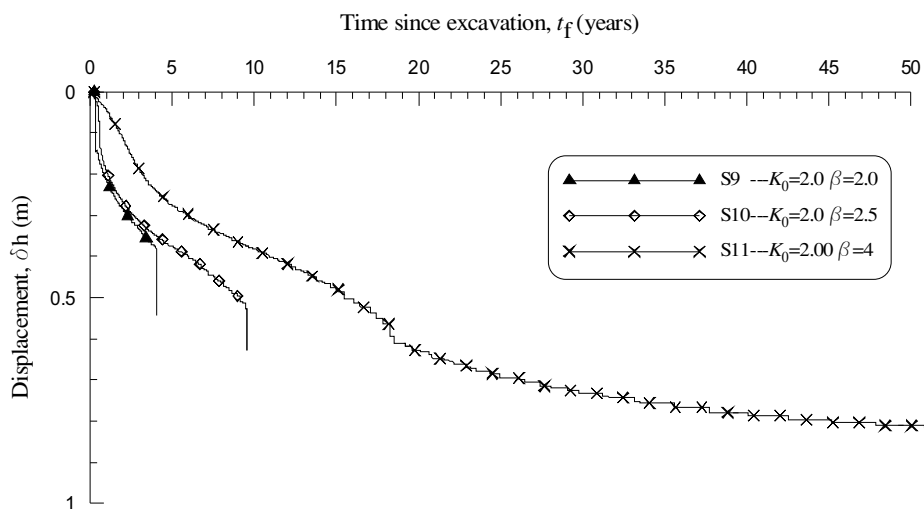


Fig. 5.46 Mid-slope horizontal displacement with time for S9-S11

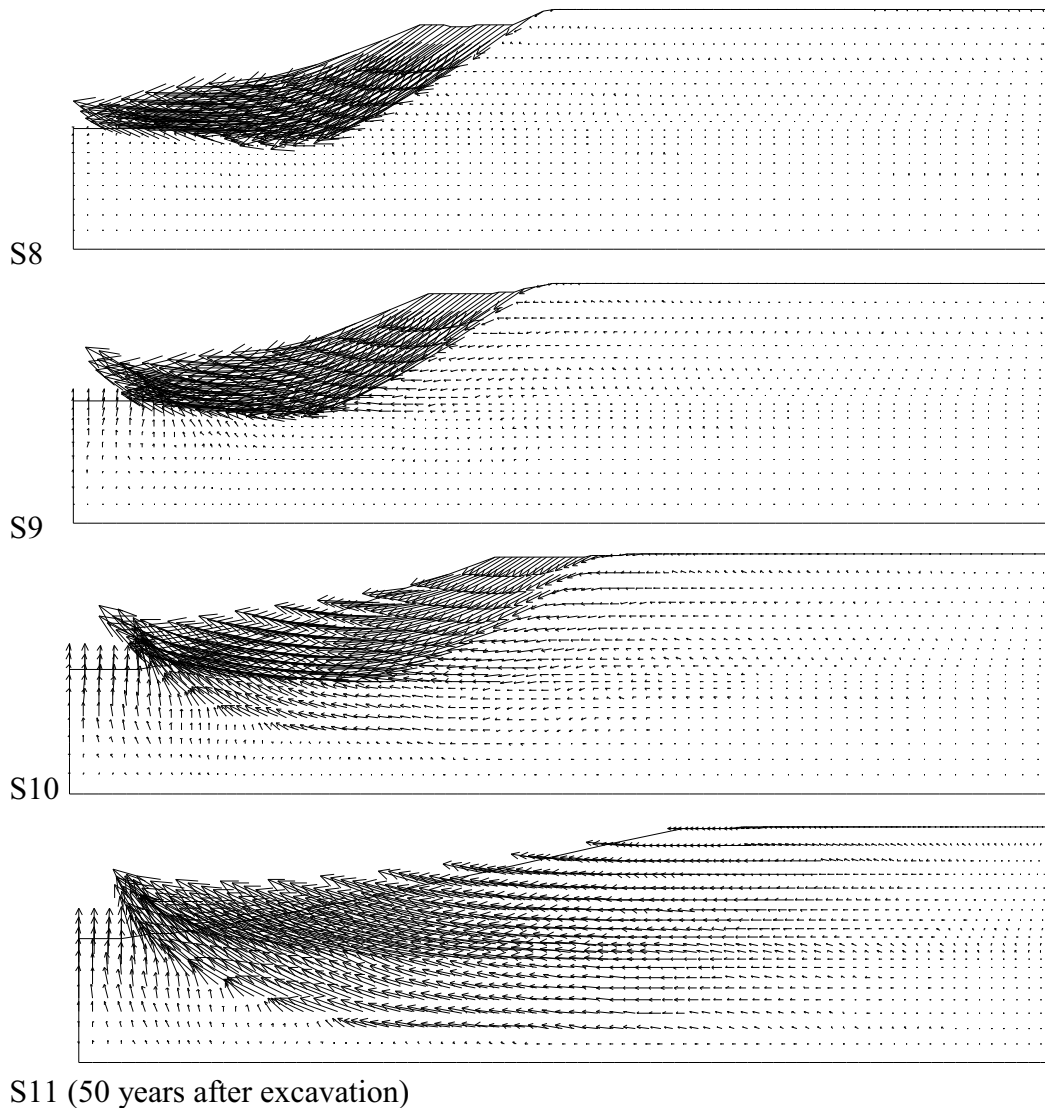


Fig. 5.47 Displacement vectors for S8-S11

Analysis S11 was of a 4:1 slope, 10 m high, with $K_0 = 1.5$ and a surface suction $u_b = -10$ kPa. The development of deformation with time is shown in Fig. 5.46. The flatter slope is more stable than the steeper slope and a very long time after excavation is needed for collapse to occur.

Fig. 5.47 and Fig. 5.48 show displacement vectors and plastic shear strain for cases S9-S11. From these plots and results for S5, it is clear that, as the slope becomes flatter, the horizontal rupture surface tends to be longer and deeper. Consequently, the clay mass involved in large deformations extends to the deeper and inner region of the slope. As shown in Fig. 5.48 for S10, there are three parts of rupture: (1) the back slip surface extending to the ground surface; (2) the outspread horizontal rupture surface; (3) the less deformed slip surface below the horizontal part. As for case S11, the back slip surface is not formed even long after excavation, whereas the deep rupture zone below horizontal rupture surface develops with more deformation.

Moreover, it is seen from Table 5.3 that both the mid-slope horizontal displacement at collapse and collapse time increase with slope parameter β .

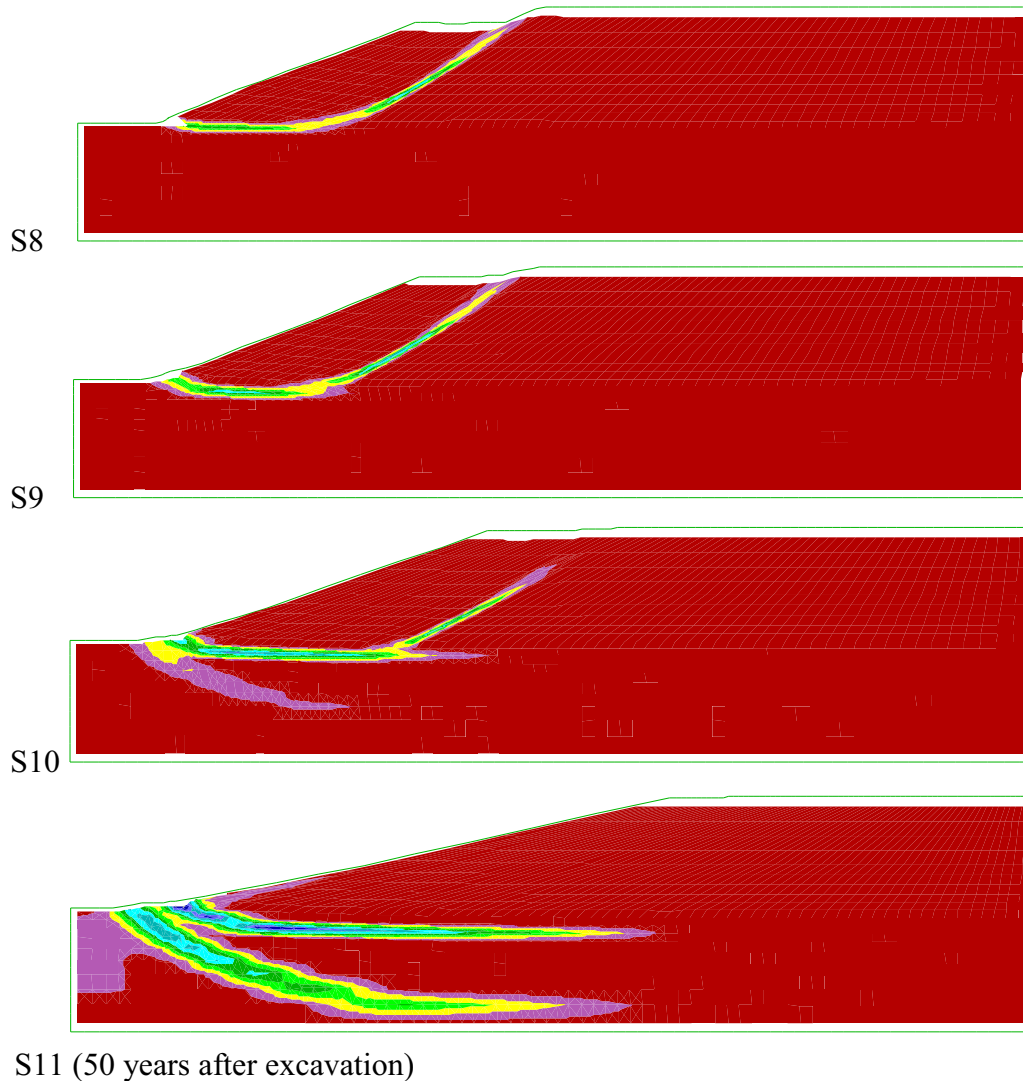


Fig. 5.48 Accumulated plastic shear strain for S8-S11

5.3.4.5 Summary for non-softening and one-stage softening analyses

All the analysis results shown in Table 5.3 demonstrate:

1. For non-softening analyses, slope collapse time t_f and displacement at collapse increase with K_0 . A zero dilation angle ψ facilitates slope collapse and a non-zero dilation angle could be considered as a brake factor controlling the collapse.
2. For softening analyses S1-S6, S8 and S9, slope collapse time t_f and displacement at collapse increase generally with K_0 although there is a small (not significant) reduction when K_0 changes from 1.0 to 1.25.
3. By comparing results of analyses S5 and S7, it can be seen that surface suction reduces the rate of slope failure.
4. It is evident by comparison of results of analyses S9, S10, S5 and S11 that slope collapse time t_f and displacement at collapse reduce as slope angle increases. When

the slope reaches 1:4, the slope is stable during a quite long period, more than 100 years, and perhaps indefinitely.

5.3.5 Two-stage softening analyses with bulk peak strength

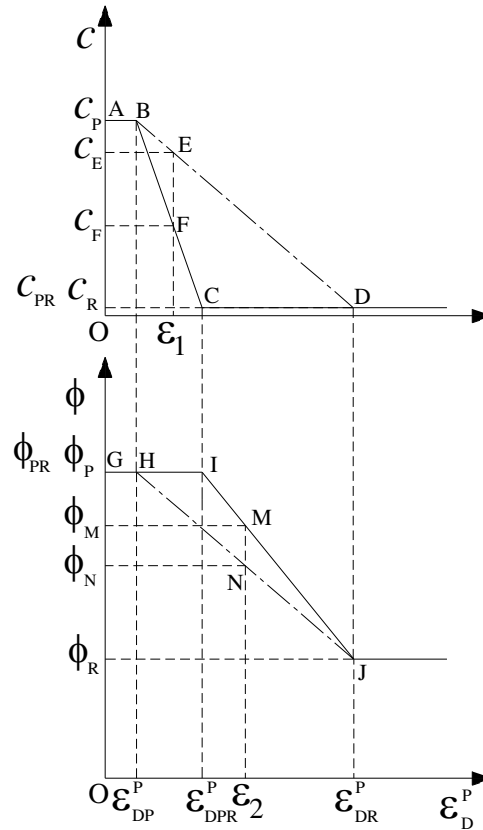


Fig. 5.49 Friction angle and cohesion variations with plastic shear strain

As described before in this thesis, stiff clays exhibit two-stage softening as seen in Fig. 5.49. Therefore the two-stage softening model incorporating post-rupture strength was used in this section. This model gives a more realistic description of progressive failure with rapid reduction from bulk peak strength to post-rupture strength, followed by a more gradual reduction to residual strength.

Table 5.4 Results of two-stage softening modelling

| Analysis | Height (m) | Slope ($\cot \beta$) | K_0 | ψ (deg) | u_b (kPa) | Middle slope XDisplacement at collapse (mm) | t_f (years) |
|----------|------------|------------------------|-------|--------------|-------------|---|---------------|
| TS1 | 10 | 3 | 1.00 | 0 | -10 | 82.9 | 5.4 |
| TS2 | 10 | 3 | 1.25 | 0 | -10 | 224 | 5.9 |
| TS3 | 10 | 3 | 1.50 | 0 | -10 | 407 | 15.2 |
| TS4 | 10 | 3 | 1.75 | 0 | -10 | 574 | 19.6 |
| TS5 | 10 | 3 | 2.00 | 0 | -10 | 740 | 28.0 |
| TS6 | 10 | 3 | 2.15 | 0 | -10 | 892 | 37.7 |
| TS7 | 10 | 3 | 2.00 | 0 | -20 | >688 | >100* |
| TS8 | 10 | 2 | 1.50 | 0 | -10 | 183 | 1.00 |
| TS9 | 10 | 2 | 2.00 | 0 | -10 | 457 | 6.4 |
| TS10 | 10 | 2.5 | 2.00 | 0 | -10 | 562 | 14.6 |
| TS11 | 10 | 4 | 2.00 | 0 | -10 | >840 | >100* |

* Final calculation time

For the computations, a post-rupture strength ($c'_{pr} = 2\text{kPa}$, $\phi'_{pr} = 20^\circ$) was postulated between the bulk peak strength ($c'_p = 7\text{kPa}$, $\phi'_p = 20^\circ$) and the residual strength ($c'_r = 2\text{kPa}$, $\phi'_r = 13^\circ$) with corresponding plastic strain limits as $\gamma_p = 0.015$, $\gamma_{pr} = 0.020$, $\gamma_r = 0.115$.

All the calculation schemes and the relevant results are listed in Table 5.4.

5.3.5.1 Results of analysis TS3

Fig. 5.50 shows computed vectors of displacement at 9 years after excavation, and 15.2 years after excavation just at collapse. The vectors show the current mechanism of movement and indicate the eventual collapse mechanism. The figures show that the outer part of the slip surface has developed after 9 years, and that the complete slip surface formed after 15.2 years.

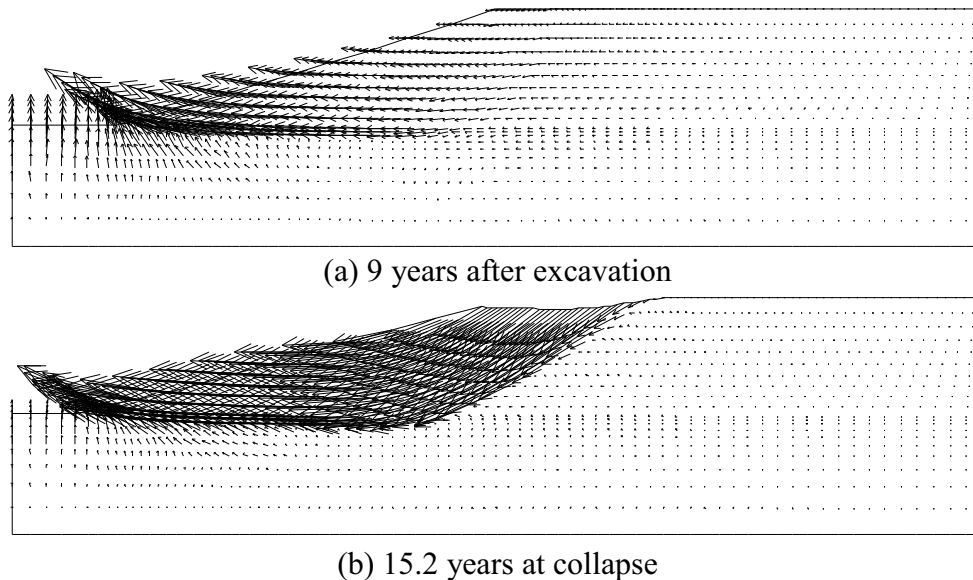
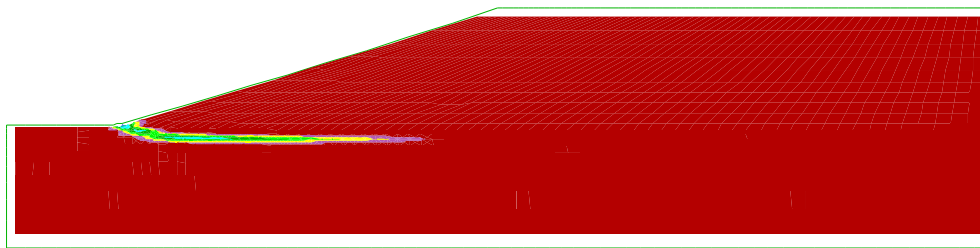
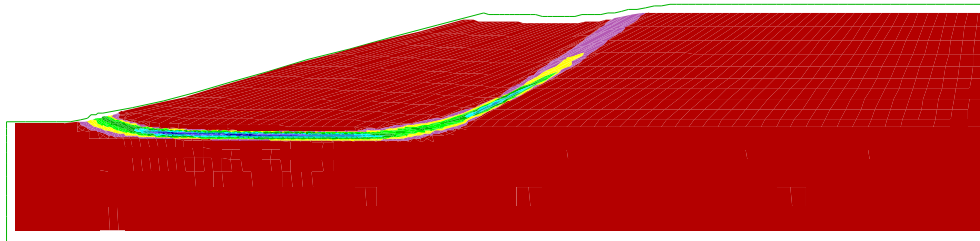


Fig. 5.50 Vectors of displacement for TS3

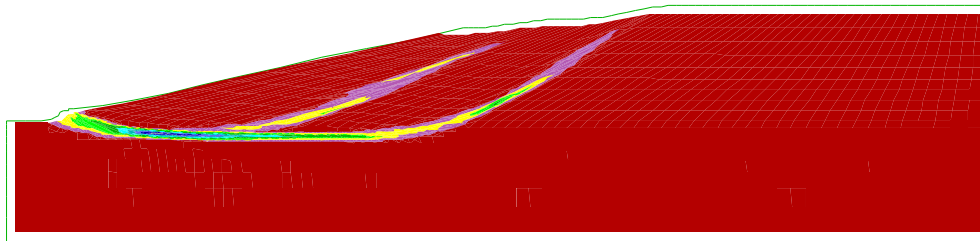
Fig. 5.51 presents the accumulated plastic shear strain at different time since excavation. In comparison with both Fig. 5.30 and Fig. 5.31, the shape of final failure surface is similar except that the horizontal rupture surface for TS3 is located deeper than that for S3. In addition, there is more localization of shear strain at the slope toe for TS3 than that for S3. The deformation at collapse for TS3 is larger than that for S3 as shown in Table 5.3 and Table 5.4. Moreover, it is interesting to note from Fig. 5.51c that, during ongoing post-collapse process, a secondary failure occurred within the failed soil mass formed in the first failure.



(a) 9 years after excavation



(b) 15.2 years at collapse



(c) Post-collapse (secondary failure)

Fig. 5.51 Accumulated plastic shear strain for TS3

Fig. 5.52 shows the volumetric strains which develop due to swelling. It is obvious that there is abrupt change in volumetric strains across the rupture surface. This trend extends to the inner side of the slope indicating the complete formation of slip surface. Furthermore, in addition to the abrupt change in volumetric strains along the first failure, a less abrupt change in volumetric strains also develops within the slip soil mass. This complements further the conclusion drawn from Fig. 5.51c.

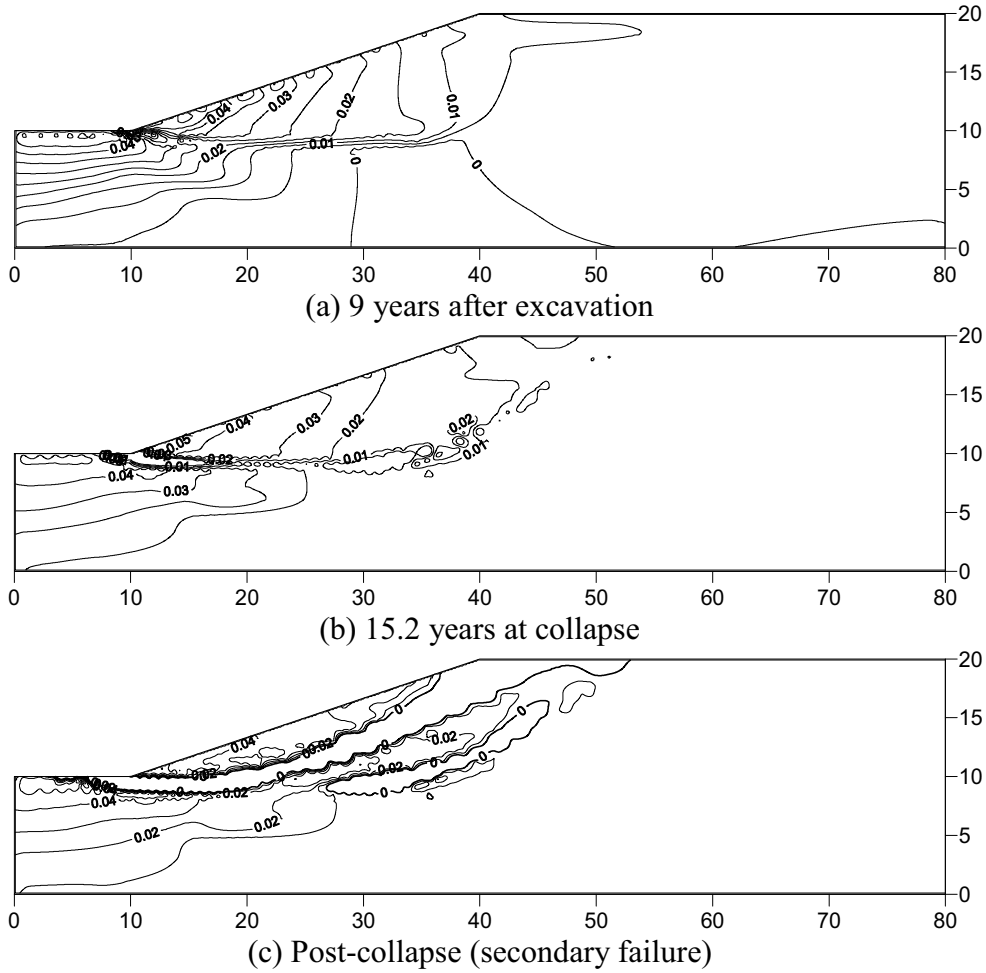


Fig. 5.52 Contours of volumetric strain for TS3

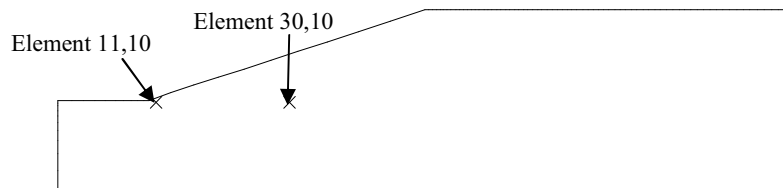


Fig. 5.53 Representative elements

Fig. 5.54 shows the development of shear strain increment with time in elements (11,10) and (30,10) (indicated in Fig. 5.53) which are located at the slope toe and on the inner part of the rupture surface, respectively.

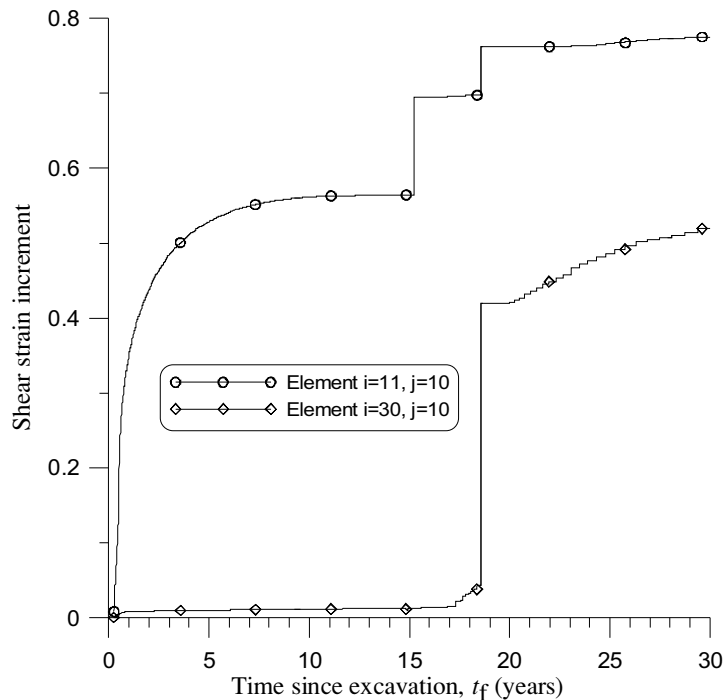


Fig. 5.54 Development of shear strain increment with time

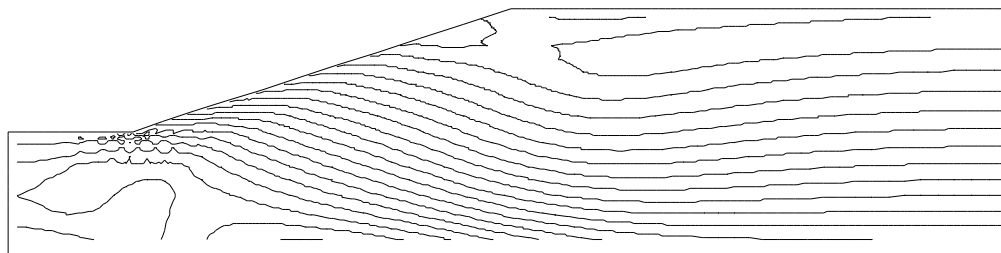
Pore water pressure development for TS3 exhibits the same tendency as shown in Fig. 5.33, Fig. 5.34 and Fig. 5.35 and it is not shown for brevity.

For case TS3, the average shear and normal stresses at failure are respectively 22.64 kPa and 64.05 kPa. With the use of Eq. (1.3), the residual factor R is calculated to be 0.522 indicating the substantial amount of progressive failure. This value of residual factor R means that the average strength has dropped 52.2% of the way from peak to residual. All these values are similar to those for case S3.

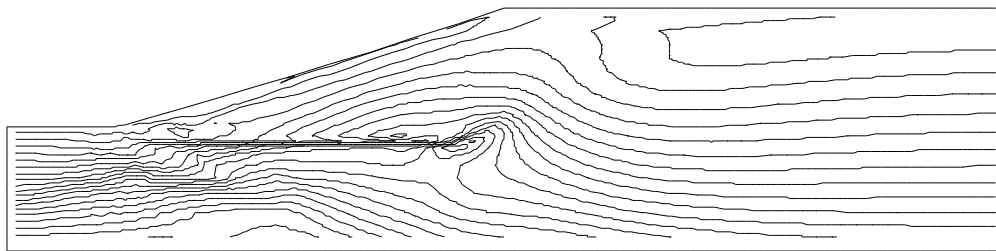
Fig. 5.36 shows the change with time of the predicted average pore pressure ratio on the rupture surface. It can be seen that the average pore pressure ratio on the final rupture surface has increased from -0.197 after excavation to 0.193 at collapse. The long term equilibrium pore pressure ratio is equivalent to 0.370 . Thus, on the rupture surface, the pore water pressure has changed 52% of the way towards long term equilibrium.

The average strength at collapse predicted in TS3 is shown in Fig. 5.37. The post-rupture strength is very close to the backcalculated field strength. The operational strength predicted by *FLAC* analysis (TS3) is a little lower than, but close to both the field and post-rupture strengths. This strength is also very similar to that of case S3.

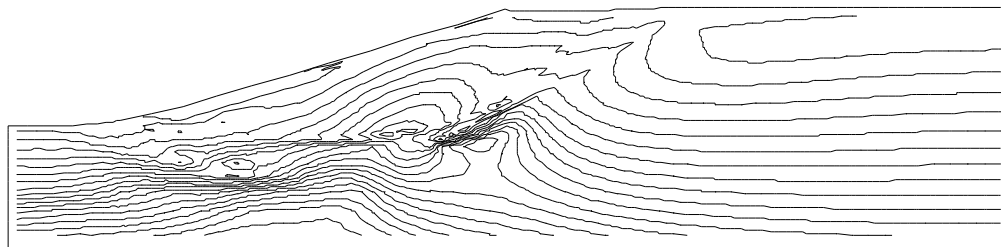
Overall, the use of post-rupture strength does not change the mechanism of progressive failure but has some influence on the time to collapse and on the development of pore pressure with time.



(a) Just after excavation



(b) 9 years after excavation



(d) 15.2 years at collapse

Princ. Stress Dif. contours
 Contour interval= 1.00E+04
 Minimum: 0.00E+00
 Maximum: 2.00E+05

Fig. 5.55 Development of principal stress difference with time (TS3)

Fig. 5.55 shows the development of principal stress difference with time for TS3. Again, it is apparent that the shear stress concentration proceeds gradually with time.

Fig. 5.56, Fig. 5.57 and Fig. 5.58 exhibit the current shear stress (calculated via Eq. (5.6)) distribution along the failure surface at different time. In these figures the peak, post-rupture, residual and current strength values calculated via Eq. (5.3) with the corresponding strength parameters are also shown. In the beginning (Fig. 5.56), the shear stress did not mobilise to the peak strength value along most part of the slip surface and the current shear strength was equal to peak strength value indicating that softening had not occurred at this moment. At 9 years after excavation (Fig. 5.57), the shear stress along the horizontal part of the slip surface reached the residual strength value whereas that of the back part of failure surface has not yet reached to the peak strength value. Meanwhile, there existed an intermediate zone between the horizontal part and the back part of the slip surface, where the current shear stress value lies between peak and residual values. Especially in the intermediate zone there was a very short part where the current shear stress was approximately equal to the post-rupture strength value. At collapse at 15.2 years (Fig. 5.58), the current shear stress along the slip surface was almost completely mobilised to the residual strength value except for most of the back part of the slip surface.

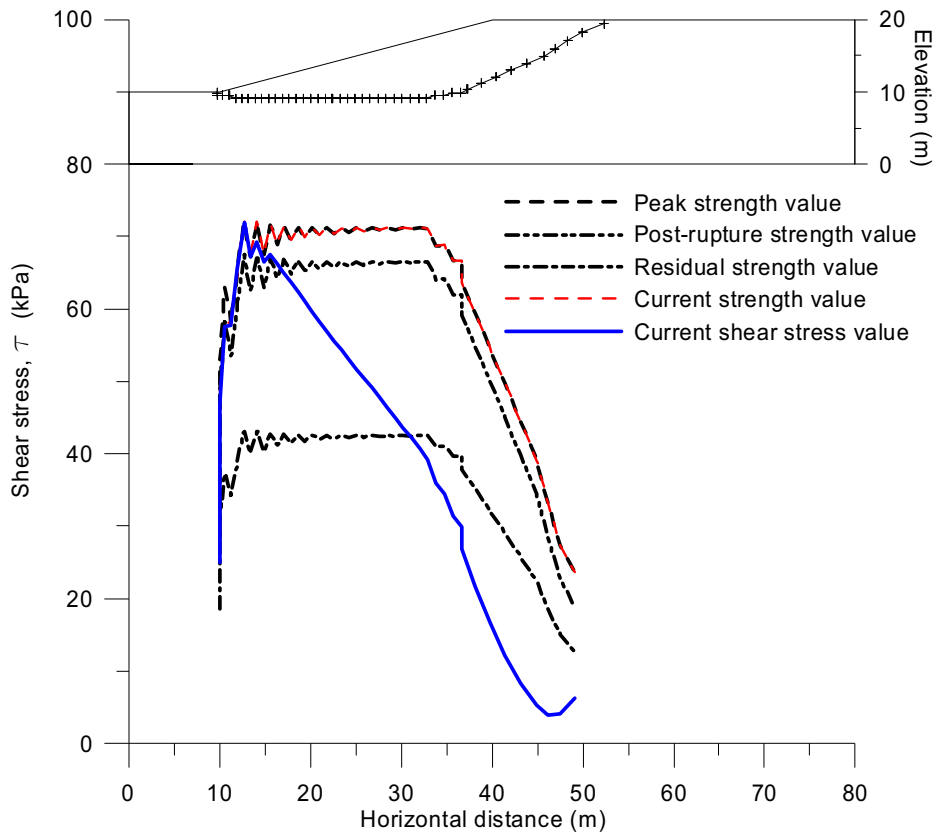


Fig. 5.56 Shear stress distribution along failure surface just after excavation

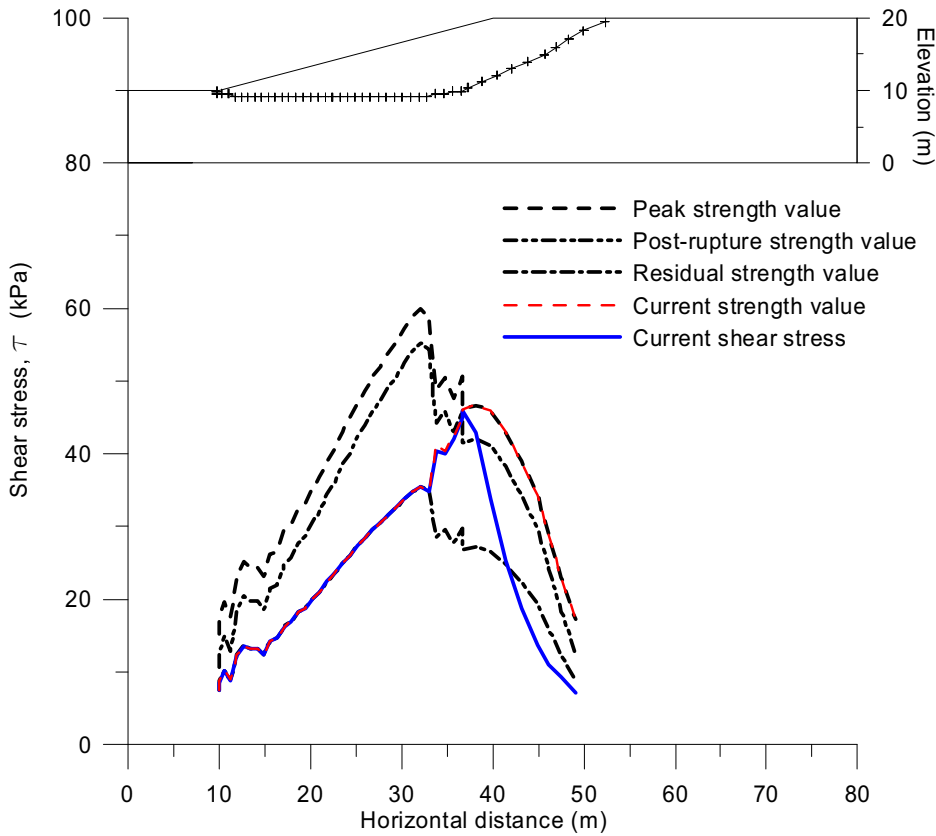


Fig. 5.57 Shear stress distribution along failure surface 9 years after excavation

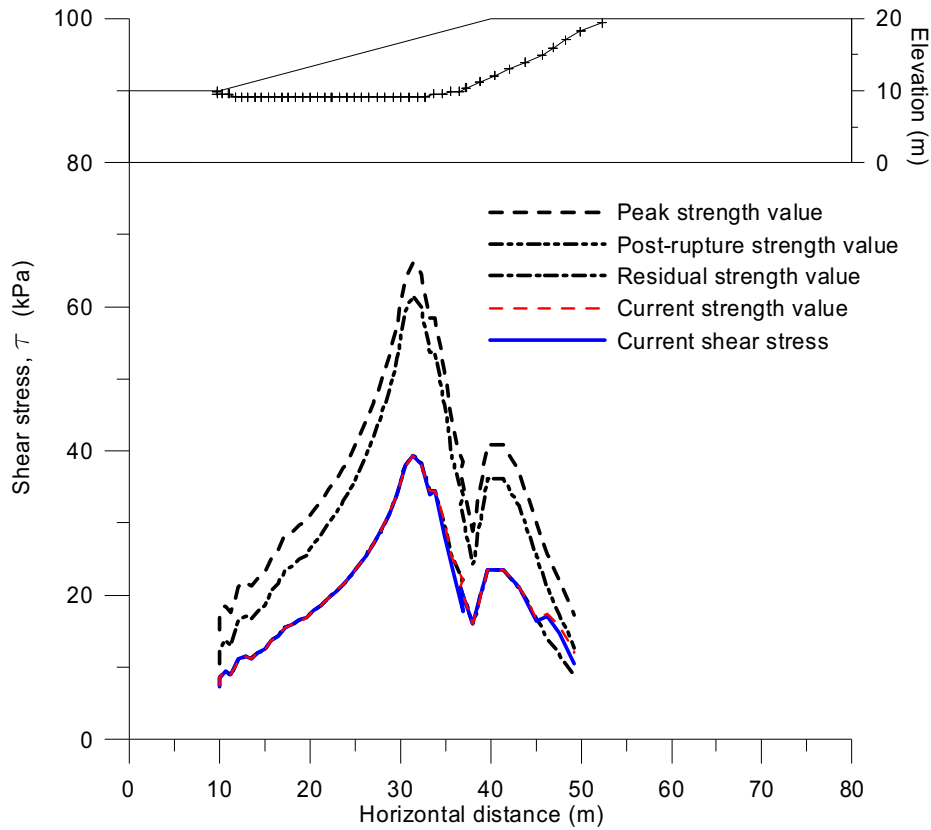


Fig. 5.58 Shear stress distribution along failure surface 15.2 years at collapse

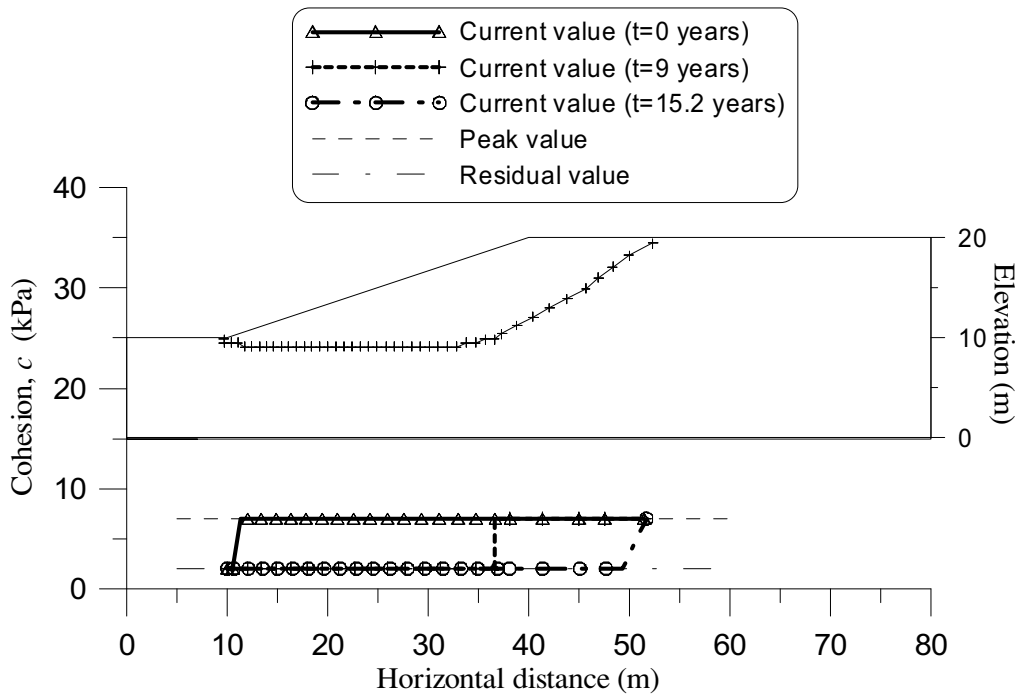


Fig. 5.59 Development of cohesion along failure surface

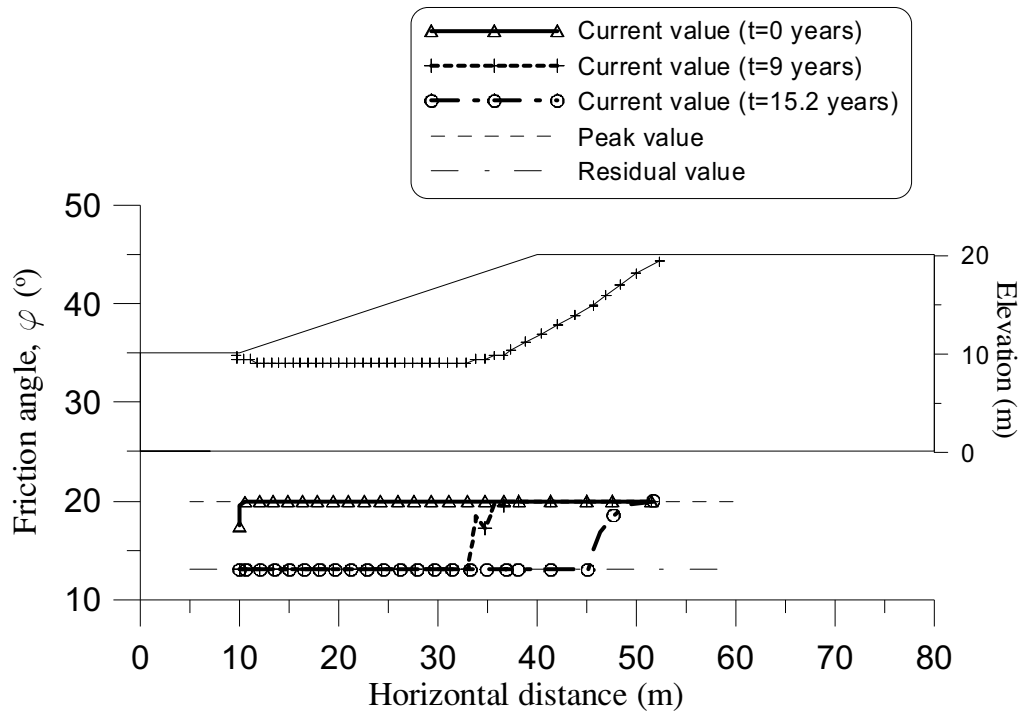


Fig. 5.60 Development of friction along failure surface

At the same time, the current shear strength parameters along slip surface are shown in Fig. 5.59 and Fig. 5.60. It is evident from these figures that the development process of shear strength parameters along the failure surface looks like a wave propagation associated with progressive failure.

In the beginning the strength parameters along most part of the slip surface are equal to the peak values. As time elapsed, residual values were reached along the failed surface whereas most of the rest kept the peak values. Again, there was a short intermediate part where the values were between peak and residual values. In particular, Fig. 5.59 exhibits the rapid reduction of cohesion, which is incorporated in the post-rupture strength concept.

Fig. 5.61 shows the pore pressure distribution along the failure surface. Just after excavation, the pore pressure close to the slope toe had a high negative value. With the increase of horizontal distance to the slope toe, the pore pressure along the failure surface became positive and reached the maximum value at the zone of transition from horizontal part to the back slip part. As time elapsed, the pore pressure became positive tending towards the steady state value.

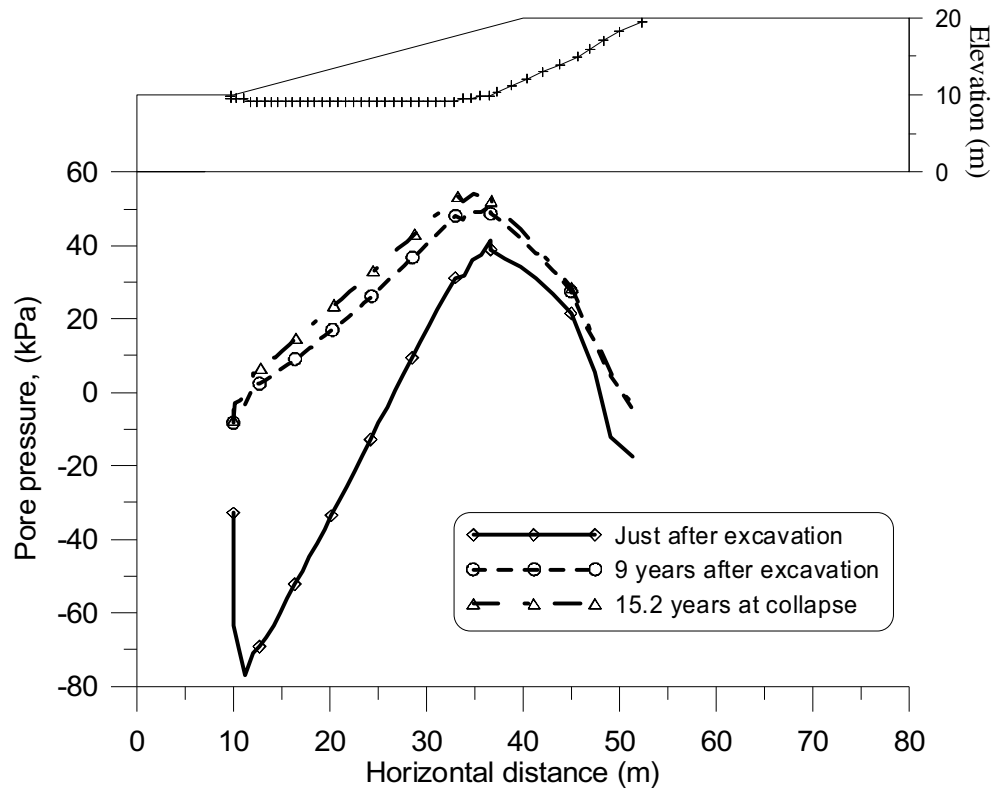


Fig. 5.61 Development of pore pressure along failure surface

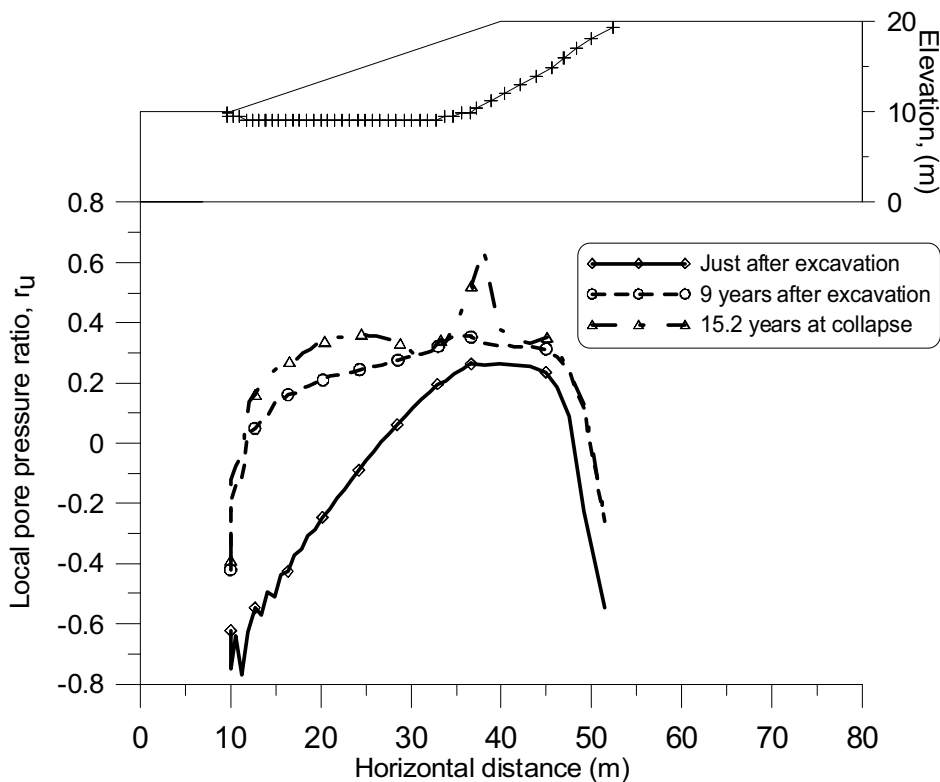


Fig. 5.62 Development of local pore pressure ratio along failure surface

The local pore pressure ratio along failure surface (as seen in Fig. 5.62) has a similar variation tendency as the pore pressure.

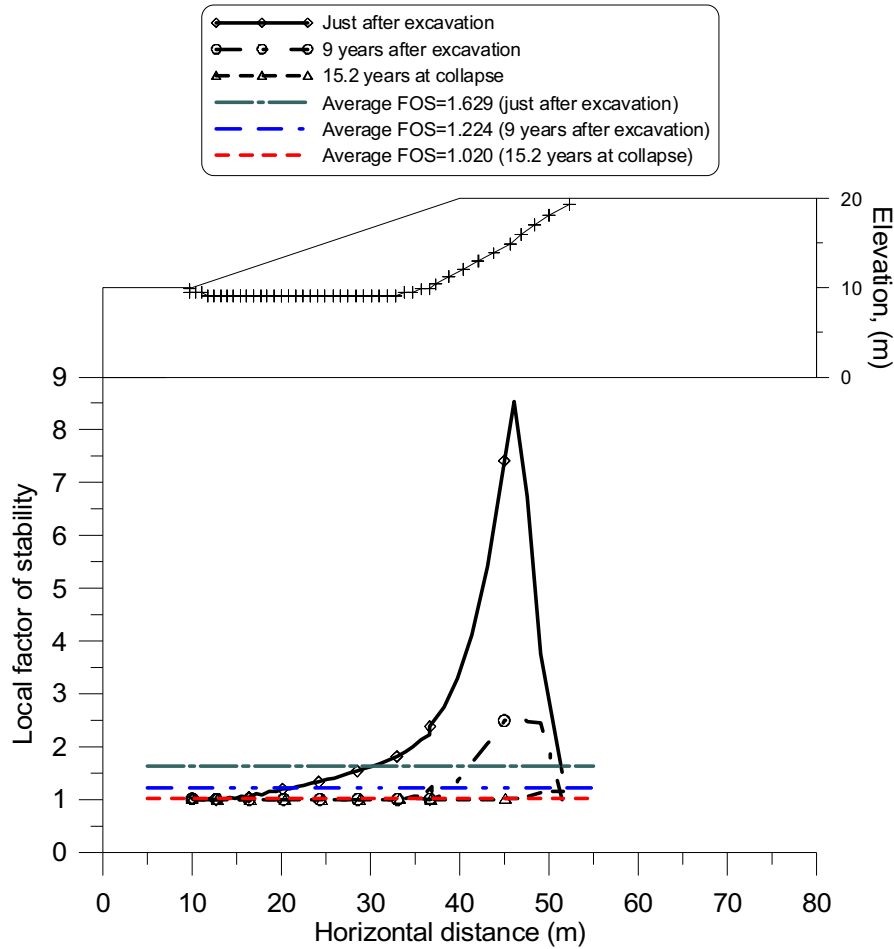


Fig. 5.63 Development of local factor of stability along failure surface

It is particularly interesting to observe the distribution of the local factor of stability along the failure surface as shown in Fig. 5.63. The local factor of stability is calculated as

$$FOS_{local} = \frac{S_{cur}}{S_{mob}} = \frac{\tau_{cur}l}{\tau_{mob}l} \quad (5.5)$$

where l is the local element length along slip surface; τ_{mob} is obtained from Eq. (5.3); and τ_{cur} is calculated under plane strain conditions by

$$\tau_{cur} = (\sigma'_1 - \sigma'_2) / 2 \quad (5.6)$$

where σ'_1 and σ'_2 are respectively the maximum and minor principal effective stresses.

Accordingly, the average factor of stability can be worked out by dividing available shear resistance by mobilised shear stress as given by

$$FOS_{ave} = \frac{\sum S_{cur}}{\sum S_{mob}} = \frac{\sum \tau_{cur}l}{\sum \tau_{mob}l} \quad (5.7)$$

In Fig. 5.63, the development of progressive failure can be readily seen. Just after excavation, the local factors of stability along most part of the slip surface were larger

than 1.0 and the average FOS was 1.629 which meant that the slope was stable at this moment. At 9 years after excavation, the local factors of stability along horizontal part of the slip surface were almost equal to 1.0 whereas those along the back part of the failure surface were still larger than 1.0. The average FOS was 1.224 and the slope was generally stable although it was in an intermediate course towards final failure. Eventually at 15.2 years after excavation, the slope collapsed and the local factors of stability along the slip surface were equal to 1.0 or very close to 1.0. The average FOS was 1.020 consistent with a slope at a critical condition (i.e. just at failure).

5.3.5.2 Effect of K_0

Similar to analyses with one-stage softening model, analyses TS1 – TS6 were all performed for a 10 m high 3:1 slope with K_0 varying from 1.0 to 2.15. Fig. 5.64 shows the mid-slope horizontal displacement variations with time. The mid-height displacements start to accelerate after a gradual relatively steady increase. Final collapse is quite abrupt, without significant warning from accelerating displacement. This agrees with the results indicated in Fig. 5.39.

The collapse time is strongly dependent on K_0 and increases continuously with K_0 (Fig. 5.40). As in case S1, the final collapse in case TS1 occurs after an initial small-scale failure. The mid-slope horizontal displacement at collapse increases also with K_0 (as indicated in Table 5.4).

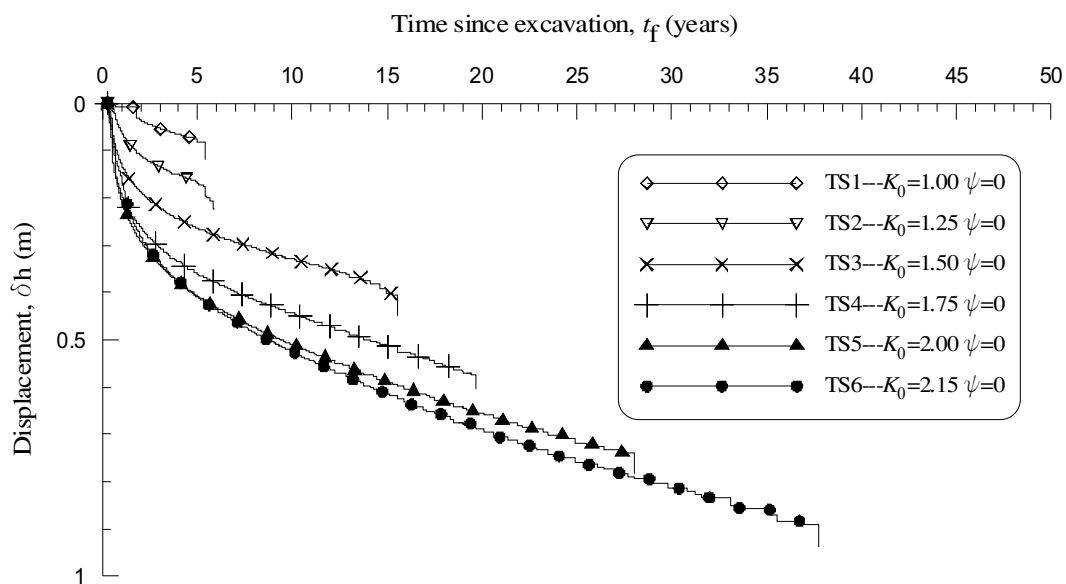


Fig. 5.64 Mid-slope horizontal displacement with time for TS1-TS6

It is important to see from Fig. 5.64 and Figure 5.39 that the collapse times with two-stage softening model are longer than those with one-stage softening model when $K_0 > 1.25$. This may be due to that the friction angle in two-stage softening model is larger than that for one-stage softening model with the same plastic shear strain, especially during the second softening stage. This can be seen as $\phi_M > \phi_N$ in Fig. 5.49 where \overline{ABD} and \overline{GHJ} represent the one-stage softening whereas \overline{ABCD} and \overline{GHIJ} indicate the two-stage softening. \overline{ABCD} and \overline{GHIJ} exhibit one-stage softening feature because $c_{pr} = c_r$ and $\phi_{pr} = \phi_r$. This will increase the shear strength in the

second softening stage and therefore delay further the collapse time to failure. As a matter of fact, during the first softening stage, the relevant cohesion is smaller than that for one-stage softening model at the same plastic shear strain (as seen as $c_F < c_E$ in Fig. 5.49). Arguably, there should be some influence on the slope stability. However, the analysis results indicate that this is not the case.

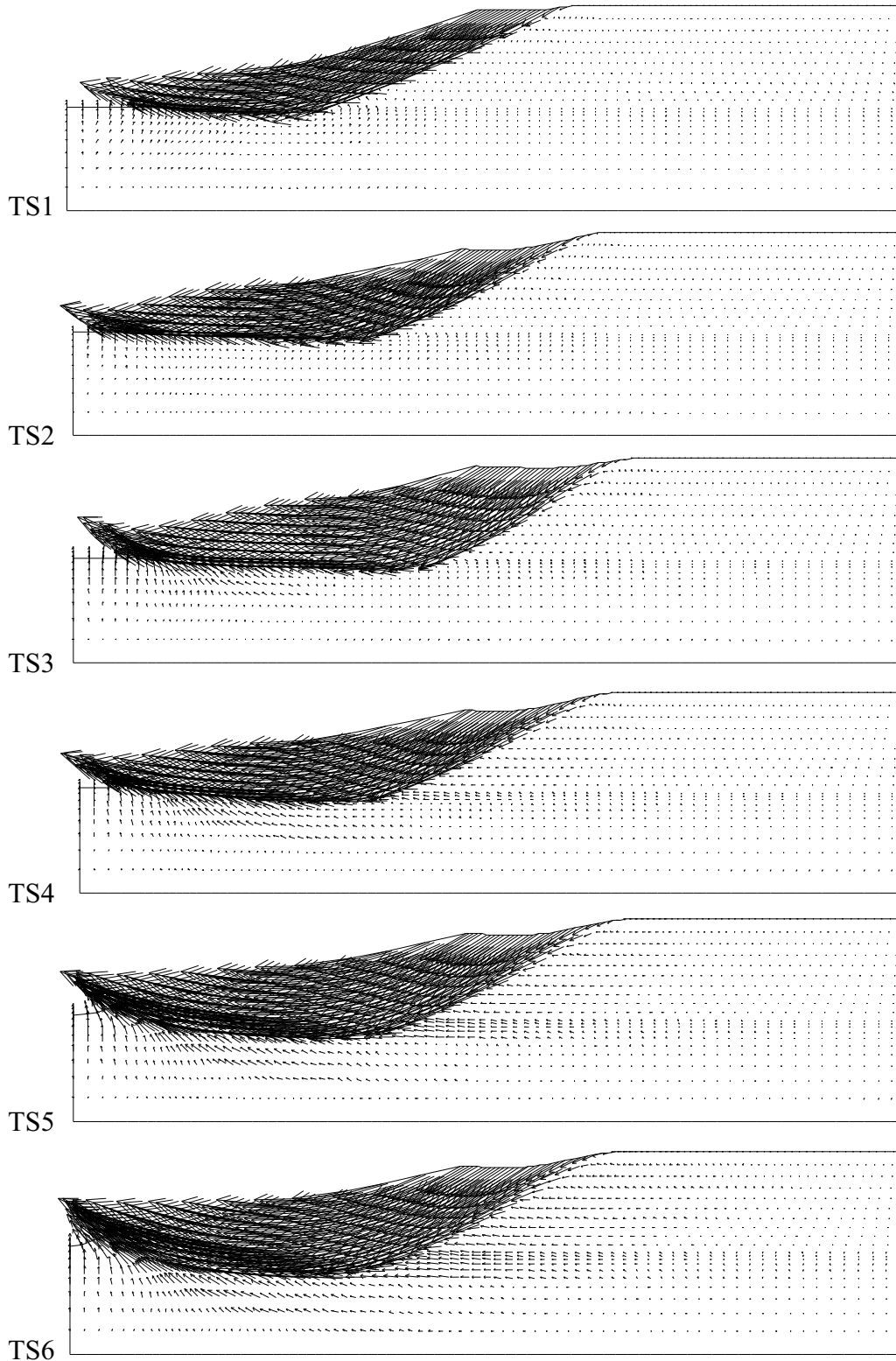


Fig. 5.65 Displacement vectors for TS1-TS6

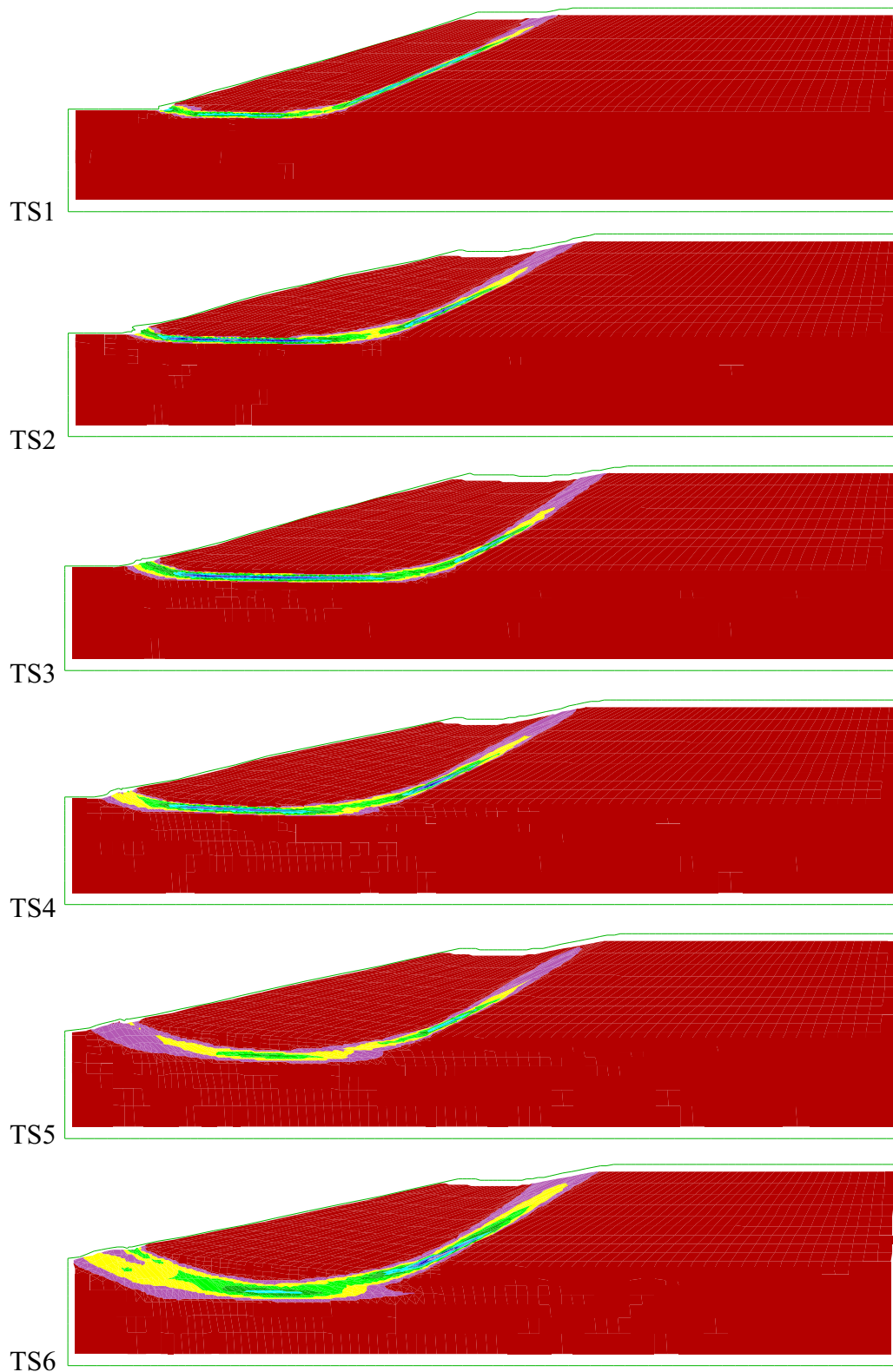


Fig. 5.66 Accumulated plastic shear strain for TS1-TS6

The shapes of the rupture surface expressed by displacement vectors and accumulated plastic shear strain for each analysis are shown in Fig. 5.65 and Fig. 5.66. Again, the influence of K_0 is apparent. The slip surfaces become deeper as K_0 increases from 1.0 to 2.15. As K_0 increases from 1.00 to 1.50, the back of the slip extends towards

the inner part of the slope. At $K_0 = 1.5$, the distance from the intersection of the back slip surface with the ground surface to the slope crest is the largest. As K_0 increases further from 1.75, the back of the slip moves back towards the slope.

Moreover, as shown in both Fig. 5.65 and Fig. 5.66, the length of the horizontal rupture surface which develops from the toe of the slope increases with K_0 . With high values of K_0 it extends beyond the crest of the slope. Then the back of the final rupture surface develops subsequently closer to the slope, and the inner part of the horizontal rupture surface is not incorporated in the final rupture surface.

5.3.5.3 Effect of slope geometry

Analysis TS8 is of a 2:1 slope, 10 m high, with $K_0 = 1.5$ and surface suction $u_b = -10$ kPa. Again the steeper slope failed earlier (1.00 years compared to 15.2 years).

Analyses TS9 and TS10 were performed to examine the stability of 2:1 and 2.5:1 slopes, 10 m high, with $K_0 = 2.0$. Results may be compared with analysis S5 for the 3:1 slope. Analysis S11 was of a 4:1 slope, 10 m high, with $K_0 = 1.5$ and surface suction $u_b = -10$ kPa. The development of deformation with time is shown in Fig. 5.67. As the slope becomes flatter, the collapse time tends to be longer and the slope is more stable.

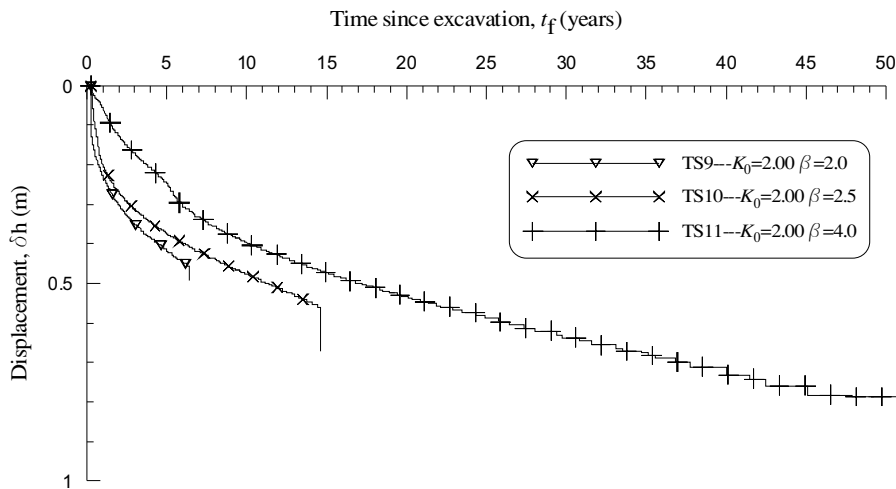


Fig. 5.67 Mid-slope horizontal displacement with time for TS9-TS11

Compared with results for one-stage softening model, collapse time is longer. For case TS8 with $K_0 = 1.5$, the collapse time is the same as that for case S8.

Moreover, it is seen from Table 5.4 that both the mid-slope horizontal displacement at collapse and collapse time rise with slope parameter β .

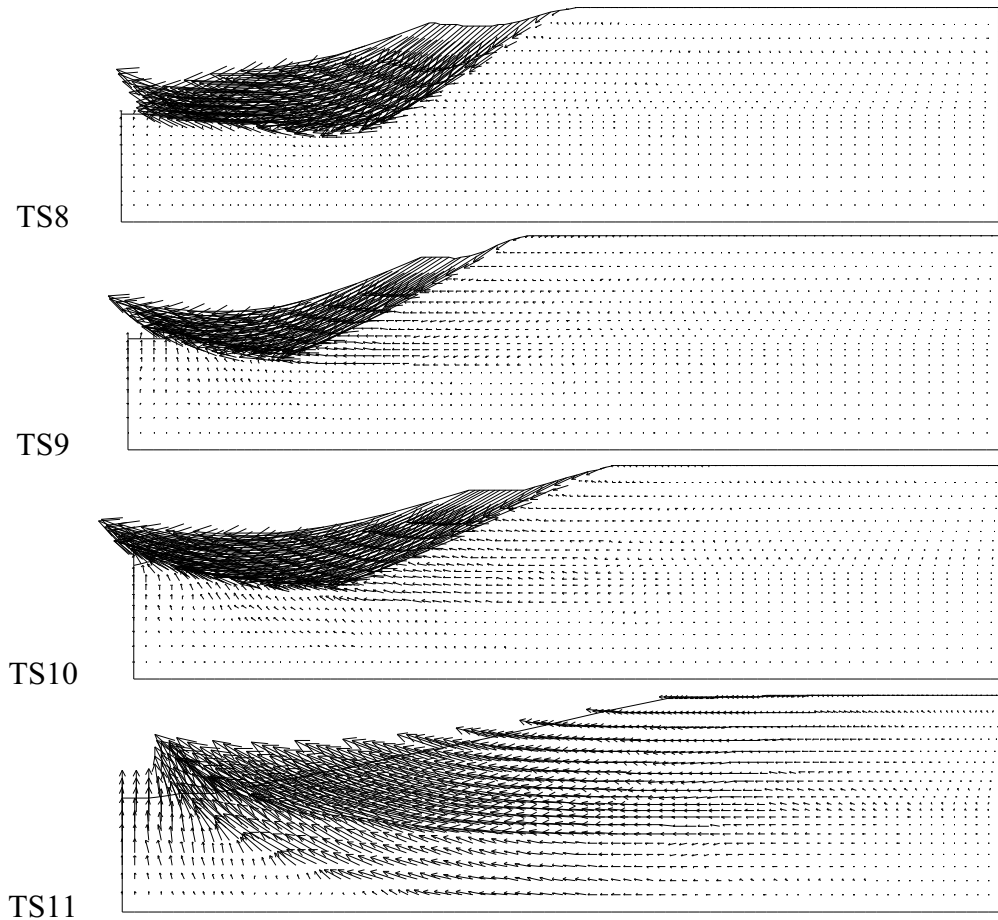


Fig. 5.68 Displacement vectors for TS8-TS11

Fig. 5.68 and Fig. 5.69 show displacement vectors and plastic shear strain for cases TS8-TS11. From these plots, it is clear that, as the slope becomes flatter, the back slip surface tends to be closer to the slope. For case TS11 ($\beta = 4$), the clay mass experiencing large deformations extends to the deeper and inner region of the slope.

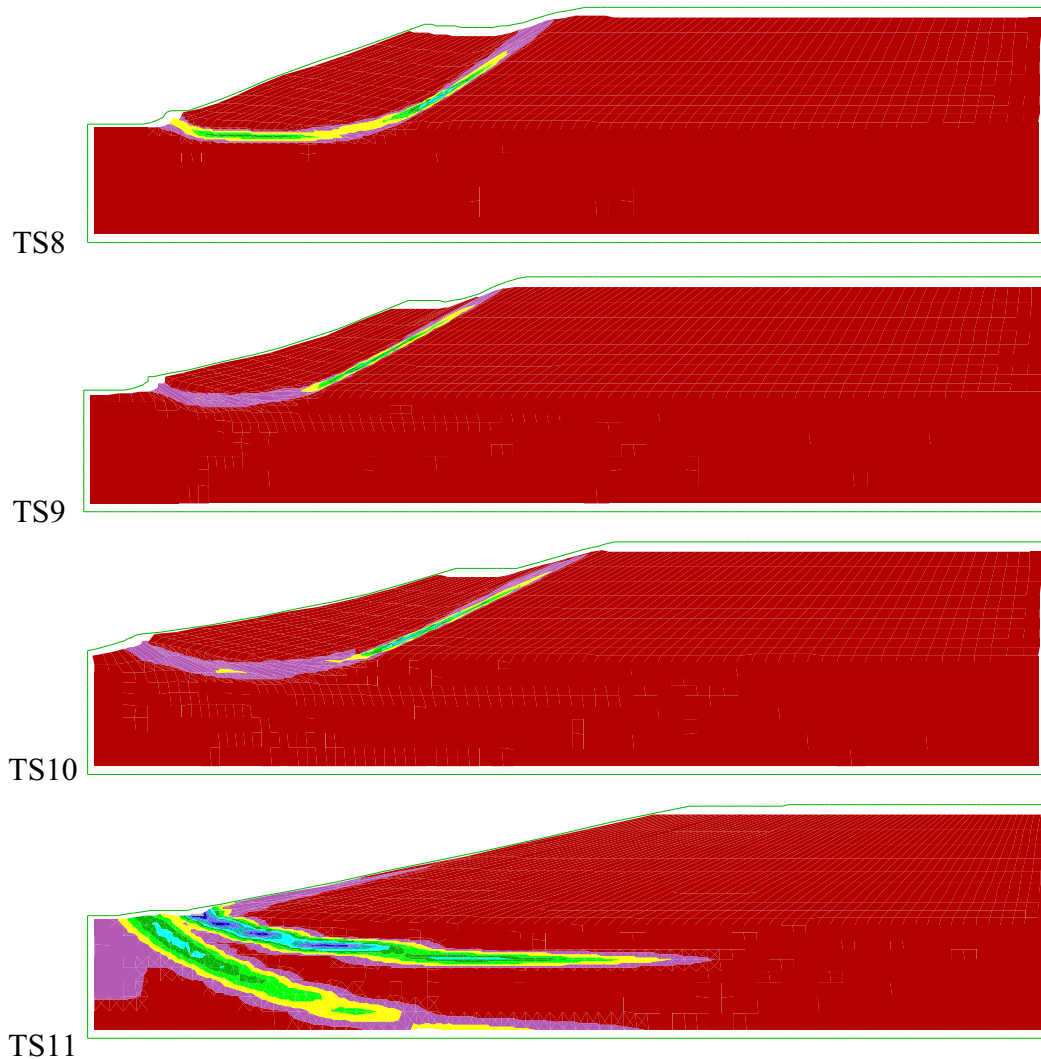


Fig. 5.69 Accumulated plastic shear strain for TS8-TS11

5.3.5.4 Summary for two-stage softening with bulk peak strength

From Table 5.4, it can be concluded that:

1. For two-stage softening analyses TS1-TS6, TS8 and TS9, slope collapse time t_f and displacement at collapse increase generally with K_0 .
2. By comparing results of analyses TS5 and TS7, it can be seen that the surface suction may also reduce the occurrence of slope failure. Planting vegetation on slope surface can stabilise slope through increasing slope surface suction.
3. By comparison of results of TS9, TS10, TS5 and TS11, it is evident that slope collapse time t_f and displacement at collapse reduce with slope angle. When the slope reaches 1:4, the slope is stable during a quite long period which is more than 100 years.

Furthermore, by comparison of results in Table 5.4 for two-stage softening analyses with those in Table 5.3 for one-stage softening analyses, it can be stated that:

4. Slope collapse times t_f in most two-stage softening analyses with bulk peak strength are generally a little longer than those in one-stage softening analyses although this trend is reversed in a few cases.
5. Displacements at collapse in two-stage softening analyses are generally larger than those in one-stage softening analyses.

5.3.6 Sensitivity analysis of softening strength parameters

Table 5.5 Results of two-stage softening modelling with different softening rate

| Analysis | Height (m) | Slope ($\cot \beta$) | K_0 | ψ (deg) | u_b (kPa) | Middle slope XDisplacement at collapse (mm) | t_f (years) |
|----------|------------|------------------------|-------|--------------|-------------|---|---------------|
| TS1N | 10 | 3 | 1.00 | 0 | -10 | 93.6 | 6.7 |
| TS2N | 10 | 3 | 1.25 | 0 | -10 | 234 | 11.4 |
| TS3N | 10 | 3 | 1.50 | 0 | -10 | 429 | 14.5 |
| TS4N | 10 | 3 | 1.75 | 0 | -10 | 596 | 20.1 |
| TS5N | 10 | 3 | 2.00 | 0 | -10 | 791 | 23.4 |
| TS6N | 10 | 3 | 2.15 | 0 | -10 | 914 | 26.1 |
| TS7N | 10 | 3 | 2.00 | 0 | -20 | >803 | >100* |
| TS8N | 10 | 2 | 1.50 | 0 | -10 | 180 | 0.80 |
| TS9N | 10 | 2 | 2.00 | 0 | -10 | 427 | 5.0 |
| TS10N | 10 | 2.5 | 2.00 | 0 | -10 | 537 | 9.7 |
| TS11N | 10 | 4 | 2.00 | 0 | -10 | >869 | >100* |

* Final calculation time

A series of sensitivity analyses were carried out to study the influence of softening strength parameters including both the strength magnitude and softening rate. All the calculation schemes and the relevant analysis results are listed in Table 5.5 and Table 5.6.

Table 5.6 Strength parameters of different softening analyses and relevant results

| Analysis | γ_p | γ_{pr} | γ_r | c_p | c_{pr} | c_r | ϕ_p | ϕ_{pr} | ϕ_r | Middle slope XDisplacement at collapse (mm) | t_f (years) |
|------------|------------|---------------|------------|-------|----------|-------|----------|-------------|----------|---|---------------|
| TS1-TS11 | 0.015 | 0.020 | 0.115 | 7 | 2 | 2 | 20 | 20 | 13 | - | - |
| TS1N-TS11N | 0.025 | 0.030 | 0.100 | 7 | 2 | 2 | 20 | 20 | 13 | - | - |
| TS3A* | 0.015 | 0.020 | 0.115 | 7 | 2 | 2 | 20 | 20 | 13 | 407 | 15.2 |
| TS3B | 0.025 | 0.040 | 0.100 | 7 | 2 | 2 | 20 | 19 | 13 | 444 | 15.2 |
| TS3C | 0.025 | 0.040 | 0.100 | 7 | 2 | 2 | 20 | 18.6 | 13 | 441 | 15.2 |
| TS3D | 0.0 | 0.010 | 0.100 | 7 | 2 | 2 | 20 | 19 | 13 | 370 | 9.3 |
| TS3E | 0.005 | 0.015 | 0.105 | 7 | 2 | 2 | 20 | 19 | 13 | 417 | 15.2 |
| TS3F | 0.010 | 0.020 | 0.200 | 7 | 2 | 2 | 20 | 19 | 13 | 391 | 12.7 |

* TS3A is the alias of TS3

5.3.6.1 Comparison of analyses TS1-TS11 with analyses TS1N-TS11N

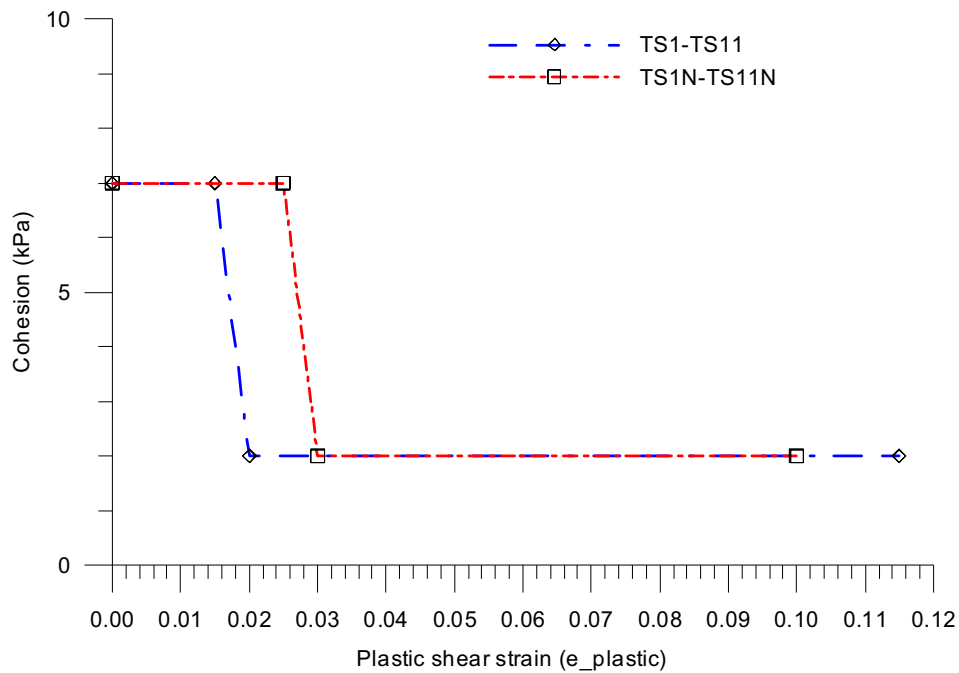


Fig. 5.70 Cohesion variation with plastic shear strain for different analyses

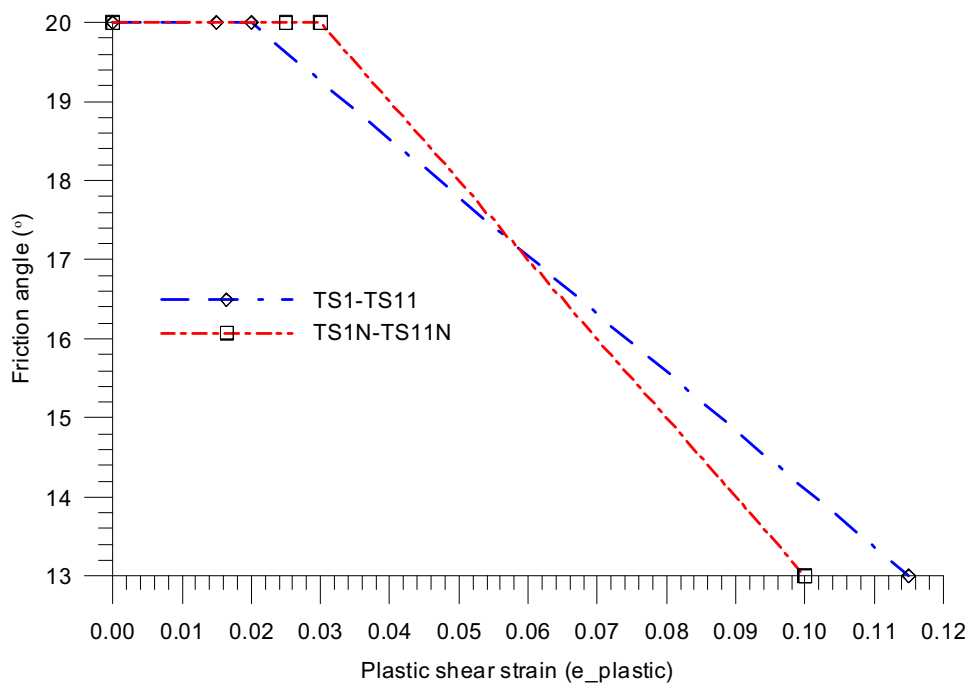


Fig. 5.71 Friction angle variation with plastic shear strain for different analyses

In Table 5.5, all the strength parameters adopted in analyses TS1N-TS11N were chosen as $c'_p = 7\text{kPa}$, $\phi'_p = 20^\circ$, $c'_{pr} = 2\text{kPa}$, $\phi'_{pr} = 20^\circ$, $c'_r = 2\text{kPa}$, $\phi'_r = 13^\circ$ and $\gamma_p = 0.025$, $\gamma_{pr} = 0.030$, $\gamma_r = 0.100$ (shown in Fig. 5.70 and Fig. 5.71). Compared with those used in Table 5.4, both γ_p and γ_{pr} herein are 0.01 larger than those applied in Table 5.4. Whereas γ_r is 0.015 smaller than that in Table 5.4. This means

that softening rate from peak state to residual state in analyses TS1N-TS11N is greater than that in Table 5.4 although the softening rate from peak state to post-rupture state is the same as that in Table 5.4.

Results in Table 5.5 illustrate the same tendency of collapse time and displacement at collapse with K_0 and same surface suction influence as in the series TS1-TS11.

By comparison of results in Table 5.4 and those in Table 5.5 and Table 5.6, it can be concluded that:

1. As shown in Fig. 5.72, Table 5.4 and Table 5.5, slope collapse time t_f for analyses TS1N-TS4N with K_0 varying from 1.00 to 1.75 is longer than that for analyses TS1-TS4. But slope collapse time t_f for analyses TS5N-TS6N with K_0 larger than 1.75 (2.00 and 2.15) is shorter than that for analyses TS5-TS6.

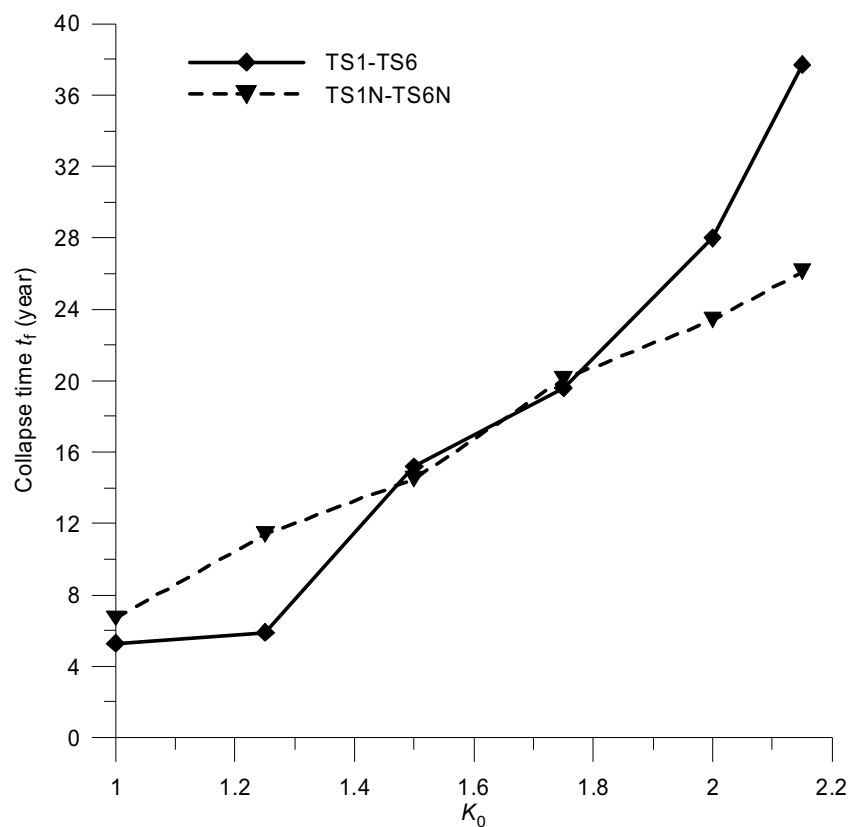


Fig. 5.72 Variation of collapse time with K_0

2. Slope collapse time t_f for analyses TS8N-TS10N with slope steeper than 1:3 in Table 5.5 is shorter than that for analyses TS8-TS10 in Table 5.4.
3. Displacement at collapse for analyses TS1N-TS7N in Table 5.5 is generally larger than that for analyses TS1-TS7 in Table 5.4.
4. Displacement at collapse for analyses TS8N-TS11N with slope steeper than 1:3 in Table 5.5 is generally shorter than that for analyses TS8-TS11 in Table 5.4.
5. The conclusions 1-4 demonstrate that the influence of changing softening rate is not straightforward according to the comparison of results in Table 5.6 and Table 5.5 and those in Table 5.4.

In addition, similar conclusions as those for analyses TS1-TS11 can be drawn on the effect of K_0 and slope geometry for analyses TS1N-TS11N.

5.3.6.2 Comparisons among results of analyses TS3A-TS3F

A series of analyses TS3A-TS3F (shown in Table 5.6) were carried out to study further the influence of softening strength parameters by using different strength parameters (shown in Fig. 5.73 and Fig. 5.74).

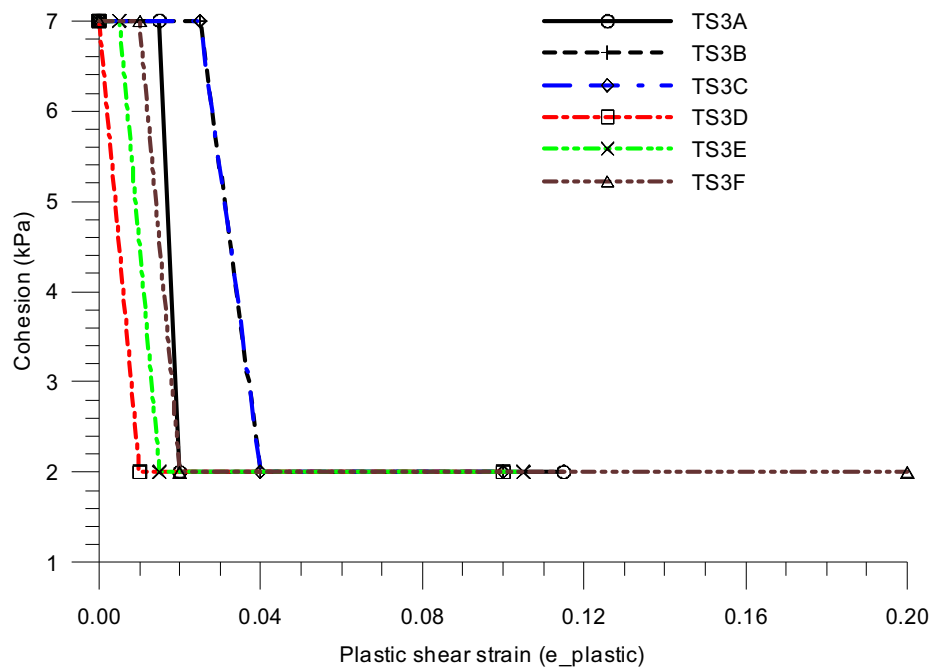


Fig. 5.73 Cohesion variation with plastic shear strain for different analyses

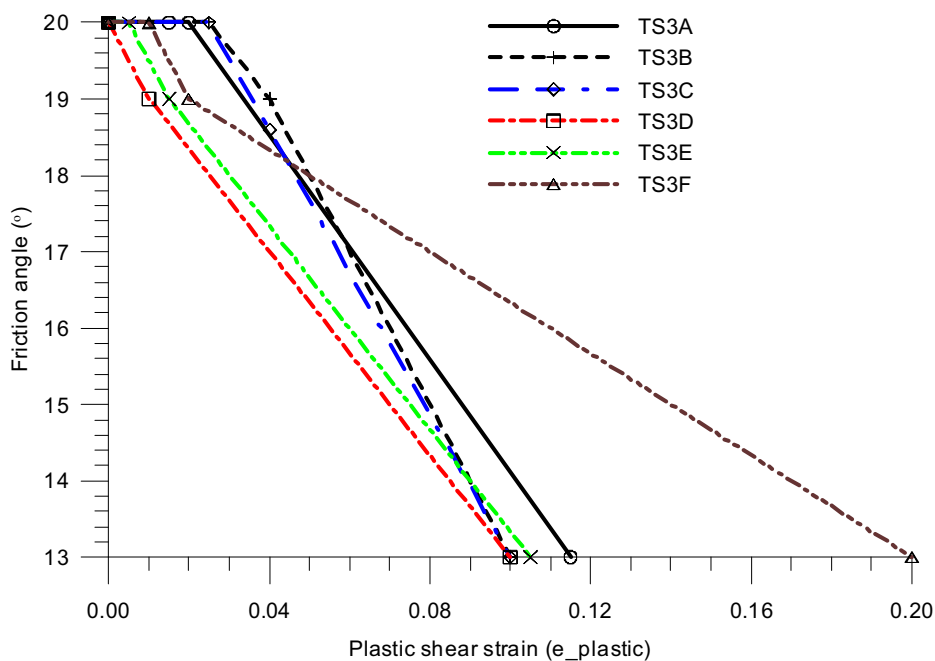


Fig. 5.74 Friction angle variation with plastic shear strain for different analyses

In TS3B a little lower friction angles, larger γ_p and γ_{pr} , and smaller γ_r than those in TS3A are adopted. The relevant collapse time does not change whereas the displacement at collapse is larger due to the larger γ_p and γ_{pr} . Parameters for TS3C are almost the same as those in TS3B except a slightly smaller friction angle.

TS3D, TS3E and TS3F use the same strength parameters for cohesion and friction angle but different strain-softening rate. In case TS3E, the collapse time is the same as those for TS3B and TS3C with smaller displacement at collapse. In case TS3D, γ_p and γ_{pr} are much smaller, which causes shorter collapse time and smaller displacements at collapse. In case TS3F, the collapse time is shorter than for case TS3E.

5.3.7 Softening analyses with intact peak strength

As seen in Table 5.1 and Table 5.6, the bulk peak strength parameters are applied in view of the highly fissured property of clay. The theoretical parameters of post-rupture strength are selected by keeping the relevant frictional angle same as the peak value and slightly lower cohesion. However, in consideration of the whole formation process of highly fissured clay, the intact peak strength ($c'_p = 20\text{kPa}$, $\phi'_p = 20^\circ$, Potts et al., 1997) might be reckoned as the initial original peak strength and the bulk peak strength could be reasonably assumed as the so-called relevant post-rupture strength ($c'_{pr} = 7\text{kPa}$, $\phi'_{pr} = 20^\circ$) accounting for the fissures in clay. Meanwhile, the residual strength ($c'_r = 2\text{kPa}$, $\phi'_r = 13^\circ$) is kept the same as that applied in former *FLAC* analyses. With this set of softening strength parameters ($c'_p = 20\text{kPa}$, $\phi'_p = 20^\circ$, $c'_{pr} = 7\text{kPa}$, $\phi'_{pr} = 20^\circ$, $c'_r = 2\text{kPa}$, $\phi'_r = 13^\circ$), another series of analyses (seen in Table 5.7 and Table 5.8) were conducted to investigate the influence of applying intact peak strength and the whole softening process of stiff clay. Now, slopes of different heights are analyzed.

Table 5.7 Strength parameters for softening analyses with intact peak strength

| Analysis | γ_p | γ_{pr} | γ_r | c_p | c_{pr} | c_r | ϕ_p | ϕ_{pr} | ϕ_r |
|------------------|--------------|---------------|--------------|-----------|----------|----------|-----------|-------------|-----------|
| TS12H10 | 0.020 | 0.025 | 0.100 | 20 | 7 | 2 | 20 | 20 | 13 |
| TS12H12 | 0.020 | 0.025 | 0.100 | 20 | 7 | 2 | 20 | 20 | 13 |
| TS12H12_5 | 0.020 | 0.025 | 0.100 | 20 | 7 | 2 | 20 | 20 | 13 |
| TS12H13 | 0.020 | 0.025 | 0.100 | 20 | 7 | 2 | 20 | 20 | 13 |
| TS12H14 | 0.020 | 0.025 | 0.100 | 20 | 7 | 2 | 20 | 20 | 13 |
| S12H13_5 | 0.020 | - | 0.100 | 20 | - | 2 | 20 | - | 13 |
| S12H13_7 | 0.020 | - | 0.100 | 20 | - | 2 | 20 | - | 13 |
| S12H14 | 0.020 | - | 0.100 | 20 | - | 2 | 20 | - | 13 |
| TS12H14N1 | 0.010 | 0.025 | 0.100 | 20 | 7 | 2 | 20 | 20 | 13 |
| TS12H14N2 | 0.005 | 0.010 | 0.100 | 20 | 7 | 2 | 20 | 20 | 13 |
| TS12H14N3 | 0.001 | 0.005 | 0.100 | 20 | 7 | 2 | 20 | 20 | 13 |
| TS12H14N3N1 | 0.001 | 0.005 | 0.100 | 20 | 7 | 2 | 20 | 18 | 13 |
| TS12H14N3N2 | 0.001 | 0.005 | 0.100 | 20 | 4 | 2 | 20 | 20 | 13 |
| TS12H14N4 | 0.020 | 0.025 | 0.100 | 20 | 7 | 2 | 20 | 18 | 13 |
| TS12H14N5 | 0.020 | 0.025 | 0.100 | 20 | 2 | 2 | 20 | 20 | 13 |
| TS12H10N1 | 0.010 | 0.025 | 0.100 | 20 | 7 | 2 | 20 | 20 | 13 |
| TS12H10N2 | 0.005 | 0.010 | 0.100 | 20 | 7 | 2 | 20 | 20 | 13 |
| TS12H10N3 | 0.001 | 0.005 | 0.100 | 20 | 7 | 2 | 20 | 20 | 13 |

Table 5.8 Results of stable slope height of softening analyses with intact peak strength

| Analysis | Slope height H (m) | Slope (cot β) | K_0 | Stable state | Middle slope XDisplacement at collapse/at stable state (mm) | t_f (years) |
|------------------|--------------------|----------------------|-------------|-----------------|---|-----------------|
| TS12H10 | 10 | 3 | 1.50 | Stable | >459 | >100* |
| TS12H12 | 12 | 3 | 1.50 | Stable | >670 | >100* |
| TS12H12_5 | 12.5 | 3 | 1.50 | Unstable | 636 | 50.8 |
| TS12H13 | 13 | 3 | 1.50 | Unstable | 645 | 40.0 |
| TS12H14 | 14 | 3 | 1.50 | Unstable | 734 | 29.1 |
| S12H13_5 | 13.5 | 3 | 1.50 | Stable | 688 | >100* |
| S12H13_7 | 13.7 | 3 | 1.50 | Unstable | 758 | 71.6 |
| S12H14 | 14 | 3 | 1.50 | Unstable | 770 | 55.0 |
| TS12H14N1 | 14 | 3 | 1.50 | Unstable | 718 | 26.4 |
| TS12H14N2 | 14 | 3 | 1.50 | Unstable | 644 | 20.8 |
| TS12H14N3 | 14 | 3 | 1.50 | Unstable | 565 | 13.9 |
| TS12H14N3N1 | 14 | 3 | 1.50 | Unstable | 544 | 13.6 |
| TS12H14N3N2 | 14 | 3 | 1.50 | Unstable | 553 | 13.5 |
| TS12H14N4 | 14 | 3 | 1.50 | Unstable | 738 | 28.0 |
| TS12H14N5 | 14 | 3 | 1.50 | Unstable | 729 | 27.3 |
| TS12H10N1 | 10 | 3 | 1.50 | Stable | >476 | >100* |
| TS12H10N2 | 10 | 3 | 1.50 | Unstable | 493 | 63.0 |
| TS12H10N3 | 10 | 3 | 1.50 | Unstable | 447 | 19.5 |

* Final calculation time

In addition, the cohesion and friction angle variations with plastic shear strain for different analyses are shown in Fig. 5.75 and Fig. 5.76.

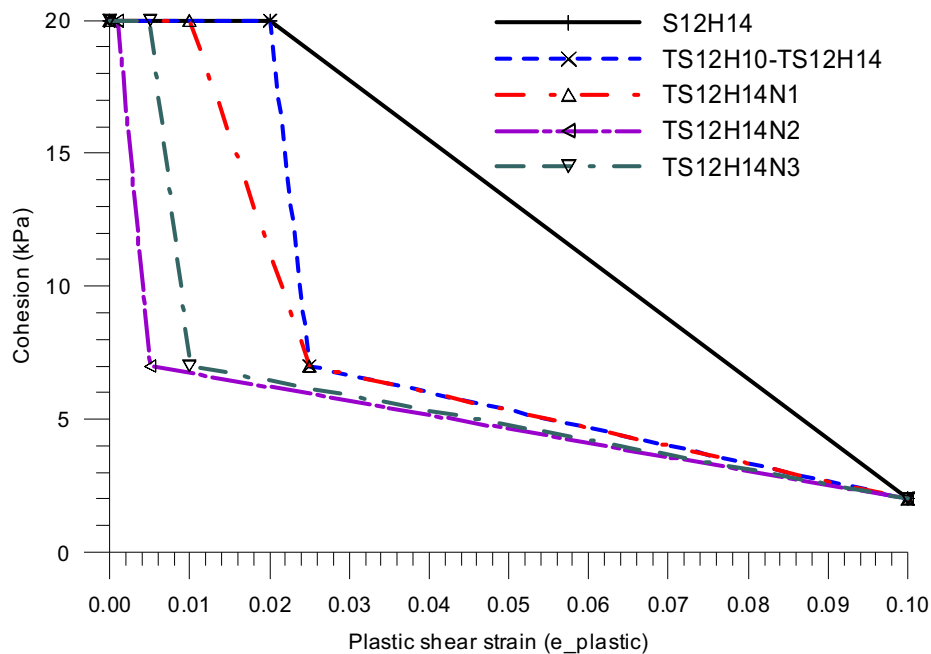


Fig. 5.75 Cohesion variation with plastic shear strain for different analyses

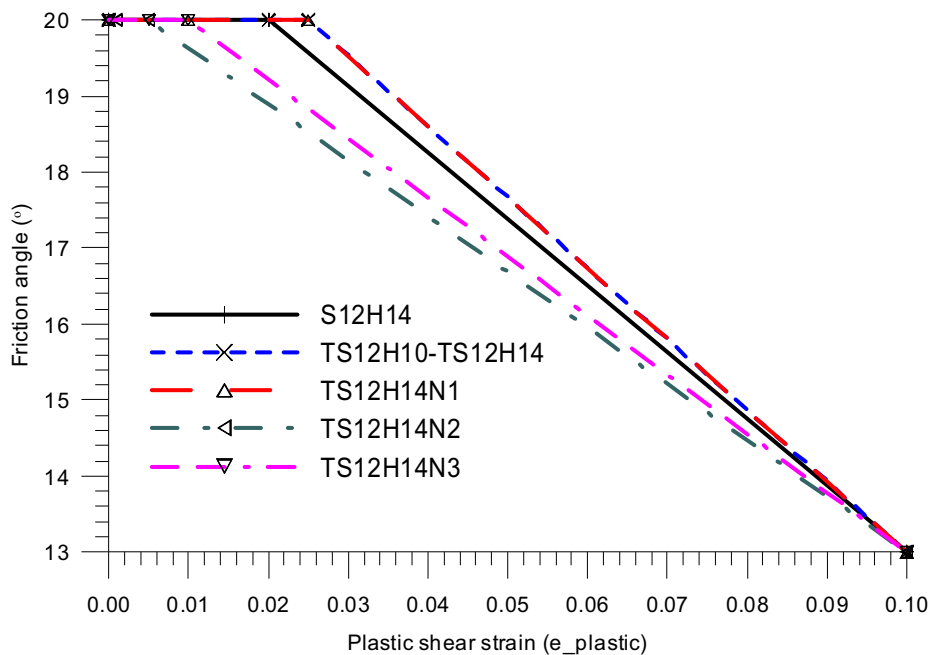


Fig. 5.76 Friction angle variation with plastic shear strain for different analyses

The peak and residual strength parameters analysis S12H14 are the same as those adopted in analysis TS12H14. In analyses TS12H14N1-TS12H14N3, the only difference lies in the plastic shear strain threshold values γ_p and γ_{pr} . In analyses TS12H14N3N1, TS12H14N3N2, TS12H14N4 and TS12H15, there are small variations in cohesion and friction angle.

Analysis TS12H10 is taken as a reference where the plastic shear strain threshold values are set as $\gamma_p = 0.020$, $\gamma_{pr} = 0.025$, $\gamma_r = 0.1$. It is clear that the post-rupture plastic shear strain $\gamma_{pr} = 0.025$ in analysis TS12H10 is equal to the peak plastic shear strain $\gamma_p = 0.025$ in analyses via one-stage softening model stated in section 5.3.4. At the same time the residual plastic shear strain γ_r is kept unchanged. However, the slope collapse time t_f in analysis TS12H10 is longer than 100 years and the slope is assumed to be basically stable after the slope cut.

Meanwhile, a series of analyses TS12H10N1-TS12H10N3 in which the softening rate in the first softening stage of two-stage softening model is increased are performed. In analysis TS12H10N1, the slope does not fail even 100 years after the cut. But the corresponding collapse times for the analyses TS12H10N2 and TS12H10N3 are respectively 63.0 years and 19.5 years.

All the analyses TS12H10 and TS12H10N1-TS12H10N3 imply that increasing the softening rate in the first softening stage of two-stage softening model will accelerate the slope failure.

It should be noted that, in all the analyses described in sections 5.3.3, 5.3.4, 5.3.5 and 5.3.6 (shown in Table 5.3, Table 5.4, Table 5.5 and Table 5.6), the slope height is all set as 10 m which is also the slope height in all the analyses TS12H10 and TS12H10N1-TS12H10N3.

On the other hand, another series analyses TS12H10, TS12H12, TS12H12_5, TS12H13 and TS12H14 are conducted by setting the plastic shear strain threshold values as $\gamma_p = 0.020$, $\gamma_{pr} = 0.025$, $\gamma_r = 0.1$ and keeping them constant. It can be concluded from Table 5.8 that the higher the slope, the shorter the slope collapse time. The same conclusion can be drawn from the results of analyses S12H13_5, S12H13_7 and S12H14 in which one-stage softening model is adopted with $\gamma_p = 0.020$, $\gamma_r = 0.1$.

It can also be demonstrated from Table 5.7 and Table 5.8 that the collapse time reduces with the increase in softening rate in analyses TS12H14 and TS12H14N1-TS12H14N3 with two-stage softening model, where the plastic shear strain threshold values γ_p and γ_{pr} diminish gradually whereas γ_r is unchanged.

Furthermore, it may be seen by comparison of analyses TS12H14N3N1 and TS12H14N3N2 and analysis TS12H14N3 that the collapse time decreases with the reduction of post-rupture strength parameter c_{pr} or ϕ_{pr} . The same conclusion can be drawn by comparison of analyses TS12H14N4 and TS12H14N5 and analysis TS12H14.

Finally, according to Table 5.7 and Table 5.8, the collapse time (29.1 years) in analysis TS12H14 using two-stage softening model is approximately half of the collapse time (55.0 years) in analysis S12H14 applying one-stage softening model. This also indicates that the quicker reduction of cohesion in the first softening stage of the two-stage softening model plays a significant role in determining the collapse time.

To examine the outcome of the modelling in more detail, representative results of analyses S12H14, TS12H14 and TS12H14N3, in which the slope is set as 14 m high, 3:1 slope and with the coefficient of earth pressure at rest, $K_0 = 1.5$, are presented in the subsequent sections. Fig. 5.77 shows the representative model mesh.

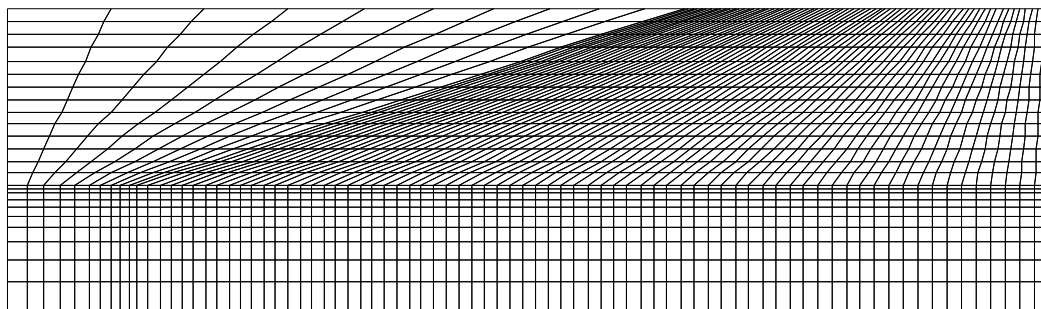
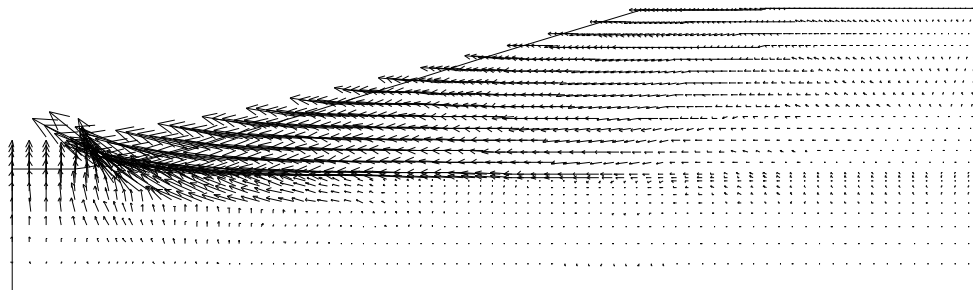


Fig. 5.77 Geometry of slope in stiff clay in analyses S12H14, TS12H14 and TS12H14N3

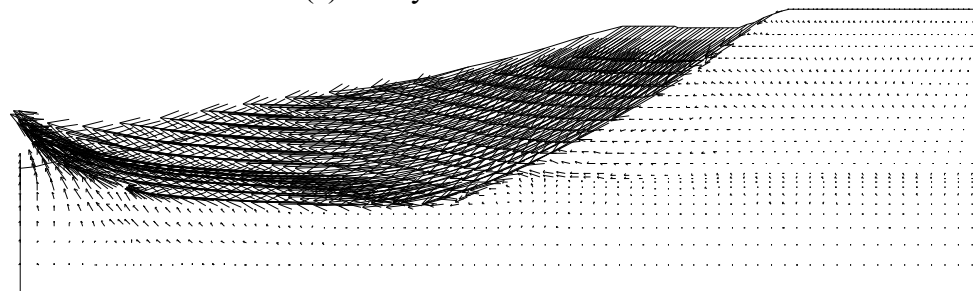
5.3.7.1 Results of analysis TS12H14

In analysis TS12H14, two-stage softening model is applied.

Fig. 5.78 shows the computed vectors of displacement at 15.3 years after excavation, and 29.1 years after excavation just at collapse. The vectors show the current mechanism of movement and indicate the eventual collapse mechanism. According to Fig. 5.78, the outer part of the slip surface has developed after 15.3 years, and the complete slip surface has developed after 29.1 years. The development of accumulated plastic shear strain shown in Fig. 5.79 also indicated the failure with the same failure surface.

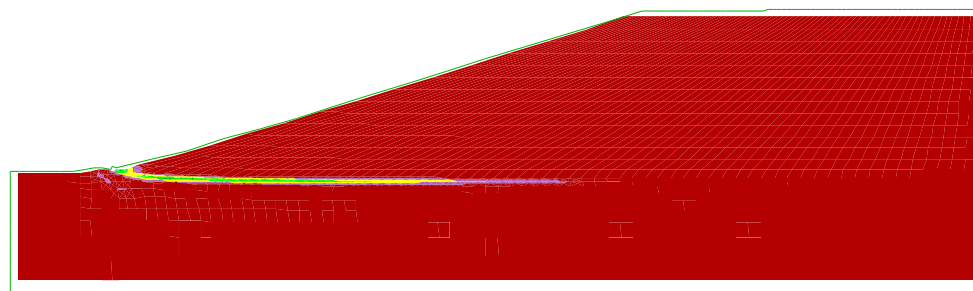


(a) 15.3 years after excavation

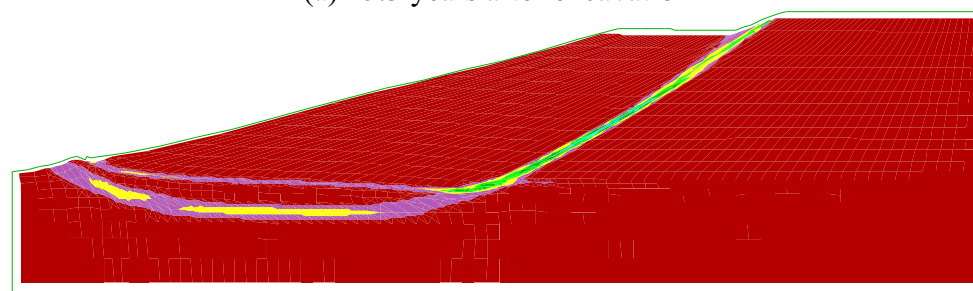


(b) 29.1 years at collapse

Fig. 5.78 Vectors of displacement for TS12H14



(a) 15.3 years after excavation

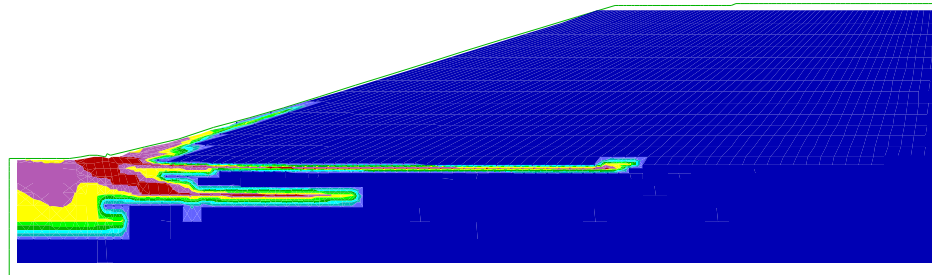


(b) 29.1 years at collapse

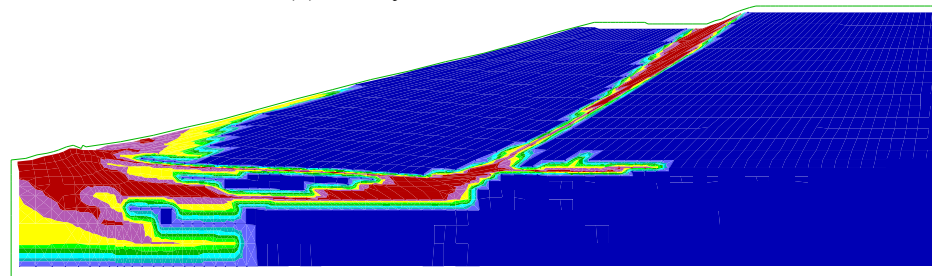
Fig. 5.79 Accumulated plastic shear strain for TS12H14

Fig. 5.80 and Fig. 5.81 show the progressive softening of strength parameters (cohesion and frictional angle) along the failure surface. It is evident that the progressive failure initiates at the toe of the slope, then extends further horizontally into the slope and finally connects with the back of slope with evident degradation of cohesion and frictional angle concentrated in the slip surface.

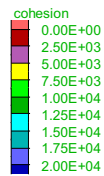
All these results predict that a complete thin rupture zone has formed 29.1 years after excavation. Residual strength has been reached along all the horizontal part of the zone and the amount of progressive failure is substantial.



(a) 15.3 years after excavation

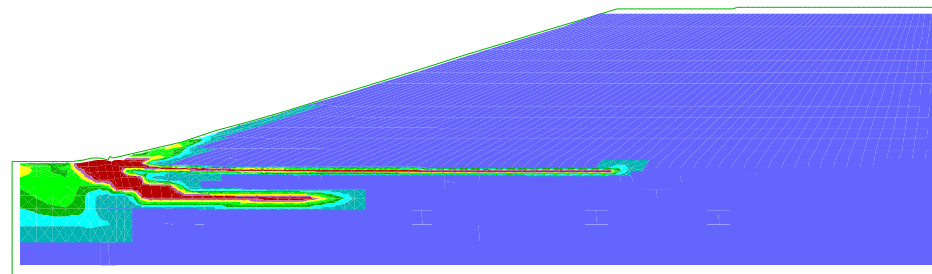


(b) 29.1 years at collapse

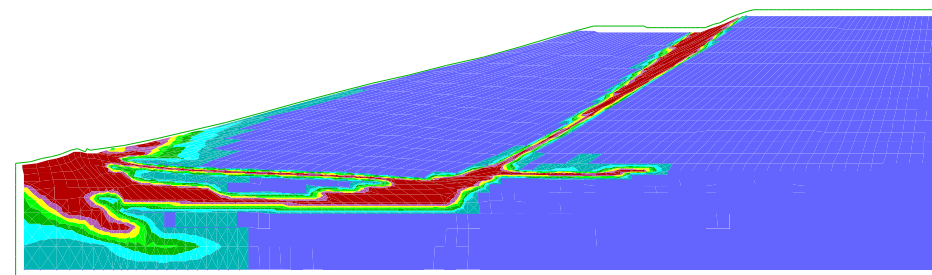


Contour interval= 2.50E+03

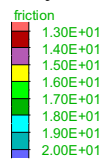
Fig. 5.80 Cohesion softening for TS12H14 (unit: Pa)



(a) 15.3 years after excavation



(b) 29.1 years at collapse



Contour interval= 1.00E+00

Fig. 5.81 Friction angle softening for TS12H14 (unit: °)

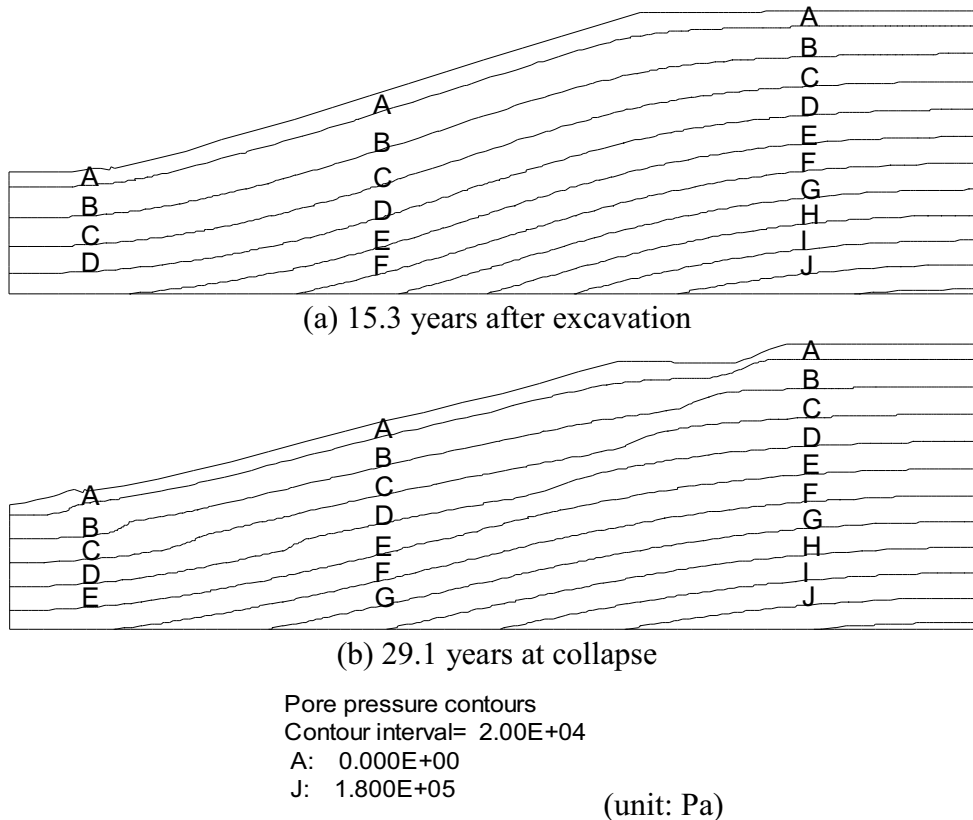


Fig. 5.82 Contours of pore pressure for TS12H14

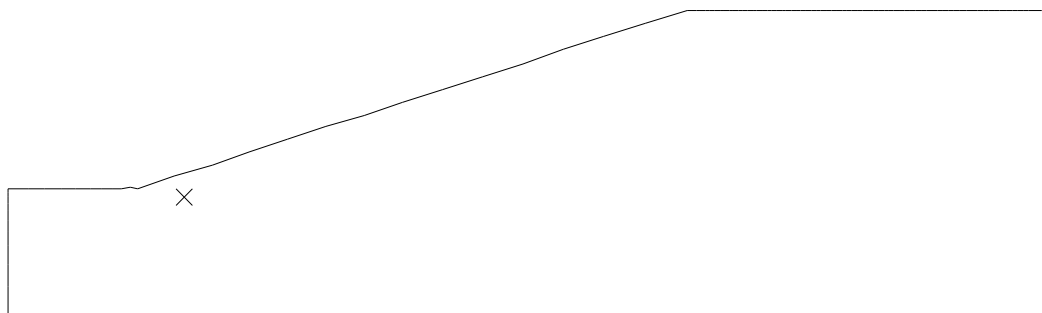


Fig. 5.83 Position of element (15,9) for S12H14, TS12H14 and TS12H14N3

Pore water pressure development is shown as contours in Fig. 5.82.

Fig. 5.84 presents the change of pore pressure of element (15,9) (seen in Fig. 5.83) which increases from -103 kPa just after excavation to 9 kPa 29.1 years after excavation. The pore pressure tends to be stable at this point during the progressive failure process.

Fig. 5.85 shows the horizontal displacement variations at mid-height of the slope with time. The mid-height displacements start to accelerate rapidly after gradual relative steady increase. Final collapse occurs abruptly 29.1 years after excavation without significant warning from accelerating displacements. Therefore it is not reliable, in this case, to monitor the displacement for assessing the slope safety.

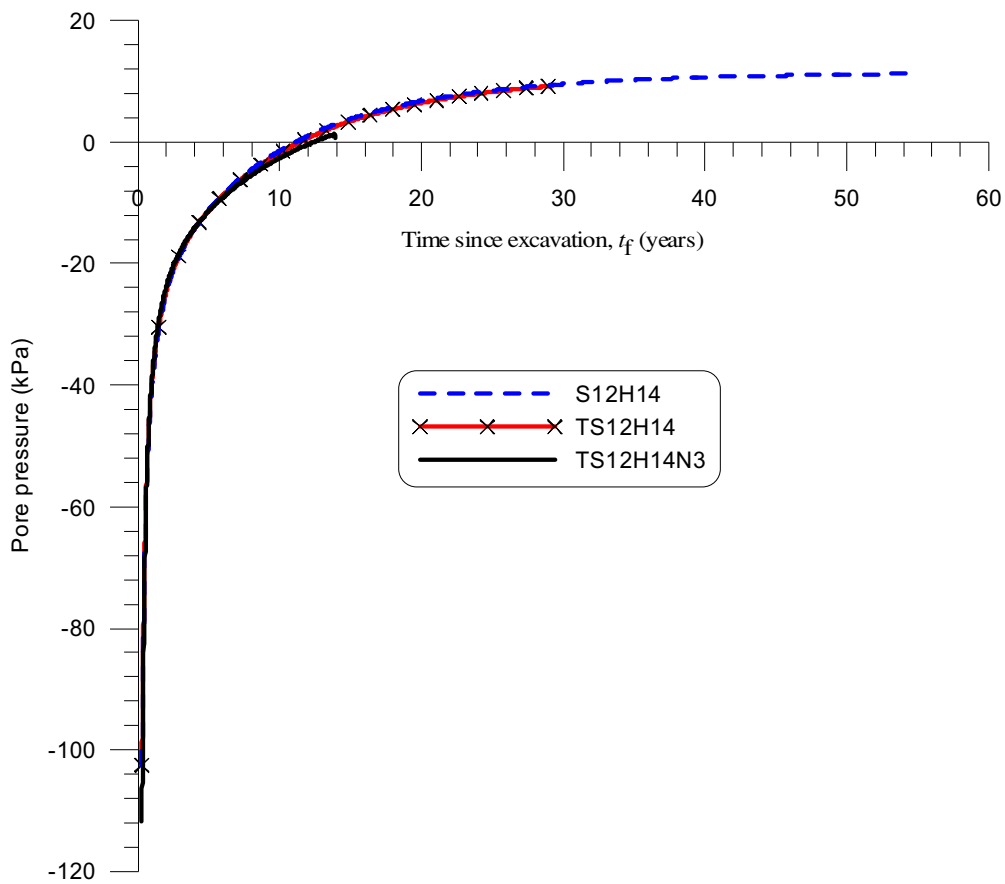


Fig. 5.84 Development of pore pressure of element (15,9) with time for S12H14, TS12H14 and TS12H14N3

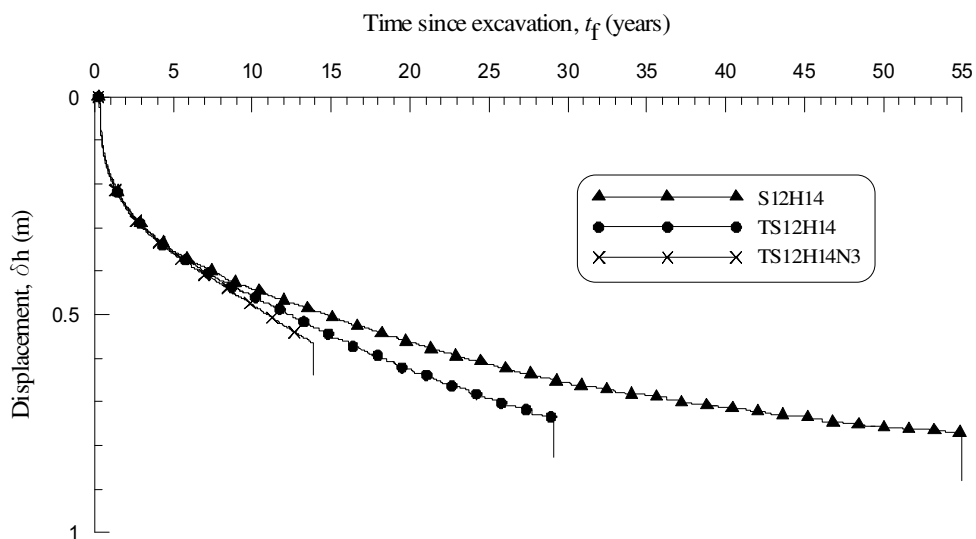


Fig. 5.85 Mid-slope horizontal displacement with time for S12H14, TS12H14 and TS12H14N3

5.3.7.2 Results of analysis S12H14

One-stage softening model is applied in analysis S12H14. The results show similar tendency to those of analysis TS12H14 and are summarised as

- (a) The collapse time is 55.0 years when the complete slip surface developed as shown in Fig. 5.86.
- (b) The failure surface is predicted by the development of accumulated plastic shear strain as shown in Fig. 5.87.
- (c) The progressive softening process is presented clearly in Fig. 5.88 and Fig. 5.89.
- (d) Pore water pressure development is shown as contours in Fig. 5.90 and Fig. 5.84 presents the change of pore pressure of element (15,9) in analysis S12H14 (seen in Fig. 5.83) which increases from -103 kPa just after excavation to 11 kPa 55.0 years after excavation.
- (e) The mid-height horizontal displacements shown in Fig. 5.85 start to accelerate rapidly after gradual relative steady increase. Final collapse occurs abruptly 55.0 years after excavation.

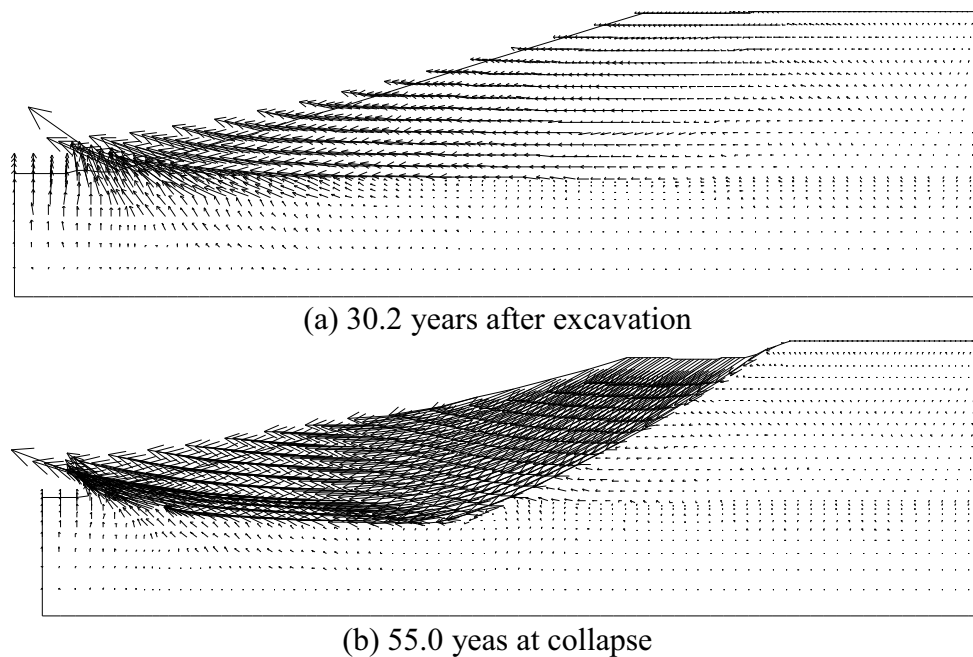
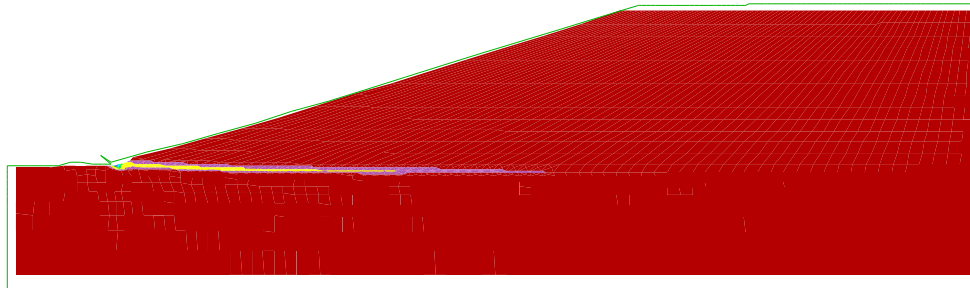
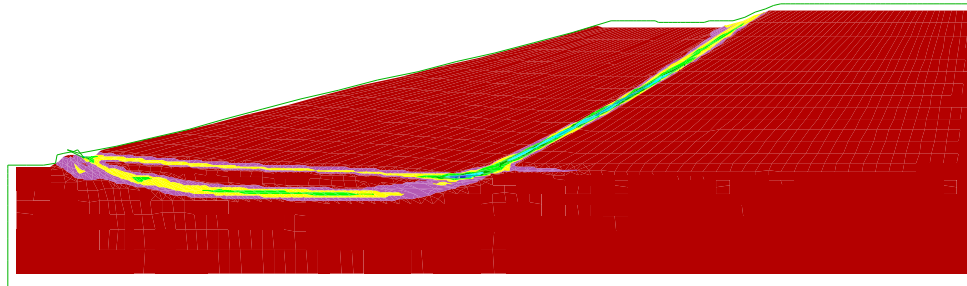


Fig. 5.86 Vectors of displacement for S12H14

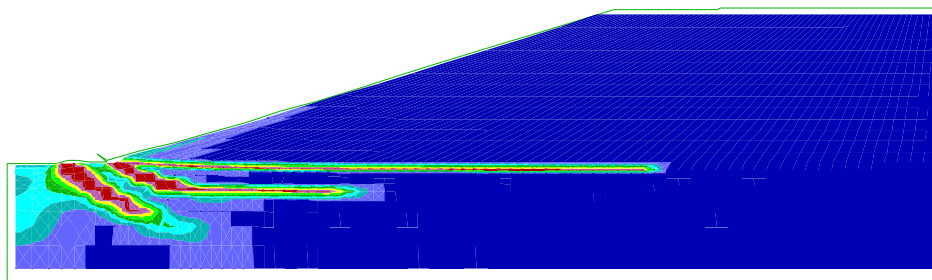


(a) 30.2 years after excavation

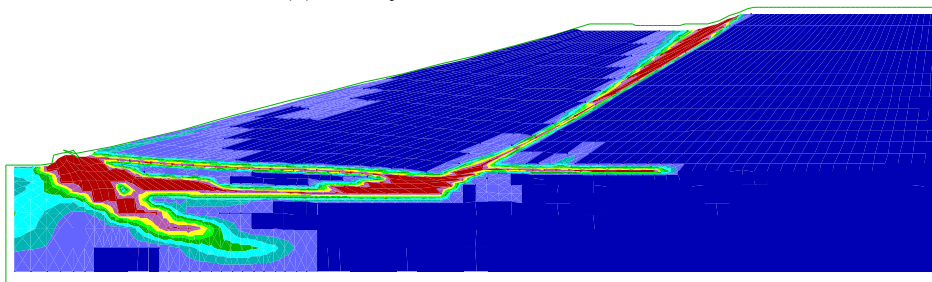


(b) 55.0 years at collapse

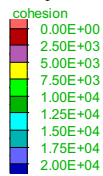
Fig. 5.87 Accumulated plastic shear strain for S12H14



(a) 30.2 years after excavation

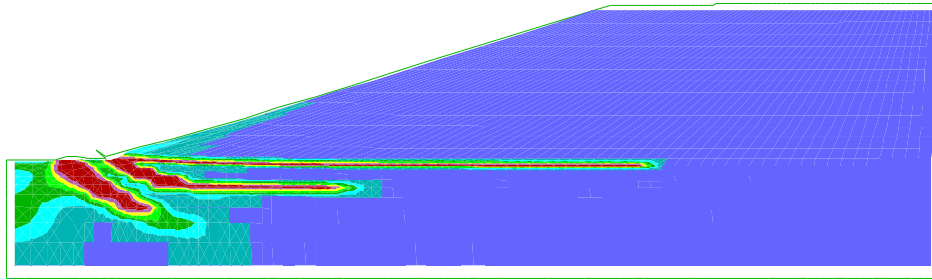


(b) 55.0 years at collapse

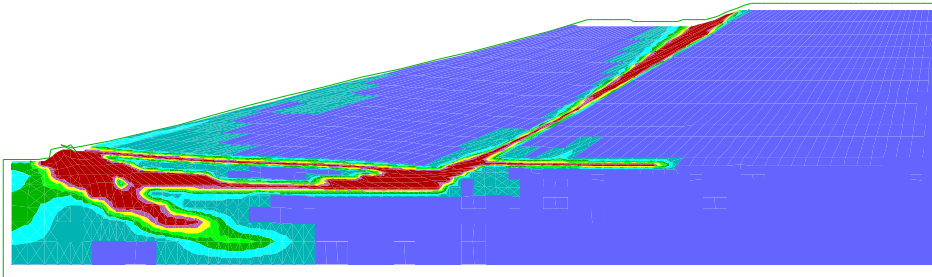


Contour interval= 2.50E+03

Fig. 5.88 Cohesion softening for S12H14 (unit: Pa)



(a) 30.2 years after excavation



(b) 55.0 years at collapse

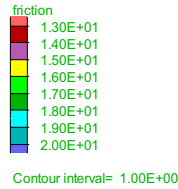
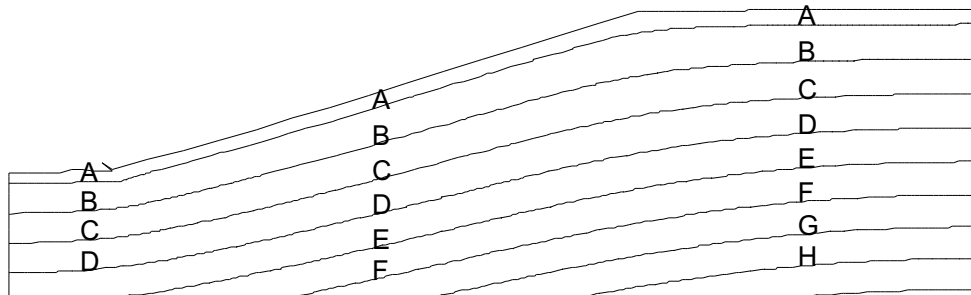
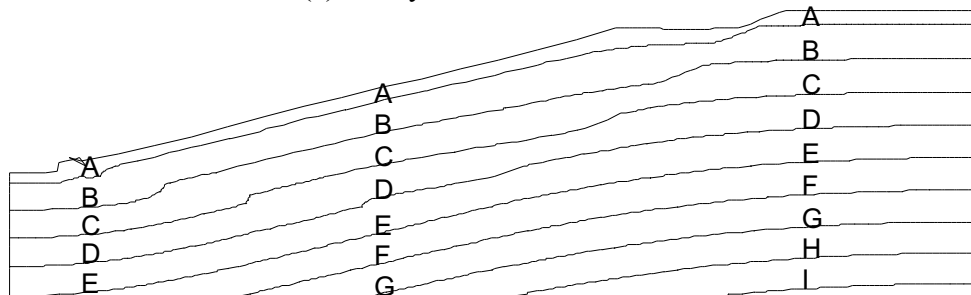


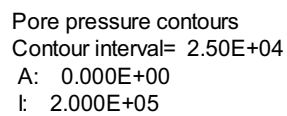
Fig. 5.89 Friction angle softening for S12H14 (unit: °)



(a) 30.2 years after excavation



(b) 55.0 years at collapse



(unit: Pa)

Fig. 5.90 Contours of pore pressure for S12H14

5.3.7.3 Results of analysis TS12H14N3

Two-stage softening model is applied in analysis TS12H14N3. The only difference from analysis TS12H14 is the plastic shear strain threshold values γ_p and γ_{pr} .

The results of analysis TS12H14N3 are summarised as

- (a) The outer part of the slip surface developed after 7.3 years and the complete slip surface has developed after 13.9 years (Fig. 5.91).
- (b) The shape of failure surface is given in Fig. 5.92.
- (c) Fig. 5.93 and Fig. 5.94 explain the progressive failure with softening.
- (d) Pore water pressure development is presented in Fig. 5.95 and Fig. 5.84 presents the change of pore pressure of element (15,9) (seen in Fig. 5.83) which increases from -112 kPa just after excavation to 1 kPa 13.9 years after excavation. It is interesting to find that the change of pore pressure of element (15,9) in analyses TS12H14, S12H14 and TS12H14N3 follows almost the same path although the value at collapse differs.
- (e) The mid-height horizontal displacements shown in Fig. 5.85 start to accelerate rapidly after a gradual relatively steady increase. Final collapse occurs abruptly 13.9 years after excavation.

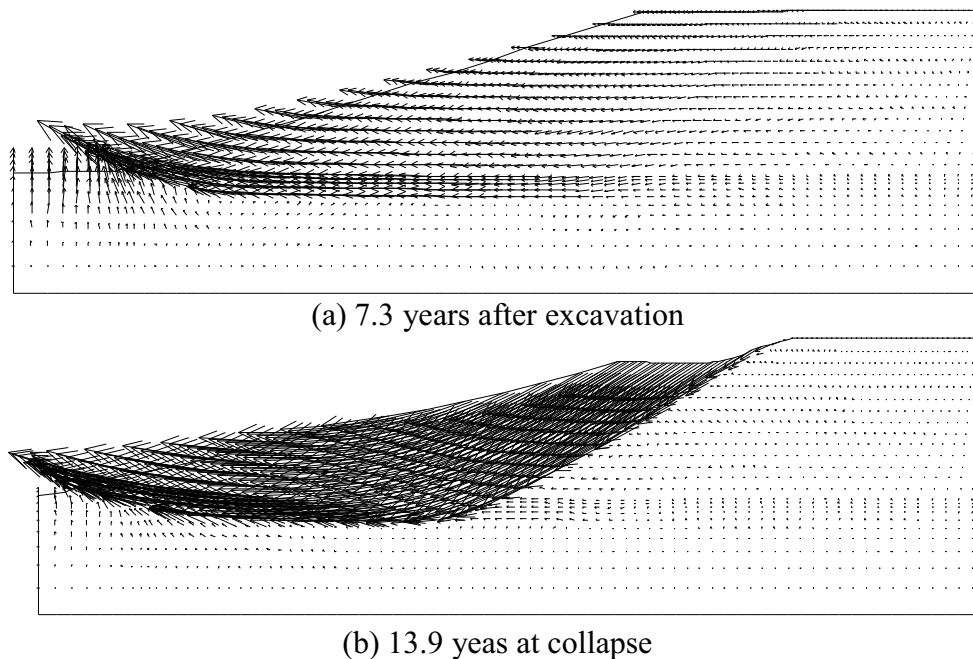
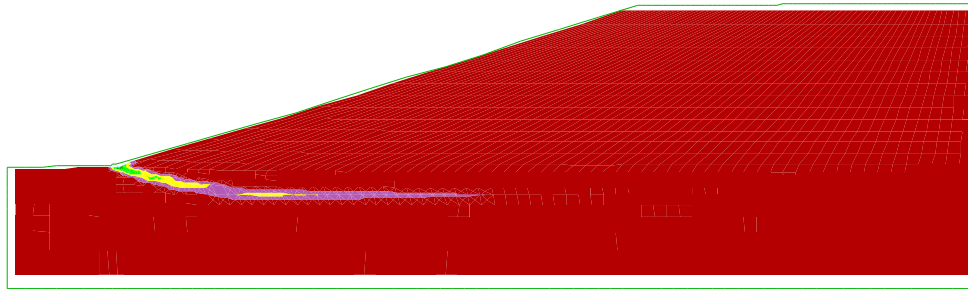
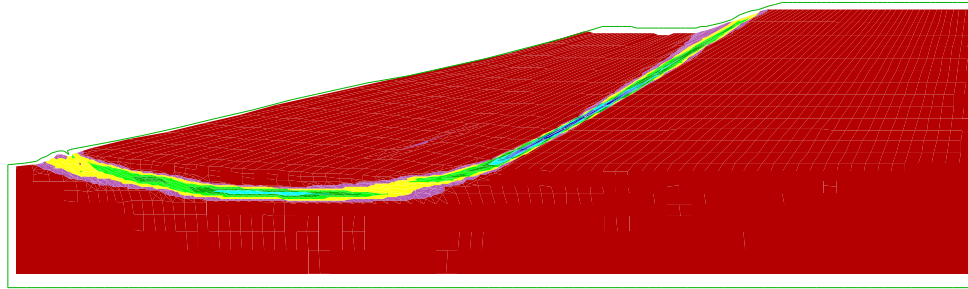


Fig. 5.91 Vectors of displacement for TS12H14N3

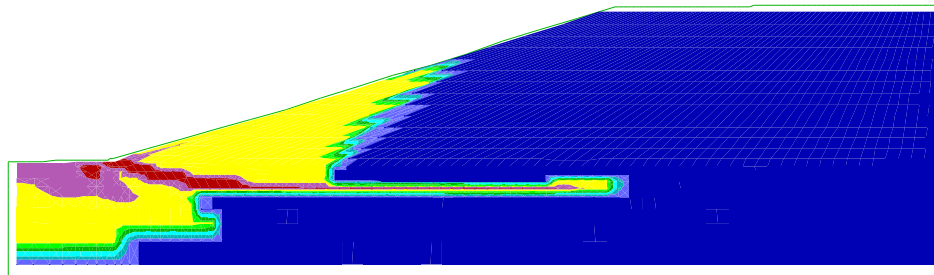


(a) 7.3 years after excavation

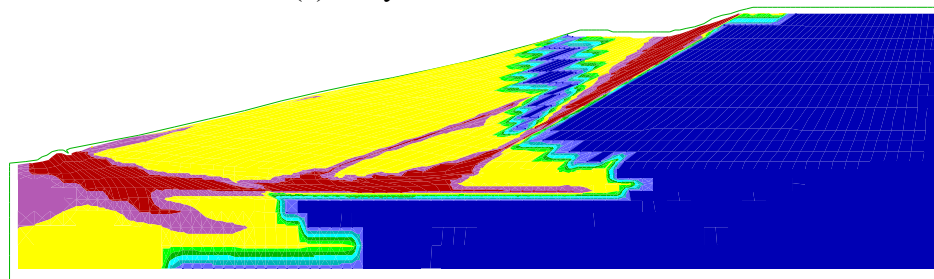


(b) 13.9 years at collapse

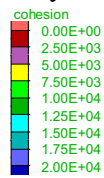
Fig. 5.92 Accumulated plastic shear strain for TS12H14N3



(a) 7.3 years after excavation

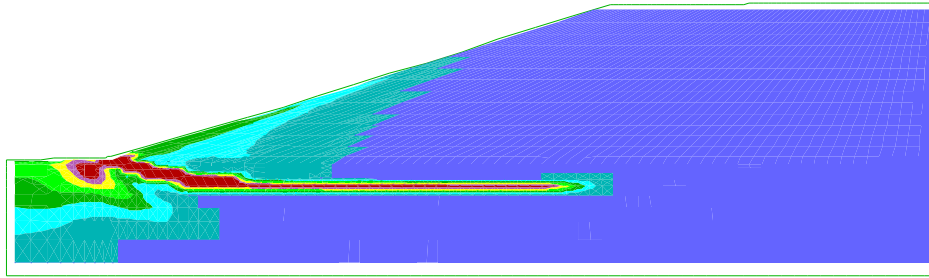


(b) 13.9 years at collapse

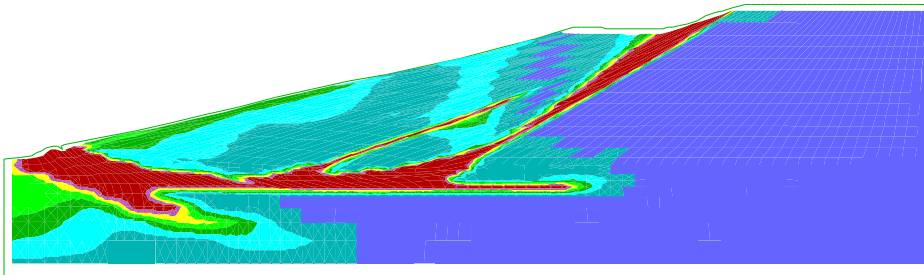


Contour interval= 2.50E+03

Fig. 5.93 Cohesion softening for TS12H14N3 (unit: Pa)



(a) 7.3 years after excavation



(b) 13.9 years at collapse

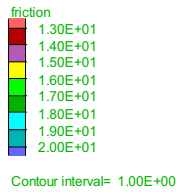
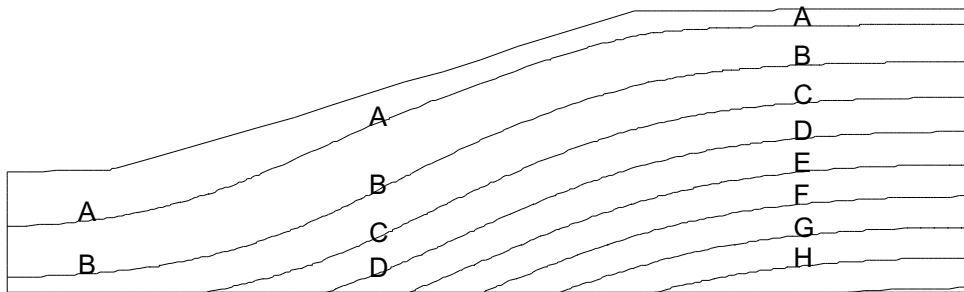
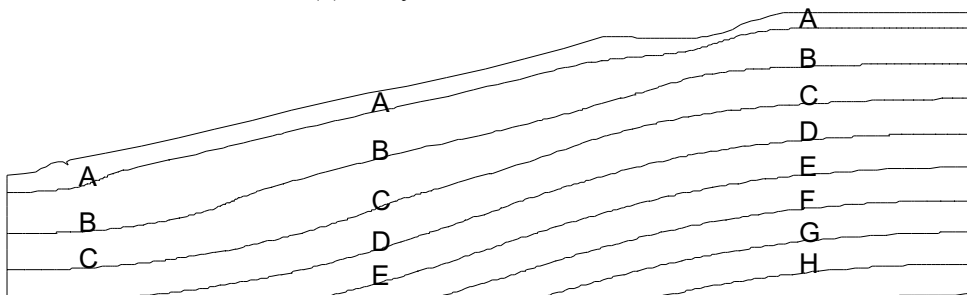


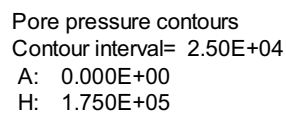
Fig. 5.94 Friction angle softening for TS12H14N3 (unit: °)



(a) 7.3 years after excavation



(b) 13.9 years at collapse



(unit: Pa)

Fig. 5.95 Contours of pore pressure for TS12H14N3

5.3.8 Determination of critical stable cutting height

A new aspect of this study is the determination of the minimum height of a cutting that would just reach failure for a given slope angle. Analyses were performed with one-stage model and two-stage softening model incorporating post-rupture strength. The ‘failure height’ for a given slope angle was established by undertaking a series of analyses, generally at 0.5 m intervals in height. The ‘critical stable height’ is taken as the average between the highest stable and the lowest unstable slope height. For this purpose, a slope is considered stable when it does not fail during the first 100 years of analysis.

5.3.8.1 Results of softening analyses with bulk peak strength

Table 5.9 Calculation schemes for softening analyses with bulk peak strength

| Analysis | Strength parameters |
|---|---|
| S3H8 S3H8.5 S3H9 S3H10 | $c'_p = 7\text{kPa}, \phi'_p = 20^\circ$ $c'_r = 2\text{kPa}, \phi'_r = 13^\circ$ $\gamma_p = 0.025, \gamma_r = 0.1$ |
| TS3H7.5 TS3H8 TS3H8.5 TS3H9 TS3H10 | $c'_p = 7\text{kPa}, \phi'_p = 20^\circ$ $c'_{pr} = 2\text{kPa}, \phi'_{pr} = 20^\circ$ $c'_r = 2\text{kPa}, \phi'_r = 13^\circ$ $\gamma_p = 0.015, \gamma_{pr} = 0.020, \gamma_r = 0.115$ |
| TS3H7.5N TS3H8N TS3H8.5N TS3H9N TS3H10N | $c'_p = 7\text{kPa}, \phi'_p = 20^\circ$ $c'_{pr} = 2\text{kPa}, \phi'_{pr} = 20^\circ$ $c'_r = 2\text{kPa}, \phi'_r = 13^\circ$ $\gamma_p = 0.025, \gamma_{pr} = 0.030, \gamma_r = 0.1$ |

Table 5.10 Results of stable slope height of softening analyses with bulk peak strength

| Analysis | Slope height H (m) | Slope ($\cot \beta$) | K_0 | Stable state | Middle slope XDisplacement at collapse/at stable state (mm) | t_f (years) |
|----------|--------------------|------------------------|-------|--------------|---|---------------|
| S3H8 | 8 | 3 | 1.50 | Stable | >167 | >100* |
| S3H8.5 | 8.5 | 3 | 1.50 | Unstable | 249 | 24.8 |
| S3H9 | 9 | 3 | 1.50 | Unstable | 275 | 20.8 |
| S3H10 | 10 | 3 | 1.50 | Unstable | 394 | 14.0 |
| TS3H7.5 | 7.5 | 3 | 1.50 | Stable | >142 | >100* |
| TS3H8 | 8 | 3 | 1.50 | Unstable | 203 | 60.8 |
| TS3H8.5 | 8.5 | 3 | 1.50 | Unstable | 279 | 24.8 |
| TS3H9 | 9 | 3 | 1.50 | Unstable | 297 | 20.3 |
| TS3H10 | 10 | 3 | 1.50 | Unstable | 407 | 15.2 |
| TS3H7.5N | 7.5 | 3 | 1.50 | Stable | >168 | >100* |
| TS3H8N | 8 | 3 | 1.50 | Unstable | 196 | 47.8 |
| TS3H8.5N | 8.5 | 3 | 1.50 | Unstable | 274 | 20.8 |
| TS3H9N | 9 | 3 | 1.50 | Unstable | 301 | 19.6 |
| TS3H10N | 10 | 3 | 1.50 | Unstable | 429 | 14.5 |

* Final calculation time

All the analyses applying one-stage and two-stage softening models adopting bulk peak strength with relevant strain-softening rates are listed in Table 5.9 where analyses S3H10, TS3H10 and TS3H10N are the same as S3 (Table 5.3), TS3 (Table 5.4) and TS3N (Table 5.5). In S3, TS3 and TS3N analysis series, the number after H of analysis name denotes the corresponding slope height.

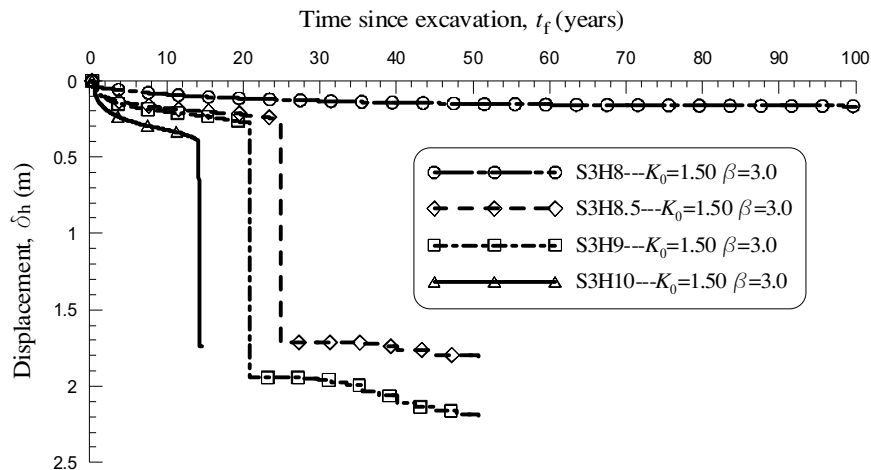


Fig. 5.96 Development of mid-slope displacement with time for S3H8-S3H10

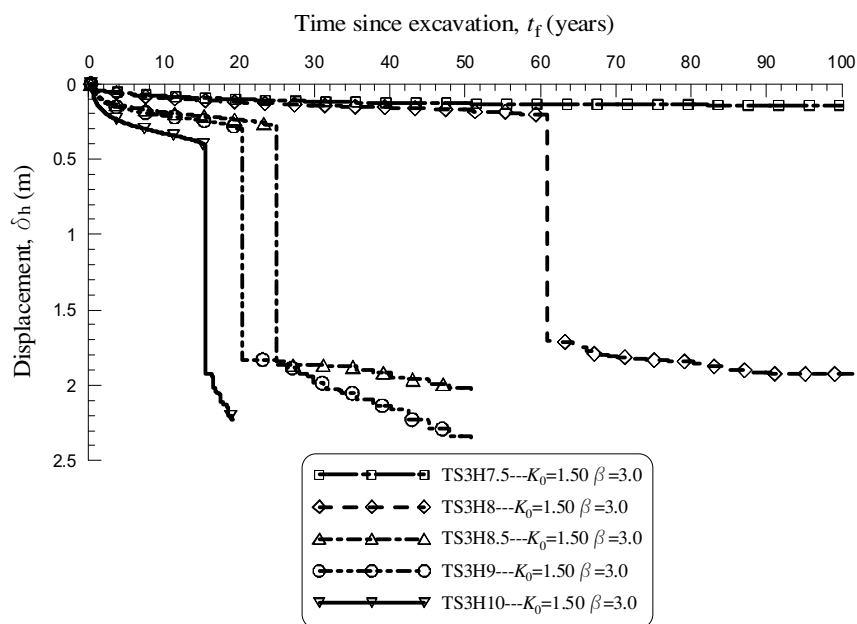


Fig. 5.97 Development of mid-slope displacement with time for TS3H7.5-TS3H10

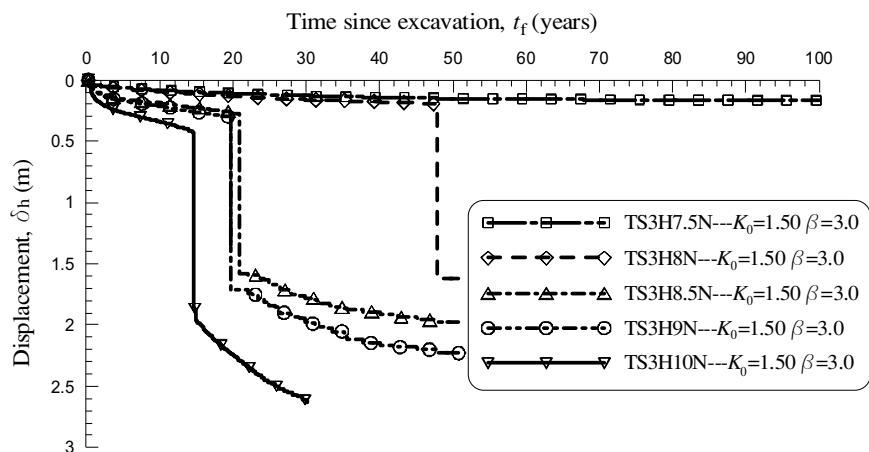


Fig. 5.98 Development of mid-slope displacement with time for TS3H7.5N-TS3H10N

Table 5.10 shows all the results of stable and unstable slope height of softening analyses with bulk peak strength.

Fig. 5.96, Fig. 5.97 and Fig. 5.98 show the development of horizontal displacement of the cutting at the middle height for a variety of heights and constant slope angle of 1(v):3(h) in S3, TS3 and TS3N analysis series respectively.

The results in Table 5.10 imply that:

1. For S3 analysis series with one-stage softening model:

a. The collapse time decreases with the increase in slope height. The 8.5 m cutting failed 24.8 years after excavation which indicates the abrupt increase in displacement after 0.5 m increase in slope height (seen in Fig. 5.96). The corresponding collapse times for 9 m and 10 m cuttings are respectively 20.8 years and 14.0 years.

b. For S3 analysis series, the ‘critical’ stable height is taken as 8.25 m (the average of 8.0 m and 8.5 m).

2. For TS3 analysis series with two-stage softening model:

a. The collapse time decreases with the increase in slope height. The 8.0 m cutting failed 60.8 years after excavation which indicates the abrupt increase in collapse time after 0.5 m increase in slope height. The corresponding collapse times for 8.5m, 9m and 10m cuttings are respectively 24.8 years, 20.3 years and 15.2 years.

c. With the same method used for S3 analysis series, the nominal ‘critical’ stable height for TS3H series is 7.75 m (the average of 7.5 m and 8 m). This value is 0.5 m lower than that for S3 analysis series. Although the collapse times for failed slopes are nearly identical, the displacements at collapse are larger in TS3 analysis series than those in S3 analysis series (seen in Table 5.10).

3. For TS3N analysis series with two-stage softening model:

a. The collapse time decreases with the increase in slope height. The 8.0 m cutting failed 47.8 years after excavation which indicates the abrupt increase in collapse time after 0.5 m increase in slope height. The corresponding collapse times for 8.5 m, 9 m and 10 m cuttings are respectively 20.8 years, 19.6 years and 14.5 years.

c. With the same method used for S3 analysis series, the nominal ‘critical’ stable height for TS3N analysis series is 7.75 m (the average of 7.5 m and 8 m). This value is 0.5 m lower than that for S3 analysis series. Although the collapse times for failed slopes are nearly identical, the displacements at collapse are larger in TS3N analysis series than those in S3 analysis series (seen in Table 5.10).

4. Comparisons

a. The collapse time in TS3 analysis series is longer than that in TS3N analysis series, which could be due to the slower softening rate from peak state to residual state in TS3 analysis series.

b. The nominal ‘critical’ stable height for TS3 analysis series is the same as that for TS3N analysis series. This may be due to the small difference of strength parameters between peak and post-rupture strengths.

c. All the results demonstrate that slope stability with the adoption of two-stage softening model is reduced compared with that with one-stage softening model. This implies the significant influence of rapid cohesion reduction with deviatoric plastic strain in the first softening stage of two-stage softening model.

5.3.8.2 Results of softening analyses with intact peak strength

As stated formerly in section 5.3.7 the determination of critical stable height adopting intact peak strength parameters ($c'_p = 20\text{kPa}$, $\phi'_p = 20^\circ$) is indicated in Table 5.7 and Table 5.8 through two analysis series (TS12H10-TS12H14 and S12H13_5-S12H14). The following relevant results can be noted:

1. Critical stable height for analyses TS12H10-TS12H14

a. The collapse time of analyses TS12H12_5-TS12H14 decreases with the increase in slope height. The 12.5 m cutting failed 50.8 years after excavation. The corresponding collapse times for 13.0 m and 14.0 m cuttings are respectively 40.0 years and 29.1 years.

b. The critical stable height for TS12H10-TS12H14 analysis series is 12.25 m (the average of 12.0 m and 12.5 m).

2. Critical stable height for analyses S12H13_5-S12H14

a. The collapse time of analyses S12H13_7-S12H14 decreases drastically with the increase in slope height. The 13.7 m high cutting failed 71.6 years after excavation. The corresponding collapse time for 14.0 m high cutting is 55.0 years.

c. The critical stable height for S12H13_5-S12H14 series is 13.6 m (the average of 13.5 m and 13.7 m).

3. Comparisons

a. The collapse time for analyses TS12H10-TS12H14 is shorter than that for analyses S12H13_5-S12H14. This is contrary to the comparison among S3 and TS3 analysis series due to the small difference of peak and post-rupture cohesion and the dominating role of friction angle. However, the notable cohesion difference between peak and post-rupture strengths in analysis series TS12H10-TS12H14 and S12H13_5-S12H14 surpasses the effect of friction angle on collapse time.

- b. The critical stable height applying intact peak strength for analyses TS12H10-TS12H14 is lower than that adopting bulk peak strength for analyses S12H13_5-S12H14. This is the same as stated in S3 and TS3 analysis series using bulk peak strength as the determination of critical stable height is concerned.
- c. Those observations shed light on the significance of post-rupture strength accounting for quicker cohesion degradation at the first stage in two-stage softening model.

5.4 Summary

A series of analyses of delayed progressive failure of cut slopes in stiff clays with *FLAC* similar to those conducted by Potts et al. (1997) have been performed using both one-stage and two-stage softening models. The results obtained are quite consistent with those by *FEM* (Potts et al., 1997). The numerical results reproduce well the progressive failure process, position of failure surface and failure time, and prove further the validity of the procedure proposed to simulate progressive failure with softening model.

Parametric analyses such as K_0 effect, surface suction effect, slope geometry effect, influence of post-rupture strength parameters and critical safe cutting height are also carried out to demonstrate the general influence of post-rupture strength while taking bulk peak strength as the initial peak strength in two-stage softening model. Moreover, the local FOS and average FOS are used to evaluate the slope stability in stiff clays with softening behaviour.

In analyses adopting bulk peak strength as initial peak strength in two-stage softening model, the critical stable cutting height using post-rupture strength parameters is 0.5 meter lower than that using only one-stage softening parameters whereas the collapse time with two-stage softening model is longer than that with one-stage softening model.

Meanwhile, in consideration of the whole formation process of highly fissured clay, the intact peak strength might be reckoned to be the initial original peak strength ($c'_p = 20\text{kPa}$, $\phi'_p = 20^\circ$) and the bulk peak strength could be reasonably assumed as the so-called relevant post-rupture strength ($c'_{pr} = 7\text{kPa}$, $\phi'_{pr} = 20^\circ$) accounting for the fissures in clay. At the same time, the residual strength ($c'_r = 2\text{kPa}$, $\phi'_r = 13^\circ$) is kept constant in all analyses. Based on this assumption, another series of analyses, incorporating post-rupture strength and S12H14 without considering post-rupture strength, were conducted to investigate the influence of applying intact peak strength and the entire softening process of stiff clay.

Furthermore, sensitivity analyses applying one-stage and two-stage models were performed by varying strength parameters such as softening rate, cohesion and friction angle.

The results of analyses using one-stage and two-stage models and the comparison between them indicate that:

- (a) The softening rate of strength parameters has remarkable influence on the collapse time and plays the main role of controlling collapse time.
- (b) The collapse time with two-stage softening model applying intact peak strength is shorter than that with one-stage softening model due to the notable cohesion difference between peak and post-rupture strengths.
- (c) The critical stable height with two-stage softening model applying intact peak strength is lower than that with one-stage softening model adopting bulk peak strength.
- (d) Slope stability with the adoption of two-stage softening model is lower than that using one-stage softening model due to the quicker cohesion reduction with deviatoric plastic strain in the first softening stage of two-stage softening model. Post-rupture strength is significant due to the faster cohesion degradation at the first stage in two-stage softening model.